

# **Chronology and Genealogy of Early Solar System Materials from Chromium Isotopes**

Inaugural dissertation  
of the Faculty of Science,  
University of Bern

presented by

**Aryavart Anand**

from India

Supervisor of the doctoral thesis:  
Prof. Dr. Klaus Mezger

Institut für Geologie



Unless otherwise stated (i.e., Chapter 2), this work is licensed under a Creative Commons Attribution 4.0 International License

<https://creativecommons.org/licenses/by/4.0/>

# **Chronology and Genealogy of Early Solar System Materials from Chromium Isotopes**

Inaugural dissertation  
of the Faculty of Science,  
University of Bern

presented by

**Aryavart Anand**

from India

Supervisor of the doctoral thesis:  
Prof. Dr. Klaus Mezger  
Institut für Geologie

Accepted by the Faculty of Science.

Bern, 30<sup>th</sup> August 2022

The Dean  
Prof. Dr. Zoltan Balogh

## Abstract

This thesis establishes crucial constraints on the chronology, source, transport and mixing of various solar system materials using high-precision Cr isotopes as chronological and genealogical tools. It includes individual studies based on the determination of radiogenic and nucleosynthetic Cr isotope variations in meteorites and terrestrial impactites with meteoritic contaminations.

The first study presents the  $^{53}\text{Mn}$ - $^{53}\text{Cr}$  isotope systematics in ordinary chondrites constraining the accretion and onset and progressive metamorphism of their parent bodies. Both chromite model ages and isochron ages are obtained that correlate with the petrological grade of the samples and are consistent with an onion-shell structure of the chondrite parent bodies. The oldest chromite model age obtained for type 3 samples along with the established Al-Mg chondrule formation ages constrain the accretion of the parent bodies to  $\geq 2.1$  Ma after CAI formation, implying that planetesimal accretion immediately followed chondrule formation.

The second study presents chromite/daubréelite model ages from IIAB, IIIAB and IVA magmatic iron meteorites. The model ages are within  $\sim 1.5$  Ma after the formation of calcium-aluminium-rich inclusions (CAIs) and define the time of metal core formation in the respective parent bodies, assuming metal-silicate separation was an instantaneous event that induced strong chemical fractionation of Mn from the more siderophile Cr. The calibration of Mn-Cr ages with the established Hf-W ages of samples from the same magmatic iron meteorite groups constrains the initial  $\epsilon^{53}\text{Cr}$  of the solar system to  $-0.30 \pm 0.05$ , and thus lower than previously estimated.

The third study focuses on the  $^{53}\text{Mn}$ - $^{53}\text{Cr}$  chronology and  $\epsilon^{54}\text{Cr}$ - $\Delta^{17}\text{O}$  genealogy of Erg Chech 002, which is the oldest andesite in the Solar System. Both  $^{53}\text{Mn}$ - $^{53}\text{Cr}$  isochron and chromite model ages for EC 002 predate the chondrule formation interval or are at the earlier side of this interval. Additionally, neutron-rich  $^{54}\text{Cr}$  excesses (nucleosynthetic anomalies) combined with mass-independent isotope variations of  $^{17}\text{O}$  provide genealogical constraints on the accretion region of the EC 002 parent body. The  $^{54}\text{Cr}$  and  $^{17}\text{O}$  isotope compositions of EC 002 confirm its origin in the non-carbonaceous reservoir and overlap with the vestoid material NWA 12217 and anomalous eucrite EET 92023.

The fourth study employs Cr isotopes in the identification of the type of impactor involved in the formation of the Dhala impact structure, India. The depleted  $\epsilon^{54}\text{C}$  isotope composition of the Dhala impact melt breccia D6-57 indicates an inheritance of the composition from an impactor originating in the non-carbonaceous reservoir. Furthermore, the binary mixing calculations using Cr isotopes indicate contamination of ~1.2 wt% from a ureilite or 2-3 wt% from an acapulcoite-like impactor.

## Acknowledgements

I owe my greatest debt to Prof. Klaus Mezger for giving me the opportunity to work on such an exciting project. You have been the best supervisor one could imagine, and it is my honour to have worked with you. Your patience and encouragement have nurtured me as a better scientist. I am also grateful to my co-supervisor, Prof. Beda Hofmann for his guidance throughout the course of this project. The time that I spent in Oman with the ‘Omani-Swiss Meteorites Search 2022’ team is the most cherished time of my PhD project. I am also thankful to you for providing me with samples from the Natural History Museum Bern to carry out this research. I am deeply thankful to Prof. Herbert Palme, who agreed to evaluate this thesis as an external reviewer.

This thesis work would not have been possible without the Swiss Government Excellence Scholarship awarded to me to pursue this project. I thank the Federal Department of Economy, Education and Research of the Swiss Confederation for granting the scholarship.

I am grateful to Dr. Martin Wille for training me in the PicoTrace and TIMS lab and helping me develop the analytical skills which were essential for this research work. I would like to thank Jonas Pape, Om Prakash Panday, Arathy Ravindran and Dipankar Pathak for their guidance and many discussions that helped me develop and plan this project.

I have been fortunate to have a great group of friends and colleagues in the Institute of Geological Sciences including David Mair, Jan Hofmann, Qasid Ahmad, Pascal Kruttasch, Sukalpa Chatterjee, Adrianus Damanik and many more. Thank you all for countless scientific and non-scientific discussions, friendships and support that made my PhD experience memorable.

Finally, I would like to thank my family Mrs. Abha Anand, Dr. H. K. Chourasia, Amrita Anand, Ishant Vyas and Tejaswini Karra for all the love, encouragement and support throughout the time of my PhD studies and beyond.

# Table of Contents

Abstract .....	3
Acknowledgements .....	5
List of Figures .....	8
List of Tables .....	10
 <b>Introduction .....</b>	 <b>11</b>
 <b>1. Chronological constraints on the thermal evolution of ordinary chondrite parent bodies from the <math>^{53}\text{Mn}</math>-<math>^{53}\text{Cr}</math> system</b>	
Abstract .....	26
1.1 Introduction .....	27
1.2 Samples and Analytical Methods .....	28
1.2.1 Model for $\epsilon^{53}\text{Cr}$ evolution in chondrites .....	30
1.3 Results .....	33
1.3.1 Mineral compositions .....	33
1.3.2 Olivine-spinel thermometry .....	33
1.3.3 Mn/Cr ratio in chromite and silicate fractions .....	35
1.3.4 Cr isotope compositions .....	39
1.3.5 Correction for spallogenic Cr .....	39
1.3.6 Chromite model ages .....	41
1.3.7 Isochron ages .....	43
1.4 Discussion .....	45
1.4.1 The onset and progression of metamorphism in ordinary chondrites .....	45
1.4.2 Closure temperature of the Mn-Cr system in spinel .....	47
1.4.3 Significance of initial $^{53}\text{Cr}/^{52}\text{Cr}$ and $^{53}\text{Mn}$ abundances for chromite model ages .....	52
1.4.4 Chromite model ages vs. two-point isochron ages .....	53
1.4.5 Time of accretion and cooling history for chondrite parent bodies .....	55
1.5 Conclusions .....	59
 <b>2. Early differentiation of magmatic iron meteorite parent bodies from Mn-Cr chronometry</b>	
Abstract .....	75
2.1 Introduction .....	76

2.2	Methods .....	77
2.2.1	Model for $\epsilon^{53}\text{Cr}$ evolution in chondritic reservoir .....	77
2.3	Results .....	79
2.4	Discussion .....	79

### **3. $^{53}\text{Mn}$ - $^{53}\text{Cr}$ chronology and $\epsilon^{54}\text{Cr}$ - $\Delta^{17}\text{O}$ genealogy of Erg Chech 002: the oldest andesite in the Solar System**

Abstract .....	89
3.1 Introduction .....	90
3.2 Analytical Methods .....	91
3.3 Results .....	95
3.4 Discussion .....	97
3.4.1 $^{53}\text{Mn}$ - $^{53}\text{Cr}$ chronology of Erg Chech 002 .....	97
3.4.2 $\epsilon^{54}\text{Cr}$ - $\Delta^{17}\text{O}$ genealogy of Erg Chech 002 .....	100
3.5 Conclusions and Outlook .....	104

### **4. Chromium isotopes identify the extraterrestrial component in impactites from Dhala Impact Structure, India**

Abstract .....	117
4.1 Introduction .....	118
4.2 Geological Setting of the Dhala Impact Structure .....	120
4.3 Samples and Analytical Methods .....	121
4.4 Results .....	123
4.5 Discussion .....	126

### **Appendix**

A1.	Cr and O isotopes link IVA irons and LL chondrites .....	143
A2.	IIAB and IIG iron meteorites originated from a single parent body .....	146
S1.	Supplementary Information of Chapter 1 .....	151
S2.	Supplementary Information of Chapter 2 .....	160



## List of Figures

- 1.1. Backscattered electron (BSE) images showing typical occurrences of spinel grains/aggregates in type 3 and 6 ordinary chondrites.
- 1.2. Individual temperature values estimated with the olivine-spinel thermometer in type 3 and 6 ordinary chondrites.
- 1.3. Mn/Cr ratios in chromite and silicate fractions from ordinary chondrites.
- 1.4.  $\epsilon^{53}\text{Cr}$  vs  $\epsilon^{54}\text{Cr}$  diagram for the chromite and silicate fractions from the ordinary chondrites.
- 1.5. Model ages for chromite fractions from type 3 and 6 ordinary chondrites plotted on a curve representing the  $\epsilon^{53}\text{Cr}$  evolution of the chondritic reservoir.
- 1.6.  $\epsilon^{53}\text{Cr}$  vs  $^{55}\text{Mn}/^{52}\text{Cr}$  diagrams for type 3 and 6 ordinary chondrites.
- 1.7. Closure temperature of the Mn-Cr system in spinel grains.
- 1.8. A comparison between chromite model ages and two-point isochron ages determined for the studied ordinary chondrite samples.
- 2.1.  $\epsilon^{53}\text{Cr}$  values of chromite/daubréelite from magmatic iron meteorites plotted on Cr isotope evolution curve determined for a chondritic reservoir through time.
- 2.2. Comparison between Mn-Cr and Hf-W core formation ages in magmatic irons.
- 2.3. Timeline of early solar system formation showing parent body differentiation in magmatic iron meteorites, chondrule formation, and parent body metamorphism on ordinary chondrites.
- 3.1. Separation scheme for EC 002 fractions.
- 3.2.  $\epsilon^{53}\text{Cr}$  vs. Fe/Cr and spallogenic Cr corrected and uncorrected  $\epsilon^{54}\text{Cr}$  vs.  $\epsilon^{53}\text{Cr}$  data for EC 002 fractions.
- 3.3.  $^{53}\text{Mn}$ - $^{53}\text{Cr}$  systematics of EC 002 fractions.
- 3.4.  $\Delta^{17}\text{O}$  diagram showing EC 002, NWA 12217, 12319, and 12562 in relation to other achondrite groups and anomalous HEDs.
- 3.5.  $\Delta^{17}\text{O}$ - $\epsilon^{54}\text{Cr}$  diagram showing EC 002 with other achondrite and chondrite groups within 'non-carbonaceous (NC)' reservoir.
- 3.6. Compilation of chronological data for EC 002, angrites and magmatic irons.
- 4.1. Comparison between Cr isotopic composition of the rock samples from Dhala impact structure and terrestrial rock samples.

- 4.2.** Comparison between Cr isotopic composition of the rock samples from Dhala impact structure and meteorite groups within the non-carbonaceous reservoir.
- 4.3.** (a)  $^{187}\text{Os}/^{188}\text{Os}$  vs Os composition of the rock samples from Dhala impact structure and meteorite groups (b)  $\epsilon^{54}\text{Cr}$  vs Os composition of the rock samples from the Dhala impact structure and meteorite groups.
- A1.1.**  $\Delta^{17}\text{O}-\epsilon^{54}\text{Cr}$  diagram of IVA irons and LL/L ordinary chondrites.
- A2.1.** Spallogenic Cr correction in troilite fractions from Twannberg (IIG) and Cape York (IIIAB) iron meteorites.
- A2.2.**  $\Delta^{17}\text{O}-\epsilon^{54}\text{Cr}$  diagram for Twannberg (IIG) and Sikhote Alin (IIAB).
- S1.1.** Drift in  $\epsilon^{53}\text{Cr}$  over a period of 9 months in Cr standard NIST SRM 979.
- S1.2.** Comparison between the  $\epsilon^{53}\text{Cr}$  evolution curve of the chondritic reservoir using initial  $\epsilon^{53}\text{Cr} = -0.23$ , canonical  $^{53}\text{Mn}/^{55}\text{Mn} = 6.28 \times 10^{-6}$  as reported by Trinquier *et al.* (2008) and initial  $\epsilon^{53}\text{Cr} = -0.177$ , canonical  $^{53}\text{Mn}/^{55}\text{Mn} = 6.8 \times 10^{-6}$  as reported by Göpel *et al.* (2015).
- S2.1.** (a)  $\epsilon^{54}\text{Cr}$  vs  $\epsilon^{53}\text{Cr}$  and (b) Fe/Cr vs  $\epsilon^{53}\text{Cr}$  plots for magmatic iron meteorites.
- S2.2.** Mn-Cr model ages plotted on an  $\epsilon^{53}\text{Cr}$  evolution curve and solar system initials  $\epsilon^{53}\text{Cr}_i = -0.23$  and  $\epsilon^{53}\text{Cr}_i = -0.30$ .
- S2.3.** Comparison between Mn-Cr and Hf-W core formation ages.

## List of Tables

- 1.1.** Olivine compositions in ordinary chondrites determined by EPMA and end member classification.
- 1.2.** Spinel composition in ordinary chondrites determined by EPMA and end member classification.
- 1.3.** Average temperature and range of temperatures derived from olivine-spinel thermometry in ordinary chondrites.
- 1.4.** Mn/Cr, Fe/Cr and Cr isotopic compositions of ordinary chondrites.
- 1.5.** Chromite model ages and two-point isochron ages determined in type 3 and 6 ordinary chondrites.
- 2.1.** Mn/Cr, Fe/Cr and Cr isotopic compositions of chromite and daubréelite fractions from iron meteorites.
- 3.1.** Sequential dissolution procedure and proportion of Mn and Cr leached in each sequential dissolution step for EC 002.
- 3.2.**  $^{55}\text{Mn}/^{52}\text{Cr}$ , Fe/Cr and Cr isotopic compositions of EC 002 fractions.
- 4.1.** Chromium isotope compositions and Cr, Ni, Co abundances of the bulk rock samples from Dhala impact structure and meteorites.
- 4.2.** Os concentration and  $^{187}\text{Os}/^{188}\text{Os}$  isotopic composition of the bulk rock samples from Dhala impact structure, meteorites and upper continental crust.
- A2.1.** Cr-and O-isotope composition of Twannberg (IIG), Cape York (IIIAB) and Sikhote Alin (IIAB) chromite/daubréelite/troilite fractions.
- S1.1.** Cr, Mn and Fe concentrations and Mn/Cr ratios in the chromite and silicate fractions of ordinary chondrites and BHVO2 rock standard.
- S1.2.**  $\epsilon^{53}\text{Cr}$  and  $\epsilon^{54}\text{Cr}$  compositions of the ordinary chondrite samples.
- S2.1.**  $\epsilon^{53}\text{Cr}$  and  $\epsilon^{54}\text{Cr}$  compositions of the magmatic iron meteorites.
- S2.2.** Summary of  $(^{53}\text{Mn}/^{55}\text{Mn})_i$  and  $(\epsilon^{53}\text{Cr})_i$  solar system initial abundances.

# Introduction

Our solar system formed 4567.18 million years ago (Amelin *et al.*, 2010) from the collapse of a dense core inside an interstellar molecular cloud. Conservation of angular momentum transformed the material accreted by the Sun into the shape of a protodisk which we now call the solar protoplanetary disk. In the inner part of this disk, the first solids condensed with near-solar composition (Grossman 1972, Grossman and Larimer 1974) and along with dust grains and gas, accreted into kilometre-sized planetesimals within less than  $10^4$  years (e.g., Chambers, 2004). The current state-of-the-art of research on dust evolution into planetesimals is that the initial dust (siliceous materials and monomers  $\sim 1 \mu\text{m}$  large) grew by sticking collisions that led to mm to cm-sized aggregates (“pebbles”) and then the formation of planetesimals from the accretion of these pebbles can be explained by the following two scenarios: (i) the gravitational-collapse which requires a high spatial concentration of the “pebbles”, which could be achieved by streaming instability (Youdin and Goodman, 2005), and a subsequent gravitational collapse (Johansen *et al.*, 2007), or (ii) the mass transfer scenario, in which the aggregates further grow by high-velocity collisions between small projectile aggregates and larger target aggregates (Windmark *et al.*, 2012a,b; Garaud *et al.*, 2013; Booth *et al.*, 2018 and see Blum 2018 for a review). Afterwards, under the influence of gravitation and gas drag forces, the planetesimals started to collide and accumulate into Moon- to Mars-size planetary embryos within a few  $10^6$  years (Weidenschilling *et al.*, 1997). Collisions among the early planetary embryos mark the late stages of accretion that ultimately led to the formation of terrestrial planets accreting almost all the other smaller bodies. Numerical simulations suggest that this stage may have taken  $10^7$ – $10^8$  years (e.g., Chambers and Wetherill, 1998; Agnor *et al.*, 1999). The modelling results and predictions about our own solar system have been supported by astronomical observations of other protoplanetary disks in the universe, which are being studied to link the physicochemical state in these discs to the properties of exoplanets that form in them. Such results have been published for Spitzer/IRS data (SED, mid-IR line fluxes), VLT/CRIRES (CO ro-vib), VLT/PIONEER (H-band visibilities), Herschel (far-IR continuum & lines), ALMA (millimetre continuum & lines) as well as from different radio telescopes.

Determining the timescales (chronological studies) for the accretion of planetesimals that later formed the terrestrial planets and asteroids and linking this information to the source reservoir of their precursor material (genealogical studies) is key to understanding the temporal and spatial constraints on early solar system processes. Meteorites, rocks that formed during the early stages of the solar system and made their way to the Earth, are our most powerful

means to retrace the formation, transport and evolution of early planetesimals at different times and locations in the protoplanetary disk and beyond. They sample various asteroids, the Moon and Mars and are the most accessible source of extraterrestrial matter for direct study in the laboratory.

The aim of this thesis is to better understand the chronology and genealogy of the various solar system materials using high-precision Cr isotopes as chronological and genealogical tools. These studies are based on the determination of radiogenic and nucleosynthetic Cr isotope variations in meteorites and terrestrial impactites with meteoritic contaminations. The following sections will first give a general overview of meteorites and their classification, followed by radiogenic and nucleosynthetic Cr isotopes as tools to study them.

## **Meteorites and their classification**

Meteorites represent the debris generated from planetary collisions and are mostly derived from the main belt asteroids located between the orbits of Mars and Jupiter. The parent bodies of meteorites are the earliest formed planetesimals that survived the late stages of accretion when the growing planets swept almost all the other smaller bodies.

Petrologically, meteorites can be categorized into (1) differentiated meteorites and (2) undifferentiated meteorites. Differentiated meteorites originate from parent bodies that accreted as early as the first 2 Ma after the birth of the solar system or several Ma later. During the early stages of planetary formation large-scale impacts and decay of short-lived radioisotopes (especially  $^{26}\text{Al}$ ) caused the planetary interiors to heat up, melt and differentiate into a metallic core and a silicate mantle (e.g., Walter and Tronnes, 2004). Magmatic iron meteorites represent the core of such early formed differentiated bodies whereas meteorite groups such as basaltic eucrites, Angrites and unclassified meteorites including Erg Chech (EC) 002, Graves Nunataks (GRA) 06128 and 016129, ALM-A and NWA 11119, represent the material derived from the crust of differentiated protoplanets after metal-silicate equilibration (Shearer *et al.*, 2010; Bischoff *et al.*, 2014; Srinivasan *et al.*, 2018; Barrat *et al.*, 2021). Unlike the parent bodies of differentiated meteorites, the parent bodies of undifferentiated meteorites either formed later when the major heat source  $^{26}\text{Al}$  had decayed or were too small to undergo global melting and differentiation. Undifferentiated meteorites contain the most primitive

materials that existed during the nebular phase of the solar system and during the formation of their parent bodies. These primitive materials include (1) high-temperature condensates, such as the Ca, Al-rich inclusions (CAIs) that also represent the oldest Solar System objects dated so far, (2) chondrules, which are (sub-) millimetre-sized spherical objects, formed when dust-like precursors were partially or completely molten by rapid heating and subsequent fast cooling in space and, (3) fine-grained matrix that includes primitive organic molecules and presolar grains from previous star generations. Due to the abundance of chondrules in undifferentiated meteorites, they are known as chondrites and further classified into three major classes: carbonaceous chondrites, ordinary chondrites and enstatite chondrites. The carbonaceous chondrites were named so because of an appreciable amount of carbonaceous material (other than free carbon i.e., diamond and graphite), and are the most pristine rock samples of our solar system. The carbonaceous chondrites can have abundant water and other volatiles and they are attributed to having brought these compounds to dry proto-Earth as part of the giant impact and as the late veneer that ultimately enabled the emergence of life (Wänke 1988, Mezger *et al.*, 2021). The ordinary chondrites are the most common group of meteorites in our collections, with a relative fall frequency of 79.9% (Keil *et al.*, 1994). Although the parent bodies of ordinary chondrites never experienced global melting and differentiation, they were metamorphosed to different degrees and are divided into petrological types ranging from petrological type 3 (unequilibrated, low thermal overprint) to types 4-6 (equilibrated, higher metamorphic grades) (Van Schmus and Wood, 1967). Enstatite chondrites (ECs) are characterized by very reduced and anhydrous assemblages and are the only meteorite group isotopically identical to the Earth and hence, are considered to be good analogues of the precursor material from which the Earth formed (Javoy *et al.*, 2010).

## Cr isotope cosmochemistry

Chromium has four stable isotopes,  $^{50}\text{Cr}$  (4.35%),  $^{52}\text{Cr}$  (83.79%),  $^{53}\text{Cr}$  (9.50%) and  $^{54}\text{Cr}$  (2.36%) (Rossman and Taylor 1998). Cr isotope cosmochemistry studies mostly focus on the radiogenic and nucleosynthetic variability of Cr isotopes, namely radiogenic effects on  $^{53}\text{Cr}$  (radiogenic product of the extinct nuclide  $^{53}\text{Mn}$ ,  $t_{1/2} = 3.7$  Myr, Honda and Imamura 1971) and nucleosynthetic effects on  $^{54}\text{Cr}$  (also known as isotope anomalies).

## Cr isotopes as a chronological tool: $^{53}\text{Mn}$ - $^{53}\text{Cr}$ short-lived chronometer

Short-lived radionuclides (SLRs,  $^{26}\text{Al}$ ,  $^{36}\text{Cl}$ ,  $^{41}\text{Ca}$ ,  $^{53}\text{Mn}$ ,  $^{60}\text{Fe}$ ,  $^{107}\text{Pd}$ ,  $^{129}\text{I}$ ,  $^{182}\text{Hf}$ ,  $^{244}\text{Pu}$ ) were produced in supernovae before the formation of the solar system. The majority of the stellar nucleosynthetic hypotheses argue that a stellar source injected SLRs into the presolar molecular cloud shortly before the formation of the solar system (e.g., Cameron *et al.*, 1995; Sahijpal & Soni 2006; Wasserburg *et al.*, 2006; Huss *et al.*, 2009; Sahijpal and Gupta 2009; Dauphas and Chaussidon 2011; Dwarkadas *et al.*, 2017; Lugaro *et al.*, 2018; Kaur and Sahijpal 2019). Particularly,  $^{53}\text{Mn}$  remnants from evolved massive stars from the cluster contaminated the local medium associated with the presolar molecular cloud (Kaur and Sahijpal 2019). For a brief period of  $\sim 15$  Ma (4-5 half-lives of the  $^{53}\text{Mn}$ - $^{53}\text{Cr}$  system) after the birth of the solar system, significant  $^{53}\text{Mn}$  was extant and during the early differentiation of the solar system materials, the varying Mn/Cr ratios caused by chemical and mineralogical differentiation led to variable amounts of radiogenic  $^{53}\text{Cr}$  ingrowth. Excesses or deficits (deviation from the mass-dependent fractionation line) of  $^{53}\text{Cr}$  observed today provide evidence that differentiation events occurred prior to  $^{53}\text{Mn}$  becoming extinct (Qin *et al.*, 2017). The  $^{53}\text{Mn}$ - $^{53}\text{Cr}$  system is a useful tool to date with high precision and accuracy early solar system processes that occurred within the first few million years of the birth of the solar system and are associated with Mn/Cr fractionation.

Similar to the long-lived isotope chronometers, the excess of the radiogenic daughter,  $^{53}\text{Cr}$ , correlates with the concentration of the parent isotope,  $^{53}\text{Mn}$ . However, since  $^{53}\text{Mn}$  is now extinct, the correlation line gives the initial concentration of  $^{53}\text{Mn}$  (relative to a stable counterpart,  $^{55}\text{Mn}$ ) and may represent an isochron. The isochron can be interpreted as an age only if all the samples defining the isochron originated from a common reservoir and at one time had a uniform concentration of the radionuclide. When the initial abundance of  $^{53}\text{Mn}/^{55}\text{Mn}$  inferred from the slope of this isochron is compared with the slope of an ‘anchor’, a relative age with respect to the anchor can be obtained. If the anchor has a precise absolute U-isotope corrected Pb-Pb age, the relative age can be translated into an absolute age.

The Chapter 1 of this thesis focuses on  $^{53}\text{Mn}$ - $^{53}\text{Cr}$  chronometry of low and high petrological grade ordinary chondrites using two-point isochrons obtained from the pairs consisting of chromite and corresponding silicate-sulfide-metal fractions from each sample. The chromites formed from the surrounding silicate-sulfide-metal matrix and thus both the components had the same initial Cr-isotope composition. The two components provide significant spread in the



isotope space yielding precise ages constraining the timing of onset and progressive metamorphism in the ordinary chondrite parent bodies. Similarly, Chapter 3 presents the  $^{53}\text{Mn}$ - $^{53}\text{Cr}$  chronometry of an ungrouped achondrite, EC 002, using the isochron approach. To obtain the data from phases with various Mn/Cr ratios, a sequential digestion experiment on the whole rock material is performed. The isochron yields the  $^{53}\text{Mn}/^{55}\text{Mn}$  ratio at the last time the sample EC 002 crystallized and Mn became immobile. The EC 002 crystallization age predates the chondrule formation interval providing implications for the formation and differentiation of the earliest accreted planetesimals.

In addition to the isochron approach for dating, the short-lived  $^{53}\text{Mn}$ - $^{53}\text{Cr}$  isotope system can also be used to obtain precise ‘model ages’ from a mineral phase/fraction with a near-zero parent/daughter ratio. These model ages are interpreted as the time at which the parent/daughter ratio froze, which could be an event that practically removed the parent radionuclide from this mineral phase/fraction. In the absence of the parent radionuclide, this mineral phase/fraction preserves the initial abundance of the radiogenic daughter isotope. A model age can be obtained by measuring the radiogenic daughter abundance of this mineral phase/fraction and comparing it to its modelled evolution in a reservoir from which the sample presumably originated.

In Chapters 1 and 3, chromites from ordinary chondrites and EC 002 are used to determine model ages of chromite formation (cooling ages) in these meteorites by measuring the initial  $^{53}\text{Cr}/^{52}\text{Cr}$  composition of the chromite fraction in each sample and comparing it with the Cr-isotope evolution of the assumed chondritic source reservoir. The chromite model ages from ordinary chondrites and EC 002 agree with the respective isochron ages confirming the validity of key model parameters including initial abundance of  $^{53}\text{Mn}/^{55}\text{Mn}$  in the solar system, its homogeneity, decay constant and near-chondritic Mn/Cr of parent bodies. Similarly, Chapter 2 presents chromite/daubréelite model ages from IIAB, IIIAB and IVA magmatic iron meteorites. The  $^{53}\text{Cr}$  isotope composition of the chromite/daubréelite fraction when plotted on the modelled evolution of the chondritic source reservoir gives the timing of metal-silicate separation in the parent bodies of magmatic iron meteorites. This is based on the assumption that core formation was an instantaneous event that induced strong chemical fractionation of Mn from the more siderophile Cr. The determined core formation ages for IIAB, IIIAB and IVA iron meteorites support the accretion and differentiation of the magmatic iron meteorite parent bodies prior to the chondrule formation episode. Moreover, the estimated  $^{53}\text{Mn}$ - $^{53}\text{Cr}$

core formation ages are combined with the Hf-W systematics for the magmatic iron meteorites and  $\epsilon^{53}\text{Cr} = -0.31$  is proposed as a better estimate of the solar system initial  $\epsilon^{53}\text{Cr}$ .

### **Cr isotopes as a genealogical tool: $^{54}\text{Cr}$ isotopic anomalies**

The solar system in its protoplanetary disk stage contained material that was accreted from a variety of chemically and isotopically distinct stellar sources. With improvements in mass spectrometer precision, it has become clear that the formation of early solar system materials started from a not-so-well-homogenized cloud as it was thought earlier. This is evident from the detection of mass-independent isotopic variations in chondritic components and bulk meteorites that cannot be explained by radiogenic (decay of radioactive nuclides) or spallogenic (exposure to the cosmic radiations in the space) contributions. The variations are in fact, nucleosynthetic, and mostly carried by resistant presolar grains and refractory inclusions. The variable abundances of these carrier phases in different bulk meteorites (and chondrite components such as chondrules) led to resolvable isotopic anomalies that can be used as a genealogical tool to trace the source, transport and mixing processes in the early solar system.

The first study that identified mass-independent  $^{54}\text{Cr}$  isotope heterogeneity within bulk solar system materials was by Rotaru *et al.* (1992). The later studies expanded the Cr isotope dataset for solar system materials and identified that bulk meteorites show a range of  $\epsilon^{54}\text{Cr}$  compositions due to heterogeneous spatial or temporal distribution of a carrier phase (Rotaru *et al.*, 1992; Trinquier *et al.*, 2007; Qin *et al.*, 2010). Dauphas *et al.* (2010) reported that this carrier phase of  $\epsilon^{54}\text{Cr}$  anomalies is most likely a refractory phase, possibly a Cr-spinel that formed in an SN II nucleosynthesis environment. Together with the nucleosynthetic anomalies in O and Ti, Warren (2011) showed that bulk meteorites fall into two distinct populations in multi-elemental isotope space ( $\epsilon^{54}\text{Cr}$  vs.  $\Delta^{17}\text{O}$  or  $\epsilon^{54}\text{Cr}$  vs.  $\epsilon^{50}\text{Ti}$ ) and termed these populations as the non-carbonaceous (NC) and carbonaceous (CC) supergroups. This dichotomy has now become a new classification scheme for solar system materials. Moreover, isotopic compositions of different meteorite groups on a multi-element isotope space allow genetic relationships among planetary materials to be identified. For instance, the combination of  $^{54}\text{Cr}/^{52}\text{Cr}$  (expressed as  $\epsilon^{54}\text{Cr}$ ) and O isotopes (expressed as  $\Delta^{17}\text{O}$ ), has established genealogical connections between different meteorite groups such as IIIAB irons, main group pallasites and HEDs (e.g., Wasson, 2013). In Chapter 3, the combined  $^{54}\text{Cr}$  and  $^{17}\text{O}$  isotope compositions of

EC 002 confirm its origin in the “non-carbonaceous” reservoir that overlaps with the vestoid material NWA 12217 and anomalous eucrite EET 92023. In addition, in the Appendix of this thesis, two conference abstracts are provided that were presented during the course of this project. The abstracts describe the potential genealogical connections between IVA irons and L/LL chondrites, and IIG and IIAB irons using combined  $^{54}\text{Cr}$  and  $^{17}\text{O}$  isotope compositions of the samples.

Mass independent Cr isotopic anomalies have also been established as an excellent tool to identify the type of impactor involved in the formation of terrestrial impact structures (Koeberl *et al.*, 2007; Foriel *et al.*, 2013; Magna *et al.*, 2017; Mougél *et al.*, 2019). Chapter 4 presents the use of Cr isotopes in identifying the type of impactor involved in the formation of the Dhala structure. The idea is that almost all of the meteorite groups have much higher Cr concentrations than crustal rocks on Earth which makes Cr sensitive in identifying small contributions ( $\approx 1$  wt. %) of the extraterrestrial component in the impactites and other impact-generated debris. Since different meteorite groups have distinct Cr isotopic compositions, the Cr isotopic composition of the impactites can identify the type of the projectile (Shukolyukov and Lugmair, 1998). Unlike siderophile element compositions and inter-element ratios that may get compromised due to the extreme energy generated during an impact, Cr isotopes can retain the distinct meteoritic composition of the impactor. The depleted  $\epsilon^{54}\text{C}$  isotope composition of the Dhala impact melt breccia D6-57 indicates an inheritance of the composition from an impactor originating in the non-carbonaceous reservoir. The binary mixing calculations using Cr isotopes indicate contamination of  $\sim 1.2$  wt% from a ureilite or 2-3 wt% from an acapulcoite-like impactor. Together with the previously identified impactors involved in the formation of other impact structures, the Cr isotopic compositions of the Dhala impactites argue for a much more diverse source of the objects that collided with the Earth over its history than has been supposed previously.

## References

- Agnor, C. B., Canup, R. M., Levison, H. F. (1999) On the character and consequences of large impacts in the late stage of terrestrial planet formation. *Icarus*, 142(1), 219-237.
- Amelin, Y., Kaltenbach, A., Iizuka, T., Stirling, C. H., Ireland, T. R., Petaev, M., Jacobsen, S. B. (2010) U-Pb chronology of the Solar System's oldest solids with variable  $^{238}\text{U}/^{235}\text{U}$ . *Earth and Planetary Science Letters*, 300, 343-350.
- Anand, A., Pape, J., Wille, M., Mezger, K., Hofmann, B. (2021a) Early differentiation of magmatic iron meteorite parent bodies from Mn–Cr chronometry. *Geochemical Perspectives Letters* 20, 6-10.
- Anand, A., Pape, J., Wille, M., Mezger, K. (2021b) Chronological constraints on the thermal evolution of ordinary chondrite parent bodies from the  $^{53}\text{Mn}$ - $^{53}\text{Cr}$  system. *Geochimica et Cosmochimica Acta*, 307, 281-301.
- Anand, A., Kruttasch, P. M., Mezger, K., Windmill, R., Hofmann, B. A., Greenwood, R. C., Leya, I. (2022) IIAB and IIG iron meteorites originated from a single parent body. *LPI Contributions*, 2678, p.1891.
- Barrat, J. A., Chaussidon, M., Yamaguchi, A., Beck, P., Villeneuve, J., Byrne, D. J., Broadley, M. W., Marty, B. (2021) A 4,565-My-old andesite from an extinct chondritic protoplanet. *Proceedings of the National Academy of Sciences*, 118(11).
- Bischoff, A., Horstmann, M., Barrat, J.A., Chaussidon, M., Pack, A., Herwartz, D., Ward, D., Vollmer, C., Decker, S. (2014) Trachyandesitic volcanism in the early Solar System. *Proceedings of the National Academy of Sciences*, 111(35), 12689-12692.
- Blum, J. (2018) Dust evolution in protoplanetary discs and the formation of planetesimals. *Space Science Reviews*, 214(2), 1-19.
- Booth, R. A., Meru, F., Lee, M. H., Clarke, C. J. (2018) Breakthrough revisited: investigating the requirements for growth of dust beyond the bouncing barrier. *Monthly Notices of the Royal Astronomical Society*, 475(1), 167-180.

Cameron, A. G. W., Höflich, P., Myers, P. C., Clayton, D. D. (1995) Massive supernovae, Orion gamma rays, and the formation of the solar system. *The Astrophysical Journal*, 447(1), p.L53.

Chambers, J. E. and Wetherill, G. W. (1998) Making the terrestrial planets: N-body integrations of planetary embryos in three dimensions. *Icarus*, 136(2), 304-327.

Chambers, J. E. (2004) Planetary accretion in the inner Solar System. *Earth and Planetary Science Letters*, 223(3-4), 241-252.

Dauphas, N., Remusat, L., Chen, J. H., Roskosz, M., Papanastassiou, D. A., Stodolna, J., Guan, Y., Ma, C., Eiler, J.M. (2010) Neutron-rich chromium isotope anomalies in supernova nanoparticles. *The Astrophysical Journal*, 720(2), 1577.

Dauphas, N. and Chaussidon, M. (2011) A perspective from extinct radionuclides on a young stellar object: The Sun and its accretion disk. *Annual Review of Earth and Planetary Sciences*, 39, 351-386.

Dwarkadas, V. V., Dauphas, N., Meyer, B., Boyajian, P., Bojazi, M. (2017) Triggered star formation inside the shell of a Wolf-Rayet bubble as the origin of the solar system. *The Astrophysical Journal*, 851(2), 147.

Foriel, J., Moynier, F., Schulz, T., Koeberl, C. (2013) Chromium isotope anomaly in an impactite sample from the El'gygytgyn structure, Russia: Evidence for a ureilite projectile? *Meteoritics & Planetary Science*, 48(7), 1339-1350.

Garaud, P., Meru, F., Galvagni, M., Olczak, C. (2013) From dust to planetesimals: an improved model for collisional growth in protoplanetary disks. *The Astrophysical Journal*, 764(2), 146.

Glavin, D., Kubny, A., Jagoutz, E., Lugmair, G. (2004) Mn-Cr isotope systematics of the D'Orbigny angrite. *Meteoritics & Planetary Science*, 39, 693-700.

Grossman, L. (1972) Condensation in the primitive solar nebula. *Geochimica et Cosmochimica Acta*, 36(5), 597-619.

Grossman, L. and Larimer, J. W. (1974) Early chemical history of the solar system. *Reviews of Geophysics*, 12(1), 71-101.

Honda, M. and Imamura, M. (1971) Half-life of Mn53. *Physical Review C*, 4(4), 1182.

Huss, G. R., Meyer, B. S., Srinivasan, G., Goswami, J. N., Sahijpal, S. (2009) Stellar sources of the short-lived radionuclides in the early solar system. *Geochimica et Cosmochimica Acta*, 73(17), 4922-4945.

Javoy, M., Kaminski, E., Guyot, F., Andraut, D., Sanloup, C., Moreira, M., Labrosse, S., Jambon, A., Agrinier, P., Davaille, A., Jaupart, C. (2010) The chemical composition of the Earth: Enstatite chondrite models. *Earth and Planetary Science Letters*, 293(3-4), 259-268.

Johansen, A., Oishi, J.S., Low, M. M. M., Klahr, H., Henning, T., Youdin, A. (2007) Rapid planetesimal formation in turbulent circumstellar disks. *Nature*, 448(7157), 1022-1025.

Kaur, T. and Sahijpal, S. (2019) Heterogeneous evolution of the galaxy and the origin of the short-lived nuclides in the early solar system. *Monthly Notices of the Royal Astronomical Society*, 490(2), 1620-1637.

Keil, K., Haack, H., Scott, E. R. D. (1994) Catastrophic fragmentation of asteroids: Evidence from meteorites. *Planetary and Space Science*, 42(12), 1109-1122.

Koeberl C., Shukolyukov A., Lugmair G. W. (2007) Chromium isotopic studies of terrestrial impact craters: Identification of meteoritic components at Bosumtwi, Clearwater East, Lappajärvi, and Rochechouart. *Earth and Planetary Science Letters*, 256, 534-546.

Magna T., Zak K., Pack A., Moynier F., Mougél B., Peters S., Skala R., Jonasova S., Mizera J., Randa Z. (2017) Zhamanshin astrobleme provides evidence for carbonaceous chondrite and post-impact exchange between ejecta and Earth's atmosphere. *Nature Communications*, 8, 1-8.

Mezger, K., Maltese, A., Vollstaedt, H. (2021) Accretion and differentiation of early planetary bodies as recorded in the composition of the silicate Earth. *Icarus*, 365, 114497.

Mougel, B., Moynier, F., Koeberl, C., Wielandt, D., Bizzarro, M. (2019) Identification of a meteoritic component using chromium isotopic composition of impact rocks from the Lonar impact structure, India. *Meteoritics & Planetary Science*, 54(10), 2592-2599.

Lugaro, M., Ott, U., Kereszturi, Á. (2018) Radioactive nuclei from cosmochemistry to habitability. *Progress in Particle and Nuclear Physics*, 102, 1-47.

Qin, L., Alexander, C. M. D., Carlson, R. W., Horan, M. F., Yokoyama, T. (2010) Contributors to chromium isotope variation of meteorites. *Geochimica et Cosmochimica Acta*, 74(3), 1122-1145.

Qin, L. and Wang, X. (2017) Chromium isotope geochemistry. *Reviews in Mineralogy and Geochemistry*, 82(1), 379-414.

Rosman, K. J. R. and Taylor, P. D. P. (1998) Isotopic compositions of the elements 1997 (Technical Report). *Pure and Applied Chemistry*, 70(1), 217-235.

Rotaru, M., Birck, J. L., Allègre, C. J. (1992) Clues to early solar system history from chromium isotopes in carbonaceous chondrites. *Nature*, 358(6386), 465-470.

Sahijpal, S. and Gupta, G. (2009) The plausible source(s) of  $^{26}\text{Al}$  in the early solar system: A massive star or the X-wind irradiation scenario? *Meteoritics & Planetary Science*, 44(6), 879-890.

Sahijpal, S. and Soni, P. (2006) Stellar nucleosynthetic contribution of extinct short-lived nuclei in the early solar system and the associated isotopic effects. *Meteoritics & Planetary Science*, 41(6), 953-976.

Sanborn, M. E., Wimpenny, J., Williams, C. D., Yamakawa, A., Amelin, Y., Irving, A. J., Yin, Q. Z. (2019) Carbonaceous achondrites Northwest Africa 6704/6693: Milestones for early Solar System chronology and genealogy. *Geochimica et Cosmochimica Acta*, 245, 577-596.

Shearer, C. K., Burger, P. V., Neal, C., Sharp, Z., Spivak-Birndorf, L., Borg, L., Fernandes, V. A., Papike, J. J., Karner, J., Wadhwa, M., Gaffney, A. (2010) Non-basaltic asteroidal magmatism during the earliest stages of solar system evolution: A view from Antarctic

achondrites Graves Nunatak 06128 and 06129. *Geochimica et Cosmochimica Acta*, 74(3), 1172-1199.

Shukolyukov A. and Lugmair G. W. (1998) Isotopic evidence for the Cretaceous-Tertiary impactor and its type. *Science*, 282, 927-929.

Srinivasan, P., Dunlap, D. R., Agee, C. B., Wadhwa, M., Coleff, D., Ziegler, K., Zeigler, R., McCubbin, F.M. (2018) Silica-rich volcanism in the early solar system dated at 4.565 Ga. *Nature Communications*, 9(1), 1-8.

Trinquier, A., Birck, J. L., Allègre, C. J. (2007) Widespread  $^{54}\text{Cr}$  heterogeneity in the inner solar system. *The Astrophysical Journal*, 655 (2), 1179.

Van Schmus W. R. and Wood J. A. (1967) A chemical-petrologic classification for the chondritic meteorites. *Geochimica et Cosmochimica Acta*, 31, 747-765.

Walter, M. J. and Trønnes, R. G. (2004) Early earth differentiation. *Earth and Planetary Science Letters*, 225(3-4), 253-269.

Wänke, H. and Dreibus, G. (1988) Chemical composition and accretion history of terrestrial planets. *Philosophical Transactions of the Royal Society of London. Series A, Mathematical and Physical Sciences*, 325(1587), 545-557.

Wasserburg, G.J., Busso, M., Gallino, R., Nollett, K.M. (2006) Short-lived nuclei in the early Solar System: Possible AGB sources. *Nuclear Physics A*, 777, 5-69.

Wasson, J. T. (2013) Vesta and extensively melted asteroids: Why HED meteorites are probably not from Vesta. *Earth and Planetary Science Letters*, 381, 138-146.

Weidenschilling, S. J., Spaute, D., Davis, D. R., Marzari, F. and Ohtsuki, K. (1997) Accretional evolution of a planetesimal swarm. *Icarus*, 128(2), 429-455.

Windmark, F., Birnstiel, T., Ormel, C. W., Dullemond, C. P. (2012) Breaking through: The effects of a velocity distribution on barriers to dust growth. *Astronomy & Astrophysics*, 544, L16.



Windmark, F., Birnstiel, T., Güttler, C., Blum, J., Dullemond, C.P., Henning, T. (2012) Planetesimal formation by sweep-up: how the bouncing barrier can be beneficial to growth. *Astronomy & Astrophysics*, 540, A73.

Youdin, A. N. and Goodman, J. (2005) Streaming instabilities in protoplanetary disks. *The Astrophysical Journal*, 620(1), 459.

## 1

# Chronological constraints on the thermal evolution of ordinary chondrite parent bodies from the $^{53}\text{Mn}$ - $^{53}\text{Cr}$ system

**Manuscript published in *Geochimica et Cosmochimica Acta***

Anand, A., Pape, J., Wille, M. and Mezger, K., (2021)

*Geochimica et Cosmochimica Acta*, 307, 281-30.

## Abstract

The  $^{53}\text{Mn}$ - $^{53}\text{Cr}$  isotope systematics in ordinary chondrites constrains the accretion and thermal history of their parent bodies. Mineralogical observations and olivine-spinel geothermometry suggest that chromite in ordinary chondrites formed during prograde thermal metamorphism with the amount of chromite increasing with petrologic grades in type 3 to type 6 ordinary chondrites. Assuming a chondritic evolution of the respective parent bodies,  $^{53}\text{Cr}/^{52}\text{Cr}$  model ages for chromite range from  $3.99^{+0.93}_{-0.79}$  to  $11.1^{+6.0}_{-2.8}$  Ma after the formation of calcium-aluminium-rich inclusions (CAIs). Chromite and silicate-metal-sulphide isochrons define an age range from  $2.78^{+0.55}_{-0.50}$  to  $15.4^{+2.4}_{-1.6}$  Ma. Both chromite model ages and isochron ages correlate with the petrological grade of the samples, which is consistent with an onion-shell structure of the chondrite parent bodies. The study shows that unlike the isochron ages, which are prone to impact-related disturbances or partial re-equilibration during cooling from high temperatures, the chromite model ages are not easily affected by thermal metamorphism or later events and yield robust mineral growth ages. The results are consistent with a homogenous distribution of  $^{53}\text{Mn}$  and an initial canonical  $^{53}\text{Mn}/^{55}\text{Mn} = 6.28 \times 10^{-6}$ . The estimated closure temperatures for the Mn-Cr system in chromites range from  $\sim 760$  °C for type 6 to  $\sim 540$ - $620$  °C for type 3 ordinary chondrites. The high closure temperatures estimated for type 3 and type 6 ordinary chondrites imply that the chromite ages correspond to the peak metamorphic temperature reached during the thermal history of the chondrite parent bodies. The oldest chromite model age obtained for type 3 samples along with the established Al-Mg chondrule formation ages constrain the accretion of the parent bodies to  $>2.1$  Ma after CAI formation, implying that planetesimal accretion immediately followed chondrule formation.

## 1.1 Introduction

Ordinary chondrites are among the solar system's most primitive materials, containing early formed solids, including chondrules, calcium-aluminium rich inclusions (CAIs), metallic Fe-Ni grains and fine-grained matrix. The ordinary chondrite clan is subdivided into H, L and LL groups based on distinct metal to silicate ratios and each of these groups is thought to sample a distinct parent body in the Main Asteroid Belt. The ordinary chondrites were metamorphosed to different degrees, but never experienced global melting and differentiation. They are divided into petrological types ranging from petrological type 3 (unequilibrated, low thermal overprint) to types 4-6 (equilibrated, higher metamorphic grades) (Van Schmus and Wood, 1967). The degree of chemical homogeneity of various phases in relationship to the petrologic type and response to the onset and progressive thermal metamorphism has been an important issue in numerous studies of ordinary chondrites (e.g., Grossman and Brearley, 2005; Kimura *et al.*, 2006; Kessel *et al.*, 2007). The onset of metamorphism is manifested in the formation of new phases and the homogenisation in and among minerals in a given sample. Critical time information about the accretion and metamorphism of the parent bodies of ordinary chondrites can be acquired from chronological studies using short-lived radionuclides (e.g.,  $^{182}\text{Hf}$ ,  $^{53}\text{Mn}$ ,  $^{26}\text{Al}$ ) with half-lives of  $10^5$ - $10^8$  years.

Grossman and Brearley (2005) showed that the onset of metamorphism in ordinary chondrites leads to the exsolution of Cr from olivine as fine-grained opaque phases, probably in the form of chromite ( $\text{FeCr}_2\text{O}_4$ ). Kimura *et al.* (2006) reported an increase in the abundance and compositional changes of spinel group minerals that can be explained with progressive thermal metamorphism. Chromite, together with olivine has also been used in olivine-spinel thermometry and shows a systematic increase in the maximum temperature correlating with the metamorphic type, recorded by individual chondrites (Wlotzka, 2005; Kessel *et al.*, 2007).

The formation of chromite can potentially be dated with the  $^{53}\text{Mn}$ - $^{53}\text{Cr}$  system thus providing time constraints on new mineral growth on the parent body. The short-lived radionuclide  $^{53}\text{Mn}$  ( $t_{1/2} = 3.7 \pm 0.4$  Ma, Honda and Imamura, 1971) has long been recognized (Birck and Allègre, 1985a) and used for high-resolution chronological studies of chondrites to date processes and events within the first  $\sim 20$  Ma of solar system history (Lugmair and Shukolyukov, 1998; Nyquist *et al.*, 2001; Shukolyukov and Lugmair, 2006; Trinquier *et al.*,

2008a, b; Göpel *et al.*, 2015). One of the advantages of using the Mn-Cr chronometer is that Mn and Cr are abundant elements in ordinary chondrites and their components have variable and/or high Mn/Cr ratios, which makes them suitable for dating by constructing an isochron. Alternatively, the Cr-isotopes can be used to obtain precise “model ages” for minerals with a Mn/Cr ratio near zero, which is the case for chromite, a mineral that occurs in meteorites of all ordinary chondrite groups. Chromite preserves initial  $^{53}\text{Cr}/^{52}\text{Cr}$  ratios corresponding to the time of isotope closure of the Mn-Cr system and this isotope ratio can be measured with high precision. A model age can be obtained by comparing the Cr-isotopic composition of the chromite with the Cr-isotope evolution of its assumed reservoir. The Mn-Cr chromite model ages for ordinary chondrites along with the closure temperature estimate of Cr in spinel open up the possibility of using the Mn-Cr system to construct well constrained thermal evolution models or evaluating the validity of existing ones.

In addition to the derivation of model ages, chromites in combination with silicates in single meteorite samples can also be used to construct isochrons. The combination of the two types of age estimates provides temporal constraints on the thermal evolution of meteorite parent bodies, sets time limits for the interval of their accretion and their cooling history, which are a function of accretion time and size of the bodies.

This study reports chromite model ages along with two-point isochron ages from a group of type 3 (unequilibrated) and type 6 (equilibrated) samples. The age data along with petrographical and olivine-spinel geothermometry provides new constraints on the accretion time and metamorphic history of the ordinary chondrite parent bodies.

## 1.2 Samples and Analytical Methods

A total of 8 samples of H and L ordinary chondrites were selected for  $^{53}\text{Mn}$ - $^{53}\text{Cr}$  dating. The samples are from the Omani-Swiss meteorite search collection stored at the Natural History Museum Bern. Four of these samples are of low petrologic grade (type 3) and include Sayh al Uhaymir 246 (SaU 246, H3/4), Ramlat as Sahmah 337 (RaS 337, H3.6), Jiddat al Harasis 596 (JaH 596, L3) and Ramlat as Sahmah 265 (RaS 265, L3). The other four chondrites are of petrologic type 6 and include Jiddat al Harasis 578 (JaH 578, H6), Sayh al Uhaymir 228 (SaU 228, H6), Dhofar 1012 (Dho 1012, L6) and Al Huwaysah 017 (no official abbreviation,

henceforth AHu 017, L6). Most samples record low shock (S1-2) except Dho 1012 (S3) and AHu 017 (S4). The samples SaU 246, RaS 337 and JaH 596 are classified as W3 on the W0-W6 weathering classification of Wlotzka (1993), while all the other samples are classified as W1 or W2.

Petrographical studies were performed with an Olympus BX51 microscope equipped with a digital camera using plane and cross-polarized light. Thin section mosaics were created with an MIA (multiple imaging analyzer) stage attached to the microscope and used as a reference during subsequent scanning electron microscope (SEM) and electron microprobe investigations at the Institute of Geological Sciences, University of Bern.

Backscattered electron (BSE) imaging and mineral identification via energy-dispersive X-ray spectroscopy (EDS) were conducted on a ZEISS EVO50 SEM. Spinel (*sensu lato*) grains were identified in all the samples and their textural response to metamorphism in relationship to the petrologic type was evaluated. Olivine-spinel pairs in the chondrules of type 3 and chondrules and matrices of type 6 chondrites were selected for Fe-Mg exchange geothermometry. Only those pairs were selected where olivine and spinel are in direct contact, following the approach described in Kessel *et al.* (2007).

The major and minor element abundances in olivine and spinel were measured with a JEOL JXA-8200 Superprobe. Analyses were conducted as individual point measurements with the beam focused to 1  $\mu\text{m}$ , the acceleration voltage set at 15 kV (all measurements) and a beam current between 15 and 20 nA. Elemental concentrations were measured using five wavelength-dispersive spectrometers (WDS) and calibrated using a set of synthetic and natural reference materials. The detection limits for all elements were typically below 100  $\mu\text{g/g}$ . Automated matrix correction was done with the built-in CITZAF package (Armstrong, 1995).

For each sample, 1-1.5 g of whole-rock meteorite was hand crushed using a pre-cleaned agate mortar and transferred into a separate 15 ml Savillex® beaker. The material was partially dissolved in conc. aqua regia on a hot plate set to 90 °C for 48 hrs. The dissolved metal-sulfide fraction was transferred into a separate 60 ml Savillex® beaker. The remaining undissolved solid was rinsed with high-purity (18.2 M $\Omega$ ) MilliQ® water twice and the supernatant was added to the metal-sulfide fraction. To dissolve the silicate fraction, 4 ml of a 3:1 mixture of conc. HF and HNO<sub>3</sub> were added and heated up to 90 °C for 48 hrs. After cooling, the sample

was dried, 4 ml 6.4 M HCl was added and put on a hot plate at 140 °C for 24 hrs. to break down fluorides. Afterwards, the dissolved silicate fraction was recombined with the metal-sulfide fraction. From visual inspection, two undissolved residual phases could be identified in the beaker: chromite (spinel) and organic matter. The residual chromite grains together with the undissolved organic matter were transferred into a 15 ml centrifuge vial, gravitationally separated from each other, and siphoned into a separate beaker. The complete sample digestion process resulted in three distinct sample splits: (1) residual material consisting of pure chromite (2) dissolved material that is mostly derived from silicates, metal, and sulfides and (3) organic residue. The refractory chromite grains were handpicked into 200  $\mu$ L Savillex® vials and digested in PTFE-lined stainless-steel pressure bombs (Parr® bombs) with 10 ml conc. inverse aqua regia and placed in an oven for 96 hrs. at 190 °C. With this procedure, the chromite could be brought into solution. Hereafter, both chromite and silicate-metal-sulfide fractions were analyzed separately. The term ‘silicate’ is used to refer to the silicate-metal-sulfide fraction. All beakers, jars and centrifuge tubes used in the sample processing were pre-cleaned and all acids were cleaned by sub-boiling distillation.

The dissolved chromite and silicate fractions from each sample were divided into two aliquots. The first aliquot was used for the determination of Mn/Cr ratios. The second aliquot was used for chemical separation of Cr and measurement of Cr isotopes on Triton™ Plus thermal ionization mass spectrometer (TIMS) in the isotope laboratory at the University of Bern. Whenever possible, Cr isotopes of a sample were measured multiple times to obtain higher precision. The long term (9 months) reproducibility (2SD) for  $\epsilon^{53}\text{Cr}$  and  $\epsilon^{54}\text{Cr}$  including the temporal drift was 0.07 and 0.28 respectively (n=53). The details of Mn/Cr ratio determination, chemical separation of Cr and TIMS measurement protocol are provided in the Supplementary Material (Appendix).

### 1.2.1 Model for $\epsilon^{53}\text{Cr}$ evolution in chondrites

The model for  $\epsilon^{53}\text{Cr}$  evolution in chondrites assumes that they represent an isotopically homogeneous reservoir in Cr and Mn space that evolved with a distinct Mn/Cr ratio after primordial nebular Mn/Cr fractionation and isolation of the precursor material of chondrites, terrestrial planets and differentiated planetesimals (Trinquier *et al.*, 2008b). The evolution of the  $^{53}\text{Cr}/^{52}\text{Cr}$  isotopic composition of the chondrite reservoir through time can be expressed as:

$$(^{53}\text{Cr}/^{52}\text{Cr})_p = (^{53}\text{Cr}/^{52}\text{Cr})_i + (k)(^{53}\text{Mn}/^{55}\text{Mn})_i \times (1 - e^{-\lambda t}) \quad (1.1)$$

where  $p$  refers to the present values,  $i$  refers to the initial values and  $\lambda$  denotes the  $^{53}\text{Mn}$  decay constant. The  $^{55}\text{Mn}/^{52}\text{Cr}$  of the reservoir is denoted by  $k$ ; and  $t$  represents the time elapsed since the start of the solar system, which is equated with the time of CAI formation. Eq. 1.1 describes the evolution of  $^{53}\text{Cr}/^{52}\text{Cr}$  with time for the chondritic reservoir with a pre-determined Mn/Cr ratio and can be used to derive a model age for a chondrite sample by measuring the Cr isotopic composition of its chromite fraction only. Due to its very low Mn/Cr ratio, chromite preserves the Cr isotopic composition of its growth environment because the in-growth of radiogenic  $^{53}\text{Cr}$  in chromite from in-situ decay of  $^{53}\text{Mn}$  is negligible. For instance, a Mn/Cr ratio of 0.01 in typical chromite would result in an in-situ radiogenic  $\epsilon^{53}\text{Cr}$  contribution of 0.006 within 10 Myr after CAI formation, which is insignificant, compared to the  $\epsilon^{53}\text{Cr}$  evolution of 0.33 in the chondritic reservoir during this period.

Using the Cr isotopic composition of chromites to obtain model ages of their formation relies on the following assumptions: (i) homogenous distribution of  $^{53}\text{Mn}$  in the solar system, (ii) known abundance of  $^{53}\text{Mn}$  and  $^{53}\text{Cr}$  at the beginning of the solar system or any point in time thereafter, and (iii) an estimate for the Mn/Cr in the relevant reservoir.

It can be assumed that the solar system had a homogeneous distribution of  $^{53}\text{Cr}$  and  $^{53}\text{Mn}$  at or shortly after its formation. This is evident from the identical ages of meteorites or their components derived from the Mn-Cr system and other short-lived isotope systems (e.g., Hf-W) as shown in several studies (Trinquier *et al.*, 2008b; Nyquist *et al.*, 2009; Kleine *et al.*, 2012). These comparisons also give confidence in the definitions of  $(^{53}\text{Mn}/^{55}\text{Mn})_i$  and  $\epsilon^{53}\text{Cr}_i$  (Göpel *et al.*, 2015).

The abundances of  $^{53}\text{Mn}$  and  $^{53}\text{Cr}/^{52}\text{Cr}$  at the beginning of the solar system has been determined in several studies with distinct approaches:

(i) Shukolyukov and Lugmair (2006), Moynier *et al.* (2007) and Göpel *et al.* (2015) determined the  $^{53}\text{Mn}/^{55}\text{Mn}_i$  and  $\epsilon^{53}\text{Cr}_i$  by evaluating the Mn/Cr data for bulk rock carbonaceous chondrites (CC) on a  $^{55}\text{Mn}/^{52}\text{Cr}$  versus  $\epsilon^{53}\text{Cr}$  diagram. Shukolyukov and Lugmair (2006) reported that the correlation line yields a  $^{53}\text{Mn}/^{55}\text{Mn}$  of  $8.5 \pm 1.5 \times 10^{-6}$  and initial  $\epsilon^{53}\text{Cr} = -0.21 \pm 0.09$  at the time of Mn/Cr fractionation. Göpel *et al.* (2015) obtained a canonical  $^{53}\text{Mn}/^{55}\text{Mn}_i$



$= 6.8 \times 10^{-6}$  and  $\varepsilon^{53}\text{Cr}_i$  corresponding to -0.177 from the bulk rock CC isochron with respect to the age of the solar system. It should be noted that the whole rock CC isochrons depend strongly on the choice of which samples to include in or exclude from the linear regression (Qin *et al.*, 2010).

(ii) Trinquier *et al.* (2008b) constrained  $^{53}\text{Mn}/^{55}\text{Mn}_i = 6.28 \pm 0.66 \times 10^{-6}$  using an isochron based on  $^{54}\text{Cr}$ -poor fractions of CI Orgueil and reported it as the best estimate for the initial solar system  $^{53}\text{Mn}$  abundance. The authors back-calculated  $\varepsilon^{53}\text{Cr}_i$  for a wide range of chondritic reservoirs using present-day  $^{53}\text{Cr}/^{52}\text{Cr}$  and Mn/Cr ratios to the time of CAI formation and reported the average of all  $\varepsilon^{53}\text{Cr}_i$  as solar system initial  $\varepsilon^{53}\text{Cr}_i = -0.23 \pm 0.09$ . They additionally determined  $^{53}\text{Mn}/^{55}\text{Mn}_i = 6.38 \pm 1.2 \times 10^{-6}$  at the time of CAI formation by anchoring the  $^{53}\text{Mn}/^{55}\text{Mn}$  value obtained for H4 chondrite Ste. Marguerite with its predetermined  $^{207}\text{Pb}$ - $^{206}\text{Pb}$  phosphates age of  $4562.7 \pm 0.6$  Ma (Göpel *et al.*, 1994). However, Blackburn *et al.* (2017) reported an updated U-corrected  $^{207}\text{Pb}$ - $^{206}\text{Pb}$  phosphate age ( $= 4561.7$  Ma after CAIs) for Ste. Marguerite with which the  $^{53}\text{Mn}/^{55}\text{Mn}_i$  derived using Ste. Marguerite systematics can be recalculated as  $7.68 \times 10^{-6}$ , at the time of CAI formation ( $4567.18 \pm 0.50$  Ma, Amelin *et al.*, 2010).

For the model ages, it is assumed that the Cr isotopic evolution of the reservoir from which the chromites formed was governed by a Mn/Cr elemental ratio identical to CI chondrites (Birck *et al.*, 1999). This approach is supported by the observation that all chondrites (except enstatites chondrites) plot on a single Mn-Cr isotopic evolution line within error starting from CI and with Mn/Cr indistinguishable from the CI reservoir (Birck *et al.*, 1999). Bulk analyses of ordinary chondrites also indicate that their Mn/Cr is similar to the ratio in CI chondrites (Wasson and Allemeyn, 1988, Trinquier *et al.*, 2008b; Qin *et al.*, 2010; Pedersen *et al.*, 2019). Moreover, bulk analyses of single chondrules from ordinary chondrites also show close to chondritic Mn/Cr ratios (e.g. Mahan *et al.*, 2018). Hence, the Mn/Cr ratio of the CI chondrites can be used as a representative for the Mn/Cr value of the chondritic reservoir in the  $\varepsilon^{53}\text{Cr}$  chondritic evolution model.

## 1.3 Results

### 1.3.1 Mineral compositions

Average compositions, end-member mole percentage and corresponding standard deviations measured for olivine and spinel pairs in each sample are given in Table 1.1 and 1.2. End member mole % for spinel (Table 1.2) were calculated using End Member Generator (EMG) (Ferracutti *et al.*, 2015).

Olivine in all the samples is Mg-rich with Fayalite (Fa) ranging from 18.1 to 24.8 mole %. Olivine crystals in type 6 chondrites are equilibrated as indicated by smaller standard deviations in Fa mole % as compared to type 3 samples, RaS 265 (L3) and JaH 596 (L3), that show unequilibrated olivine compositions with larger standard deviations (Table 1.1). However, type 3 samples of higher petrologic subtype, SaU 246 (H3/4) and RaS 337 (H3.6), also have small standard deviations in Fa mole % similar to those of type 6 samples (see Table 1.1). Overall, the olivine compositions determined in this study agree with the sample classification (Table 1.1).

The average chromite ( $\text{FeCr}_2\text{O}_4$ ) component of spinel in all samples is 71.5 mole %. Type 3 samples show much higher standard deviations in chromite mole % compared to type 6 samples (Table 1.2), which agrees with the previously reported spinel data for unequilibrated and equilibrated chondrites (Bunch *et al.*, 1967; Keil *et al.*, 1978a,b; Johnson and Prinz, 1991; Yanai and Kojima, 1991; Ruzicka *et al.*, 1998).

### 1.3.2 Olivine-spinel thermometry

The olivine-spinel thermometer provides a semi-quantitative tool to relate thermal metamorphic conditions to primary indicators of the petrologic types (i.e. texture and phase homogeneity) (Kessel *et al.*, 2007). Olivine-spinel temperatures were determined using an online version of the olivine-spinel thermometer ([http://melts.ofm-research.org/CORBA\\_CTserver/Olv\\_Spn\\_Opx/index.php](http://melts.ofm-research.org/CORBA_CTserver/Olv_Spn_Opx/index.php)) based on thermodynamic models developed in Sack and Ghiorso (1989, 1991a, b) assuming a pressure of 1 bar. The uncertainty associated with the model is approximately  $\pm 50$  °C ( $1\sigma$ ) (e.g., Benedix *et al.*, 2005) which is much larger than any contribution due to analytical uncertainties and is considered as uncertainty on individual temperatures. Table 1.3 reports the average temperature and range of

temperatures derived from all the olivine-spinel pairs selected for thermometric calculations in each sample. Figure 1.2 shows individual temperature values determined from each pair in each sample. Type 6 samples SaU 288, Dho 1012 and AHu 017 yield an average temperature of  $\sim 700$  °C, which is in perfect agreement with previous temperature estimates for L6 and H6 samples (Sack and Ghiorso 1991b; Kessel *et al.*, 2007; Wlotzka, 2005). However, a significantly higher average temperature of  $865 \pm 32$  °C (2SD uncertainty based on multiple measurements in a single sample) is derived for sample JaH 578 (H6). In type 3 samples, RaS 337 (H3.6) gives an average temperature of  $688 \pm 27$  °C. All the other type 3 samples, RaS 265 (L3), JaH 596 (L3) and SaU 246 (H3/4), give a relatively wider scatter of temperatures which reflects the unequilibrated nature of the olivine and spinel compositions in these samples, additionally supporting their low-metamorphic grade formation.

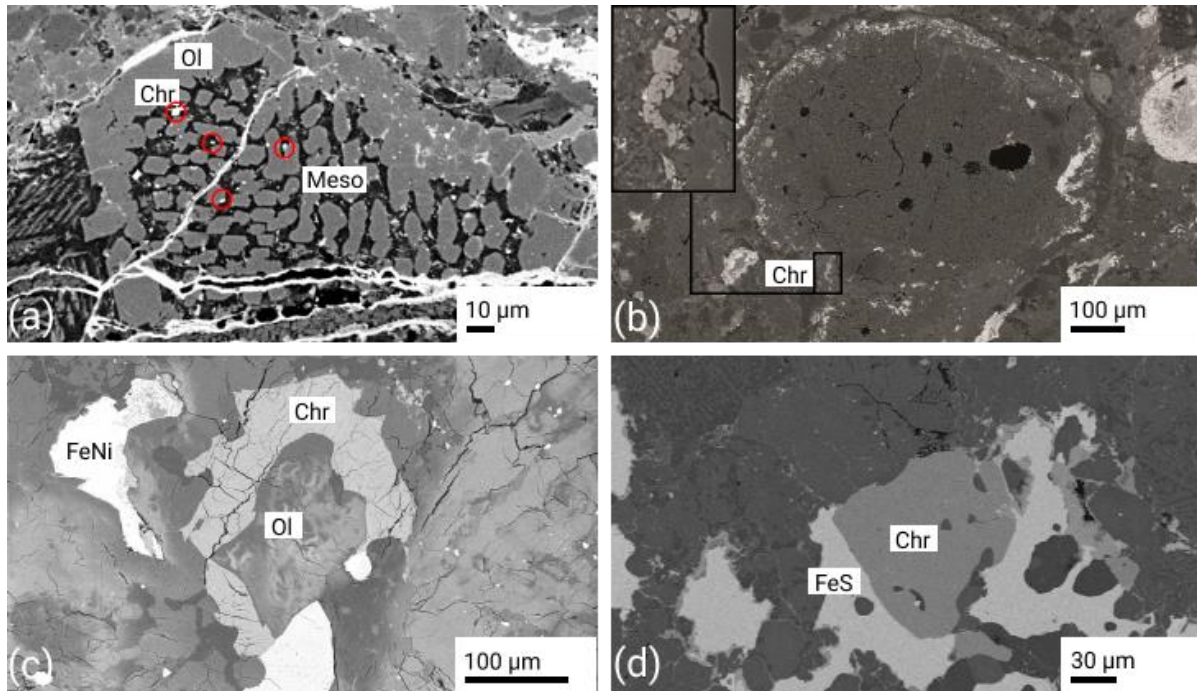


**Figure 1.1.** Backscattered electron (BSE) images showing typical occurrences of spinel grains/aggregates in type 3 and type 6 ordinary chondrites (a) Cr-rich grains within olivine or between the grain boundaries of olivine and adjacent phases in a chondrule of sample JaH 596 (L3); (b) Spinel grains aggregating along the rim around a chondrule in sample RaS 337 (H3.6), inset shows an enlarged image of the spinel aggregate; (c, d) Spinel in close association with Fe-Ni metal, mafic silicates and troilite in the matrices of samples Dho 1012 (L6) and JaH 578 (H6). Chr = chromite; FeS = troilite; Ol = Olivine, Meso = mesostasis, Fe-Ni = Fe-Ni metal.

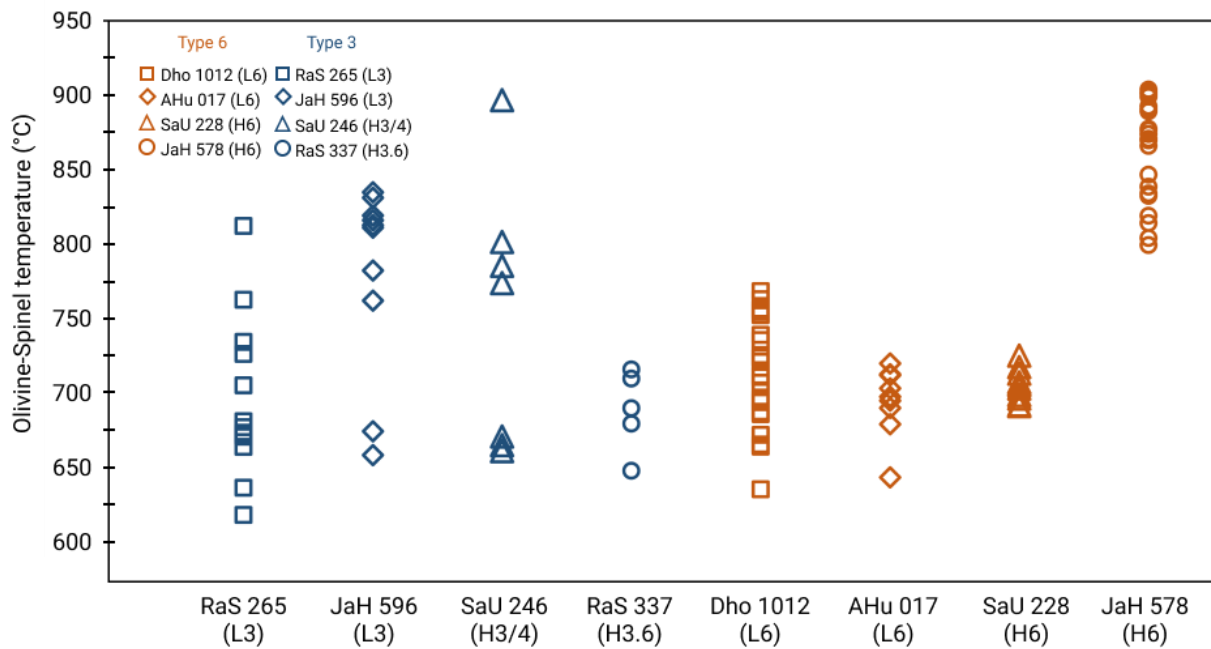


**Figure 1.2.** Individual temperature values estimated with the olivine-spinel thermometer. Type 3 samples show a wider scatter of temperatures compared to type 6 samples due to incomplete equilibration of the phases. Significantly higher temperatures are derived for sample JaH 578 (H6) among all type 6 samples. Uncertainties associated with each temperature estimate are approximately  $\pm 50$  °C ( $1\sigma$ ) (Benedix *et al.*, 2005) and are not shown for the sake of clarity.

### 1.3.3 Mn/Cr ratio in chromite and silicate fractions

The Mn/Cr ratios of chromite and silicate fractions for all samples are listed in Table 1.4. The Mn/Cr ratios of silicate fractions range from  $1.12 \pm 0.02$  to  $4.13 \pm 0.13$  and show a bifurcation into unequilibrated ( $1.12 \pm 0.02$  to  $2.18 \pm 0.06$ ) and equilibrated ( $2.13 \pm 0.08$  to  $4.13 \pm 0.13$ ) chondrites (Fig. 1.3). Mn/Cr ratios of chromite fractions range from  $0.0064 \pm 0.0002$  to  $0.0108 \pm 0.0002$  with systematically higher Mn/Cr ratios in chromites from H chondrites ( $0.0093 \pm 0.0002$  to  $0.0108 \pm 0.0002$ ) as compared to chromites in L chondrites ( $0.0064 \pm 0.0002$  to  $0.0075 \pm 0.0001$ ) (Fig. 1.3). The Mn/Cr ratios of chromite fractions in the H chondrites are in good agreement with previously reported Mn/Cr ratios of chromite components in Dimmitt (H3/4) ( $\text{Mn/Cr} = 0.009 \pm 5\%$ ) and Plainview (H5) ( $\text{Mn/Cr} = 0.011 \pm 5\%$ ) chondrites (Lugmair and Shukolyukov, 1998). They also agree with the  $\text{Mn/Cr} = 0.01 \pm 1\%$  in the chromite component from meteorite sample Ste. Marguerite (H4) (Trinquier *et al.*, 2008b). However, the  $\text{Mn/Cr} = 0.025 \pm 5\%$  for chromite in the L chondrite Finney (L5) reported in Lugmair and Shukolyukov (1998) is significantly higher than the range of Mn/Cr ratios in chromites from L chondrites analyzed in the present study. The range of Mn/Cr ratios

for silicate fractions in the unequilibrated chondrites analyzed in the present study agrees within uncertainties with the Mn/Cr ratios for silicate components in Dimmitt (H3/4) ( $\text{Mn/Cr} = 1.73 \pm 5\%$ ), Plainview (H5) ( $\text{Mn/Cr} = 2.45 \pm 5\%$ ) and Finney (L5) ( $\text{Mn/Cr} = 2.45 \pm 5\%$ ) meteorites (Lugmair and Shukolyukov, 1998).

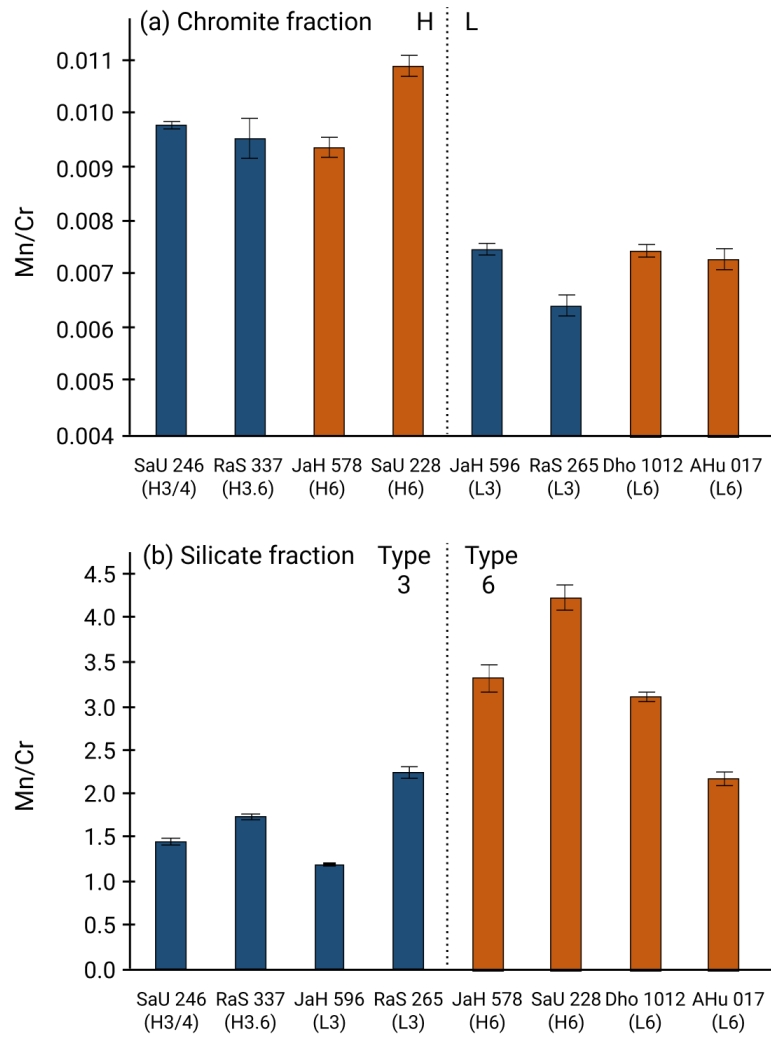


**Figure 1.3.** (a) Mn/Cr ratios in chromite fractions. The ratios are systematically higher in H chondrites than L chondrites (b) Mn/Cr ratios in silicate fractions. The dashed line highlights the dichotomy between lower Mn/Cr ratios in type 3 samples and higher Mn/Cr ratios in type 6 samples. Uncertainties associated with the Mn/Cr ratios determined by replicate measurements are shown as 2SE.

**Table 1.1.**

Olivine compositions (wt %) determined by EPMA and end member classification.

Sample	SaU 228	JaH 578	Dho 1012	AHu 017	SaU 246	RaS 337	RaS 265	JaH 596
Class/Type	H6	H6	L6	L6	H3/4	H3.6	L3	L3
# <sup>a</sup>	13	27	22	9	5	25	29	90
Al <sub>2</sub> O <sub>3</sub>	0.01 ± 0.02 <sup>b</sup>	0.02 ± 0.04	0.02 ± 0.06	0.01 ± 0.03	0.03 ± 0.06	0.02 ± 0.02	0.03 ± 0.06	0.04 ± 0.14
CaO	0.02 ± 0.03	0.03 ± 0.03	0.02 ± 0.04	0.02 ± 0.02	0.07 ± 0.09	0.03 ± 0.03	0.06 ± 0.07	0.10 ± 0.18
FeO	17.20 ± 0.80	18.4 ± 1.2	22.9 ± 1.5	21.1 ± 2.6	17.9 ± 1.3	17.30 ± 0.98	23.1 ± 4.4	20.4 ± 11.5
SiO <sub>2</sub>	40.25 ± 0.46	39.55 ± 0.74	38.4 ± 1.2	39.61 ± 0.44	39.94 ± 0.75	39.81 ± 0.88	38.29 ± 0.94	38.6 ± 2.2
MgO	43.37 ± 0.66	42.0 ± 1.1	38.6 ± 1.4	39.8 ± 1.9	42.33 ± 0.79	42.77 ± 0.89	39.0 ± 3.9	41.0 ± 9.2
MnO	0.49 ± 0.03	0.50 ± 0.03	0.49 ± 0.03	0.48 ± 0.04	0.47 ± 0.06	0.47 ± 0.07	0.46 ± 0.09	0.41 ± 0.21
Cr <sub>2</sub> O <sub>3</sub>	0.18 ± 0.32	0.08 ± 0.23	0.21 ± 0.49	0.17 ± 0.27	0.12 ± 0.05	0.03 ± 0.04	0.06 ± 0.13	0.15 ± 0.40
TiO <sub>2</sub>	0.01 ± 0.02	0.01 ± 0.04	0.01 ± 0.03	0.02 ± 0.02	0.03 ± 0.02	0.03 ± 0.07	0.03 ± 0.08	0.01 ± 0.04
Total	101.53	100.6	100.62	101.22	100.89	100.46	100.99	100.84
Fa <sup>c</sup>	18.1 ± 0.9	19.6 ± 1.4	24.8 ± 1.8	22.9 ± 2.9	19.0 ± 1.4	18.4 ± 1.1	24.8 ± 5.4	21.9 ± 13.2
Lit Fa <sup>d</sup>	18.7	19.6	24.8	22.9	18.2 - 23.2	18.1 ± 0.5	11.9 - 26.3	25.7 ± 6.7

<sup>a</sup> refers to the total number of olivine grains analyzed in each sample.

<sup>b</sup> 2SD of the distribution of average grain composition.

<sup>c</sup> Mole % of fayalite (Fa).

<sup>d</sup> Source: Meteoritical Bulletin Database (<https://www.lpi.usra.edu/meteor/metbull.php>).

**Table 1.2.**

Spinel composition (wt %) determined by EPMA and end member classification.

Sample	SaU 228	JaH 578	Dho 1012	AHu 017	SaU 246	RaS 337	RaS 265	JaH 596
Class/Type	H6	H6	L6	L6	H3/4	H3.6	L3	L3
# <sup>a</sup>	31	26	22	22	19	6	35	17
Al <sub>2</sub> O <sub>3</sub>	5.89 ± 0.51 <sup>b</sup>	5.43 ± 0.34	5.70 ± 0.53	4.66 ± 0.38	6.2 ± 3.2	4.4 ± 1.6	4.7 ± 3.6	7.7 ± 10.3
CaO	0.01 ± 0.01	0.01 ± 0.01	0.02 ± 0.05	0.03 ± 0.03	0.12 ± 0.21	0.10 ± 0.24	0.04 ± 0.05	0.06 ± 0.08
FeO <sup>c</sup>	28.96 ± 0.41	27.6 ± 2.0	31.0 ± 1.6	30.8 ± 1.5	28.4 ± 2.3	28.5 ± 1.2	31.0 ± 2.0	29.8 ± 2.4
MgO	3.18 ± 0.31	4.64 ± 0.65	2.44 ± 0.45	2.43 ± 0.51	2.9 ± 1.8	2.63 ± 0.55	2.2 ± 1.7	3.0 ± 1.7
MnO	1.22 ± 0.23	1.18 ± 0.07	1.07 ± 0.10	0.82 ± 0.10	1.25 ± 0.19	1.28 ± 0.08	0.96 ± 0.32	0.95 ± 0.19
Cr <sub>2</sub> O <sub>3</sub>	57.90 ± 0.83	58.7 ± 1.3	56.9 ± 2.2	57.4 ± 1.7	58.3 ± 3.4	58.6 ± 1.1	57.7 ± 7.4	55.4 ± 9.1
TiO <sub>2</sub>	2.34 ± 0.33	2.88 ± 0.20	2.94 ± 0.80	2.86 ± 0.52	1.46 ± 0.84	1.80 ± 0.83	2.6 ± 2.2	2.1 ± 1.9
Total	99.5	100.41	100.02	99.04	98.75	97.44	99.27	99.04
MgAl <sub>2</sub> O <sub>4</sub> (spinel)	2.1 ± 0.2	2.7 ± 0.4	1.5 ± 0.3	1.3 ± 0.6	2.0 ± 2.5	1.4 ± 0.7	1.3 ± 1.1	2.9 ± 5.7
FeAl <sub>2</sub> O <sub>4</sub> (hercynite)	11.0 ± 1.0	8.9 ± 0.4	11.0 ± 1.0	9.0 ± 1.0	11.4 ± 4.5	8.4 ± 2.7	9.1 ± 6.8	13.0 ± 14.0
FeCr <sub>2</sub> O <sub>4</sub> (chromite)	70.1 ± 1.2	64.6 ± 2.6	72.8 ± 1.6	74.1 ± 5.1	70.7 ± 12.2	74.9 ± 5.1	76.1 ± 16.5	68.4 ± 19.9
MgCr <sub>2</sub> O <sub>4</sub> (picrochromite)	13.8 ± 1.3	19.6 ± 2.7	10.0 ± 2.0	11.0 ± 4.0	13.3 ± 6.7	12.4 ± 1.9	9.3 ± 7.1	12.0 ± 3.4
Fe <sub>2</sub> TiO <sub>4</sub> (ulvöspinel)	2.7 ± 0.4	3.0 ± 0.2	4.0 ± 1.0	3.5 ± 0.6	1.7 ± 0.9	2.2 ± 0.9	3.3 ± 2.7	2.5 ± 2.5
Mg <sub>2</sub> TiO <sub>4</sub> (qandilite)	0.5 ± 0.1	0.9 ± 0.1	0.5 ± 0.2	0.5 ± 0.2	0.3 ± 0.3	0.4 ± 0.2	0.5 ± 0.4	0.4 ± 0.3
Fe <sub>3</sub> O <sub>4</sub> (magnetite)	0.2 ± 0.6	0.4 ± 1.6	0.3 ± 1.7	0.5 ± 1.6	0.3 ± 0.8	0.3 ± 0.8	0.5 ± 0.9	0.4 ± 1.1

Mole % of spinel group end members: spinel, hercynite, chromite, picrochromite, ulvöspinel, qandilite and magnetite are calculated using End Member Generator (EMG) (Ferracutti *et al.*, 2015).

<sup>a</sup> refers to the total number of olivine grains analyzed in each sample.

<sup>b</sup> 2SD of the distribution of average grain compositions.

<sup>c</sup> All Fe expressed as FeO.

**Table 1.3.**

Average temperature and range of temperatures derived from olivine-spinel thermometry.

Sample	Average temperature (°C)	Range of temperatures (°C)	No. of pairs
SaU 228 (H6)	704 ± 10 (15)	690-724	11
JaH 578 (H6)	865 ± 32 (10)	798-902	26
Dho 1012 (L6)	712 ± 35 (10)	635-767	23
AHu 017 (L6)	694 ± 23 (17)	648-719	9
SaU 246 (H3/4)	750 ± 88 (19)	660-895	7
RaS 337 (H3.6)	688 ± 27 (23)	679-715	5
RaS 265 (L3)	693 ± 51 (13)	617-811	14
JaH 596 (L3)	779 ± 64 (16)	658-834	10

Average temperature refers to the mean of the individual temperatures determined in each sample. The associated uncertainties shown in parenthesis are given in 2SD of the distribution of the average temperature.

### 1.3.4 Cr isotope compositions

The  $\epsilon^{53}\text{Cr}$  of chromite and silicate fractions determined in all samples are listed in Table 1.4. The  $\epsilon^{53}\text{Cr}$  of chromite fractions range from  $-0.02 \pm 0.03$  to  $0.11 \pm 0.03$ . The chromite fractions from L3 samples JaH 596 and RaS 265 record an average  $\epsilon^{53}\text{Cr}$  of  $-0.02 \pm 0.02$  (2SD). In case of H3 samples, RaS 337 gives an  $\epsilon^{53}\text{Cr} = -0.02 \pm 0.03$  in agreement with that of L3 samples. Chromite fraction in sample SaU 246 (H3/4) has a higher  $\epsilon^{53}\text{Cr}$  ( $= 0.06 \pm 0.05$ ) than chromite fractions from all the other type 3 samples. It agrees within uncertainties with the average  $\epsilon^{53}\text{Cr}$  ( $0.09 \pm 0.04$ , 2SD) determined in chromite fractions from type 6 samples. The  $\epsilon^{53}\text{Cr}$  in silicate fractions range from  $0.19 \pm 0.03$  to  $0.77 \pm 0.03$  and agree within uncertainties with previously reported  $\epsilon^{53}\text{Cr}$  for silicate fractions in ordinary chondrites, such as  $\epsilon^{53}\text{Cr} = 0.59 \pm 0.10$ ,  $0.65 \pm 0.13$  and  $0.52 \pm 0.10$  for samples Dimmitt (H3,4), Plainview (H5) and Finney (L5), respectively (Lugmair and Shukolyukov, 1998).

### 1.3.5 Correction for spallogenic Cr

Spallation reactions induced by cosmic-ray exposure (CRE) can alter  $^{53}\text{Cr}/^{52}\text{Cr}$  ratios in solar system objects. This alteration depends on the duration of cosmic ray exposure, its intensity, Fe/Cr ratio and shielding condition for any given sample and requires a correction before the Cr isotope systematics can be used as a dating tool (Liu *et al.*, 2019). Figure 1.4 shows an  $\epsilon^{54}\text{Cr}$  vs  $\epsilon^{53}\text{Cr}$  diagram for the chromite and silicate fractions of all samples. Due to



significantly high radiogenic  $\epsilon^{53}\text{Cr}$  and low Fe/Cr ratios in the chromite fractions, cosmogenic contributions are negligible and hence no correction is needed. However, silicate fractions with higher Fe/Cr ratios may require correction for spallogenic Cr (Table 1.4). Since chromite and silicate fractions formed from the same reservoir and the correlation between  $\epsilon^{53}\text{Cr}$  and  $\epsilon^{54}\text{Cr}$  is unaffected by the spallogenic reactions (Liu *et al.*, 2019),  $\epsilon^{54}\text{Cr}$  of the chromite fractions can be used to internally correct the Cr isotopic composition of the silicate fractions. From Figure 1.4 such correction appears necessary in samples RaS 265 and JaH 578 that show  $\epsilon^{54}\text{Cr}$  values remarkably higher than the mean  $\epsilon^{54}\text{Cr}$  found in ordinary chondrites (whole rock and components), compiled from the literature (Trinquier *et al.*, 2007, 2008b; Qin *et al.*, 2010; Schneider *et al.*, 2020). To reconcile the  $\epsilon^{54}\text{Cr}$  values of the silicate fractions of samples RaS 265 and JaH 578 with their chromite fractions, the Cr isotopic compositions are corrected using the equation given in Table 1.2 in Trinquier *et al.* (2007) and a  $^{53}\text{Cr}$  and  $^{54}\text{Cr}$  production rate of  $2.9 \times 10^{11}$  atoms/Ma in Fe targets (Birck and Allègre, 1985b). The correction estimates a CRE age of 237 Ma for RaS 265 and 169 Ma for JaH 578. The corrected  $\epsilon^{53}\text{Cr}$  and  $\epsilon^{54}\text{Cr}$  are reported in Table 1.4.

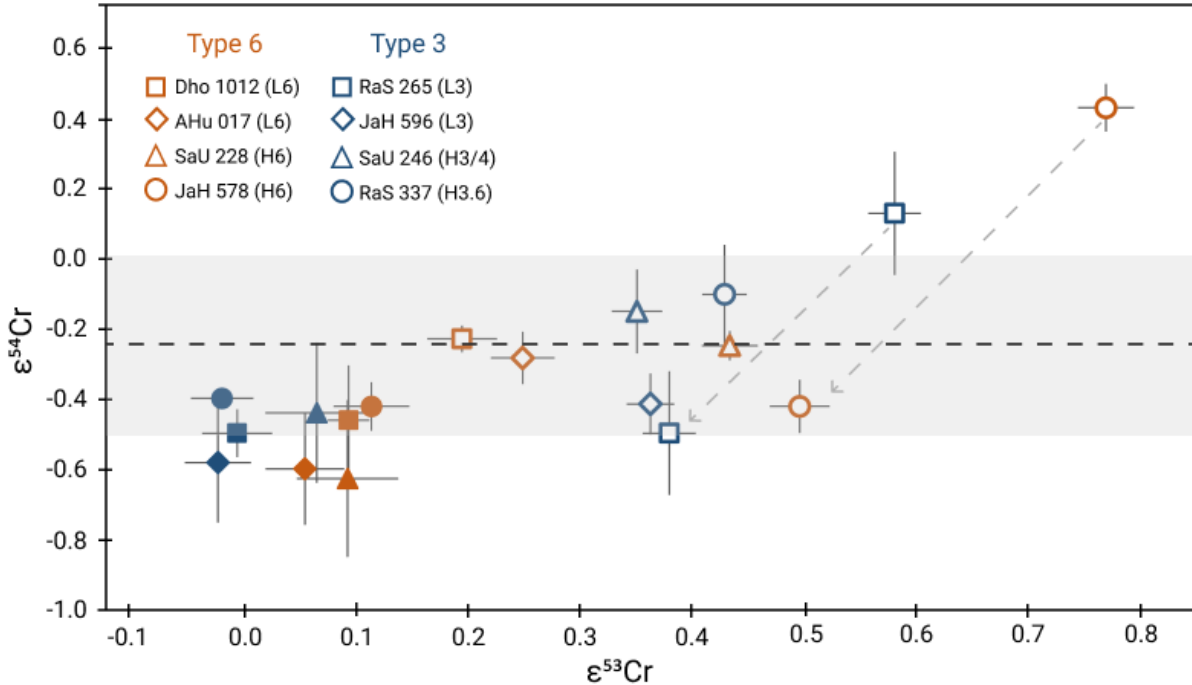


**Figure 1.4.**  $\epsilon^{53}\text{Cr}$  vs  $\epsilon^{54}\text{Cr}$  diagram for the chromite and silicate fractions from the studied samples. The shaded region represents the mean and 1 standard deviation ( $= -0.24 \pm 0.26$ ) of the  $\epsilon^{54}\text{Cr}$  in ordinary chondrites (whole rock and components), compiled from the literature (Trinquier *et al.*, 2007, 2008b; Qin *et al.*, 2010; Schneider *et al.*, 2020). The dashed arrows show the correction applied for spallogenic Cr in samples RaS 265 and JaH 578 (see text).

**Table 1.4.**

Mn/Cr, Fe/Cr and Cr isotopic compositions of studied samples.

Sample	Fraction	Mn/Cr	2SE <sup>a</sup>	Fe/Cr	2SE <sup>a</sup>	$\epsilon^{53}\text{Cr}$	2SE (n <sup>a</sup> )	$\epsilon^{54}\text{Cr}$	2SE
SaU 246 (H3/4)	Chromite	0.0098	0.0001	0.44	0.01	0.06	0.05(4)	-0.43	0.20
	Silicate	1.39	0.04	172.6	3.6	0.35	0.02(5)	-0.14	0.12
RaS 337 (H3.6)	Chromite	0.0095	0.0004	0.41	0.01	-0.02	0.03(2)	-0.40	0.01
	Silicate	1.69	0.03	215.6	2.0	0.43	0.02(4)	-0.10	0.14
JaH 578 (H6)	Chromite	0.0093	0.0002	0.43	0.01	0.11	0.03(8)	-0.41	0.07
	Silicate (UC)	3.24	0.15	399.2	17.3	0.77	0.03(4)	0.44	0.07
	Silicate (C)	-	-	-	-	0.50	0.03(4)	-0.41	0.08
SaU 228 (H6)	Chromite	0.0108	0.0002	0.44	0.02	0.09	0.05(4)	-0.62	0.22
	Silicate	4.13	0.13	556.5	17.5	0.43	0.03(5)	-0.24	0.04
JaH 596 (L3)	Chromite	0.0075	0.0001	0.46	0.01	-0.03	0.03(6)	-0.57	0.17
	Silicate	1.12	0.02	91.7	1.1	0.36	0.02(5)	-0.41	0.09
RaS 265 (L3)	Chromite	0.0064	0.0002	0.43	0.01	-0.01	0.03(5)	-0.49	0.07
	Silicate (UC)	2.18	0.06	209.4	4.6	0.58	0.02(5)	0.14	0.18
	Silicate (C)	-	-	-	-	0.38	0.02(3)	-0.49	0.18
Dho 1012 (L6)	Chromite	0.0074	0.0001	0.46	0.01	0.09	0.02(5)	-0.45	0.16
	Silicate	3.03	0.06	298.3	3.3	0.19	0.03(5)	-0.22	0.04
AHu 017 (L6)	Chromite	0.0073	0.0002	0.44	0.01	0.05	0.04(4)	-0.59	0.16
	Silicate	2.13	0.08	203.7	6.3	0.25	0.03(5)	-0.28	0.08

<sup>a</sup> Number of replicates measured for each sample.

The uncertainties associated with Mn/Cr, Fe/Cr, and Cr isotopic compositions are given in 2SE of the replicate measurements. See Table A1.2 for Cr isotopic compositions of the individual runs. Cr isotopic compositions in the silicate fractions of samples RaS 265 and JaH 578 are reported after correction for spallogenic reactions. (C): corrected, (UC): uncorrected.

### 1.3.6 Chromite model ages

The evolution of  $\epsilon^{53}\text{Cr}$  in a chondritic reservoir as expressed by Eq. 1.1 is used to derive model ages from the chromite fractions. The model ages are calculated relative to the CAI formation age of  $4567.18 \pm 0.50$  Ma (Amelin *et al.*, 2010) assuming solar system initial  $\epsilon^{53}\text{Cr} = -0.23$ , CI chondritic  $^{55}\text{Mn}/^{52}\text{Cr} = 0.71$  and a canonical  $^{53}\text{Mn}/^{55}\text{Mn} = 6.28 \times 10^{-6}$  (Trinquier *et al.*, 2008b). These ages are reported in Table 1.5 and plotted on the chondritic  $\epsilon^{53}\text{Cr}$  evolution diagram (Fig. 1.5).

The chromite model ages correlate with the petrologic grade of the samples and yield two distinct “clusters” (Fig. 1.5). The first cluster comprises samples RaS 337 (H3.6), JaH 596 (L3) and RaS 265 (L3), all of which are of petrologic type 3 and yield model ages from  $3.99^{+0.93}_{-0.79}$  Ma to  $4.51^{+1.10}_{-0.91}$  Ma after CAI formation. The chromite fraction from sample SaU 246 (H3/4) displays a younger age ( $7.4^{+3.4}_{-2.1}$  Ma) than the chromites from other type 3 samples. It lies closer to the second cluster that comprises all the type 6 samples. The model ages for the second cluster range from  $6.9^{+2.1}_{-1.5}$  Ma to  $11.1^{+6.0}_{-2.8}$  Ma. There is no systematic difference in model ages for both H and L chondrites, therefore they are discussed together assuming similar structures, sizes, accretion time and high-temperature cooling histories of their parent bodies.

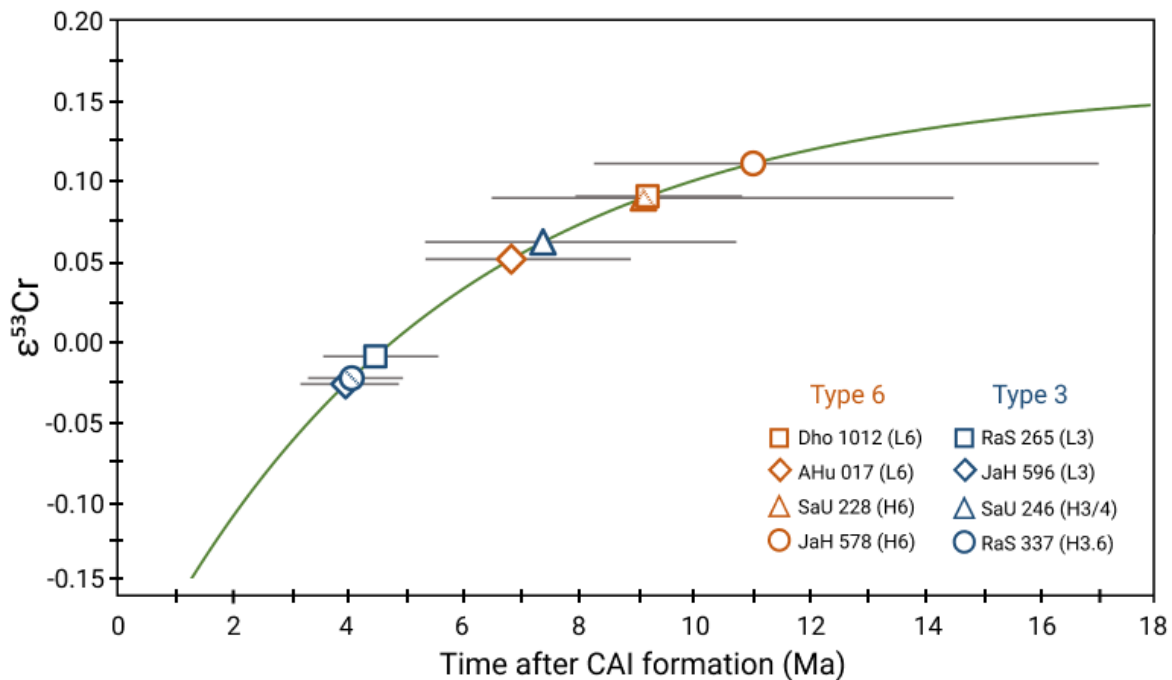


**Figure 1.5.** The model ages are plotted on a curve representing the  $\epsilon^{53}\text{Cr}$  evolution of the chondritic reservoir through time. Uncertainties on the model ages are determined using uncertainties on the  $\epsilon^{53}\text{Cr}$  values of the samples. The model ages correlate with the petrologic grade of the samples and yield two distinct “clusters”. The first cluster comprises type 3 samples except sample SaU 246 (H3/4) that lies closer to the second cluster that comprises type 6 samples.

**Table 1.5.**

Chromite model ages and two-point isochron ages determined for the studied chondrites.

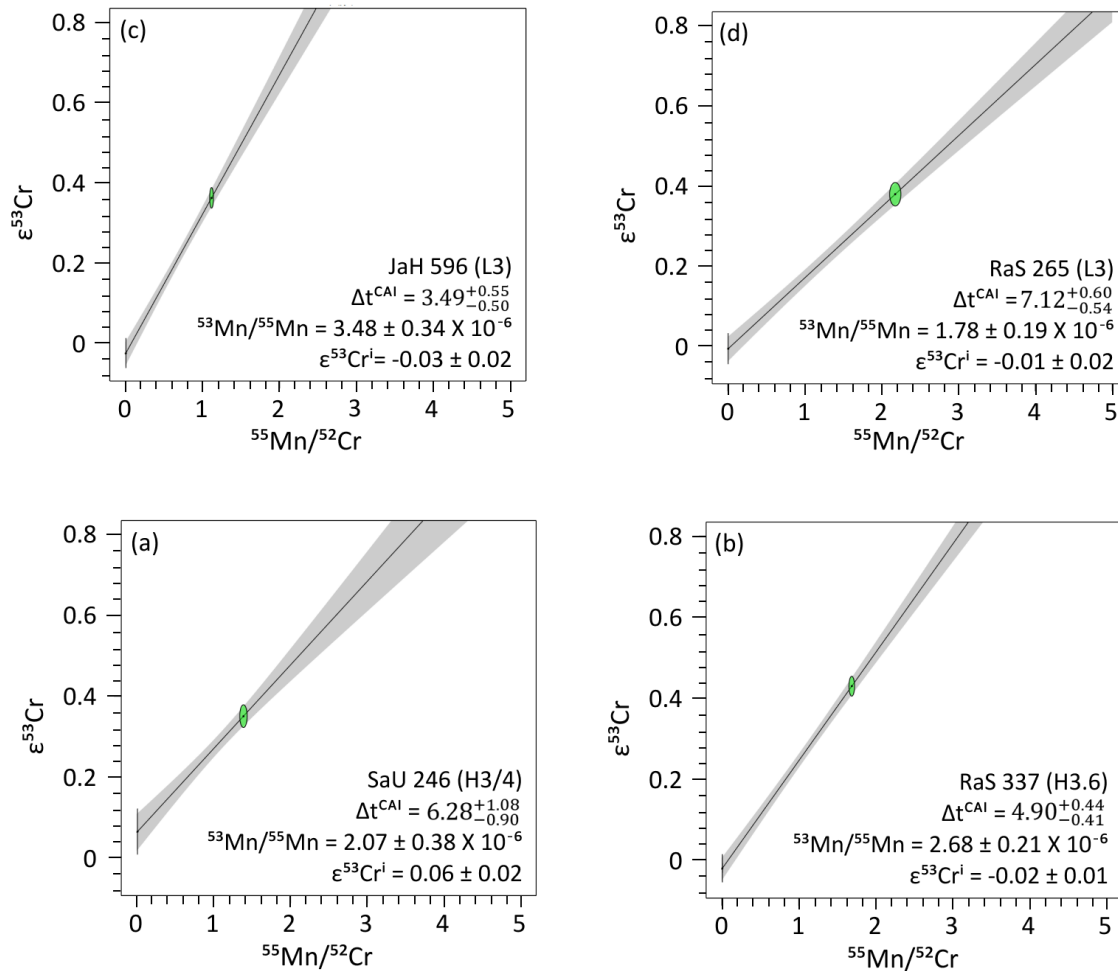
Chromite model age		isochron ages		
Sample	(Ma after CAIs)	<sup>53</sup> Mn/ <sup>55</sup> Mn	2σ	Age (Ma after CAIs)
This study				
SaU 246 (H3/4)	7.4 <sup>+3.4</sup> <sub>-2.1</sub>	2.35 X 10 <sup>-6</sup>	0.43 X 10 <sup>-6</sup>	5.60 <sup>+1.08</sup> <sub>-0.90</sub>
RaS 337 (H3.6)	4.10 <sup>+0.89</sup> <sub>-0.76</sub>	3.03 X 10 <sup>-6</sup>	0.24 X 10 <sup>-6</sup>	4.24 <sup>+0.44</sup> <sub>-0.41</sub>
JaH 578 (H6)	11.1 <sup>+6.0</sup> <sub>-2.8</sub>	1.34 X 10 <sup>-6</sup>	0.16 X 10 <sup>-6</sup>	8.62 <sup>+0.70</sup> <sub>-0.62</sub>
SaU 228 (H6)	9.2 <sup>+5.4</sup> <sub>-2.6</sub>	9.41 X 10 <sup>-7</sup>	1.48 X 10 <sup>-7</sup>	10.54 <sup>+0.92</sup> <sub>-0.79</sub>
JaH 596 (L3)	3.99 <sup>+0.93</sup> <sub>-0.79</sub>	3.96 X 10 <sup>-6</sup>	0.39 X 10 <sup>-6</sup>	2.78 <sup>+0.55</sup> <sub>-0.50</sub>
RaS 265 (L3)	4.51 <sup>+1.10</sup> <sub>-0.91</sub>	2.02 X 10 <sup>-6</sup>	0.21 X 10 <sup>-6</sup>	6.43 <sup>+0.61</sup> <sub>-0.55</sub>
Dho 1012 (L6)	9.3 <sup>+1.6</sup> <sub>-1.3</sub>	3.80 X 10 <sup>-7</sup>	1.35 X 10 <sup>-7</sup>	15.4 <sup>+2.4</sup> <sub>-1.6</sub>
AHu 017 (L6)	6.9 <sup>+2.1</sup> <sub>-1.5</sub>	1.04 X 10 <sup>-6</sup>	0.24 X 10 <sup>-6</sup>	10.0 <sup>+1.4</sup> <sub>-1.1</sub>
Literature				
Finney (L5) <sup>a</sup>	-	2.70 X 10 <sup>-7</sup>	-	~17.20
Ste. Marguerite (H4) <sup>b</sup>	-	2.78 x 10 <sup>-6</sup>	0.46 X 10 <sup>-6</sup>	4.7 ± 1.0

Uncertainties on the model ages are determined using uncertainties on  $\epsilon^{53}\text{Cr}$  values of the samples.  $^{53}\text{Mn}/^{55}\text{Mn}$  ratio refers to the slope of the two-point isochron. Associated error on slope is given at  $2\sigma$  level. Uncertainties on two-point isochron ages are determined using uncertainties on  $^{53}\text{Mn}/^{55}\text{Mn}$  ratios. Sources for literature data: (a)  $^{53}\text{Mn}/^{55}\text{Mn}$  and corresponding isochron age for Finney (L5) is determined by regression in IsoplotR (Vermeesch, 2018) using  $\epsilon^{53}\text{Cr}$  of silicate, whole rock and chromite fractions reported in Lugmair and Shukolyukov (1998) and anchored to achondrite NWA 6704 (b)  $^{53}\text{Mn}/^{55}\text{Mn}$  for Ste. Marguerite (H4) is taken from Trinquier *et al.* (2008b) and corresponding isochron age is determined by anchoring to NWA 6704 (see text).

### 1.3.7 Isochron ages

In addition to the chromite model ages, two-point isochron ages are obtained from pairs consisting of chromite and corresponding silicate fractions from each sample. Figure 1.6 (a)-(h) illustrates the data from Table 1.4 for each chondrite sample. The  $\epsilon^{53}\text{Cr}$  and  $^{55}\text{Mn}/^{52}\text{Cr}$  data are used to construct two-point isochrons by regression in IsoplotR (Vermeesch, 2018) taking the maximum likelihood regression model. The use of two-point isochrons is justified for these samples because the chromites formed from their surrounding matrix and thus both components had the same initial Cr-isotope composition when the chromite grew. This is similar to the approach commonly used in meteorite studies where only two components can be used to obtain a significant spread in isotope space (e.g., Birck and Allegre, 1988). The slope of the isochron then yields the initial  $^{53}\text{Mn}/^{55}\text{Mn}$  ratio of the sample at the time of Mn-Cr

fractionation. Comparison of this isotope ratio with  $^{53}\text{Mn}/^{55}\text{Mn} = 2.59 \pm 0.34 \times 10^{-6}$  at the time of isotopic closure in the carbonaceous achondrite NWA 6704 (Sanborn *et al.*, 2019) yields the age of thermal metamorphism of the sample relative to NWA 6704. The inferred initial  $^{26}\text{Al}/^{27}\text{Al}_0 = 3.15 \pm 0.38 \times 10^{-7}$  of NWA 6704 (Sanborn *et al.*, 2019) and corresponding  $^{26}\text{Al}$ - $^{26}\text{Mg}$  age of  $5.2 \pm 0.2$  Ma relative to the canonical  $^{26}\text{Al}/^{27}\text{Al}_0$  value of CAIs (Jacobsen *et al.* 2008; Larsen *et al.*, 2011), is used to calculate the Mn-Cr age of the samples relative to the CAI formation. The  $^{53}\text{Mn}/^{55}\text{Mn}$  ratios and two-point isochron ages for each sample are reported along with the chromite model ages in Table 1.5. The table also includes reported isochron ages for equilibrated ordinary chondrites.



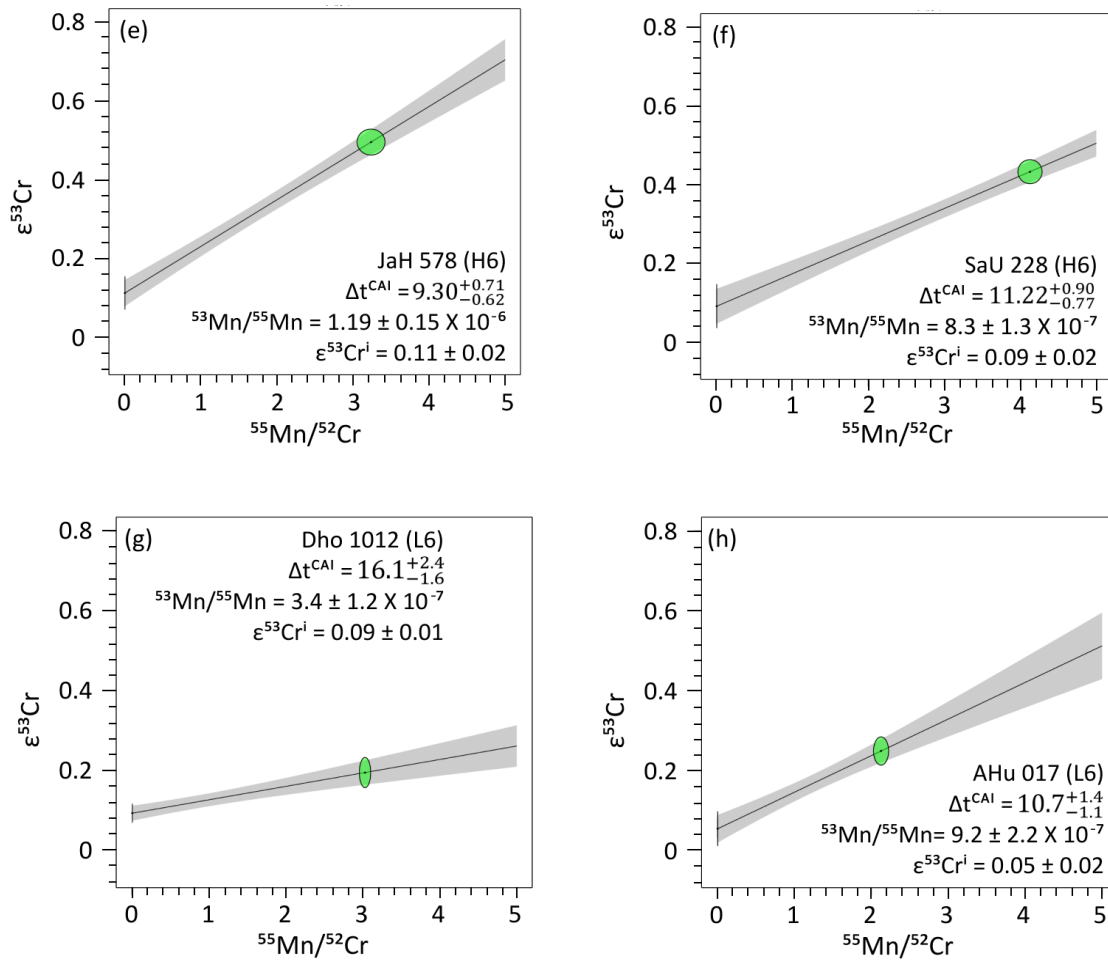


**Figure 1.6.** (a-h)  $\epsilon^{53}\text{Cr}$  vs  $^{55}\text{Mn}/^{52}\text{Cr}$  diagrams for the studied sample. The  $\epsilon^{53}\text{Cr}$  and  $^{55}\text{Mn}/^{52}\text{Cr}$  data points for the chromite and silicate fractions in each sample are used to construct a two-point isochron.  $\Delta t^{\text{CAI}}$  refers to formation interval relative to CAIs.

## 1.4 Discussion

### 1.4.1 The onset and progression of metamorphism in ordinary chondrites

Spinel group minerals have widely been used to study the onset and progressive thermal metamorphism in ordinary chondrites (e.g., Johnson and Prinz, 1991; Grossman and Brearley, 2005; Kimura *et al.*, 2006). Kimura *et al.* (2006) studied LL3.0-LL6 chondrites and reported multiple origins and formation mechanisms of spinel group minerals, especially in type 3.0-3.9 ordinary chondrites. The authors showed that the occurrence of nearly pure chromite and a wide compositional variation can distinguish spinel group minerals in types 3.0-3.3 from those in the other types. Spinel group minerals in types 3.5-3.9 show a narrower range of compositions, and those in types 4-6 are homogeneous. Most of the spinel group minerals in

chondrules of type 3.0-3.3 crystallized from the chondrule melt and give olivine-spinel temperatures of  $\geq 1000$  °C, reflecting chondrule crystallization conditions (Johnson and Prinz, 1991). The two L3 samples, JaH 596 and RaS 265, investigated in the present study show olivine-spinel temperatures within the range of 620-830 °C which is typical of type 3.5-3.9 samples. Such low temperatures reflect either reset or formation during progressive thermal metamorphism.

Thermal metamorphism can produce chromite grains by exsolution of Cr incorporated into olivine at higher temperature. The onset of thermal metamorphism in ordinary chondrites leads to the chemical homogenization of olivine and eventually a decrease in its Cr-content (Grossman and Brearley, 2005). This equilibration can be observed starting as early as in petrologic type 3.0 to 3.3. (McCoy *et al.*, 1991, DeHart *et al.*, 1992). Grossman and Brearley (2005) found a Cr-rich phase,  $<1$   $\mu\text{m}$  large, exsolving from olivine in type L3.10 chondrites. Similar sub- $\mu\text{m}$  Cr-rich grains within olivine or between the grain boundaries of olivine and adjacent phases are also observed in chondrules of sample JaH 596 (L3) and RaS 265 (L3) (Fig. 1.1a) and inferred to be chromite. With increasing metamorphic grade, such small grains coalesce to form larger chromite grains, first aggregating along the rim around chondrules as seen in SaU 246 (H3/4) and RaS 337 (H3.6) (Fig. 1.1b), and then becoming equant phases in the matrix of type 6 samples (Fig. 1.1c, d). In addition to the crystallization from the chondrule melt or formation due to thermal metamorphism, relic origin of spinel in chondrule is also identified (Kimura *et al.*, 2006). These 5-35  $\mu\text{m}$  spherical to irregular grains that survived the melting of the chondrule precursor materials were described in LL3.15-LL3.3 chondrites (Kimura *et al.*, 2006), however, not observed in type 3 samples investigated in the present study; indicating the possibility of their higher petrologic subgrade.

The chemical equilibration of olivine and newly formed chromite commenced with the exsolution of chromite grains at the onset of thermal metamorphism and continued with the inter-and intragrain homogenization of the olivine crystals. Chemical equilibration is evident in the studied samples when comparing the abundance and chemistry of chromite grains in type 3 and type 6 samples. The gradual equilibration of spinel and its reactivity during prograde metamorphism is also reflected in the result of the olivine-spinel thermometry. Type 3 samples yield a relatively wider range of temperature estimate in individual samples (Fig. 1.2) as compared to type 6 samples. The olivine-spinel temperatures in type 6 samples show chemical

homogenization and equilibration of the phases acquired at higher metamorphic temperature. Kessel *et al.* (2007) studied equilibrated type 4-6 chondrites from H, L and LL classes applying olivine-spinel thermometry and showed that the maximum temperatures (interpreted as equilibration temperatures) recorded by individual chondrites increase subtly, but systematically with the metamorphic type and are tightly clustered. They observed a correlation between the spinel grain sizes and the determined temperatures: larger spinel grains are resistant and preserve the peak temperature above the closure temperature of the Fe-Mg diffusion in olivine-spinel pairs, while smaller spinel grains continued to re-equilibrate during retrograde metamorphism, recording a range of lower closure temperatures. Wlotzka (2005) incorporated “unequilibrated” type 3.7 and 3.8 chondrites and for the first-time calculated temperatures, that can be interpreted as “equilibrium temperatures” for these samples. Wlotzka (2005) argued that subtypes 3.7 to 3.9 are already partially equilibrated by a Fe-Mg exchange between Fe-Mg silicates and Cr-spinel and thus temperatures derived from the olivine-Cr-spinel pairs represent equilibrium temperatures. Sample RaS 337 (H3.6) gives an average temperature value of 688 °C which is within the temperature range of 619-699 °C (Fig. 1.2) reported by Wlotzka (2005) for type H3.7-3.8 samples.

#### **1.4.2 Closure temperature of the Mn-Cr system in spinel**

The interpretation of Mn-Cr isochron and chromite model ages requires estimates for the diffusivity of Cr in different minerals as a function of temperatures. Chromium diffusion data are available for olivine (Ito and Ganguly, 2006), orthopyroxene (Ganguly *et al.*, 2007) and chromite (Posner *et al.*, 2016). The Mn-Cr isochron ages for several H and L chondrites have been investigated in previous studies (e.g., Lugmair and Shukolyukov, 1998) and mostly rely on whole rock, chromite and silicate fractions. However, the silicates with high Mn/Cr ratios dominate the slope and the resulting age. Due to uncertainties concerning which phase dominates the Mn budget and, hence, which closure temperature should be applied, the Mn-Cr chondrite cooling ages are generally ignored in the thermal history models to constrain the metamorphic evolution of ordinary chondrite parent bodies (Henke *et al.*, 2013). Unlike the Mn-Cr isochron, the chromite model ages require a Cr closure temperature estimate in chromite only and this information is crucial for a meaningful interpretation of chromite model ages, i.e., whether they date the time of mineral growth or some time along the cooling path.



For any mineral, the closure temperature depends on the diffusion behavior as a function of temperature, cooling rate, and effective diffusion radius; the latter can be related to the grain size (Dodson, 1973). Sugiura and Hoshino (2003) investigated Mn-Cr systematics in phosphates (sarcopside, graffonite, beusite, galileiite and johnsomervilleite) by secondary ion mass spectrometry (SIMS) in the slowly cooled IIIAB iron meteorites. They observed that the different phosphate phases yield different “ages” due to different Mn-Cr diffusion rates, and thus different closure temperatures. Only in rapidly cooled systems, where parent and daughter elements do not diffuse significantly, does the age correspond to the time of mineral formation and approximates the growth age of the phase. Since IIIAB iron meteorites cooled slowly at a rate of ca. 60-200 °C/Ma (e.g., Matthes *et al.*, 2020), the Mn-Cr chronometer does not provide the time of formation of minerals in IIIAB iron meteorites but the time of “closure” (i.e. the time at which the Mn-Cr system was frozen, Sugiura and Hoshino 2003), which can be different for different minerals.

Recently, Sievwright *et al.* (2020) reported that the diffusion coefficients of a wide range of cations in magnetite increase in the order: Cr < Mo  $\approx$  Ta < V < Ti < Al < Hf  $\approx$  Nb < Sc  $\approx$  Zr  $\approx$  Ga < In < Lu  $\approx$  Y < Ni < U  $\approx$  Zn < Mn  $\approx$  Mg < Co < Li < Cu. Isostructural with magnetite, the order should also hold for chromite. The assumed relatively low diffusion coefficient of Cr in chromite implies that the original content of Cr should be well preserved.

Posner *et al.* (2016) carried out a tracer diffusion experiment of Cr in natural spinels at 1 bar and 950-1200 °C under controlled  $f(\text{O}_2)$  conditions to determine the dependence of the Cr diffusion coefficient  $D(\text{Cr})$  and closure temperature on  $f(\text{O}_2)$  and Cr# (i.e., Cr/(Cr + Al)). They used the closure temperature calculator developed by Ganguly and Tirone (2009) as an extension of the classic work of Dodson (1973) to calculate the closure temperature of Cr in spinel as a function of (i) peak temperature, (ii) grain size, (iii) cooling rate and (iv)  $f(\text{O}_2)$ . This calculator is used in the present study to constrain the closure temperature of Cr in spinel from type 3 and 6 ordinary chondrites. The results are shown in Figure 1.7.

For type 6 ordinary chondrites, a temperature of ca. 1000 °C provides an upper limit for the possible peak temperature since the beginning of melting in chondritic material would be the eutectic melting in the FeNi-FeS system at  $\sim$ 1000 °C, but ordinary chondrites lack any indications for partial melting (Gail and Trieloff, 2019). Two-pyroxene thermometry (Lindsley and Andersen, 1983) provides peak temperature estimates of 865-926 °C for H6 and 812-934

°C for L6 chondrites (Slater-Reynolds and McSween, 2005). Schrader *et al.* (2016) investigated the compositional and textural evolution of sulfides within a wide range of thermally metamorphosed LL chondrites and reported peak temperatures of ~900 °C. The peak metamorphic temperatures in type 3 chondrites are poorly constrained because of the unequilibrated composition of phases which negates the rigorous application of commonly used geothermometers. Dodd (1981) estimated a peak temperature range of 400-600 °C for type 3 chondrites. Further work on type 3 meteorites determined a wider range of peak temperatures from 260 to 600 °C (e.g., Huss *et al.*, 2006, Busemann *et al.*, 2007). Wlotzka (2005) used the olivine-spinel thermometer and derived an “equilibrium temperature” of 619-699 °C for H3.7-3.8 chondrites. Subtypes within type 3s were found to correlate well with the estimated peak temperatures. Wlotzka (2005) furthermore argued that the equilibrium temperature may not necessarily be the peak temperature experienced by chondrites, but for type 3.7-3.8, it was not exceeded by more than 100 °C for a long time. Otherwise, they would have been equilibrated to type 4. A comparison between the thermal model of H (Henke *et al.*, 2012b, 2013) and L (Gail and Trierloff, 2019) chondrite parent bodies shows that the peak temperature reached at the burial depths of H6 meteorites is ~50 °C higher than that in L6 meteorites. Nevertheless, considering the maximum temperature of ~930 °C (Slater-Reynolds and McSween, 2005) deduced from two-pyroxene thermometry in type 6 meteorites of both H and L meteorites, it is reasonable to assume a maximum temperature of ~1000 °C for the calculation of Cr closure temperature in spinel of type 6 meteorites (H/L). In case of type 3 meteorites, a peak temperature of ~600 °C at the burial depth of type 3-4 transition derived from the thermal models is assumed to be the peak temperature for type 3 meteorites (H/L). However, it could be higher for type 3.7-3.8, but to what extent is unknown.

Figure 1.7 shows the calculated closure temperatures of Cr in spinels as a function of cooling rate, grain size (= taken as effective diffusion radius) and maximum temperature of class H and L ordinary chondrites. For the model it is assumed that the peak temperature was 1000 °C, Cr# = 0.85 and grain sizes range from 2.5 to 300 µm. Posner *et al.* (2016) calculated  $D(\text{Cr})$  and closure temperature at Cr# = 0 and 1 using a linear variation in  $\log D(\text{Cr})$  with Cr# ( $d\log D(\text{Cr})/d\text{Cr}\# = 0.08$ ) as shown by Suzuki *et al.* (2008). This linear variation in  $\log D(\text{Cr})$  and Cr# is used in the present study to calculate  $D(\text{Cr})$  at Cr# = 0.85 which has been reported as the mean Cr# in H, L and LL chondrites (e.g., Wlotzka, 2005). The grain sizes of spinel in type 6 samples are reported to range from 50 to 150 µm (Kimura *et al.*, 2006, Kessel *et al.*,

2007). Much smaller spinel grains are observed in type 3 samples, ranging from ~1 to 10  $\mu\text{m}$  (Kimura *et al.*, 2006).

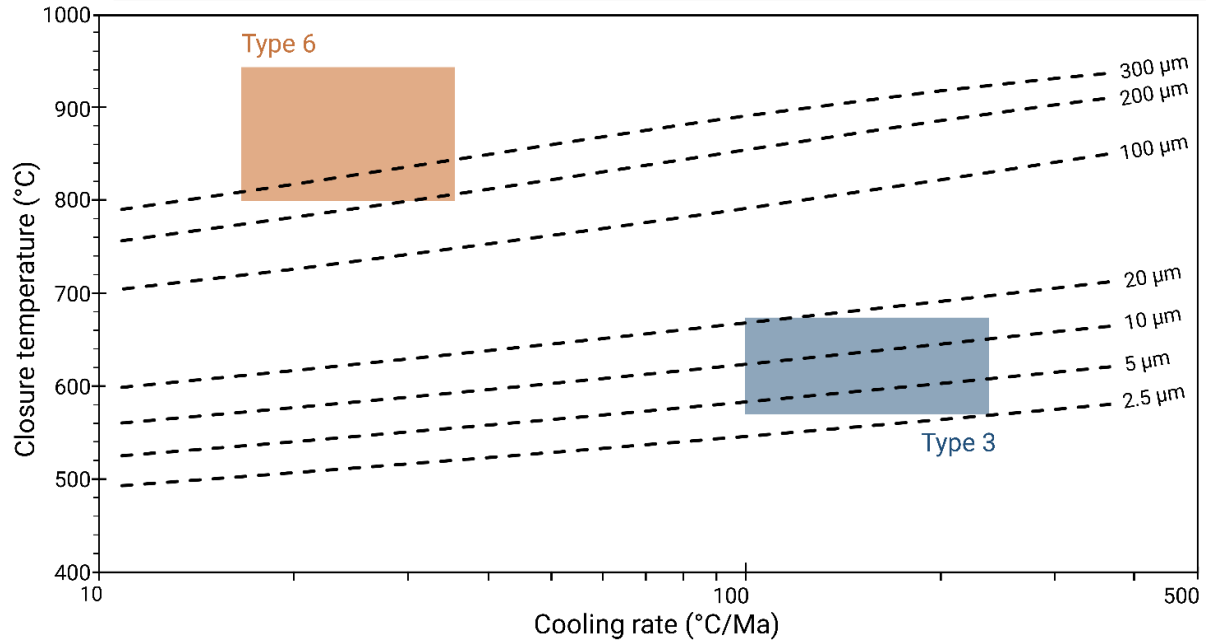


**Figure 1.7.** Closure temperature of the Mn-Cr system in spinel grains. The dashed lines represent the closure temperature curves as a function of initial temperature (= 1000 °C) at the onset of cooling and grain size (effective diffusion radius). The metamorphic peak temperature ranges for type 3 and 6 ordinary chondrites are constrained by the closure temperature curves and respective typical cooling rates (coloured boxes). Details regarding the calculations are given in the text.

The cooling rates of ordinary chondrites are the subject of an ongoing debate. Ganguly *et al.* (2013, 2016) developed a multistage cooling model for H, L and LL chondrites. They measured the composition of coexisting mineral phases in several type 4 to 6 chondrites and derived high-temperature cooling rates of ~25-100 °C/ka at high temperatures, commencing from 750-850 °C. At lower transitional temperatures (500-450 °C), an average cooling rate of ~15 °C/Ma was estimated from the Fe-Mg ordering states of orthopyroxenes. Hellmann *et al.* (2019) estimated the cooling rates in type 5 and 6 chondrites by Hf-W chronology of coarse-grained metals that plot below the isochrons defined by silicate-dominated fractions. These samples yield cooling rates between 2 and 28 °C/Ma. For those type 5 and 6 samples where metal and silicate-dominated fractions define a single Hf-W isochron, a lower limit on the cooling rate of 30-54 °C/Ma was determined. Cooling rates for type 3 chondrites are poorly constrained. Kleine *et al.* (2008) obtained cooling rates from the slopes of cooling curves for type 4-6 H chondrites. Assuming an onion shell model for the chondrite parent bodies which

predicts an inverse correlation of cooling rates with petrologic type, a cooling rate of  $\sim 100$   $^{\circ}\text{C}/\text{Ma}$  for type 4 meteorites, can thus be considered a lower limit for the cooling rate of type 3 samples.

From Figure 1.7, a Cr closure temperature of  $\sim 760$   $^{\circ}\text{C}$  is deduced for spinel from type 6 chondrites assuming  $\text{Cr}\# = 0.85$ , grain size =  $150\text{ }\mu\text{m}$  and a cooling rate of  $\sim 30$   $^{\circ}\text{C}/\text{Ma}$ . A closure temperature  $\sim 760$   $^{\circ}\text{C}$  in type 6 samples is likely a lower limit since, at higher transitional temperatures, the cooling rate would be higher which in turn, would result in higher closure temperatures. In type 3 chondrites, Cr closure temperature is estimated to be  $\sim 540\text{--}620$   $^{\circ}\text{C}$ , for a spinel grain size between  $5$  and  $10\text{ }\mu\text{m}$  and a cooling rate of  $100\text{--}150$   $^{\circ}\text{C}/\text{Ma}$ .

The Mn-Cr model ages and closure temperature estimates can be compared with the Hf-W and  $^{207}\text{Pb}\text{--}^{206}\text{Pb}$  ages and corresponding closure temperatures for respective petrological types of ordinary chondrites to constrain the thermal evolution of the respective parent bodies. The lower limit on Mn-Cr closure temperature of  $\sim 760$   $^{\circ}\text{C}$  for type 6 ordinary chondrites is  $\sim 100$   $^{\circ}\text{C}$  lower than the estimated Hf-W closure temperature ( $875 \pm 75$   $^{\circ}\text{C}$ ) for H6 chondrites (Kleine *et al.*, 2008). However, the Hf-W ages for type 5 and 6 chondrites ( $9.3 \pm 1.3$  Ma, 2SE,  $n=11$ ) determined by Hellmann *et al.* (2019) are in good agreement with Cr model ages obtained for type 6 chondrites ( $9.1 \pm 1.5$  Ma) in the present study. The agreement in the ages calculated by both the chronometers argues for a similar closure temperature for both systems, at least in type 6 samples.  $^{207}\text{Pb}\text{--}^{206}\text{Pb}$  ages provide an additional check for the accuracy and significance of Mn-Cr ages and closure temperatures. The  $^{207}\text{Pb}\text{--}^{206}\text{Pb}$  phosphate ages for type 5 chondrites range up to  $\sim 60$  Ma after CAI formation (Blackburn *et al.*, 2017). The closure temperature for Pb diffusion in phosphates is estimated to be  $\sim 530$   $^{\circ}\text{C}$  (Cherniak *et al.*, 1991) which is significantly lower than the closure temperature estimates for both Hf-W and Mn-Cr in type 6 chondrites. The younger ages and lower closure temperature for the  $^{207}\text{Pb}\text{--}^{206}\text{Pb}$  system support the interpretation of the older ages and higher closure temperature for the Mn-Cr system determined in the present study. The Hf-W ages for type 4 chondrites range from  $3.4 \pm 0.7$  to  $4.3 \pm 0.9$  Ma (Hellmann *et al.*, 2019) and are in good agreement with the Mn-Cr model ages ( $3.99^{+0.93}_{-0.79}$  Ma to  $4.51^{+1.10}_{-0.91}$  Ma) for type 3 chondrites determined in the present study. The closure temperature of the Hf-W system in H4 chondrites is  $\sim 800 \pm 50$   $^{\circ}\text{C}$  (Kleine *et al.*, 2008), which is higher than the peak metamorphic temperature in type 4 chondrites. The Mn-Cr closure temperature is similar to the peak temperatures determined for type 3 chondrites.

Consequently, Hf-W and Mn-Cr should both date the time of peak metamorphism in type 3-4 chondrites. The agreement in the ages determined by both the system provides strong confidence in the chromite model ages calculated in the present study which are interpreted to date chromite formation.

### 1.4.3 Significance of initial $^{53}\text{Cr}/^{52}\text{Cr}$ and $^{53}\text{Mn}$ abundances for chromite model ages

To derive chromite model ages using equation 1.1, the solar system initial  $^{53}\text{Cr}/^{52}\text{Cr}$  and canonical  $^{55}\text{Mn}/^{52}\text{Cr}$  at a given time have to be known and assumed to be homogenous. The model ages reported in the present study are determined using initial  $\epsilon^{53}\text{Cr} = -0.23$  and a canonical  $^{53}\text{Mn}/^{55}\text{Mn} = 6.28 \times 10^{-6}$  (Trinquier *et al.*, 2008b) (Table 1.5). Using  $^{53}\text{Mn}/^{55}\text{Mn}_i = 7.68 \times 10^{-6}$  as recalculated from Ste. Marguerite systematics with the updated U-corrected  $^{207}\text{Pb}$ - $^{206}\text{Pb}$  phosphate age (Trinquier *et al.* 2008b; Blackburn *et al.* 2017), yields a mean age of ~4.5 Ma for type 3 samples and ~8.4 Ma (after CAIs) for type 6 samples, however, with much lower  $\epsilon^{53}\text{Cr}_i = -0.29$ . Different studies have reported resolvable variations in the solar system initial  $\epsilon^{53}\text{Cr}$  and  $^{53}\text{Mn}/^{55}\text{Mn}$  values as summarized in section (2.1). Since the chromite model ages are strongly affected by the model parameters, clearly, more high-precision Cr isotope data to tightly constrain the initial  $\epsilon^{53}\text{Cr}$  and  $^{53}\text{Mn}/^{55}\text{Mn}$  are needed. Using the solar system initial  $\epsilon^{53}\text{Cr} = -0.177$  and canonical  $^{53}\text{Mn}/^{55}\text{Mn} = 6.8 \times 10^{-6}$  determined by Göpel *et al.* (2015) results in chromite model ages for type 3-6 chondrites ranging from,  $2.39^{+0.62}_{-0.56}$  Ma to  $6.2^{+1.5}_{-1.2}$  Ma after CAI formation (See Figure S1.2). These ages predate the model ages of  $3.99^{+0.93}_{-0.79}$  Ma to  $11.1^{+6.0}_{-2.8}$  Ma determined using initial  $^{53}\text{Cr}$  and  $^{53}\text{Mn}$  abundances as reported in Trinquier *et al.* (2008b). The older model ages determined using the initial  $\epsilon^{53}\text{Cr}$  and  $^{53}\text{Mn}/^{55}\text{Mn}$  values from Göpel *et al.* (2015) do not agree with the two-point isochron ages for type 3 and type 6 samples (Fig. 1.6). Moreover, the older model ages for type 3 samples predate the youngest chondrule formation ages in ordinary chondrites which are as late as ~2.9 Ma (Pape *et al.*, 2019) after CAI formation. Since type 3 samples represent the last aggregating material on the ordinary chondrite parent bodies and have Cr closure temperatures similar to the peak metamorphic temperature, the model ages cannot be older than the youngest chondrule formation ages. Kleine *et al.* (2008) reported a Hf-W isochron age of  $1.7 \pm 0.7$  Ma for the H4 chondrite Ste. Marguerite, which is older than the youngest chondrule formation age of ~2.9 Ma (Pape *et al.*, 2019). The age was interpreted as the timing of chondrule formation and not

attributed to the thermal processes on the parent body. The Hf-W isochron age for Ste. Marguerite was later updated to  $3.8 \pm 0.6$  Ma after CAI formation (Hellmann *et al.* 2019), which postdates the chondrule formation interval.

Altogether, the initial  $\epsilon^{53}\text{Cr}$  ( $= -0.23$ ) and  $^{53}\text{Mn}$  ( $= 6.28 \times 10^{-6}$ ) abundances reported in Trinquier *et al.* (2008b) produce a consistent data set for the chromite model ages that match with the Mn-Cr isochron ages in early solar system materials.

The Mn-Cr model ages reported in Table 1.5 are calculated assuming that chondrites represent an isotopically homogeneous reservoir that evolved with a distinct Mn/Cr ratio which is identical to CI chondrites (Birck *et al.*, 1999). The assumption of CI-like compositional reservoir has proved to be valid, as the chromite model ages determined using a CI-like Mn/Cr  $= 0.71$  are within uncertainties of the two-point isochron ages in the studied samples that did not reach thermal conditions above the closure temperature. A compilation of the Mn/Cr ratios (Wasson and Allemeyn, 1988; Trinquier *et al.*, 2008b; Qin *et al.*, 2010; Pedersen *et al.*, 2019) reported for ordinary chondrites gives Mn/Cr  $= 0.73$  for H chondrites and  $0.77$  for L chondrites. Using Mn/Cr  $= 0.73$  results in slightly younger model ages compared to those calculated for a CI-like Mn/Cr. For instance, the model age for type 3 sample JaH 596 and type 6 sample AHu 017 would become  $3.83^{+0.87}_{-0.75}$  Ma and  $6.5^{+1.8}_{-1.4}$  Ma instead of  $3.99^{+0.93}_{-0.79}$  Ma and  $6.9^{+2.1}_{-1.5}$  Ma, respectively. These shifts are within the overall uncertainty of the model ages.

#### 1.4.4 Chromite model ages vs. two-point isochron ages

Unlike chromite model ages, which are derived from chromite solely, two-point isochrons calculated in the present study involve chromite as well as the remaining silicate-metal bulk fraction of the same whole-rock meteorite. Isochrons based on analyses of different phases or components in a sample are prone to disturbances due to differences in the closure temperature of multiple phases. Particularly in the slowly cooled type 6 ordinary chondrites, the closure of individual minerals during different stages of the cooling history can result in a scatter of individual data point around the isochron because some phases may stay open while some of the others have already closed.

Two-point isochrons, however, are constructed from chromite and a fraction of the same sample that constitutes all of the remaining material. The two fractions represent two reservoirs

where internal dis-equilibrium in one reservoir (silicates, metal), due to difference in the closure temperature of different phases will not affect the isochron. However, the isochron would be (partially) reset if chromite and the silicate fraction reservoir re-equilibrated during cooling. The type 3 samples investigated in the present study display a good agreement between the two-point isochron and chromite model ages (Fig. 1.8). In case of type 6 chondrites, the ages calculated by both methods agree within analytical uncertainties in samples SaU 228 (H6) and JaH 578 (H6) but show a mismatch in samples AHu 017 (L6) and Dho 1012 (L6). Apart from the re-equilibration between chromites and silicate fractions during cooling, impact disruption could be another reason for a disturbed isochron in samples AHu 017 (L6) and Dho 1012 (L6) leading to a mismatch between model ages and isochron ages in these two samples.

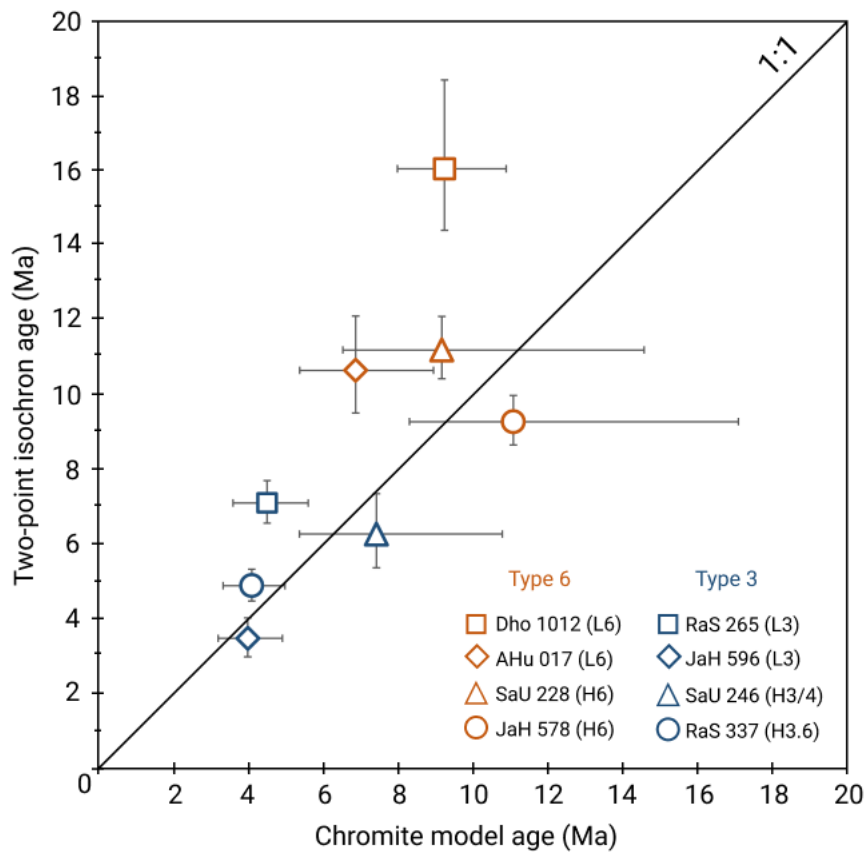


**Figure 1.8.** A comparison between chromite model ages and two-point isochron ages determined for the studied samples. Type 3 samples show a good correlation in the two-point isochron and chromite model ages. The discrepancy between the two-point isochron and chromite model ages in the type 6 sample, AHu 017 (L6) and Dho 1012 (L6) is interpreted to be the result of their probable origin from an impact disturbed region on the parent bodies or partial re-equilibration during cooling from high temperatures.

The Hf-W chronology data of ordinary chondrites indicate the possibility of impact disruptions of the ordinary chondrite parent bodies at ~10 Ma after CAI formation (Hellmann *et al.*, 2019). According to the study, impacts of sufficient size and energy excavated material from the deep interior of the parent bodies of H, L and LL chondrites, which is apparently the source of type 6 chondrite samples. Since only a few type 6 samples recorded disturbances in cooling history, an impact most likely disturbed only a limited part of the parent bodies of the ordinary chondrites. Any manifestation of the impact disrupted cooling histories in the Hf-W ages would also be recorded in Mn-Cr ages since the Hf-W ages record the cooling history at a closure temperature (~875 °C) higher than the Mn-Cr system (~760 °C).

The comparative study of two-point isochron and chromite model ages shows that two-point isochrons correlate well with the model ages in type 3 samples, but they remain prone to the impact-related disturbances or partial re-equilibration during cooling from high temperatures in type 6 samples. The results also demonstrate that the model ages derived from chromite constrain the time of mineral formation.

#### 1.4.5 Time of accretion and cooling history for chondrite parent bodies

The earliest accretion of the ordinary chondrite parent bodies is constrained by the onset of chondrule formation. Hf-W data for ordinary chondrites show that metal-silicate fractionation among H, L and LL chondrites occurred between ~2 and ~2.7 Ma after CAIs which was coeval with the chondrule formation interval and prior to the accretion of chondrite parent bodies (Hellmann *et al.* 2019). Common isotope systems applied to determine chondrule ages are the long-lived, absolute  $^{207}\text{Pb}$ - $^{206}\text{Pb}$  (e.g., Bollard *et al.*, 2017, 2019; Connelly *et al.*, 2017; and references therein) and the short-lived  $^{26}\text{Al}$ - $^{26}\text{Mg}$  (e.g., Kita *et al.*, 2000; Rudraswami and Goswami, 2007; Villeneuve *et al.*, 2009; Kita and Ushikubo, 2012, Pape *et al.*, 2019, Siron *et al.*, 2020) chronometers. The  $^{26}\text{Al}$ - $^{26}\text{Mg}$  chronometer relies on the assumption of initial homogeneous distribution of the parent radionuclide throughout the inner protoplanetary disk. Pape *et al.* (2019) presented  $^{26}\text{Al}$ - $^{26}\text{Mg}$  ages for the formation of melt in individual chondrules from a wide range of chondrule types and mesostasis compositions and determined ages between  $1.76^{+0.36}_{-0.27}$  Ma and  $2.92^{+0.51}_{-0.34}$  Ma after CAI formation with a peak in chondrule formation at 2.0 and 2.3 Ma. A narrower interval of chondrule formation from ~1.80 to ~2.16 Ma after CAIs has been reported by Siron *et al.* (2020), however, the investigated chondrules



are limited to anorthite-bearing chondrule type. Siron *et al.* (2020) noted that the youngest formation ages for anorthite-bearing chondrules are similar to the time of accretion for the ordinary chondrite parent bodies at ~2.1 Ma after CAIs, suggested in thermal evolution modelling studies (Sugiura and Fujiya, 2014; Blackburn *et al.*, 2017). The two youngest chondrules from unequilibrated ordinary chondrites reported by Pape *et al.* (2019) record an age of ~2.92 Ma, of which one sample has been interpreted to date the time of partial remelting after primary formation in the protoplanetary disk (Pape *et al.*, 2020). The melting and remelting events must have occurred before incorporation of chondrules into the chondrite parent body since the investigated samples are of low petrographic type and did not exceed temperatures in excess of ~300 °C after accretion. Moreover, since the ages are mostly defined by the Al-Mg systematics of pristine glass, they are interpreted to record the time of chondrule formation rather than a later thermal overprint. If main accretion of the chondrite parent bodies started at or shortly after ~2.1 Ma, it must have continued until ~3 Ma after CAI in order to account for the large number of chondrules recording younger melting and remelting ages.

Type 3 sample JaH 596 (L3) investigated in the present study records the oldest chromite model age of  $3.99^{+0.93}_{-0.79}$  and a two-point isochron age of  $2.78^{+0.55}_{-0.50}$  Ma after CAI formation. Neither the isochron nor the chromite model ages directly relate to the process of accretion. They date the formation of new mineral phases on their parent body which requires a thermal overprint after completion of accretion. Since type 3 chondrites represent the last accreted material on the chondrite parent bodies, the type 3 chromite model/isochron ages provide a limit for the latest time of accretion. Combined with the  $^{26}\text{Al}$ - $^{26}\text{Mg}$  chondrule formation ages, the final accretion of the ordinary chondrite parent bodies can be constrained after ~2.1 Ma but before ~3.4 Ma.

Whether the accretion of the chondrite parent bodies was instantaneous (~0.1 Myr) or protracted ( $\geq 1$  Myr) has been a subject of a number of studies (e.g., Ghosh *et al.*, 2003; Sahijpal *et al.*, 2007; Neumann *et al.*, 2012, Henke *et al.*, 2013). Theoretical models for planetesimal formation and growth imply that the main period of acquisition of matter by large bodies in a planetesimal swarm was as short as 0.1 Ma (e.g., Nagasawa *et al.*, 2007; Weidenschilling and Cuzzi, 2006; Weidenschilling, 2011). In a recent study, Roth *et al.* (2016) investigated the cosmic-ray exposure ages of chondrules from L and LL ordinary chondrites and reported absence of detectable pre compaction exposure, suggesting rapid accretion (and/or efficient

shielding from galactic cosmic ray and solar cosmic ray in the solar nebula). Chondrules from CR chondrites are reported to show some late irradiation effects consistent with the later accretion of their parent body as compared to the parent bodies of other chondrites (Beyersdorf-Kuis *et al.* 2015). An incremental or protracted accretion of the chondrite parent bodies would likely result in chemical fractionation that would appear as chemical differences between early accreting type 6 and late accreting type 3 chondrites. The lack of systematic chemical and nucleosynthetic isotopic variations between type 3 and type 6 meteorites implies that the accretion was rather instantaneous and not protracted.

Post accretion, type 3 material being farthest away from the centre of the parent bodies would have to reach peak metamorphic temperature of ~600 °C necessary to alter or produce chromites investigated in the present study. The nearly ubiquitous signs of thermal alteration of ordinary chondrites indicate that such temperatures were attained soon after accretion (Weidenschilling *et al.*, 2019).

The processes leading to the accretion of parent bodies are highly debated (e.g., Weidenschilling, 2019). The key challenge is to reconcile the early formation of the differentiated parent bodies of the oldest iron meteorites with the delayed accretion of the chondrite parent bodies.  $^{207}\text{Pb}$ - $^{206}\text{Pb}$  and Hf-W dating of most achondrites suggest that their parent body differentiation predates the formation of chondrules and the accretion of the chondrite parent bodies (Baker *et al.*, 2005; Bizzarro *et al.*, 2005, Kleine *et al.*, 2005). The radioactive decay of short-lived  $^{26}\text{Al}$  ( $t_{1/2}$  ~0.73 Ma) is considered to be the primary source of energy for asteroidal melting (e.g., Bizzarro *et al.*, 2005). Since chondrites escaped melting but were heated enough to experience thermal metamorphism, it is generally assumed that they began accreting when a substantial fraction of  $^{26}\text{Al}$  had decayed before the accretion was complete (e.g., Hevey and Sanders, 2006; Weidenschilling, 2019). Rubin (2010, 2011) proposed that in accordance with the petrographic properties, chemical and isotopic compositions, and volatile contents, different chondrite groups formed in regions at increasing heliocentric distance in the order of EH-EL, OC, R, CR, CV-CK, CM-CO and CI. Based on Mn-Cr ages of secondary carbonates, the accretion ages are proposed to be at ~3.5 Ma for CM (Fujiya *et al.*, 2012) and up to 3.9 Ma (Fujiya *et al.*, 2013) for CI parent bodies (deLeuw *et al.*, 2009, Visser *et al.*, 2020). Jogo *et al.* (2017) studied the chemical compositions of CV3 fayalite and its Mn-Cr isotope systematics and proposed that the CV parent body accreted at about 3.2-

3.3 Ma after CAI formation and is slightly younger than the ordinary chondrites parent bodies. Younger accretion ages ( $> 3$  Ma after CAIs) of the parent bodies of carbonaceous chondrites compared to ordinary chondrite parent bodies suggest an even lower fraction of short-lived  $^{26}\text{Al}$ , as the primary source of energy at the time of their accretion. This is evident in the low thermal metamorphism recorded in carbonaceous chondrites. However, both carbonaceous and ordinary chondrites yield coeval (L and LL OCs and CO and CV meteorites, Pape *et al.*, 2019) chondrule formation intervals. This suggests that the accretion of CC parent bodies was protracted and contemporary with the later stages of the chondrule formation event(s). Such a scenario buttresses the models that suggest a causal relationship between chondrule production and chondrite parent bodies accretion (Budde *et al.*, 2016; Alexander *et al.*, 2008; Edwards and Blackburn, 2020).

Metamorphism of the H and L chondrite parent bodies following the accretion of the planetesimals can be evaluated employing thermal evolution models that are constructed using increasingly complex physical input parameters (e.g., Tieloff *et al.*, 2003; Hevey and Sanders, 2006; Sahijpal *et al.*, 2007, 2011; Kleine *et al.*, 2008; Harrison and Grimm, 2010; Henke *et al.*, 2012a, b; 2013; Gail *et al.*, 2015; Gail and Tieloff, 2018). To ensure model optimization, those meteorites are generally selected for which three or more cooling ages, reflecting different steps in the thermal history of the parent bodies (i.e., closure temperatures), are available. This constrains the slope as well as the curvature of individual cooling paths at their depths within the parent bodies. Although the chondrite samples investigated in the present study have not been dated with other chronometers, their determined chromite model ages and estimated closure temperatures can be used to test the validity of existing thermal models.

For the H and L chondrite parent bodies, thermal models show that the observed properties of chondrites are consistent with an “onion shell” model and a radius of about 100 km (Benoit *et al.*, 2002; Tieloff *et al.*, 2003; Hevey and Sanders, 2006; Bouvier *et al.*, 2007; Sahijpal *et al.*, 2007, 2011; Kleine *et al.*, 2008; Harrison and Grimm, 2010; Henke *et al.*, 2012a, b; 2013; Mare *et al.*, 2014; Gail *et al.*, 2015; Blackburn *et al.*, 2017; Gail and Tieloff, 2018, Gail and Tieloff, 2019). The “onion shell” model predicts that higher temperatures are achieved at greater depths and slightly different times during the evolution of the chondrites parent bodies (e.g., Pellas, 1981; Tieloff *et al.*, 2003). The chondrite samples investigated here display similar ranges in both two-point isochron and chromite model ages and the absolute ages

correlate with the petrological grade for both H and L chondrites (Fig. 1.8) indicating similar structures, sizes, accretion time and high-temperature cooling histories for the parent bodies of both H and L classes. A narrow range in the chromite model ages for type 3 samples from  $3.99^{+0.93}_{-0.79}$  to  $4.51^{+1.10}_{-0.91}$  Ma suggests that the unmetamorphosed material surrounding the metamorphic core corresponds to a significantly narrower depth-range than the high-grade material i.e., type 6 samples that show wider timespan of chromite model ages from  $6.9^{+2.1}_{-1.5}$  to  $11.1^{+6.0}_{-2.8}$  Ma. The difference in the mean chromite model ages from type 3 and 6 samples is  $\sim 5$  Myr which agrees with the difference of  $\sim 5.5$  Myr as determined by Hf-W (Hellmann *et al.*, 2019), but is much shorter than the interval of  $\sim 50$  Myr derived from  $^{207}\text{Pb}$ - $^{206}\text{Pb}$  phosphate ages (Blackburn *et al.*, 2017). The shorter intervals defined by the Mn-Cr and Hf-W systems date the earliest evolution processes of chondrite parent bodies and play a critical role in determining the time peak temperatures were reached in thermal evolution models.

Most thermal history models for both H and L chondrites assume that the parent bodies accreted at  $\sim 2$  Ma after CAI formation, were heated dominantly by the decay of short-lived radioactive nuclides ( $^{26}\text{Al}$  and  $^{60}\text{Fe}$ ) and then cooled down after having reached the thermal peak over a period of  $\sim 100$  Ma (e.g., Henke *et al.*, 2012a, b; 2013; Gail *et al.*, 2015; Gail and Trieloff, 2018). The Mn-Cr chromite model ages (Fig. 1.4, Table 1.6) and the inferred time of accretion of the ordinary chondrite parent bodies suggested in the present study are consistent with a thermal evolution where the accretion of the parent body began at or shortly after 2.1 Ma (post CAI formation). The center of the parent body reached the peak temperature at  $\sim 9$  Ma after CAI formation, consistent with the mean chromite model age ( $9.1 \pm 1.5$  Ma, 2SE,  $n=4$ ) and closure temperature estimate ( $\sim 760$  °C) for type 6 chondrites. At shallower depths, the parent body reached a peak temperature of  $\sim 600$  °C at  $\sim 4$  Ma after CAI formation as per the mean of the two-point isochron and chromite model ages of  $4.3 \pm 1.2$  Ma (2SE,  $n=6$ ) obtained for the investigated type 3 chondrites.

## 1.5 Conclusions

The Mn-Cr chromite model ages obtained in the present study range from  $3.99^{+0.93}_{-0.79}$  Ma to  $4.51^{+1.10}_{-0.91}$  Ma for type 3 and  $6.9^{+2.1}_{-1.5}$  Ma to  $11.1^{+6.0}_{-2.8}$  Ma for type 6, H and L ordinary chondrites. Chromite-silicate isochrons for the same samples range from  $2.78^{+0.55}_{-0.50}$  to  $15.4^{+2.4}_{-1.6}$  Ma. Both chromite model ages and isochron ages support an onion-shell structure of their parent bodies.

Together with the closure temperature estimates for the Mn-Cr system in spinel, the model ages are inferred to constraint the peak metamorphic conditions for the unequilibrated type 3 chondrites and a time of Mn-Cr closure during retrograde metamorphism in type 6 chondrites. The model ages are consistent with a homogenous distribution of  $^{53}\text{Mn}$ , a canonical  $^{53}\text{Mn}/^{55}\text{Mn} = 6.28 \times 10^{-6}$  and are in good agreement with the Hf-W ages for type 4, 5 and 6 ordinary chondrites (Hellmann *et al.*, 2019). The high closure temperature estimates for Mn-Cr ( $\sim 760$  °C) and Hf-W ( $\sim 870$  °C) systems imply that the corresponding chronometers provide constraints on the peak-temperature metamorphic history of the ordinary chondrite parent bodies. This information is not obtainable from other chronometers such as  $^{207}\text{Pb}$ - $^{206}\text{Pb}$  due to their lower closure temperatures. The two-point isochron ages obtained for the chondrites agree within uncertainties with the respective chromite model ages except in samples JaH 578 (H6) and Dho 1012 (L6), where an impact-related disturbance during cooling from high temperatures could be the reason for partial re-equilibration of the Mn-Cr system. The results obtained in the present study indicate that the chromite model age approach is robust and yields age constraints that agree with those derived from chromite-silicate isochrons. This model-age approach for dating can also be extended to other meteoritic classes with chondritic Mn/Cr ratios. The oldest chromite model ages from type 3 samples, together with the Al-Mg chondrules formation ages (Kita *et al.*, 2000; Rudraswami and Goswami, 2007; Villeneuve *et al.*, 2009; Kita and Ushikubo, 2012; Pape *et al.*, 2019 and Siron *et al.*, 2020), constrain the time of accretion of the ordinary chondrite parent bodies to  $> 2.1$  Ma after CAI formation. This age is in agreement with the previously estimated time of accretion for the ordinary chondrite parent bodies (Miyamoto *et al.*, 1982; Göpel *et al.*, 1994; Harrison and Grimm, 2010; Sugiura and Fujiya 2014; Doyle *et al.*, 2015). The Mn-Cr chromite model ages and  $^{26}\text{Al}$ - $^{26}\text{Mg}$  chondrule formation ages are consistent with a thermal evolution model in which the accretion of the ordinary chondrite parent bodies began at or shortly after 2.1 Ma (post CAI formation) and the centre of the H chondrite parent body reached the peak temperature at  $\sim 9$  Ma followed by cooling. The ordinary chondrite parent bodies accreted  $\sim 1$  Ma later than the parent bodies of magmatic iron meteorites (Kleine *et al.*, 2005; Scherstén *et al.*, 2006; Burkhardt *et al.*, 2008; Qin *et al.*, 2008) and differentiated asteroids (e.g., acapulcoite-lodranite parent body, Touboul *et al.*, 2009) but prior to the accretion of the carbonaceous chondrite parent bodies providing a coherent timeline of the meteorite parent bodies accretion. The coeval chondrule formation interval in carbonaceous and ordinary chondrites but younger ( $> 3$  Ma after CAIs) accretion ages suggest that accretion of the parent bodies of carbonaceous chondrites was protracted and

contemporary to the later stages of chondrules formation event. This implies that there could be a causal relationship between chondrule formation and subsequent planetesimal accretion (Budde *et al.*, 2016; Alexander *et al.*, 2008; Edwards and Blackburn, 2020).

## **Acknowledgement**

This study was partially funded by ‘Swiss Government Excellence Scholarship (2018.0371)’. We acknowledge funding within the framework of the NCCR PlanetS supported by the Swiss National Science Foundation grant nr. 51NF40-141881. We are grateful to B. Hofmann from the Natural History Museum Bern for providing all the ordinary chondrites samples investigated in this study. We acknowledge Patrick Neuhaus from the Institute of Geography, University of Bern for technical help and assistance with the ICP-MS analysis of the samples. We also thank Y. Kadlag and J. Hoffmann for their support and helpful discussions throughout the study. We thank Noriko Kita for editorial handling and Devin Schrader and two anonymous reviewers for their constructive comments that helped to improve the paper.

## References

- Alexander C. M. O'D., Grossman J. N., Ebel D. S. and Ciesla F. J. (2008) The formation conditions of chondrules and chondrites. *Science* 320, 1617–1619.
- Amelin, Y., Kaltenbach, A., Iizuka, T., Stirling, C.H., Ireland, T.R., Petaev, M. and Jacobsen, S.B. (2010). U-Pb chronology of the Solar System's oldest solids with variable  $^{238}\text{U}/^{235}\text{U}$ . *Earth Planet. Sci. Lett.* 300 (3-4), 343–350.
- Armstrong J. T. (1995) CITZAF: A package of correction programs for the quantitative electron microbeam X-ray-analysis of thick polished materials, thin films, and particles. *Microbeam Anal.* 4, 177-200.
- Baker J., Bizzarro M., Wittig N., Connelly J. and Haack H. (2005) Early planetesimal melting from an age of 4.5662 Gyr for differentiated meteorites. *Nature* 436, 1127–1131.
- Benedix G. K., Lauretta D. S. and McCoy T. J. (2005) Thermodynamic constraints on the formation conditions of winonaites and silicate-bearing IAB irons. *Geochim. Cosmochim. Acta* 69, 5123–5131.
- Benoit P. H., Akridge G. A., Ninagawa K. and Sears D. W. G. (2002) Thermoluminescence sensitivity and thermal history of type 3 ordinary chondrites: Eleven new type 3.0-3.1 chondrites and possible explanations for differences among H, L, and LL chondrites. *Meteorit. Planet. Sci.* 37, 793–805.
- Beyersdorf-Kuis U., Ott U. and Tieloff M. (2015) Early cosmic ray irradiation of chondrules and prolonged accretion of primitive meteorites. *Earth Planet. Sci. Lett.* 423, 13–23.
- Birck J. L. and Allègre C. J. (1985a) Evidence for the presence of  $^{53}\text{Mn}$  in the early solar system. *Geophys. Res. Lett.* 12, 745–748.
- Birck J. L. and Allègre C. J. (1985b) Isotopes produced by galactic cosmic rays in iron meteorites. *Isotopic Ratios in the Solar Syst.* 1, 21–25.

Birck J. L. and Allègre C. J. (1988) Manganese-chromium isotope systematics and the development of the early Solar System. *Nature* 331, 579-584

Birck J. L., Rotaru M. and Allègre C. J. (1999)  $^{53}\text{Mn}$ - $^{53}\text{Cr}$  evolution of the early solar system. *Geochim. Cosmochim. Acta* 63, 4111–4117.

Bizzarro M., Baker J. A., Haack H. and Lundgaard K. L. (2005) Rapid timescales for accretion and melting of differentiated planetesimals inferred from  $^{26}\text{Al}$ - $^{26}\text{Mg}$  chronometry. *Astrophys. J.* 632, L41–L44.

Blackburn T., Alexander C. M. O'D., Carlson R. and Elkins-Tanton L. T. (2017) The accretion and impact history of the ordinary chondrite parent bodies. *Geochim. Cosmochim. Acta* 200, 201–217.

Bollard J., Connelly J. N., Whitehouse M. J., Pringle E. A., Bonal L., Jørgensen J. K., Nordlund Å., Moynier F. and Bizzarro M. (2017) Early formation of planetary building blocks inferred from Pb isotopic ages of chondrules. *Sci. Adv.* 3, e1700407.

Bollard J., Kawasaki N., Sakamoto N., Olsen M., Itoh S., Larsen K., Wielandt D., Schiller M., Connelly J. N., Yurimoto H. and Bizzarro M. (2019) Combined U-corrected Pb-Pb dating and  $^{26}\text{Al}$ - $^{26}\text{Mg}$  systematics of individual chondrules—Evidence for a reduced initial abundance of  $^{26}\text{Al}$  amongst inner Solar System chondrules. *Geochim. Cosmochim. Acta* 260, 62–83.

Bouvier A., Blichert-Toft J., Moynier F., Vervoort J. D. and Albarède F. (2007) Pb-Pb dating constraints on the accretion and cooling history of chondrites. *Geochim. Cosmochim. Acta* 71, 1583–1604.

Budde G., Kleine T., Kruijer T. S., Burkhardt C. and Metzler K. (2016) Tungsten isotopic constraints on the age and origin of chondrules. *Proc. Natl. Acad. Sci. U. S. A.* 113, 2886–2891.

Bunch T., Keil K. and Snetsinger K. G. (1967) Chromite composition in relation to chemistry and texture of ordinary chondrites. *Geochim. Cosmochim. Acta* 31, 1569–1582.

Burkhardt C., Kleine T., Bourdon B., Palme H., Zipfel J., Friedrich J. M. and Ebel D. S. (2008) Hf-W mineral isochron for Ca, Al-rich inclusions: Age of the solar system and the timing of core formation in planetesimals. *Geochim. Cosmochim. Acta* 72, 6177–6197.



Busemann, H., Alexander, M.O.D. and Nittler, L.R. (2007). Characterization of insoluble organic matter in primitive meteorites by microRaman spectroscopy. *Meteorit. Planet. Sci.* 42, 1387-1416.

Cherniak D. J., Lanford W. A. and Ryerson F. J. (1991) Lead diffusion in apatite and zircon using ion implantation and Rutherford Backscattering techniques. *Geochim. Cosmochim. Acta* 55, 1663–1673.

Connelly J. N., Bollard J. and Bizzarro M. (2017) Pb-Pb chronometry and the early Solar System. *Geochim. Cosmochim. Acta* 201, 345–363.

DeHart J. M., Lofgren G. E., Jie L., Benoit P. H. and Sears D. W. G. (1992) Chemical and physical studies of chondrites: X. Cathodoluminescence and phase composition studies of metamorphism and nebular processes in chondrules of type 3 ordinary chondrites. *Geochim. Cosmochim. Acta* 56, 3791–3807.

de Leuw S., Rubin A.E., Schmitt A.K., Wasson J.T. (2009)  $^{53}\text{Mn}$ - $^{53}\text{Cr}$  systematics of carbonates in CM chondrites: implications for the timing and duration of aqueous alteration *Geochim. Cosmochim. Acta*, 73, 7433-7442.

Dodd R. T. (1981) *Meteorites-A Petrologic-Chemical Synthesis*, Cambridge, p. 368.

Dodson M. H. (1973) Closure temperature in cooling geochronological and petrological systems. *Contrib. to Mineral. Petrol.* 40, 259–274.

Doyle P. M., Jogo K., Nagashima K., Krot A. N., Wakita S., Ciesla F. J. and Hutcheon I. D. (2015) Early aqueous activity on the ordinary and carbonaceous chondrite parent bodies recorded by fayalite. *Nat. Commun.* 6, 1–10.

Edwards G. H. and Blackburn T. (2020) Accretion of a large LL parent planetesimal from a recently formed chondrule population. *Sci. Adv.* 6, 1–9.

Ferracutti G. R., Gargiulo M. F., Ganuza M. L., Bjerg E. A. and Castro S. M. (2015) Determination of the spinel group end-members based on electron microprobe analyses. *Mineral. Petrol.* 109, 153–160.

Fujiya W., Sugiura N., Hotta H., Ichimura K. and Sano Y. (2012) Evidence for the late formation of hydrous asteroids from young meteoritic carbonates. *Nat. Commun.* 3, 1-6.

Fujiya W., Sugiura N., Sano Y. and Hiyagon H. (2013) Mn-Cr ages of dolomites in CI chondrites and the Tagish Lake ungrouped carbonaceous chondrite. *Earth Planet. Sci. Lett.* 362, 130–142.

Gail H. P., Henke S. and Tieloff M. (2015) Thermal evolution and sintering of chondritic planetesimals: II. Improved treatment of the compaction process. *Astron. Astrophys.* 576.

Gail H. P. and Tieloff M. (2018) Thermal evolution and sintering of chondritic planetesimals IV. Temperature dependence of heat conductivity of asteroids and meteorites. *Astron. Astrophys.* 615.

Gail H. P. and Tieloff M. (2019) Thermal history modelling of the L chondrite parent body. *Astron. Astrophys.* 628, A77.

Ganguly J., Ito M. and Zhang X. (2007) Cr diffusion in orthopyroxene: Experimental determination,  $^{53}\text{Mn}$ - $^{53}\text{Cr}$  thermochronology, and planetary applications. *Geochim. Cosmochim. Acta* 71, 3915–3925.

Ganguly J. and Tirone M. (2009) Closure Temperature, Cooling Age and High Temperature Thermochronology. *Phys. Chem. Earth's Inter.*, 89–99. Springer, New York, NY.

Ganguly J., Tirone M., Chakraborty S. and Domanik K. (2013) H-chondrite parent asteroid: A multistage cooling, fragmentation and re-accretion history constrained by thermometric studies, diffusion kinetic modeling and geochronological data. *Geochim. Cosmochim. Acta* 105, 206–220.

Ganguly J., Tirone M. and Domanik K. (2016) Cooling rates of LL, L and H chondrites and constraints on the duration of peak thermal conditions: Diffusion kinetic modeling and implications for fragmentation of asteroids and impact resetting of petrologic types. *Geochim. Cosmochim. Acta* 192, 135–148.

Ghosh A., Weidenschilling S. J. and McSween H. Y. (2003) Importance of the accretion process in asteroid thermal evolution: 6 Hebe as an example. *Meteorit. Planet. Sci.* 38, 711–724.

Göpel C., Manhès G. and Allègre C. J. (1994) U-Pb systematics of phosphates from equilibrated ordinary chondrites. *Earth Planet. Sci. Lett.* 121, 153–171.

Göpel C., Birck J. L., Galy A., Barrat J. A. and Zanda B. (2015) Mn-Cr systematics in primitive meteorites: Insights from mineral separation and partial dissolution. *Geochim. Cosmochim. Acta* 156, 1–24.

Grossman J. N. and Brearley A. J. (2005) The onset of metamorphism in ordinary and carbonaceous chondrites. *Meteorit. Planet. Sci.* 40, 87–122.

Harrison K. P. and Grimm R. E. (2010) Thermal constraints on the early history of the H-chondrite parent body reconsidered. *Geochim. Cosmochim. Acta* 74, 5410–5423.

Hellmann J. L., Kruijer T. S., Van Orman J. A., Metzler K. and Kleine T. (2019) Hf-W chronology of ordinary chondrites. *Geochim. Cosmochim. Acta* 258, 290–309.

Henke S., Gail H. P., Tieloff M., Schwarz W. H. and Kleine T. (2012a) Thermal evolution and sintering of chondritic planetesimals. *Astron. Astrophys.* 537.

Henke S., Gail H. P., Tieloff M., Schwarz W. H. and Kleine T. (2012b) Thermal history modelling of the H chondrite parent body. *Astron. Astrophys.* 545.

Henke S., Gail H. P., Tieloff M. and Schwarz W. H. (2013) Thermal evolution model for the H chondrite asteroid-instantaneous formation versus protracted accretion. *Icarus* 226, 212–228.

Hevey P. J. and Sanders I. S. (2006) A model for planetesimal meltdown by  $^{26}\text{Al}$  and its implications for meteorite parent bodies. *Meteorit. Planet. Sci.* 41, 95–106.

Honda M. and Imamura M. (1971) Half-life of  $^{53}\text{Mn}$ . *Phys. Rev. C* 4, 1182–1188.

Huss G. R., Rubin A. E. and Grossman J. N. (2006) Thermal Metamorphism in Chondrites. *Meteorites early Sol. Syst. II*, 567–586.

Ito M. and Ganguly J. (2006) Diffusion kinetics of Cr in olivine and  $^{53}\text{Mn}$ - $^{53}\text{Cr}$  thermochronology of early solar system objects. *Geochim. Cosmochim. Acta* 70, 799–809.

Jacobsen B., Yin Q.-Z., Moynier F., Amelin Y., Krot A. N., Nagashima K., Hutcheon I. D. and Palme H. (2008)  $^{26}\text{Al}$ - $^{26}\text{Mg}$  and  $^{207}\text{Pb}$ - $^{206}\text{Pb}$  systematics of Allende CAIs: Canonical solar initial  $^{26}\text{Al}/^{27}\text{Al}$  ratio reinstated. *Earth Planet. Sci. Lett.* 272, 353–364.

Jogo K., Nakamura T., Ito M., Wakita S., Zolotov M. Y. and Messenger S. R. (2017) Mn-Cr ages and formation conditions of fayalite in CV3 carbonaceous chondrites: Constraints on the accretion ages of chondritic asteroids. *Geochim. Cosmochim. Acta* 199, 58–74.

Johnson C. A. and Prinz M. (1991) Chromite and olivine in type II chondrules in carbonaceous and ordinary chondrites: Implications for thermal histories and group differences. *Geochim. Cosmochim. Acta* 55, 893–904.

Keil K., Lange D., Ulbrich M. N. C., Gomes C. B., Jarosewich E., Roisenberg A. and Souza M. J. (1978a) Studies of Brazilian meteorites XIII. Mineralogy, petrology, and chemistry of the Putinga, Rio Grande do Sul, chondrite. *Meteoritics* 13, 165–175.

Keil K., Lux G., Brookins D. G., King E. A., King T. V. V. and Jarosewich E. (1978b) The Inman, McPherson County, Kansas meteorite. *Meteoritics* 13, 11–22.

Kessel R., Beckett J. R. and Stolper E. M. (2007) The thermal history of equilibrated ordinary chondrites and the relationship between textural maturity and temperature. *Geochim. Cosmochim. Acta* 71, 1855–1881.

Kimura M., Nakajima H., Hiyagon H. and Weisberg M. K. (2006) Spinel group minerals in LL3.00-6 chondrites: Indicators of nebular and parent body processes. *Geochim. Cosmochim. Acta* 70, 5634–5650.

Kita N. T., Nagahara H., Togashi S. and Morishita Y. (2000) A short duration of chondrule formation in the solar nebula: Evidence from  $^{26}\text{Al}$  in Semarkona ferromagnesian chondrules. *Geochim. Cosmochim. Acta* 64, 3913–3922.

Kita N. T. and Ushikubo T. (2012) Evolution of protoplanetary disk inferred from  $^{26}\text{Al}$  chronology of individual chondrules. *Meteorit. Planet. Sci.* 47, 1108–1119.

Kleine T., Hans U., Irving A. J. and Bourdon B. (2012) Chronology of the angrite parent body and implications for core formation in protoplanets. *Geochim. Cosmochim. Acta* 84, 186–203.

Kleine T., Mezger K., Palme H., Scherer E. and Münker C. (2005) Early core formation in asteroids and late accretion of chondrite parent bodies: Evidence from  $^{182}\text{Hf}$ - $^{182}\text{W}$  in CAIs, metal-rich chondrites, and iron meteorites. *Geochim. Cosmochim. Acta* 69, 5805–5818.

Kleine T., Touboul M., Van Orman J. A., Bourdon B., Maden C., Mezger K. and Halliday A. N. (2008) Hf-W thermochronometry: Closure temperature and constraints on the accretion and cooling history of the H chondrite parent body. *Earth Planet. Sci. Lett.* 270, 106–118.

Larsen K. K., Trinquier A., Paton C., Schiller M., Wielandt D., Ivanova M. A., Connelly J. N., Nordlund A., Krot A. N. and Bizzarro M. (2011) Evidence for magnesium isotope heterogeneity in the solar protoplanetary disk. *Astrophys. J. Lett.* 735, L37–L44.

Lindsley D. H. and Andersen D. J. (1983) A two-pyroxene thermometer. *J. Geophys. Res.* 88, A887–A906.

Liu, J., Qin, L., Xia, J., Carlson, R.W., Leya, I., Dauphas, N. and He, Y. (2019) Cosmogenic effects on chromium isotopes in meteorites. *Geochim. Cosmochim. Acta*, 251, pp.73-86.

Lugmair G. W. and Shukolyukov A. (1998) Early solar system timescales according to  $^{53}\text{Mn}$ - $^{53}\text{Cr}$  systematics. *Geochim. Cosmochim. Acta* 62, 2863–2886.

Mahan B., Moynier F., Siebert J., Gueguen B., Agranier A., Pringle E. A., Bollard J., Connelly J. N. and Bizzarro M. (2018) Volatile element evolution of chondrules through time. *Proc. Natl. Acad. Sci.* 115, 8547–8552.

Mare E. R., Tomkins A. G. and Godel B. M. (2014) Restriction of parent body heating by metal-troilite melting: Thermal models for the ordinary chondrites. *Meteorit. Planet. Sci.* 49, 636–651.

Matthes M., van Orman J. A. and Kleine T. (2020) Closure temperature of the Pd-Ag system and the crystallization and cooling history of IIIAB iron meteorites. *Geochim. Cosmochim. Acta* 285, 193–206.

McCoy T. J., Scott E. R. D., Jones R. H., Keil K. and Taylor G. J. (1991) Composition of chondrule silicates in LL3-5 chondrites and implications for their nebular history and parent body metamorphism. *Geochim. Cosmochim. Acta* 55, 601–619.

Miyamoto M., Fujii N. and Takeda H. (1982) Ordinary chondrite parent body-An internal heating model. *Lunar and planetary science conference proceedings* 12, 1145-1152.

Moynier F., Yin Q.-Z. and Jacobsen B. (2007) Dating the first stage of planet formation. *Astrophys. J.* 671, L181–L183.

Nagasawa, M., Thommes, E.W., Kenyon, S.J., Bromley, B.C., Lin, D.N.C., 2007. The diverse origins of terrestrial-planet systems. *Protostars Planets V*, 639–654.

Neumann W., Breuer D. and Spohn T. (2012) Differentiation and core formation in accreting planetesimals. *Astron. Astrophys.* 543, A141.

Nyquist L. E., Kleine T., Shih C. Y. and Reese Y. D. (2009) The distribution of short-lived radioisotopes in the early solar system and the chronology of asteroid accretion, differentiation, and secondary mineralization. *Geochim. Cosmochim. Acta* 73, 5115–5136.

Nyquist L., Lindstrom D., Mittlefehldt D., Shih C. Y., Wiesmann H., Wentworth S. and Martinez R. (2001) Manganese-chromium formation intervals for chondrules from the Bishunpur and Chainpur meteorites. *Meteorit. Planet. Sci.* 36, 911–938.

Pape J., Mezger K., Bouvier A. S. and Baumgartner L. P. (2019) Time and duration of chondrule formation: Constraints from  $^{26}\text{Al}$ - $^{26}\text{Mg}$  ages of individual chondrules. *Geochim. Cosmochim. Acta* 244, 416–436.

Pape J, Rosén Å. V., Mezger K. and Guillong M. (2021) Primary crystallization and partial remelting of chondrules in the protoplanetary disk: Petrographic, mineralogical and chemical constraints recorded in zoned type-I chondrules. *Geochim. Cosmochim. Acta* 292, 499-517.

Pedersen S. G., Schiller M., Connelly J. N. and Bizzarro M. (2019) Testing accretion mechanisms of the H chondrite parent body utilizing nucleosynthetic anomalies. *Meteorit. Planet. Sci.* 54, 1215–1227.

Pellas P. S. D. (1981)  $^{244}\text{Pu}$  fission track thermometry and its application to stony meteorites. *Proc. R. Soc. London. A. Math. Phys. Sci.* 374, 253–270.

Posner E. S., Ganguly J. and Hervig R. (2016) Diffusion kinetics of Cr in spinel: Experimental studies and implications for  $^{53}\text{Mn}$ - $^{53}\text{Cr}$  cosmochronology. *Geochim. Cosmochim. Acta* 175, 20–35.

Qin L., Alexander C. M. O. D., Carlson R. W., Horan M. F. and Yokoyama T. (2010) Contributors to chromium isotope variation of meteorites. *Geochim. Cosmochim. Acta* 74, 1122–1145.

Qin L., Dauphas N., Wadhwa M., Masarik J. and Janney P. E. (2008) Rapid accretion and differentiation of iron meteorite parent bodies inferred from  $^{182}\text{Hf}$ - $^{182}\text{W}$  chronometry and thermal modeling. *Earth Planet. Sci. Lett.* 273, 94–104.

Roth A. S. G., Metzler K., Baumgartner L. P. and Leya I. (2016) Cosmic-ray exposure ages of chondrules. *Meteorit. Planet. Sci.* 51, 1256–1267.

Rubin A. E. (2011) Origin of the differences in refractory-lithophile-element abundances among chondrite groups. *Icarus* 213, 547–558.

Rubin A. E. (2010) Physical properties of chondrules in different chondrite groups: Implications for multiple melting events in dusty environments. *Geochim. Cosmochim. Acta* 74, 4807–4828.

Rudraswami N. G. and Goswami J. N. (2007)  $^{26}\text{Al}$  in chondrules from unequilibrated L chondrites: Onset and duration of chondrule formation in the early solar system. *Earth Planet. Sci. Lett.* 257, 231–244.

Ruzicka A., Snyder G. A. and Taylor L. A. (1998) Mega-chondrules and large, igneous-textured clasts in Julesberg (L3) and other ordinary chondrites: vapor-fractionation, shock-melting, and chondrule formation. *Geochim. Cosmochim. Acta* 62, 1419–1442.

Sack R. O. and Ghiorso M. S. (1989) Importance of considerations of mixing properties in establishing an internally consistent thermodynamic database: thermochemistry of minerals in the system  $\text{Mg}_2\text{SiO}_4\text{-Fe}_2\text{SiO}_4\text{-SiO}_2$ . *Contrib. to Mineral. Petrol.* 102, 41–68.

Sack Richard O. and Ghiorso M. S. (1991a) An internally consistent model for the thermodynamic properties of Fe-Mg-titanomagnetite-aluminate spinels. *Contrib. to Mineral. Petrol.* 106, 474–505.

Sack R. O. and Ghiorso M. S. (1991b) Chromian spinels as petrogenetic indicators: thermodynamics and petrological applications. *Am. Mineral.* 76, 827–847.

Sahijpal S. and Gupta G. (2011) Did the carbonaceous chondrites evolve in the crustal regions of partially differentiated asteroids? *J. Geophys. Res.* 116, E6.

Sahijpal S., Soni P. and Gupta G. (2007) Numerical simulations of the differentiation of accreting planetesimals with  $^{26}\text{Al}$  and  $^{60}\text{Fe}$  as the heat sources. *Meteorit. Planet. Sci.* 42, 1529–1548.

Sanborn M. E., Wimpenny J., Williams C. D., Yamakawa A., Amelin Y., Irving A. J. and Yin Q.-Z. (2019) Carbonaceous achondrites Northwest Africa 6704/6693: milestones for early solar system chronology and genealogy. *Geochim. Cosmochim. Acta* 245, 577–596.

Scherstén A., Elliott T., Hawkesworth C., Russell S. and Masarik J. (2006) Hf-W evidence for rapid differentiation of iron meteorite parent bodies. *Earth Planet. Sci. Lett.* 241, 530–542.

Schneider, J. M., Burkhardt, C., Marrocchi, Y., Brennecka, G. A. and Kleine, T., (2020). Early evolution of the solar accretion disk inferred from Cr-Ti-O isotopes in individual chondrules. *Earth Planet. Sci. Lett.* 551, 116585

Schrader D. L., Davidson J. and McCoy T. J. (2016) Widespread evidence for high-temperature formation of pentlandite in chondrites. *Geochim. Cosmochim. Acta* 189, 359–376.

Siron, G., Fukuda, K., Kimura, M., & Kita, N. T. (2020) New constraints from  $^{26}\text{Al}$ - $^{26}\text{Mg}$  chronology of anorthite bearing chondrules in unequilibrated ordinary chondrites. *Geochim. Cosmochim. Acta.* 293, 103–126.



Shukolyukov A. and Lugmair G. W. (2006) Manganese-chromium isotope systematics of carbonaceous chondrites. *Earth Planet. Sci. Lett.* 250, 200-213.

Sievwright R. H., O'Neill H. S. C., Tolley J., Wilkinson J. J. and Berry A. J. (2020) Diffusion and partition coefficients of minor and trace elements in magnetite as a function of oxygen fugacity at 1150 °C. *Contrib. to Mineral. Petrol.* 175.

Slater-Reynolds V. and McSween H. Y. (2005) Peak metamorphic temperatures in type 6 ordinary chondrites: An evaluation of pyroxene and plagioclase geothermometry. *Meteorit. Planet. Sci.* 40, 745–754.

Sugiura N. and Fujiya W. (2014) Correlated accretion ages and  $\varepsilon^{54}\text{Cr}$  of meteorite parent bodies and the evolution of the solar nebula. *Meteorit. Planet. Sci.* 49, 772-787.

Sugiura N. and Hoshino H. (2003) Mn-Cr chronology of five IIIAB iron meteorites. *Meteorit. Planet. Sci.* 38, 117–143.

Suzuki A. M., Yasuda A. and Ozawa K. (2008) Cr and Al diffusion in chromite spinel: Experimental determination and its implication for diffusion creep. *Phys. Chem. Miner.* 35, 433–445.

Touboul M., Kleine T., Bourdon B., Van Orman J. A., Maden C. and Zipfel J. (2009) Hf-W thermochronometry: II. Accretion and thermal history of the acapulcoite-lodranite parent body. *Earth Planet. Sci. Lett.* 284, 168–178.

Trieloff M., Jessberger E. K., Herrwerth I., Hopp J., Fléniel C., Ghéllis M., Bourot-Denise M. and Pellas P. (2003) Structure and thermal history of the H-chondrite parent asteroid revealed by thermochronometry. *Nature* 422, 502–506.

Trinquier A., Birck J.-L. and Allègre C. J. (2007) Widespread  $^{54}\text{Cr}$  heterogeneity in the inner solar system. *Astrophys. J.* 655, 1179–1185.

Trinquier A., Birck J. L. and Allègre C. J. (2008a) High-precision analysis of chromium isotopes in terrestrial and meteorite samples by thermal ionization mass spectrometry. *J. Anal. At. Spectrom.* 23, 1565–1574.

Trinquier A., Birck J. L., Allègre C. J., Göpel C. and Ulfbeck D. (2008b)  $^{53}\text{Mn}$ - $^{53}\text{Cr}$  systematics of the early Solar System revisited. *Geochim. Cosmochim. Acta* 72, 5146–5163.

Van Schmus W. R. and Wood J. A. (1967) A chemical-petrologic classification for the chondritic meteorites. *Geochim. Cosmochim. Acta* 31, 747–765.

Vermeesch P. (2018) IsoplotR: A free and open toolbox for geochronology. *Geosci. Front.* 9, 1479–1493.

Villeneuve J., Chaussidon M. and Libourel G. (2009) Homogeneous distribution of  $^{26}\text{Al}$  in the solar system from the Mg isotopic composition of chondrules. *Science* 325, 985–988.

Visser, R., John, T., Whitehouse, M. J., Patzek, M., & Bischoff, A. (2020) A short-lived  $^{26}\text{Al}$  induced hydrothermal alteration event in the outer solar system: Constraints from Mn/Cr ages of carbonates. *Earth Planet. Sci. Lett.* 547, 116440.

Wasson J. T. and Allemeyn G. W. K. (1988) Compositions of chondrites. *Philos. Trans. R. Soc. London. Ser. A, Math. Phys. Sci.* 325, 535–544.

Weidenschilling S. J. (2019) Accretion of the asteroids: Implications for their thermal evolution. *Meteorit. Planet. Sci.* 54, 1115–1132.

Weidenschilling S. J. (2011) Initial sizes of planetesimals and accretion of the asteroids. *Icarus* 214, 671–684.

Weidenschilling, S. J., Cuzzi, J. N. (2006) Accretion dynamics and timescales: Relation to chondrites. In: Lauretta, D., McSween, H. (Eds.), *Meteorites and the Early Solar System*. Univ. of Arizona Press, Tucson, pp. 473–485.

Wlotzka, F. (1993) A weathering scale for the ordinary chondrites. *Meteoritics* 28, 460.

Wlotzka F. (2005) Cr spinel and chromite as petrogenetic indicators in ordinary chondrites: Equilibration temperatures of petrologic types 3.7 to 6. *Meteorit. Planet. Sci.* 40, 1673–1702.

Yanai K. and Kojima H. (1991) Yamato-74063: Chondritic meteorite classified between E and H chondrite groups. *Antarctic Meteorite Research*, 4, 118.

## 2

# Early differentiation of magmatic iron meteorite parent bodies from Mn-Cr chronometry

**Manuscript published in Geochemical Perspectives Letters**

Anand, A., Pape, J., Wille, M., Mezger, K. and Hofmann, B., (2021)

Geochemical Perspectives Letters (2021) 20, 6-10.



Published by the European Association of Geochemistry under Creative Commons License CC BY-NC-ND 4.0

<https://creativecommons.org/licenses/by-nc-nd/4.0/deed.en>

## Abstract

Magmatic iron meteorite groups such as IIAB, IIIAB and IVA, represent the largest sampling of extra-terrestrial core material from the earliest accreted distinct planetary bodies in the solar system. Chromium isotope compositions of chromite/daubréelite from seven samples, translated into  $^{53}\text{Cr}/^{52}\text{Cr}$  model ages, provide robust time information on planetary core formation. These ages are within  $\sim 1.5$  Ma after formation of calcium-aluminium-rich inclusions (CAIs) and define the time of metal core formation in the respective parent bodies, assuming metal-silicate separation was an instantaneous event that induced strong chemical fractionation of Mn from the more siderophile Cr. The early core formation ages support accretion and differentiation of the magmatic iron meteorite parent bodies to have occurred prior to the chondrule formation interval. The calibration of Mn-Cr ages with established Hf-W ages of samples from the same magmatic iron meteorite groups constrains the initial  $\epsilon^{53}\text{Cr}$  of the solar system to  $-0.30 \pm 0.05$ , and thus lower than previously estimated.

## 2.1 Introduction

Members of the different magmatic iron meteorite groups are thought to sample the cores of distinct parent bodies that experienced large-scale chemical fractionation, most notably metal-silicate separation. The absolute time of core formation provides a key time marker for the evolution of early-formed planetesimals including accretion and cooling of the respective parent body. The most commonly used chronological system to date iron meteorites is the  $^{182}\text{Hf}$ - $^{182}\text{W}$  system (Kruijer *et al.*, 2017 and references therein), constraining core formation in iron meteorite parent bodies over an interval of  $\sim 1$  Myr and their accretion to  $\sim 0.1 - 0.3$  Ma after the formation of Ca-Al-rich inclusions ( $4567.18 \pm 0.50$  Ma, Amelin *et al.*, 2010). These early accretion ages predate or are contemporaneous with the chondrule formation interval (e.g., Connelly *et al.*, 2012; Pape *et al.*, 2019). However, correct interpretation of Hf-W data depends on the accurate knowledge of initial  $\epsilon^{182}\text{W}$  of the solar system and Hf/W ratios of the parent bodies which are well-established but still needs to consider possible variations in Hf-isotopes due to galactic cosmic radiation (GCR) (Kruijer *et al.*, 2017).

Another powerful tool to constrain the time and duration of early solar system processes, including accretion, differentiation, metamorphism and subsequent cooling could be the short-lived  $^{53}\text{Mn}$ - $^{53}\text{Cr}$  chronometer ( $t_{1/2} = 3.7 \pm 0.4$  Ma; Honda and Imamura, 1971) (e.g., Shukolyukov and Lugmair, 2006; (A. Trinquier *et al.*, 2008). Chromite ( $\text{FeCr}_2\text{O}_4$ ) and daubréelite ( $\text{FeCr}_2\text{S}_4$ ) are the two main carrier phases of Cr in magmatic iron meteorites. Both minerals have low Mn/Cr ratios ( $\leq 0.01$ , Duan and Regelous, 2014) and thus preserve the Cr isotope composition of their growth environment at the time of isotopic closure, while the in-growth of radiogenic  $^{53}\text{Cr}$  from in-situ decay of  $^{53}\text{Mn}$  is negligible (Anand *et al.*, 2021). This makes them suitable for obtaining model ages by comparing their Cr-isotopic composition with the Cr-isotope evolution of the host reservoir. A particular advantage is that low Fe/Cr ratios in chromite and daubréelite (typically  $\sim 0.5$ ) result in negligible contribution of  $^{53}\text{Cr}$  produced by GCR from Fe; hence no correction for spallogenic Cr is required (Trinquier *et al.*, 2008; Liu *et al.*, 2019). (Supplementary Information, Appendix).

This study presents model ages for chromite and daubréelite from the largest magmatic iron meteorite group collections (IIAB, IIIAB and IVA) that constrain the earliest stages of planetesimal formation and differentiation. These Cr model ages define the timing of metal

segregation during core formation. Chromium-rich phases formed in the metal inherit the Cr-isotope composition of their low Mn/Cr host and thus constrain the time of last silicate-metal equilibration.

## 2.2 Methods

A chromite or daubréelite fraction from seven iron meteorites was analyzed. After mineral digestion and chemical purification, Cr isotopes were measured on a Triton™ Plus TIMS at the University of Bern. Each sample was measured on multiple filaments to achieve high precision for  $^{53}\text{Cr}/^{52}\text{Cr}$  ratio. Isotope compositions are reported as parts per 10,000 deviations ( $\epsilon$ -notation) from the mean value of a terrestrial Cr standard measured along with the samples in each session. External precision (2SD) for the terrestrial standard in a typical measurement session was  $\pm 0.1$  for  $\epsilon^{53}\text{Cr}$  and  $\pm 0.2$  for  $\epsilon^{54}\text{Cr}$ . (Supplementary Information, Appendix).

### 2.2.1 Model for $\epsilon^{53}\text{Cr}$ evolution in chondritic reservoir

Model  $^{53}\text{Cr}/^{52}\text{Cr}$  ages for early formed solar system bodies and their components can be determined on materials with high Cr/Mn and considering the following: (i) homogeneous distribution of  $^{53}\text{Mn}$  in the solar system (e.g., Trinquier *et al.*, 2008; Zhu *et al.*, 2019) (ii) known abundances of  $^{53}\text{Mn}$  and  $^{53}\text{Cr}$  at the beginning of the solar system (i.e., solar system initial  $\epsilon^{53}\text{Cr}$ ) or any point in time thereafter (iii) an estimate for the Mn/Cr in the relevant reservoir and (iv) known decay constant of  $^{53}\text{Mn}$ . Based on these assumptions the evolution of the  $^{53}\text{Cr}/^{52}\text{Cr}$  isotope composition of the chondritic reservoir through time can be expressed as:

$$(^{53}\text{Cr}/^{52}\text{Cr})_p = (^{53}\text{Cr}/^{52}\text{Cr})_i + (k)(^{53}\text{Mn}/^{55}\text{Mn})_i \times (1 - e^{-\lambda t}) \quad (2.1)$$

where  $p$  refers to the present-day value,  $i$  refers to the solar system initial values and  $\lambda$  denotes the  $^{53}\text{Mn}$  decay constant. The  $^{55}\text{Mn}/^{52}\text{Cr}$  of the reservoir is denoted by  $k$ ; and  $t$  represents the time elapsed since the start of the solar system, which is equated with the time of formation of CAIs. Equation 2.1 describes the evolution of  $^{53}\text{Cr}/^{52}\text{Cr}$  with time for the chondritic reservoir and can be used to derive model ages for a meteorite sample by measuring the Cr isotopic composition of its chromite/daubréelite fraction.

**Table 2.1.**

Mn/Cr, Fe/Cr and Cr isotopic compositions of chromite and daubréelite fractions from iron meteorites.

Sample (Coll. Number)	Group/Fraction	Mn/Cr	Fe/Cr	$\varepsilon^{53}\text{Cr}$	2SE	$\varepsilon^{54}\text{Cr}$	2SE	Model Age <sup>a</sup>	Model Age <sup>b</sup>	n
Agoudal (43830)	IIAB/Chromite	0.0053(4)	0.37(1)	-0.210	0.023	-0.784	0.060	$0.27^{+0.33}_{-0.31}$	$1.33^{+0.41}_{-0.38}$	12
Sikhote Alin (43380)	IIAB/Chromite	0.0052(8)	0.41(3)	-0.228	0.025	-0.923	0.051	$0.03^{+0.34}_{-0.32}$	$1.04^{+0.41}_{-0.38}$	12
NWA 11420 (43837)	IIAB/Daubréelite	0.0040(1)	0.59(1)	-0.203	0.045	-0.768	0.055	$0.37^{+0.67}_{-0.59}$	$1.45^{+0.83}_{-0.72}$	7
Saint Aubin <sup>c</sup>	IIIAB/Chromite	0.0096(2)	0.57(1)	-0.268	0.029	-0.779	0.061	$-0.47^{+0.35}_{-0.33}$	$0.44^{+0.42}_{-0.39}$	10
Cape York (33137)	IIIAB/Chromite	0.0062(3)	0.46(1)	-0.196	0.043	-0.780	0.062	$0.47^{+0.64}_{-0.57}$	$1.57^{+0.80}_{-0.70}$	13
Yanhuitlan (50084)	IVA/Daubréelite	0.0490(7)	0.54(1)	-0.272	0.027	-0.468	0.061	$-0.52^{+0.33}_{-0.31}$	$0.38^{+0.39}_{-0.36}$	10
Duchesne (50033)	IVA/Chromite	0.0048(4)	1.1(1)	-0.160	0.037	-0.487	0.156	$1.00^{+0.61}_{-0.55}$	$2.23^{+0.78}_{-0.68}$	7
IAG OKUM	whole rock std.	0.60(6)	36.6(9)	0.020	0.065	0.083	0.110			7

The uncertainties associated with Mn/Cr, Fe/Cr, and Cr isotopic compositions are reported as 2SE of the replicate measurements. See Table A2.1 for Cr isotopic composition of the individual runs. n = number of replicate measurements.

<sup>a</sup> Eq. 2.1.,  $\varepsilon^{53}\text{Cr}_i = -0.23$

<sup>b</sup> Eq. 2.1.,  $\varepsilon^{53}\text{Cr}_i = -0.30$

Collection number refer to meteorite collections of NHM Bern.

<sup>c</sup> NHM Vienna collection ID for Saint Aubin: NHMV\_#13635\_[A].



## 2.3 Results

$\epsilon^{53}\text{Cr}$  and  $\epsilon^{54}\text{Cr}$  of chromite/daubréelite fractions determined for all samples are listed in Table 2.1. No correlation is observed in  $\epsilon^{53}\text{Cr}$  vs.  $\epsilon^{54}\text{Cr}$  and  $\epsilon^{53}\text{Cr}$  vs. Fe/Cr that corroborates insignificant spallogenic contribution (Supplementary Information, Appendix). Model ages are calculated relative to the CAI formation age of  $4567.18 \pm 0.50$  Ma (Amelin *et al.*, 2010) assuming an OC-chondritic  $^{55}\text{Mn}/^{52}\text{Cr} = 0.74$  (Zhu *et al.*, 2021), a solar system initial  $\epsilon^{53}\text{Cr} = -0.23$  and a canonical  $^{53}\text{Mn}/^{55}\text{Mn} = 6.28 \times 10^{-6}$  (Trinquier *et al.*, 2008)(Fig. 2.1).

## 2.4 Discussion

The inference of Mn-Cr model ages to date core formation events is based on the assumption that metal-silicate separation was instantaneous. It occurred when the chondritic parent bodies of magmatic iron meteorites were heated by accretion energy and the decay of short-lived  $^{26}\text{Al}$ , and reached the liquidus temperature of iron-sulfur alloy (1325 °C to 1615 °C, depending on the S content in the metal melt, Kaminski *et al.*, 2020 and references therein). The metal-silicate separation induced a strong chemical fractionation of Mn from the more siderophile Cr (Mann *et al.*, 2009). The measured low Mn/Cr ( $\leq 0.01$ , Duan and Regelous, 2014) in iron meteorites corroborates the efficiency of this fractionation. Because of the low Mn/Cr of the metallic core, its Cr isotopic composition remained unchanged and reflects the composition at the time of metal-silicate differentiation. Therefore, the Cr isotopic composition of chromite/daubréelite that formed in the metallic core, no matter at what time after the metal segregation, reflects the time of Mn/Cr fractionation from a reservoir with CI-chondritic  $^{55}\text{Mn}/^{52}\text{Cr}$  and not the time of mineral formation nor its closure below a certain closure temperature.

The Mn-Cr model ages determined using Eq. 2.1. assume a Mn/Cr for the source reservoir that is represented by the average Mn/Cr of OCs. Ordinary chondrites have a CI-like Mn/Cr (e.g., Wasson and Allemeyn, 1988; Zhu *et al.*, 2021) and alongside the investigated magmatic iron meteorite groups, belong to the ‘non-carbonaceous’ reservoir (Kleine *et al.*, 2020). The effect of different Mn/Cr of the iron meteorite parent bodies and the assumption of different initial  $\epsilon^{53}\text{Cr}$  is shown in Fig. S2.1. Model ages for IIAB, IIIAB and IVA groups are unaffected

by the growth trajectory chosen, given current analytical resolution. Assuming a Mn/Cr similar to carbonaceous chondrites would change the model ages by a maximum of 1 Ma for the youngest sample. However, since all samples belong to the non-carbonaceous group, the average composition of OCs is most appropriate.

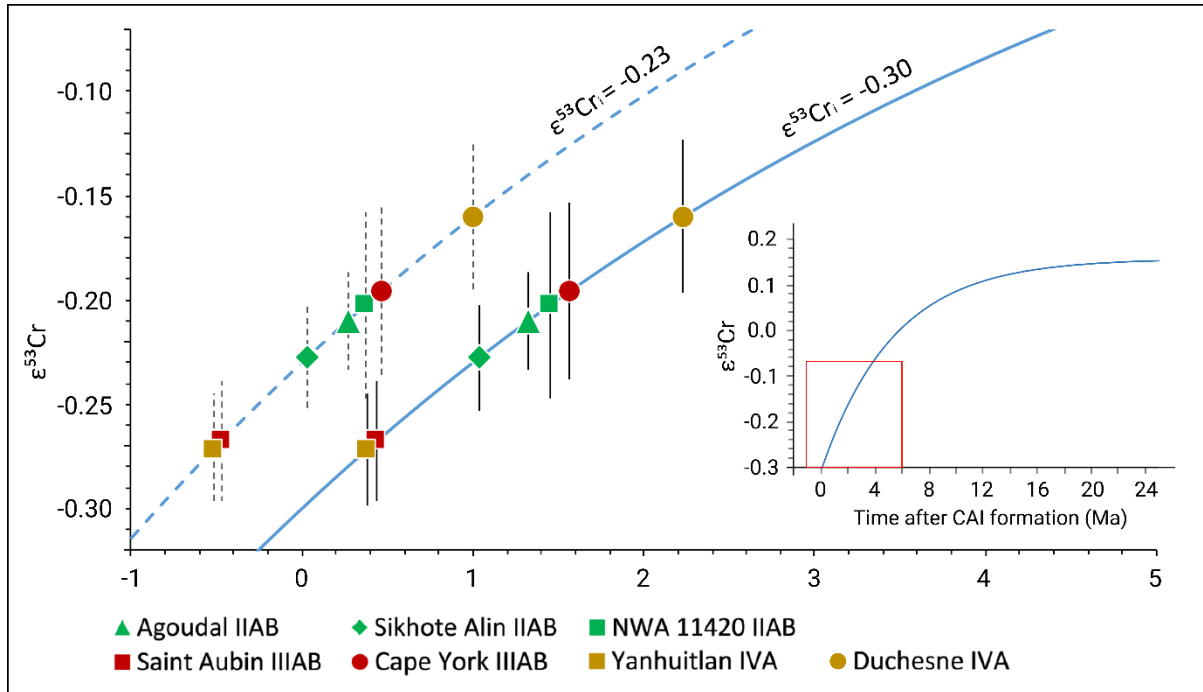


**Figure 2.1.**  $\epsilon^{53}\text{Cr}$  values of chromite/daubréelite plotted on Cr isotope evolution curve determined for a chondritic reservoir through time using Eq. 2.1. Error bars represent 2SE uncertainties.

Since the Cr isotopic composition of the samples is unaffected by contributions from spallogenic Cr (Supplementary Information, Appendix), the only major source of uncertainty in Mn-Cr model ages comes from the choice of initial  $\epsilon^{53}\text{Cr}$  and  $^{53}\text{Mn}/^{55}\text{Mn}$  values. Fig. S2.3 shows Mn-Cr model ages for the studied samples determined using initial Mn-Cr isotopic compositions from multiple studies reporting resolvable variations in the solar system initial  $\epsilon^{53}\text{Cr}$  and  $^{53}\text{Mn}/^{55}\text{Mn}$  values. Clearly, more high-precision Cr isotope data for samples dated with different chronometers are needed to further constrain the initial  $\epsilon^{53}\text{Cr}$  and  $^{53}\text{Mn}/^{55}\text{Mn}$ . Model ages determined using initial  $\epsilon^{53}\text{Cr}$  and  $^{53}\text{Mn}/^{55}\text{Mn}$  values from Göpel *et al.* (2015) and Shukolyukov and Lugmair (2006) predate the CAI formation age, contradicting the standard solar system model in which CAIs are the earliest formed solid objects. The Mn-Cr model ages determined using initial  $\epsilon^{53}\text{Cr}$  and  $^{53}\text{Mn}/^{55}\text{Mn}$  from Trinquier *et al.* (2008) mostly postdate CAI formation and thus appear generally more reliable.

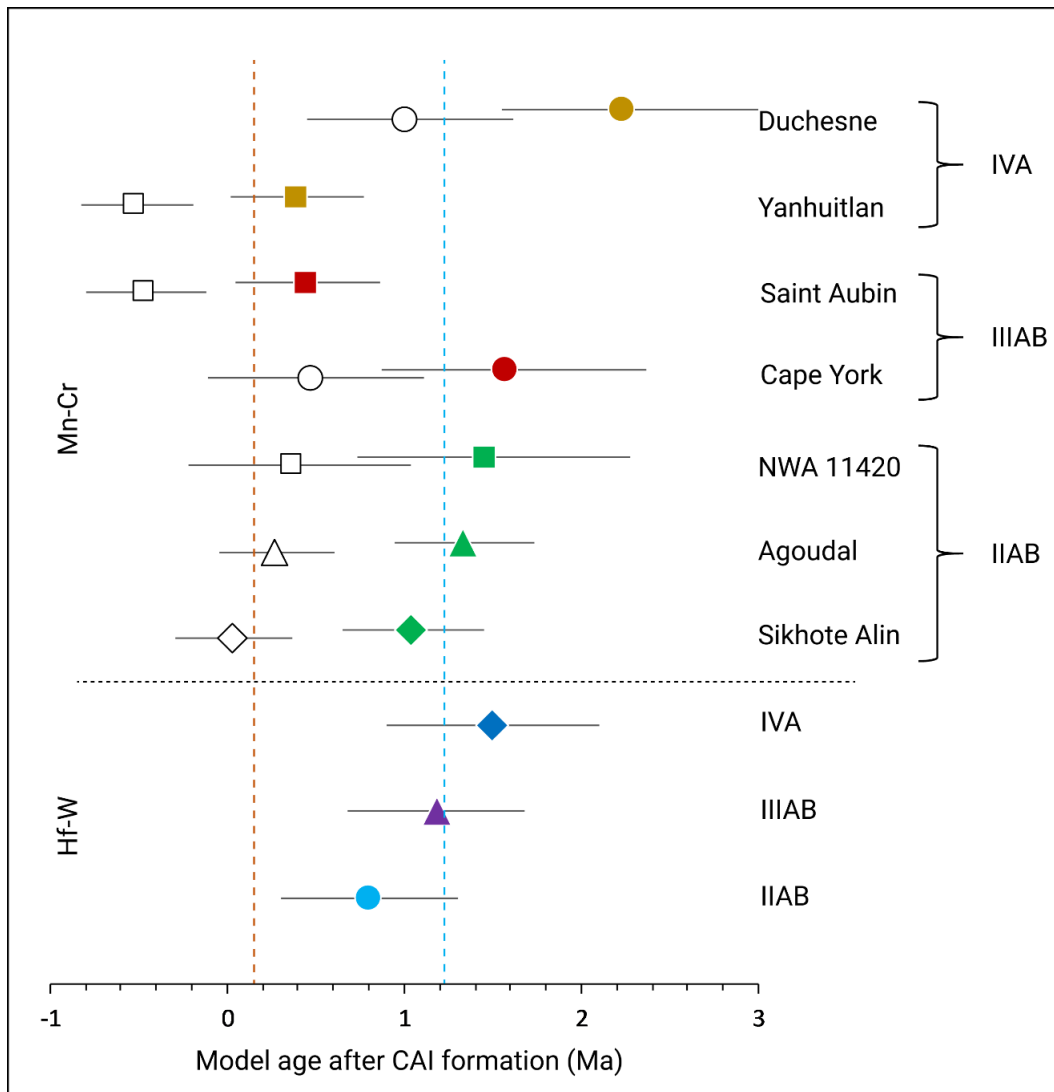


**Figure 2.2.** Comparison between Mn-Cr (present study) and Hf-W (Kruijer *et al.*, 2017) core formation ages. The Mn-Cr ages are determined using Eq. 2.1 and  $\varepsilon^{53}\text{Cr}_i = -0.23$  (open symbols) from Trinquier *et al.* (2008) and  $\varepsilon^{53}\text{Cr}_i = -0.30$  (filled symbols) proposed in the present study.

The Mn-Cr model ages can also be compared with other chronometers that have been used to date meteorites and their components.  $^{182}\text{Hf}$ - $^{182}\text{W}$ , Pb-Pb and  $^{187}\text{Re}$ - $^{187}\text{Os}$  are some of the common chronological systems providing constraints on different stages in the evolution of iron meteorite parent bodies (Goldstein *et al.*, 2009 and references therein). However, when applied to iron meteorites all other chronological systems date cooling below their respective isotopic closure with the exception of the  $^{182}\text{Hf}$ - $^{182}\text{W}$  system, which has strong similarities to the  $^{53}\text{Mn}$ - $^{53}\text{Cr}$  system. It is also suitable for examining the timescales and mechanisms of metal segregation for iron meteorite parent bodies since Hf and W have different geochemical behaviors resulting in strong Hf/W fractionation during metal/silicate separation (i.e., core

formation). However, in addition to the uncertainty on the initial  $\epsilon^{182}\text{W}$  of the solar system,  $^{182}\text{W}/^{184}\text{W}$  data are also affected by secondary neutron capture effects on W isotopes induced during cosmic-ray exposure (unlike Mn-Cr model ages reported here). Recently, Pt isotope data have been used to quantify the effects of neutron capture on W isotope compositions, making it possible to produce more reliable core formation ages (e.g., Kruijer *et al.*, 2017). The Mn-Cr core formation age corresponding to the weighted mean  $\epsilon^{53}\text{Cr}$  of combined IIAB, IIIAB and IVA groups determined using solar system initial  $\epsilon^{53}\text{Cr} = -0.23$  (Trinquier *et al.*, 2008) is  $\sim 1$  Myr older than the Hf-W core formation age corresponding to Pt-corrected weighted mean  $\epsilon^{182}\text{W}$  of the same iron groups (Fig. 2.2, Table A2.2) (Kruijer *et al.*, 2017). However, the Hf-W and Mn-Cr systems show consistent crystallization ages in angrites (internal isochrons established by minerals) that also belong to the ‘non-carbonaceous’ reservoir and originated from differentiated parent bodies (Zhu *et al.*, 2019). The different chronometers are expected to agree because of the rapid cooling of angrites indicated by their basaltic texture. A better fit between Hf-W and Cr model ages can be obtained when the uncertainties on the model parameters for Mn-Cr model age determination are considered. Uncertainties on the  $^{53}\text{Mn}$  decay constant (Honda and Imamura, 1971) and solar system  $^{53}\text{Mn}/^{55}\text{Mn}$  (Trinquier *et al.*, 2008) result in only minor shift in the model ages of generally  $<0.02$  Myrs which is insignificant. However, using a solar system initial  $\epsilon^{53}\text{Cr} = -0.30$ , which is within its reported uncertainty ( $\epsilon^{53}\text{Cr} = -0.23 \pm 0.09$ ; Trinquier *et al.*, 2008), results in a perfect fit with the mean  $^{182}\text{Hf}$ - $^{182}\text{W}$  model ages for magmatic iron meteorite groups (Fig. 2.2). Consequently,  $\epsilon^{53}\text{Cr} = -0.30$  is proposed as a better estimate for the solar system initial  $\epsilon^{53}\text{Cr}$ . To maintain a match between Hf-W and Mn-Cr model ages the uncertainty on the initial  $\epsilon^{53}\text{Cr}$  of the solar system is less than  $\pm 0.05$ .

Fig. 2.3 presents a timeline depicting chromite/daubréelite model ages for IIAB, IIIAB and IVA iron meteorites and parent body metamorphism ages for type 3 and 6 ordinary chondrites as determined in Anand *et al.* (2021) using updated parameters for model age calculation. Combined with the existing thermal models (e.g., Qin *et al.*, 2008), Hf-W core formation ages and calibrated Mn-Cr model ages constrain the accretion of the magmatic iron meteorite parent bodies to within less than 1 Myr and no later than 1.5 Myr after CAI formation. This is in perfect agreement with numerical simulations that require early and efficient accretion of larger bodies within the protoplanetary disk (e.g., Johansen *et al.*, 2007; Cuzzi *et al.*, 2008). The small spread in the model ages of samples from the same meteorite group might reflect some core-

mantle exchange during the solidification of the metal core. The range is similar to the range of individual Hf-W model ages within an iron-meteorite group (e.g., Kruijer *et al.*, 2017).

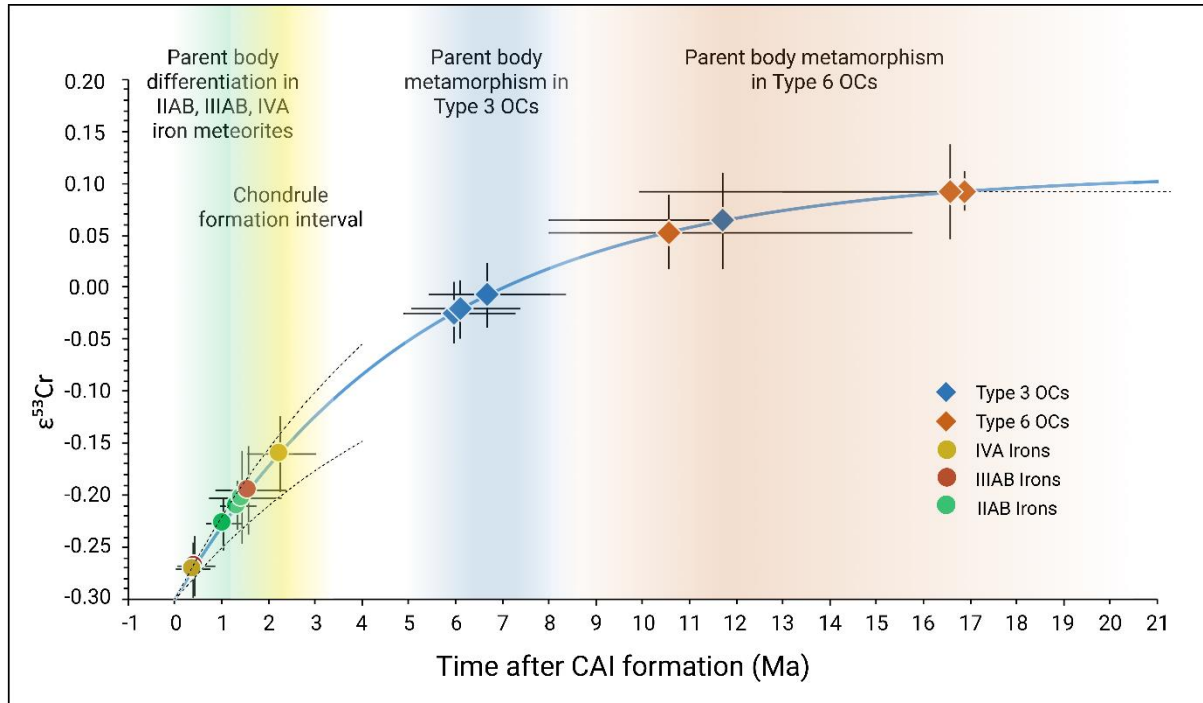


**Figure 2.3.** Timeline of early solar system formation showing parent body differentiation in magmatic iron meteorites, chondrule formation, and parent body metamorphism on ordinary chondrites (see text for references). Error envelope over iron meteorites shown by dashed lines represent the maximum variation in the evolutionary paths due to different Mn/Cr ratios of the parent bodies (see Figure S2.2).

One of the most important implications of Mn-Cr and Hf-W (e.g., Kruijer *et al.*, 2017; Spitzer *et al.*, 2021) core formation ages is that they bring the accretion and differentiation of the magmatic iron meteorite parent bodies in context with the chondrule formation interval recorded in chondrite samples (e.g., Connelly *et al.*, 2012; Pape *et al.*, 2019, 2021).  $^{207}\text{Pb}$ - $^{206}\text{Pb}$  chondrule formation ages (Connelly *et al.*, 2012) suggest that the production of chondrules began as early as the CAI condensation; hence, contemporaneous with the accretion of the parent bodies of magmatic iron meteorites as suggested by Hf-W core formation ages and collaborated by Mn-Cr model ages in the present study.  $^{26}\text{Al}$ - $^{26}\text{Mg}$  ages for the formation of melt in individual chondrules, as summarized in Pape *et al.* (2019), suggest that chondrule formation in ordinary and most carbonaceous chondrites lasted from ca. 1.8-3.0 Ma with a major phase around 2.0-2.3 Ma after CAI formation. This puts the chondrule formation interval after the accretion of the magmatic iron meteorite parent bodies. The latter implies that chondrule formation may not necessarily be an intermediate step on the way from dust to

planets, but rather early planet formation may have been the cause for the chondrule formation at least in extant chondrite samples. Thus, the early planetesimal formation (i.e., accretion of the iron meteorites parent bodies) was a local process and happened while other regions were still mostly in the stage of accreting dust particles and chondrule formation.

## **Acknowledgements**

We appreciate the support through a ‘Swiss Government Excellence Scholarship (2018.0371)’ and NCCR PlanetS supported by the Swiss National Science Foundation grant no. 51NF40-141881. We thank Dr. Ludovic Ferriere from NHM Vienna for providing chromite from Saint Aubin meteorite. Dr. Harry Becker and Smithsonian Institution are thanked for providing Allende powder sample. Patrick Neuhaus and Lorenz Gfeller from the Institute of Geography, University of Bern, are thanked for assistance with the ICP-MS analysis of the samples. We thank Dr. Maud Boyet for editorial handling and Dr. Ke Zhu and an anonymous reviewer for their constructive comments that helped to improve the manuscript.

## References

- Amelin, Y., Kaltenbach, A., Iizuka, T., Stirling, C. H., Ireland, T. R., Petaev, M., Jacobsen, S. B. (2010) U–Pb chronology of the Solar System's oldest solids with variable  $^{238}\text{U}/^{235}\text{U}$  *Earth and Planetary Science Letters* 300, 343–350.
- Anand, A., Pape, J., Wille, M., Mezger, K. (2021) Chronological constraints on the thermal evolution of ordinary chondrite parent bodies from the  $^{53}\text{Mn}$ – $^{53}\text{Cr}$  system *Geochimica et Cosmochimica Acta* 307, 281–301.
- Connelly, J. N., Bizzarro, M., Krot, A. N., Nordlund, Å., Wielandt, D., Ivanova M. A. (2012) The absolute chronology and thermal processing of solids in the solar protoplanetary disk *Science* 338, 651–655.
- Cuzzi, J. N., Hogan, R. C., Shariff, K. (2008) Towards planetesimals: Dense chondrule clumps in the protoplanetary nebula *The Astrophysical Journal* 687(2), 1432–1447.
- Duan, X., Regelous, M. (2014) Rapid determination of 26 elements in iron meteorites using matrix removal and membrane desolvating quadrupole ICP-MS *Journal of Analytical Atomic Spectrometry* 29, 2379–2387.
- Goldstein, J. I., Scott, E. R. D., Chabot, N. L. (2009) Iron meteorites: Crystallization, thermal history, parent bodies, and origin *Geochemistry* 69(4), 293–325.
- Göpel, C., Birck, J. L., Galy, A., Barrat, J. A., Zanda, B. (2015) Mn–Cr systematics in primitive meteorites: Insights from mineral separation and partial dissolution *Geochimica et Cosmochimica Acta* 156, 1–24.
- Honda, M., Imamura, M. (1971) Half-life of Mn53 *Physical Review C* 4, 1182–1188.
- Johansen, A., Oishi, J. S., Mac Low, M. M., Klahr, H., Henning, T., Youdin, A. (2007) Rapid planetesimal formation in turbulent circumstellar disks *Nature* 448(7157), 1022–1025.
- Kaminski, E., Limare, A., Kenda, B., Chaussidon, M. (2020) Early accretion of planetesimals unraveled by the thermal evolution of the parent bodies of magmatic iron meteorites *Earth and Planetary Science Letters* 548, 116469.

Kleine, T., Budde, G., Burkhardt, C., Kruijer, T. S., Worsham, E. A., Morbidelli, A., Nimmo, F. (2020) The Non-carbonaceous–Carbonaceous Meteorite Dichotomy *Space Science Reviews* 216, 1–27.

Kruijer, T. S., Burkhardt, C., Budde, G., Kleine, T. (2017) Age of Jupiter inferred from the distinct genetics and formation times of meteorites *Proceedings of the National Academy of Sciences of the United States of America* 114(26), 6712–6716.

Liu, J., Qin, L., Xia, J., Carlson, R. W., Leya, I., Dauphas, N., He, Y. (2019) Cosmogenic effects on chromium isotopes in meteorites *Geochimica et Cosmochimica Acta* 251, 73–86.

Mann, U., Frost, D. J., Rubie, D. C. (2009) Evidence for high-pressure core-mantle differentiation from the metal-silicate partitioning of lithophile and weakly-siderophile elements *Geochimica et Cosmochimica Acta* 73, 7360–7386.

Pape, J., Mezger, K., Bouvier, A. S., Baumgartner, L. P. (2019) Time and duration of chondrule formation: Constraints from  $^{26}\text{Al}$ - $^{26}\text{Mg}$  ages of individual chondrules *Geochimica et Cosmochimica Acta* 244, 416–436.

Pape, J., Rosén, V., Mezger, K., Guillong, M. (2021) Primary crystallization and partial remelting of chondrules in the protoplanetary disk: Petrographic, mineralogical and chemical constraints recorded in zoned type-I chondrules *Geochimica et Cosmochimica Acta* 292, 499–517.

Qin, L., Dauphas, N., Wadhwa, M., Masarik, J., Janney, P. E. (2008) Rapid accretion and differentiation of iron meteorite parent bodies inferred from  $^{182}\text{Hf}$ - $^{182}\text{W}$  chronometry and thermal modeling *Earth and Planetary Science Letters* 273, 94–104.

Shukolyukov, A., Lugmair, G. W. (2006) Manganese-chromium isotope systematics of carbonaceous chondrites *Earth and Planetary Science Letters* 250, 200–213.

Spitzer, F., Burkhardt, C., Nimmo, F., Kleine, T. (2021) Nucleosynthetic Pt isotope anomalies and the Hf-W chronology of core formation in inner and outer solar system planetesimals *Earth and Planetary Science Letters*, 576, p.117211.



Trinquier, A., Birck, J. L., Allègre, C. J., Göpel, C., Ulfbeck, D. (2008)  $^{53}\text{Mn}$ - $^{53}\text{Cr}$  systematics of the early Solar System revisited *Geochimica et Cosmochimica Acta* 72, 5146–5163.

Wasson, J. T., Allemeyn, G. W. K. (1988) Compositions of chondrites *Philosophical Transactions of the Royal Society of London. Series A, Mathematical and Physical Sciences* 325(1587), 535–544.

Zhu, K., Moynier, F., Schiller, M., Alexander, C. M. O., Davidson, J., Schrader, D. L., van Kooten, E., Bizzarro, M. (2021) Chromium isotopic insights into the origin of chondrite parent bodies and the early terrestrial volatile depletion *Geochimica et Cosmochimica Acta* 301, 158–186.

Zhu, K., Moynier, F., Wielandt, D., Larsen, K. K., Barrat, J. A., Bizzarro, M. (2019) Timing and Origin of the Angrite Parent Body Inferred from Cr Isotopes *The Astrophysical Journal* 877, L13.

## 3

$^{53}\text{Mn}$ - $^{53}\text{Cr}$  chronology and  $\varepsilon^{54}\text{Cr}$ - $\Delta^{17}\text{O}$   
genealogy of Erg Chech 002: the oldest  
andesite in the Solar System

**Manuscript under review in Meteoritics and Planetary Science**

Anand, A., Kruttsch, P., M. and Mezger, K.

## Abstract

The meteorite sample Erg Chech (EC) 002 is the oldest felsic igneous rock from the Solar System analysed to date and provides a unique opportunity to study the formation of felsic crusts on differentiated protoplanets immediately after metal-silicate equilibration or core formation. The extinct  $^{53}\text{Mn}$ - $^{53}\text{Cr}$  chronometer provides chronological constraints on the formation of EC 002 by applying the isochron approach using chromite, metal-silicate-sulphide and whole-rock fractions as well as ‘‘leachates’’ obtained by sequential digestion of a bulk sample. Assuming a chondritic evolution of its parent body, a  $^{53}\text{Cr}/^{52}\text{Cr}$  model age is also obtained from the chromite fraction. The  $^{53}\text{Mn}$ - $^{53}\text{Cr}$  isochron age of  $1.73 \pm 0.96$  Ma and the chromite model age constrained between  $1.46^{+0.78}_{-0.68}$  and  $2.18^{+1.32}_{-1.06}$  Ma after the formation of calcium-aluminium-rich inclusions agree with the  $^{26}\text{Al}$ - $^{26}\text{Mg}$  ages reported in previous studies and indicate rapid cooling and nearly contemporaneous closure of multiple isotope systems. Additionally, excess in the neutron-rich  $^{54}\text{Cr}$  (nucleosynthetic anomalies) combined with mass-independent isotope variations of  $^{17}\text{O}$  provide genealogical constraints on the accretion region of the EC 002 parent body. The  $^{54}\text{Cr}$  and  $^{17}\text{O}$  isotope compositions of EC 002 confirm its origin in the ‘‘non-carbonaceous’’ reservoir and overlap with the vestoid material NWA 12217 and anomalous eucrite EET 92023. This indicates a common feeding zone during accretion in the protoplanetary disk between the source of EC 002 and vestoids. The enigmatic origin of iron meteorites remains still unresolved as EC 002, which is more like a differentiated crust, has an isotope composition that does not match known irons meteorite groups that were once planetesimal cores.

### 3.1 Introduction

The majority of achondrites in our current meteorite collections are either basaltic or close to chondritic in composition. Achondrites with Si-rich evolved compositions (andesitic or trachyandesitic) are rare and include Graves Nunataks (GRA) 06128 and 016129 (Shearer *et al.*, 2010), ALM-A (Bischoff *et al.*, 2014), NWA 11119 (Srinivasan *et al.* 2018) and Erg Chech (EC) 002 (Barrat *et al.*, 2021). Among these, EC 002 represents the oldest felsic igneous rock from the Solar System analysed to date (Barrat *et al.*, 2021; Fang *et al.*, 2022). It is a 25% partial melting product of a chondritic source and provides a unique opportunity to study the formation of felsic crusts formed on a differentiated protoplanet immediately after metal-silicate equilibration or core formation (Barrat *et al.*, 2021). Magmatic iron meteorites that represent the cores of differentiated protoplanets have been extensively studied using  $^{182}\text{Hf}$ - $^{182}\text{W}$  chronometry (e.g., Kruijer *et al.*, 2017) and more recently by  $^{53}\text{Mn}$ - $^{53}\text{Cr}$  systematics (Anand *et al.*, 2021a). Both these chronometers constrain the timing of metal segregation in magmatic iron meteorite parent bodies to within 2.5 Ma after the formation of Ca-Al-rich inclusions ( $4567.18 \pm 0.50$  Ma, Amelin *et al.*, 2010). The core formation ages in magmatic iron meteorite parent bodies agree with the  $^{26}\text{Al}$ - $^{26}\text{Mg}$  isochron for EC 002 which yields an age of  $1.80 \pm 0.01$  Ma after CAIs, assuming a homogeneous distribution of  $^{26}\text{Al}$  in the early Solar System with an initial  $^{26}\text{Al}/^{27}\text{Al}$  ratio of  $5.23 \times 10^{-5}$  (Fang *et al.*, 2022; Jacobsen *et al.*, 2008). The short-lived  $^{53}\text{Mn}$ - $^{53}\text{Cr}$  ( $t_{1/2} = 3.7 \pm 0.4$  Ma; Honda *et al.*, 1971) chronometer is another powerful tool to constrain the time and duration of early Solar System processes including accretion, differentiation, metamorphism and subsequent cooling (e.g., Shukolyukov and Lugmair, 2006; Trinquier *et al.*, 2008b; Zhu *et al.*, 2021; Anand *et al.*, 2021a, b) and can help to refine the timing and extent of the formation process of a primitive igneous crust on the EC 002 parent body.

Manganese and Cr are minor elements in EC 002 mineral phases, and these phases have variable and relatively high Mn/Cr ratios, making them suitable for dating by the isochron method. Additionally, the  $^{53}\text{Cr}/^{52}\text{Cr}$  ratio can be used to obtain “model ages” for chromite which has a Mn/Cr ratio near zero (Anand *et al.*, 2021a, b). The combination of  $^{54}\text{Cr}/^{52}\text{Cr}$  (expressed as  $\epsilon^{54}\text{Cr}$ ) and O isotopes (expressed as  $\Delta^{17}\text{O}$ ), which were heterogeneously distributed in the early Solar System (Warren, 2011), can be used to identify the isotopic source reservoir of the parent body and potentially relate EC 002 to other achondritic meteorites.

Previous studies have established genealogical connections between different meteorite groups in  $\epsilon^{54}\text{Cr}$  vs.  $\Delta^{17}\text{O}$  space, such as between IIIAB irons, main group pallasites and HEDs (e.g., Wasson, 2013), IVA irons and L/LL chondrites (e.g., Anand *et al.* 2021c) and IIG and IIAB irons (Anand *et al.*, 2022). Thus  $^{53}\text{Mn}$ - $^{53}\text{Cr}$  systematics constrain the timing of felsic crust formation, and the  $\epsilon^{54}\text{Cr}$ - $\Delta^{17}\text{O}$  data provide genealogical constraints on the EC 002 parent body and its source reservoir.

### 3.2 Analytical Methods

Approximately ~2 g EC 002 meteorite fragments were obtained from Decker Meteorite Shop, Germany ([www.meteorite-museum.de](http://www.meteorite-museum.de)). After cleaning in an ultrasonic bath with ethanol, the fragments were crushed into a fine powder using an agate mortar and pestle. This whole-rock powder was successively used to perform three experiments on EC 002 as shown in Fig. 3.1. In the first experiment, ~20 mg of whole-rock powder was digested in a Parr<sup>®</sup> bomb using a concentrated HF-HNO<sub>3</sub> mixture. This fraction is labelled as “whole-rock”. The second experiment involved ~100 mg whole-rock powder subjected to a concentrated HF-HNO<sub>3</sub> mixture on a hot plate at 130 °C for 24 hours and split into two fractions: (1) completely digested sulphide-metal-silicate fraction, labelled as “silicates” and (2) refractory phase, subsequently digested in a Parr<sup>®</sup> bomb and labelled as “chromite”. The third experiment involved a sequential digestion procedure (adopted from Yamakawa *et al.*, 2010) using ~1.5 g whole rock material to obtain data from phases with various Mn/Cr ratios (Rotaru *et al.*, 1992). The whole procedure involved 6 leaching steps labelled as “leachate 1” to “leachate 6” and summarized in Table 3.1. Before chemical separation, an aliquot from digested fractions of all three experiments was diluted in 10 ml 0.5 M HNO<sub>3</sub> to produce a 10 ppb Cr solution. These aliquots were used to determine Cr, Mn, and Fe concentrations using a 7700x Agilent ICP-MS at the Institute of Geography, University of Bern. Uncertainties on  $^{55}\text{Mn}/^{52}\text{Cr}$  and Fe/Cr ratios are reported in 2 standard errors of the replicate measurements ( $n = 5$ ) and remained <5 % for all the samples.

The procedure for Cr purification was adopted from Schoenberg *et al.* (2016). It includes three steps of a combination of cation-anion exchange chromatography modified after Schoenberg and von Blanckenburg (2005) (column 1), Trinquier *et al.* (2008a) and Yamakawa *et al.* (2009) (columns 2 and 3). In brief, an aliquot containing ~15 µg of Cr from each sample

was taken up in 1 ml 6 M HCl and loaded onto the first 7.5 mL Spectrum<sup>®</sup> polypropylene column containing 2 ml anion resin (BioRad<sup>®</sup> AG 1X8 100-200 mesh size). The Cr eluate from the first column was dried down, redissolved in 400  $\mu$ l 6 M HCl, equilibrated on a hotplate set to 130 °C for ~30 min one day before the chemical separation and stored at room temperature overnight. The next day, the sample was re-equilibrated on a hot plate at 130 °C for one hour, diluted with 2 ml of MilliQ<sup>®</sup> water to obtain 2.4 ml 1 M HCl and loaded onto the second column filled with 2 ml cation resin (BioRad<sup>®</sup> AG 50W-X8 200-400 mesh size). The second column separation step produced a solution with mostly Cr, but incompletely separated from Ti and V. The eluate from the second column was dried down on a hot plate (at 90 °C), taken up in 0.5 ml conc. HNO<sub>3</sub> and dried down again immediately to transform the samples into nitrate form. The residue was redissolved in 3 ml 0.4 M HNO<sub>3</sub> for 30 min on a hotplate at 80 °C and let react cold for 5 days for the production of chloro-aquo complexes. Afterwards, each sample was loaded onto the third column containing 0.5 ml BioRad<sup>®</sup> AG 50W-X8 200-400 mesh resin in order to obtain a clean Cr separate, free of Ti and V. The matrix was eluted in 8 ml 0.5 M HF and 9.5 ml 1 M HCl, and Cr was collected in 8 ml 4 M HCl. Finally, the Cr separate was redissolved in 100  $\mu$ l conc. HNO<sub>3</sub> and dried immediately at 130 °C on a hotplate. This step was repeated 2 times to remove the residual organics from the column chemistry. Typical recovery of Cr was in excess of 80% for the whole column chemistry. Total chemistry blanks were below 20 ng, which are negligible compared to the  $\mu$ g range of Cr processed through the columns.

After column chemistry, purified Cr samples were analysed on a Thermal Ionization Mass Spectrometer (Thermo Scientific TRITON Plus) at the Institute of Geological Sciences, University of Bern. Two to three  $\mu$ g of Cr from each sample was loaded on multiple filaments and measured at a <sup>52</sup>Cr signal intensity between 7 and 10 V ( $10^{-11}$   $\Omega$  resistor). Intensities of <sup>50</sup>Cr, <sup>51</sup>V, <sup>52</sup>Cr, <sup>53</sup>Cr, <sup>54</sup>Cr, <sup>55</sup>Mn and <sup>56</sup>Fe were measured on the Faraday cups L3, L2, L1, C, H1, H2 and H3, respectively (Trinquier *et al.*, 2008a). Alignment of all the Cr peaks (peak scan) was ensured before each measurement and the peak center was monitored on <sup>53</sup>Cr in the center cup. Isobaric interference of <sup>54</sup>Fe on <sup>54</sup>Cr was corrected by monitoring <sup>56</sup>Fe. The isotope <sup>51</sup>V was measured and <sup>49</sup>Ti was monitored to correct for isobaric interferences on <sup>50</sup>Cr. However, the <sup>49</sup>Ti and <sup>51</sup>V intensities remained indistinguishable from background intensities for all samples, verifying the successful separation of V and Ti from Cr during column chromatography. A typical run for a single filament load consisted of 24 blocks with 20 cycles each (integration time = 8.389 s), obtained in static acquisition mode. Gain calibration was

done once, at the beginning of every analytical session. The baseline was measured, and the amplifiers were rotated after every block (baseline = 30 cycles, each of 1.05 s). The Cr standard reference material NIST SRM 979, was used as a terrestrial reference material. The  $^{53}\text{Cr}/^{52}\text{Cr}$  and  $^{54}\text{Cr}/^{52}\text{Cr}$  ratios were normalized to  $^{52}\text{Cr}/^{50}\text{Cr} = 19.28323$  (Shields *et al.*, 1966) by applying the exponential mass fractionation law and are reported as  $\epsilon^i\text{Cr}$ , where  $\epsilon^i\text{Cr} = ([^i\text{Cr}/^{52}\text{Cr}]_{\text{sample}} / [^i\text{Cr}/^{52}\text{Cr}_{\text{NIST SRM 979}}] - 1) \times 10^4$  ( $i = 53$  or  $54$ ).

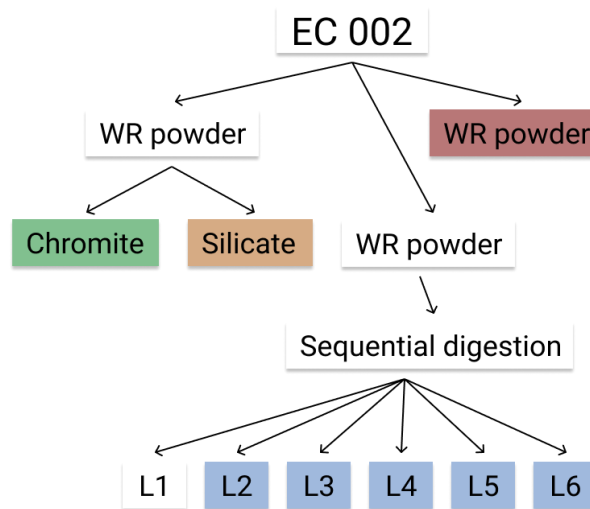


**Figure 3.1.** Separation scheme for EC 002 fractions. All fractions with coloured labels were analysed. WR: whole rock, L1-6: sequential digestion leachates.

The  $\epsilon^i\text{Cr}$  reported for any one sample represents the mean of the replicate measurements ( $n = 3-5$ , Tables 1). The replicate measurements for each sample are used to determine the external precision reported as 2 standard errors. The isotope compositions of each sample are reported relative to the mean value of the standard reference material (NIST SRM 979) measured along with the samples in each measurement session (single turret). The external precision (2 standard errors,  $n = 8$ ) for the standard reference material (NIST SRM 979) in each measurement session was  $\sim 0.05$  for  $\epsilon^{53}\text{Cr}$  and  $\sim 0.11$  for  $\epsilon^{54}\text{Cr}$ .

The model age for EC 002 is determined by comparing the  $^{53}\text{Cr}/^{52}\text{Cr}$  isotopic ratio of the chromite fraction to the theoretical  $^{53}\text{Cr}/^{52}\text{Cr}$  evolution of the chondritic reservoir (Anand *et al.*, 2021a) and assuming a homogeneous abundance of  $^{53}\text{Mn}$  in the early Solar System (e.g., Trinquier *et al.*, 2008b), known abundances of  $^{53}\text{Mn}$  and  $^{53}\text{Cr}$  at the beginning of the Solar System (or any point in time thereafter), an estimate for the  $^{55}\text{Mn}/^{52}\text{Cr}$  in the relevant reservoir and known decay constant of  $^{53}\text{Mn}$ . The spallogenic Cr contributions in the  $\epsilon^{53}\text{Cr}$  and  $\epsilon^{54}\text{Cr}$

isotopic compositions are corrected using  $^{53}\text{Cr}$  and  $^{54}\text{Cr}$  production rates in Fe targets from the Grant iron meteorite ( $2.9 \times 10^{11}$  atoms/Ma, Birck and Allegre, 1985) and the relationship described in Trinquier *et al.* (2007), assuming a spallation depth profile similar to that in Graf and Marti (1995). The cosmic-ray exposure age for EC 002 ( $^3\text{He}$  exposure age of  $26.0 \pm 1.6$  Ma) is taken from Barrat *et al.* (2021). Isochron regressions (Fig. 3.1a) are generated using IsoplotR (Vermeesch, 2018) with a maximum likelihood regression model. The O isotope data for EC 002 genealogy are taken from Gattacceca *et al.* (2021).

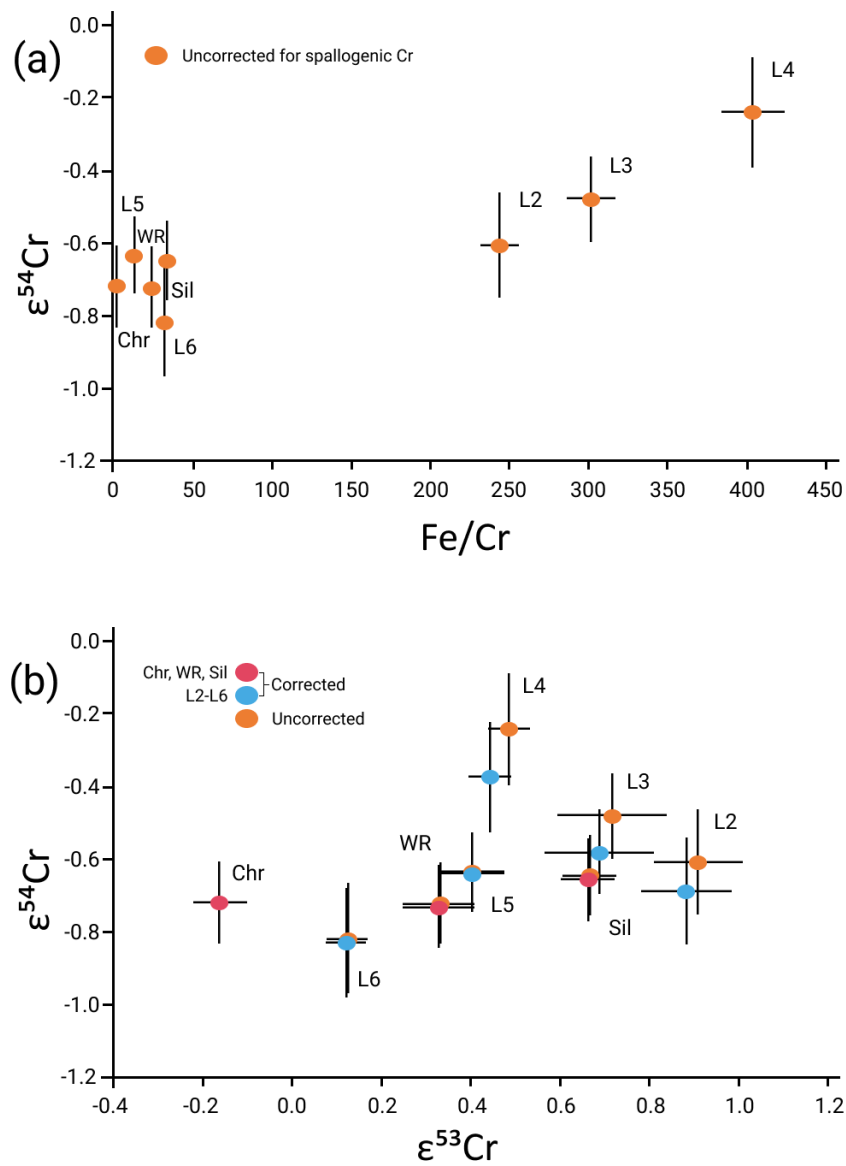


**Figure 3.2:** (a)  $\epsilon^{53}\text{Cr}$  vs.  $\text{Fe/Cr}$  data for EC 002 fractions. Leachates 2, 3 and 4 show a correlation corroborating spallogenic Cr contribution. (b) Spallogenic Cr corrected and uncorrected  $\epsilon^{54}\text{Cr}$  vs.  $\epsilon^{53}\text{Cr}$  data for EC 002 fractions.



### 3.3 Results

The Cr isotopic composition and  $^{55}\text{Mn}/^{52}\text{Cr}$  and Fe/Cr ratios of the EC 002 fractions and reference materials are provided in Table 3.2. The Cr isotopic compositions of the terrestrial reference material OKUM are indistinguishable from typical terrestrial values (Zhu *et al.*, 2021 and references therein) and Cr isotopic compositions of Allende are consistent with literature data (Trinquier *et al.*, 2008b) confirming the analytical accuracy of the Cr isotope data. The  $^{55}\text{Mn}/^{52}\text{Cr}$  ratio ( $= 1.04 \pm 0.05$ ) determined for the whole rock EC 002 agrees with  $^{55}\text{Mn}/^{52}\text{Cr} = 1.09$  (MnO = 0.46 wt. %, Cr<sub>2</sub>O<sub>3</sub> = 0.57 wt. %), determined in Carpenter *et al.* (2021), but is lower than that determined in Barrat *et al.* (2021), who obtained  $^{55}\text{Mn}/^{52}\text{Cr} = 1.51$  (MnO = 0.47 wt. %, Cr<sub>2</sub>O<sub>3</sub> = 0.42 wt. %). The difference in  $^{55}\text{Mn}/^{52}\text{Cr}$  ratio relative to Barrat *et al.* (2021) might be related to mineral scale sample heterogeneity. Due to the larger quantity of EC 002 analyzed in the present study, the  $^{55}\text{Mn}/^{52}\text{Cr}$  ratio ( $= 1.04 \pm 0.05$ ) reported here is the most representative to date. The proportion of Mn and Cr extracted in each sequential digestion step is given in Table 3.1. The Cr isotopic compositions of leachate 1 could not be measured due to the low amount of Cr leached in this step ( $< 0.03$  %, Table 3.1). The Cr isotopic composition of all the fractions are corrected for spallogenic Cr contributions and the measured and corrected ratios are listed in Table 3.2. The absolute variation in Cr isotope composition in all the EC 002 fractions is  $1.07\epsilon$  in  $^{53}\text{Cr}$  and  $0.58\epsilon$  in  $^{54}\text{Cr}$ , which reduces to  $1.04\epsilon$  in  $^{53}\text{Cr}$  and  $0.46\epsilon$  in  $^{54}\text{Cr}$  after correction for spallogenic Cr contribution. The correction for spallogenic Cr contribution appears to be significant in leachates 2, 3 and 4 which is evident in the correlation in the  $\epsilon^{54}\text{Cr}$  vs. Fe/Cr plot (Fig. 3.2a). However, Cr isotopic compositions of leachate 2 remains to be distinct from the Cr isotopic compositions of the other leachates in the  $\epsilon^{53}\text{Cr}$  vs.  $\epsilon^{54}\text{Cr}$  plot (Fig. 3.2b) after correction for spallogenic Cr. In order to obtain an age for EC 002, all the analyzed fractions, whole rock, silicates, chromite and leachates L2-L7, are plotted in an isochron diagram in Fig. 3.3a. The slope of this  $^{53}\text{Mn}$ - $^{53}\text{Cr}$  isochron ( $^{53}\text{Mn}/^{55}\text{Mn} = 4.76 \pm 0.39 \times 10^{-6}$ ) when anchored to the D'Orbigny angrite (Pb-Pb age of  $4563.37 \pm 0.25$  Ma (Brennecka and Wadhwa, 2012) and initial  $^{53}\text{Mn}/^{55}\text{Mn}$  ratio of  $3.24 \pm 0.04 \times 10^{-6}$  (Glavin *et al.*, 2004)), yields an age of  $1.73 \pm 0.96$  Ma after CAI formation (Fig. 3.3a). In addition to the isochron age, a model age of  $2.18^{+1.32}_{-1.06}$  Ma is derived for the chromite fraction relative to the CAI formation age, assuming a chondritic  $^{55}\text{Mn}/^{52}\text{Cr} = 0.74$  of the source reservoir (Zhu *et al.*, 2021), a Solar System initial  $\epsilon^{53}\text{Cr} = -0.30$  (Anand *et al.*, 2021a) and a canonical  $^{53}\text{Mn}/^{55}\text{Mn} = 6.28 \times 10^{-6}$  (Trinquier *et al.*, 2008b) (Fig. 3.2b).

**Table 3.1.** Sequential dissolution procedure and proportion of Mn and Cr leached in each sequential dissolution step for EC 002.

Sequential digestion step	Reagent	Parameters (time/temperature)	Cr %	Mn %
L1	0.5 M CH <sub>3</sub> COOH	0.5 h	0.03	0.17
L2	0.2 M HNO <sub>3</sub>	0.5 h	0.06	0.15
L3	1 M HCl	1 h	0.18	0.28
L4	6 M HCl	48 h	0.27	0.33
L5	conc. HNO <sub>3</sub> + HF (3:1)	48 h, 140 °C	62.31	88.85
L6	conc. HNO <sub>3</sub> + HF (3:1)	70 h, 190 °C	37.15	10.22

**Table 3.2.** <sup>55</sup>Mn/<sup>52</sup>Cr, Fe/Cr and Cr isotopic compositions of EC 002 fractions.

Sample	<sup>55</sup> Mn/ <sup>52</sup> Cr	Fe/Cr	ε <sup>53</sup> Cr ± 2se	ε <sup>53</sup> Cr* ± 2se	ε <sup>54</sup> Cr ± 2se	ε <sup>54</sup> Cr* ± 2se	n
Whole rock	1.04	24.36	0.329 ± 0.080	0.326 ± 0.080	-0.718 ± 0.112	-0.726 ± 0.112	4
Silicates	1.60	34.24	0.667 ± 0.060	0.664 ± 0.060	-0.645 ± 0.112	-0.656 ± 0.112	4
Chromite	0.03	1.27	-0.163 ± 0.060	-0.163 ± 0.060	-0.716 ± 0.112	-0.717 ± 0.112	3
Leachate 1	7.32	239.09	-	-	-	-	-
Leachate 2	2.36	243.29	0.908 ± 0.100	0.882 ± 0.100	-0.607 ± 0.146	-0.686 ± 0.146	4
Leachate 3	1.49	301.93	0.717 ± 0.123	0.685 ± 0.123	-0.478 ± 0.118	-0.577 ± 0.118	5
Leachate 4	1.03	403.95	0.485 ± 0.047	0.442 ± 0.047	-0.240 ± 0.154	-0.372 ± 0.154	3
Leachate 5	1.52	12.32	0.404 ± 0.069	0.402 ± 0.069	-0.634 ± 0.106	-0.638 ± 0.106	3
Leachate 6	0.29	32.44	0.123 ± 0.044	0.120 ± 0.044	-0.817 ± 0.152	-0.827 ± 0.152	4
IAG OKUM <sup>a</sup>	0.60	36.60	0.020 ± 0.065	-	0.083 ± 0.110	-	7
Allende <sup>b</sup>	-	-	0.072 ± 0.066	-	0.881 ± 0.120	-	4

Uncertainties associated with Cr isotopic compositions are reported as 2 s.e. of repeat analyses for each sample, or of NIST SRM 979 terrestrial Cr standard, whichever is larger. n = number of repeat measurements. The reproducibility of <sup>55</sup>Mn/<sup>52</sup>Cr and Fe/Cr ratios is better than 5%. ε<sup>53</sup>Cr\* and ε<sup>54</sup>Cr\* represent the spallogenic Cr corrected data (and propagated uncertainties).

<sup>a</sup>IAG OKUM: Komatiite, Ontario (Certified Reference Materials, International Association of Geoanalysts), Peters and Pettke (2017).

<sup>b</sup>Allende rock standard (Smithsonian standard powder, USNM 3529, Split 18 position 1).

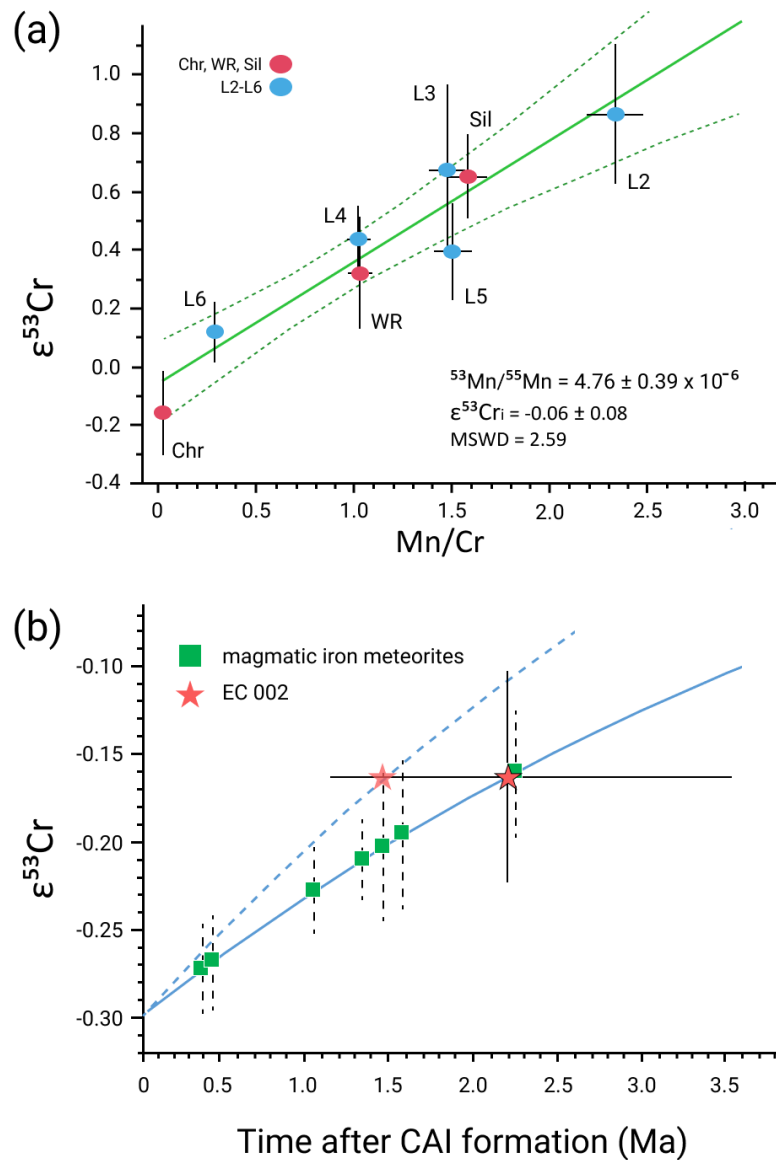


**Figure 3.3.** (a)  $^{53}\text{Mn}$ - $^{53}\text{Cr}$  systematics of EC 002 fractions (Chr: chromite, WR: whole-rock, Sil: Silicates, L2-6: sequential digestion leachates). (b)  $\epsilon^{53}\text{Cr}$  of EC 002 chromite fraction is plotted on a Cr isotope evolution curve corresponding to a chondritic reservoir (solid curve) and a reservoir with EC 002 whole rock-like  $^{55}\text{Mn}/^{52}\text{Cr}$  (dashed curve) through time (see text).  $\epsilon^{53}\text{Cr}$  values of chromite/daubréelite fractions from magmatic iron meteorites are taken from Anand *et al.* (2021a). Error bars represent 2 s.e. uncertainties.

## 3.4 Discussion

### 3.4.1 $^{53}\text{Mn}$ - $^{53}\text{Cr}$ chronology of Erg Chech 002

The  $^{53}\text{Mn}$ - $^{53}\text{Cr}$  isochron age of  $1.73 \pm 0.96$  Ma obtained for EC 002 using its chromite, silicates and whole-rock fractions and sequential digestion leachates is calculated relative to the angrite

D'Orbigny as an anchor. With another commonly used angrite anchor, LEW 86010 (Pb-Pb age of  $4557.5 \pm 0.3$  Ma (Kleine *et al.*, 2012) and initial  $^{53}\text{Mn}/^{55}\text{Mn}$  ratio of  $1.25 \pm 0.07 \times 10^{-6}$  (Lugmair and Shukolyukov, 1998)), the age would be  $2.46 \pm 0.96$  Ma after CAIs i.e., 0.73 Ma younger. However, both ages are analytically unresolvable given the  $\sim 1$  Ma uncertainty associated with the age estimates. A more significant difference in isochron ages based on the choice of anchor is reported in the  $^{26}\text{Al}$ - $^{26}\text{Mg}$  chronometry of EC 002. Fang *et al.* (2022) reported an initial  $^{26}\text{Al}/^{27}\text{Al}$  ratio of  $(8.89 \pm 0.09) \times 10^{-6}$  for an isochron from EC 002 obtained using mineral separates (pyroxenes and plagioclases) and analysed with multi-collector inductively coupled plasma mass spectrometer (MC-ICP-MS). The initial  $^{26}\text{Al}/^{27}\text{Al}$  ratio of  $(8.89 \pm 0.09) \times 10^{-6}$  yields an age of  $0.60 \pm 0.01$  Ma, when D'Orbigny angrite is used as an anchor (Brennecka and Wadhwa, 2012; Schiller *et al.*, 2015) and  $1.80 \pm 0.01$  Ma when anchored to the first-formed refractory solids (CAIs) in the Solar protoplanetary disk that are characterized by a canonical  $^{26}\text{Al}/^{27}\text{Al}$  ratio of  $5.23 \times 10^{-5}$  (Jacobsen *et al.*, 2008). In an earlier study, Barrat *et al.* (2021) analyzed the plagioclase and pyroxene crystals in EC 002 using an ion microprobe and reported an initial  $^{26}\text{Al}/^{27}\text{Al}$  ratio of  $(5.72 \pm 0.07) \times 10^{-6}$ , which translates into an age of  $1.16 \pm 0.01$  Ma when anchored to the D'Orbigny angrite and  $2.26 \pm 0.01$  Ma when anchored to the canonical  $^{26}\text{Al}/^{27}\text{Al}$  ratio derived from CAIs. First, there is a  $\sim 0.5$  Ma discrepancy between the EC 002 initial  $^{26}\text{Al}/^{27}\text{Al}$  ratios reported in Barrat *et al.* (2021) and Fang *et al.* (2022). This has been explained by Fang *et al.* (2022) as a result of the much faster diffusion of Mg in plagioclase than in pyroxene (Van Orman *et al.*, 2014; Zhang *et al.*, 2010) because of which the bulk plagioclase-rich fractions analysed by MC-ICP-MS better represent a closed system for Mg diffusion than the core of the plagioclase crystals analysed using the ion microprobe. Hence, the MC-ICP-MS  $^{26}\text{Al}$ - $^{26}\text{Mg}$  age is closer to the age of crystallization. Second, there is a discrepancy of  $\sim 1$  Ma in  $^{26}\text{Al}$ - $^{26}\text{Mg}$  chronometry of EC 002 between the choice of anchor (CAIs and D'Orbigny angrite). Previous studies have explained the discrepancy between  $^{26}\text{Al}$ - $^{26}\text{Mg}$  ages when anchored to angrites and CAIs by suggesting a lower initial  $^{26}\text{Al}/^{27}\text{Al}$  of the angrite parent body precursor material at the time of CAI formation (e.g., Larsen *et al.*, 2011; Schiller *et al.*, 2015). However, this possible heterogeneity has been questioned by other studies (Wasserburg *et al.*, 2012; Kita *et al.*, 2013). Alternatively, the robustness of  $^{26}\text{Al}$ - $^{26}\text{Mg}$  system in D'Orbigny has been questioned because of the complex petrologic history of this angrite based on its apparent disturbed Sm-Nd systematics (Sanborn *et al.*, 2019; Sanborn *et al.*, 2015). In view of these arguments, the  $^{26}\text{Al}$ - $^{26}\text{Mg}$  crystallization

age of  $1.80 \pm 0.01$  Ma obtained using CAI initial  $^{26}\text{Al}/^{27}\text{Al} = 5.23 \times 10^{-5}$  is used in the rest of the discussion.

Although the use of anchors in short-lived isotope systematics introduces systematic uncertainties due to age shifts, nevertheless, both  $^{53}\text{Mn}$ - $^{53}\text{Cr}$  and  $^{26}\text{Al}$ - $^{26}\text{Mg}$  (when anchored to CAIs) isochron ages are concordant within analytical uncertainties. The  $^{53}\text{Mn}$ - $^{53}\text{Cr}$  and  $^{26}\text{Al}$ - $^{26}\text{Mg}$  (when anchored to CAIs) isochron ages are also in agreement with the model age of  $2.18^{+1.32}_{-1.06}$  Ma after CAIs, determined using EC 002 chromite fraction (Fig. 3.6), which requires estimates for the Solar System initial  $^{53}\text{Mn}$  and  $^{53}\text{Cr}$  abundances and  $^{55}\text{Mn}/^{52}\text{Cr}$  of the source reservoir. The Solar System initial  $\epsilon^{53}\text{Cr} = -0.30$  used in the present study was determined in Anand *et al.* (2021a) by calibrating the  $^{53}\text{Mn}$ - $^{53}\text{Cr}$  core formation ages with the previously determined  $^{182}\text{Hf}$ - $^{182}\text{W}$  ages (Kruijer *et al.*, 2017) of magmatic iron meteorite groups. Moreover,  $^{55}\text{Mn}/^{52}\text{Cr}$  of the EC 002 source reservoir from which the chromite formed is assumed to be chondritic. Although a chondritic  $^{55}\text{Mn}/^{52}\text{Cr}$  is a good estimate for the EC 002 parent body (Barrat *et al.*, 2021), the source reservoir for the EC 002 meteorite is a fractionated product after metal-silicate separation on the parent body and hence, may have an evolved  $^{55}\text{Mn}/^{52}\text{Cr}$  composition. Thus, the chromite model age of  $2.18^{+1.32}_{-1.06}$  Ma after CAIs, determined assuming a chondritic  $^{55}\text{Mn}/^{52}\text{Cr}$  ratio for the source of the chromite in EC 002 provides an upper limit (younger limit). To constrain the lower limit (older limit), the  $^{55}\text{Mn}/^{52}\text{Cr}$  composition of the EC 002 parent body can be assumed to be the whole rock  $^{55}\text{Mn}/^{52}\text{Cr}$  ( $= 1.04 \pm 0.05$ ) composition of EC 002. The chromite model age determined in this case would be  $1.46^{+0.78}_{-0.68}$  Ma after CAIs, which appears to be 0.73 Ma older (Fig. 3.3b), however, still in agreement within uncertainties, given current analytical resolution. In summary, consideration of the full range of the chromite model ages indicates the crystallization of EC 002 between  $1.46^{+0.78}_{-0.68}$  Ma and  $2.18^{+1.32}_{-1.06}$  Ma after CAIs.

Figure 3.6 presents a compilation of  $^{53}\text{Mn}$ - $^{53}\text{Cr}$  and  $^{26}\text{Al}$ - $^{26}\text{Mg}$  chronometry of EC 002. For both the  $^{53}\text{Mn}$ - $^{53}\text{Cr}$  and  $^{26}\text{Al}$ - $^{26}\text{Mg}$  (when anchored to the CAIs) systems, the ages are concordant with the  $^{53}\text{Mn}$ - $^{53}\text{Cr}$  chromite model ages. This provides confidence over the estimates of  $^{53}\text{Mn}$  and  $^{53}\text{Cr}$  abundances and  $^{55}\text{Mn}/^{52}\text{Cr}$  of the source reservoir used for chromite model age determination and indicates rapid cooling of EC 002 on its parent body at around the time of isotopic closures of both  $^{53}\text{Mn}$ - $^{53}\text{Cr}$  and  $^{26}\text{Al}$ - $^{26}\text{Mg}$  systems. The internal isochrons date the crystallization of the parent melt of EC 002 and the two isotopic systems did not re-

equilibrate after initial and near-simultaneous closure. This result confirms the thermal history of EC 002 inferred by Barrat *et al.* (2021) using experimental data. The authors modelled the zoning profile of Mg# across a small xenocryst and estimated the cooling rate to be about 5°C/a between 1,200 and 1,000°C. Furthermore, only cristobalite and tridymite (PO) are observed in EC 002 with a total absence of quartz. Cristobalite transforms to tridymite above 900 °C, but it also transforms to quartz easily. The lack of this transformation to quartz implies rapid cooling at a rate of >0.1 to 1°C/d below 900°C. The initial slow cooling allowed the EC 002 to acquire its medium-grained groundmass texture and later rapid cooling enabled multiple isotopic systems to close within the given resolution. The change in the cooling rate has been explained by an impact that ejected the EC 002 rock from its parent body (Barrat *et al.*, 2021). The rapid cooling around the time of isotopic closures of multiple isotopic systems, no subsequent partial re-equilibration event and insignificant secondary processes that may have disturbed the isotopic systems make EC 002 itself a potential relative time anchor (Sanborn *et al.*, 2019).

### 3.4.2 $\epsilon^{54}\text{Cr}$ - $\Delta^{17}\text{O}$ genealogy of Erg Chech 002

Nucleosynthetic isotope variations of  $^{54}\text{Cr}$  and  $^{17}\text{O}$  are powerful tools that can provide insights into the accretion region of EC 002 parent body (e.g., Clayton and Mayeda, 1996; Greenwood *et al.*, 2012; Shukolyukov and Lugmair, 2006; Trinquier *et al.*, 2007). In addition, these isotopes can be used to deduce an affinity of EC 002 with other achondrites and chondrites. The  $\epsilon^{54}\text{Cr}$  values obtained for EC 002 whole rock and its sequential digestion leachates after correction for spallogenic Cr contribution are within the analytical uncertainties of each other, except for the leachate 4 (which hosts only 0.27% Cr of the WR). This indicates homogeneity of non-radiogenic Cr isotopes in the mineral phases on a larger scale (Table 3.2, Fig. 3.2b). An isotopic equilibrium of  $\epsilon^{54}\text{Cr}$  in mineral phases is expected in EC 002 if they all formed from the same melt since the effects of melting and planetary differentiation generally leads to homogenization of the isotopic signatures within a planetary body (can also be a disequilibrium process, see van Kooten *et al.*, 2017). However, a distinct  $\epsilon^{54}\text{Cr}$  isotopic composition of leachate 4 that represents silicate fraction of the EC 002 (Rotaru *et al.*, 1992) most likely reflects contribution from the olivine and pyroxene xenocrysts present in EC 002 (Barrat *et al.*, 2021). Nevertheless, this contribution from xenocrysts does not affect the isochron and by extension the chronology of the EC 002 (Fig. 3.3a); and hence appears to be

insignificant within uncertainties in the Cr isotopic budget. Alternatively, the high  $^{54}\text{Cr}$  corrected for spallogenic  $^{54}\text{Cr}$  derived from Fe could reflect the fractionation of Fe from Cr during leaching.

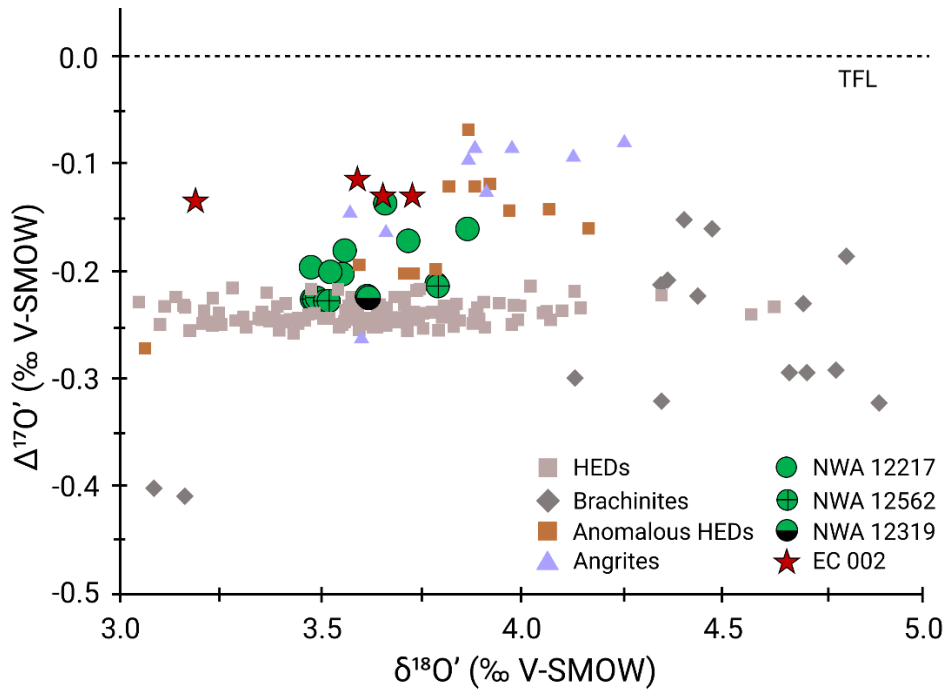


**Figure 3.4.**  $\Delta^{17}\text{O}$  diagram showing EC 002, NWA 12217, 12319, and 12562 in relation to other achondrite groups and anomalous HEDs (Gattacceca *et al.*, 2021; Vaci *et al.*, 2021; Scott *et al.*, 2009; Greenwood *et al.*, 2005, 2012; Zhang *et al.*, 2019). TFL: Terrestrial Fractional Line.

The average  $\varepsilon^{54}\text{Cr}$  of the EC 002 fractions ( $= -0.65 \pm 0.10$ ) confirms its affinity to the ‘non-carbonaceous (NC)’ reservoir (Trinquier *et al.*, 2007, 2009) as speculated in Barrat *et al.* (2021), who determined a non-carbonaceous chondrite-like negative Tm anomaly ( $\text{Tm}/\text{Tm}^* = 0.973$ , where  $\text{Tm}^*$  is the expected Tm concentration for a smooth CI-normalized REE pattern). The  $\mu^{148}\text{Nd}$  value of EC 002 reported in Fang *et al.* (2022) is also distinctly lower than any CC meteorite and falls within the NC region. The O isotope compositions of EC 002 plot distinctly away from other andesitic and trachyandesitic achondrites, GRA 06128, GRA 016129, ALM-A and NWA 11119, and lie between the fields for the majority of eucrites and Angrites (Gattacceca *et al.*, 2021; Fig. 3.4). The O isotopic compositions are also in close vicinity to anomalous eucrites, Bunburra Rockhole, Emmaville, Asuka 881394 and EET 92023 and ungrouped achondrites, NWA 12217, NWA 12562 and NWA 12319 (Fig. 3.4). Interestingly, one of the O isotope data points of EC 002 is indistinguishable from NWA 12217. The coupled

$\Delta^{17}\text{O}$  and  $\varepsilon^{54}\text{Cr}$  systematics of EC 002 could bring more clarity to this genealogical observation made solely based on O isotope compositions. In  $\varepsilon^{54}\text{Cr}$ - $\Delta^{17}\text{O}$  space, EC 002 appears to be distinct from the field of angrites, and normal and anomalous HEDs but a genetic link with meteorites NWA 12217 and EET 92023 is possible. The  $\varepsilon^{54}\text{Cr}$  and  $\Delta^{17}\text{O}$  isotope composition of EC 002 overlaps with both NWA 12217 and EET 92023 (Fig. 3.5). As reported in Gattacceca *et al.* (2021), the unbrecciated anomalous eucrite ET 92023 is mineralogically quite different from EC002 in several aspects, most notably the prevalence of highly sodic plagioclase and lower FeO/MnO ratios in pyroxenes. The ungrouped achondrites NWA 12217, NWA 12562 and, NWA 12319 are reported to be sourced from a fully differentiated parent body that is likely to be a V-type asteroid or vestoid (Vaci *et al.*, 2021). The heavier  $\Delta^{17}\text{O}$  composition of NWA 12217 compared to NWA 12562 and NWA 12319 and main group normal HEDs is explained as having been influenced by mixing with an ordinary chondrite component (Vaci *et al.*, 2021), possibly by an impact event. If EC 002 is sourced from the same vestoid reservoir as these achondrites, then the  $\Delta^{17}\text{O}$  composition of EC 002, which is similar to that of NWA 12217, would also require addition of a higher  $\Delta^{17}\text{O}$  and  $\varepsilon^{54}\text{Cr}$  component to form EC 002 (Fig. 3.5). In the case of EET 92023, admixing of an even higher  $\varepsilon^{54}\text{Cr}$  component would be required if the sample originally formed on Vesta. However, Yamaguchi *et al.*, (2017) argued that a significant amount of kamacite, taenite and platinum group elements (PGEs) in EET 92023, which are uncommon in unbrecciated crystalline eucrites, indicates incorporation of material most likely from an iron meteorite rather than a chondrite material. The dunite and lherzolite cumulates, NWA 12217, NWA 12562 and NWA 12319, characterize an olivine-rich mantle from a vestoid body that experienced core formation and silicate differentiation and may explain the low HSE abundances and oxygen fugacity required for the composition of EC 002 (Nicklas *et al.*, 2021). Alternatively, if EC 002 did not originate from the same vestoid parent body, it could have formed on a different parent body that accreted from material sourced from an overlapping feeding zone in the protoplanetary disk. Chronologically, the first eucrite melts formed approximately 3 to 5 Ma after CAIs (i.e.,  $\sim 1\text{--}3$  Ma after EC 002 crystallisation) and peaked even later at about 11 Ma after CAI formation (Zhou *et al.*, 2013; Roszjar *et al.*, 2016). Thus, if EC 002 formed on a vestoid, the parent body must have accreted and differentiated in the first few million years of the Solar System. Early accretion and differentiation of the EC 002 parent body are consistent with a modelled accretion age for Vesta of 1.50 to 1.75 Ma after CAI (Mitchell *et al.*, 2021). The early ejection of EC 002, as observed in its cooling history,



may have prevented it from destruction by the basaltic volcanism that occurred later on its parent body.

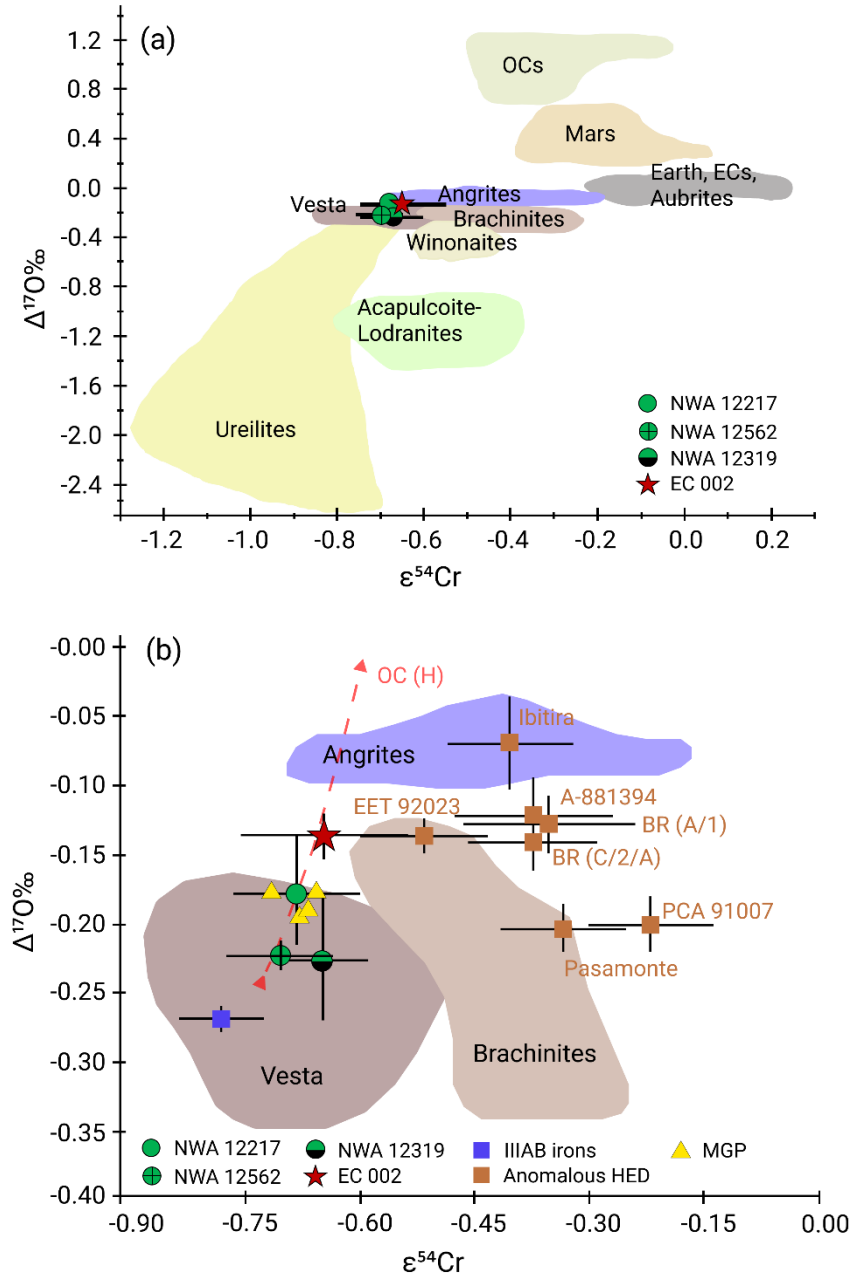


**Figure 3.5.** (a)  $\Delta^{17}\text{O}$ - $\epsilon^{54}\text{Cr}$  diagram showing EC 002 with other achondrite and chondrite groups within ‘non-carbonaceous (NC)’ reservoir (OCs: ordinary chondrites, ECs: enstatite chondrites). Error bars for EC 002 represent 2 s.e. Literature data are from Sanborn *et al.* (2019) and references therein. (b)  $\Delta^{17}\text{O}$ - $\epsilon^{54}\text{Cr}$  diagram showing EC 002 in comparison with brachinites, Angrites, main group pallasites, IIIAB iron meteorites, normal and anomalous HEDs and NWA 12217, 12319, and 12562 ultramafic achondrites (Vaci *et al.*, 2021; Anand *et al.*, 2021a; Dey *et al.*, 2022). The dashed line represents mixing between normal HEDs with H ordinary chondrites.

The crustal material, EC 002 and EET 92023, and mantle-derived samples, NWA 12217, NWA 12562 and NWA 12319, are difficult to genetically link to the existing collection of magmatic iron meteorite groups that represent iron cores of differentiated planetesimals. This is because of the rare occurrences of mineral phases such as oxides and silicates in iron meteorites that could be used for O and Cr isotope analyses. The IIIAB iron meteorite group has an O-isotopic composition close to that of the HEDs (Clayton and Mayeda, 1996). Figure 3.5 shows that in  $\epsilon^{54}\text{Cr}-\Delta^{17}\text{O}$  space, chromite fractions from IIIAB iron, Cape York lie in the HED field but not in the vicinity of EC 002 (Franchi *et al.* 2013; Anand *et al.* 2022). Magmatic iron meteorite groups such as IVA, IIAB and IIG also plot distinctly away from EC 002, NWA 12217 as well as normal HEDs (Anand *et al.* 2021c, 2022). Apart from the magmatic iron meteorites, Dey *et al.* (2022) have reported overlapping  $\epsilon^{54}\text{Cr}-\Delta^{17}\text{O}$  compositions of NWA 12217 and the main group pallasites Imilac, Hambleton and Brenham and hence these sample may also share the same heritage as EC 002 (Fig. 3.5). However, isotopic differences between metal and silicates in pallasites are also reported that imply that the silicate and metal portions of these meteorites may have distinct isotopic reservoirs (Windmill *et al.* 2022), possibly due to late accretion after core formation.

### 3.5 Conclusions and Outlook

Figure 3.6 provides a compilation of chronological data obtained for EC 002 (present study and Barrat *et al.* 2021) and the three largest magmatic iron meteorite groups, IIAB, IIIAB and IVA, within the NC reservoir (Kruijer *et al.* 2017; Anand *et al.*, 2021a). EC 002 represents the oldest magmatic rock dated so far, and it is also the only silicate material with a formation age contemporaneous with the core-mantle differentiation in the oldest planetesimals of the Solar System. EC 002 originated from the primitive igneous crust of an early accreted and differentiated planetesimal, the mantle of which may be represented by the ultramafic achondrites NWA 12217, NWA 12562 and NWA 12319 and the core represents some undiscovered magmatic iron meteorite group. Thus, the enigmatic origin of iron meteorites remains unresolved as EC 002, which is more like differentiated crust does not match known iron meteorite groups that were once cores and the silicate part belonging to these cores is still to be discovered.

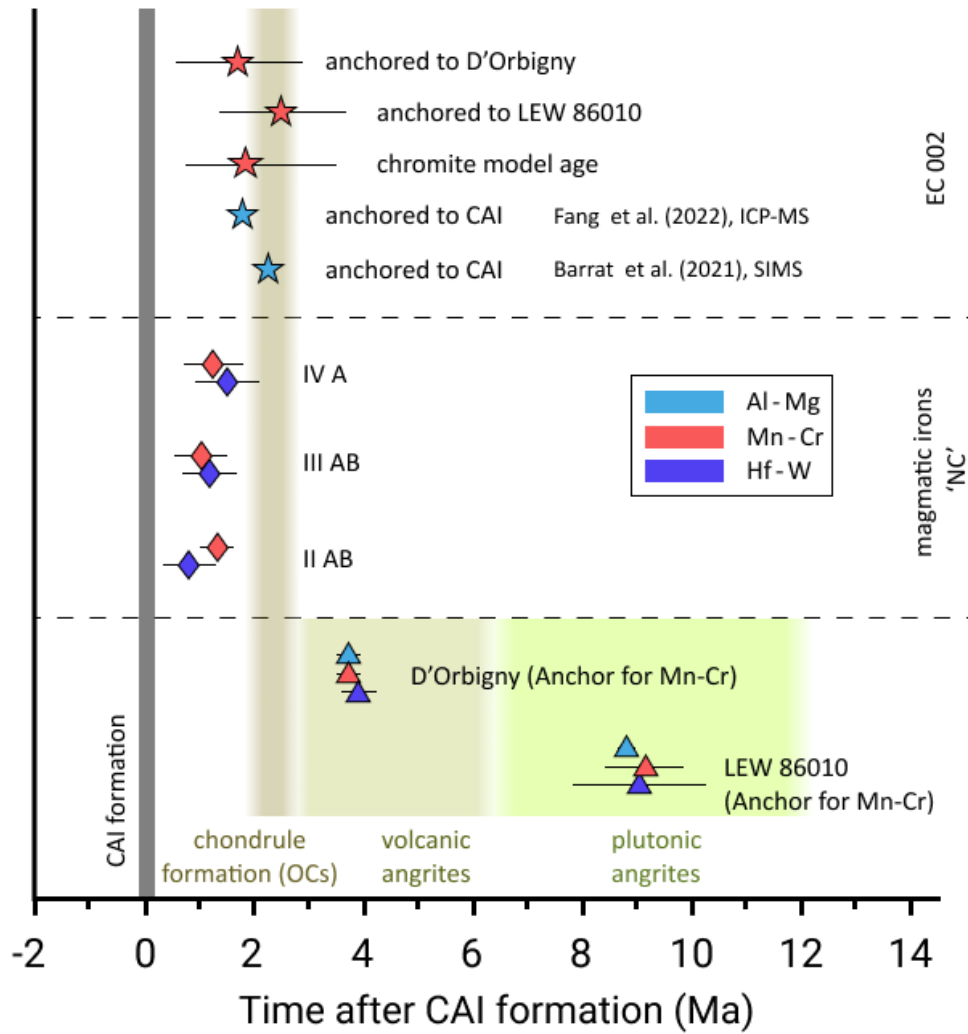


**Figure 3.6.** Compilation of chronological data for EC 002, angrites and magmatic iron meteorites. CAI formation age: Amelin *et al.*, 2010, Angrite ages: Zhu *et al.* (2019) and references therein, Iron meteorite ages: Anand *et al.* (2021a), Kruijer *et al.* (2017), EC 002 Al-Mg ages: Fang *et al.* (2022), Barrat *et al.* (2021), chondrule formation interval (OCs): Pape *et al.* (2019), Siron *et al.* (2022).

The EC 002 crystallization age and the core formation ages in the magmatic iron meteorite parent bodies either predate or are at the earlier side of the chondrule formation interval defined by the  $^{26}\text{Al}$ - $^{26}\text{Mg}$  studies of chondrules in unequilibrated ordinary chondrites (e.g., Pape *et al.* 2019; Siron *et al.*, 2022). For comparison, the second oldest felsic igneous rock, NWA 11119 (Srinivasan *et al.* 2018), previously constrained the silica-rich volcanism in the early Solar System within the first 2.5-3.5 million years of the Solar System history which is after the peak of the chondrule formation interval (e.g., Pape *et al.* 2019; Siron *et al.*, 2022). The granitoids and andesitic fragments found within two chondrite regolith breccias Adzhi-Bogdo and Study

Butte also yielded formation ages of at least 3.8 Ma after CAIs and hence, after the chondrule formation interval as well as chondrite parent body accretion (Sokol *et al.*, 2017). The EC 002 crystallization age and core formation ages in magmatic iron meteorite parent bodies predating the chondrule formation interval are in line with the argument that chondrule formation may not necessarily be an intermediate step on the way from dust to planets and early formed planetesimals may have played an active role in chondrule formation (e.g., Anand *et al.*, 2021a, b).

Chondrule formation models that link early formed planets to chondrule formation processes include collisions of planets or bow shocks caused by migrating planetesimals or early formed planets (Connolly and Jones, 2016 and references therein). Chondrule formation due to planetesimal bow shock mechanism involves early formed planetesimals (Mann *et al.*, 2016), and large planetesimals, with a diameter of at least ~1000 km. Other mechanisms that can explain chondrule formation by planetesimal collision could be impact splashes during planetesimal recycling (Lichtenberg *et al.*, 2018) and/or chondrule formation as a result of inefficient pairwise accretion, when molten or partly molten planetesimals ~30-100 km diameter, similar in size, collided at velocities similar to their two-body escape velocity ~100 m/s (Asphaug *et al.*, 2011). Since, EC 002 sample originates from a highly differentiated material, if such material was involved in chondrule formation by collisions, then it would have been hard to mix the differentiated material from metal core to silicate mantle to differentiated crust in such a way as to obtain chondritic abundances of highly siderophile and also highly incompatible elements in chondrites. Nevertheless, an experimental study by Faure (2020) showed that early silica crust formation (before complete differentiation) in planetesimals by metastable silica-rich liquid immiscibility or cristobalite crystallization can explain the possible origin of silica-rich chondrules. In a recent study, Sturtz *et al.* (2022) proposed a model of planetesimals formation and evolution for the parent bodies like that of EC 002. The authors showed that a protracted and continuous accretion of primitive chondritic material over a magma ocean generated due to early accretion of the parent body can lead to the preservation of a few km thick chondritic crust. During accretion of this material, the heat released by the radioactive decay of extant  $^{26}\text{Al}$  can induce partial melting beneath the chondritic crust leading to the production of rocks such as EC 002 within the first 1-2 Myr of the Solar System.

## **Acknowledgements**

This study was partially funded by the ‘Swiss Government Excellence Scholarship (2018.0371)’. We acknowledge funding within the framework of the NCCR PlanetS supported by the Swiss National Science Foundation grants no. 51NF40 182901 and 51NF40 205606. Dr. Harry Becker and Smithsonian Institution are thanked for providing Allende powder samples. Lorenz Gfeller from the Institute of Geography, University of Bern, is thanked for assistance with the ICP-MS analysis of the samples. We thank Dr. Gopalan Srinivasan for editorial handling and Dr. Elishevah van Kooten and an anonymous reviewer for their constructive comments that helped to improve the manuscript.

## References

- Amelin, Y., Kaltenbach, A., Iizuka, T., Stirling, C. H., Ireland, T. R., Petaev, M., Jacobsen, S.B. (2010) U–Pb chronology of the Solar System's oldest solids with variable  $^{238}\text{U}/^{235}\text{U}$ . *Earth and Planetary Science Letters* 300, 343–350.
- Anand, A., Pape, J., Wille, M., Mezger, K., Hofmann, B. (2021a) Early differentiation of magmatic iron meteorite parent bodies from Mn–Cr chronometry. *Geochemical Perspectives Letters* 20, 6–10.
- Anand, A., Pape, J., Wille, M., Mezger, K. (2021b) Chronological constraints on the thermal evolution of ordinary chondrite parent bodies from the  $^{53}\text{Mn}$ – $^{53}\text{Cr}$  system. *Geochimica et Cosmochimica Acta* 307, 281–301.
- Anand, A., Pape, J., Mezger, K. and Hofmann, B. (2021c). Cr and O Isotopes link IVA irons and LL chondrites. *LPI Contributions* 2609, p.6154.
- Anand, A., Kruttasch, P. M., Mezger, K., Windmill, R., Hofmann, B.A., Greenwood, R.C., Leya, I. (2022) IIAB and IIG iron meteorites originated from a single parent body. *Lunar and Planetary Science Conference*, p.1891.
- Asphaug, E., Jutzi, M., Movshovitz, N. (2011) Chondrule formation during planetesimal accretion. *Earth and Planetary Science Letters* 308, 369–379.
- Barrat, J. A., Chaussidon, M., Yamaguchi, A., Beck, P., Villeneuve, J., Byrne, D. J., Bradley, M. W., Marty, B. (2021) A 4,565-My-old andesite from an extinct chondritic protoplanet. *Proceedings of the National Academy of Sciences* 118(11).
- Birck J. L., Alle'gre C. J. (1985) Isotopes produced by galactic cosmic rays in iron meteorites. In *Isotopic Ratios in the Solar System. Cepadues-Editions* 21–25.
- Bischoff, A., Horstmann, M., Barrat, J. A., Chaussidon, M., Pack, A., Herwartz, D., Ward, D., Vollmer, C., Decker, S. (2014) Trachyandesitic volcanism in the early Solar System. *Proceedings of the National Academy of Sciences*, 111(35), 12689–12692.

Brennecka, G. A., Wadhwa, M. (2012) Uranium isotope compositions of the basaltic angrite meteorites and the chronological implications for the early Solar System. *Proceedings of the National Academy of Sciences* 109(24), 9299–9303.

Carpenter, P. K., Irving, A. J., Richter, M., Lapen, T. J., Tepper, J. H. (2021) Mineralogy and Bulk Elemental Composition of Ungrouped Relatively Sodic Gabbroic Achondrite Erg Chech 002: An Ancient Planetary Crustal Sample? *Lunar and Planetary Science Conference* 2548, p.2205.

Clayton, R. N., Mayeda, T. K. (1996) Oxygen isotope studies of achondrites. *Geochimica et Cosmochimica Acta*, 60(11), 1999-2017.

Connolly, H. C., Jones, R. H. (2016) Chondrules: The canonical and noncanonical views. *Journal of Geophysical Research: Planets*, 121(10), 1885-1899.

Dey, S., Yin, Q. Z., (2022) Diversity of pallasites in the early solar system. *Lunar and Planetary Science Conference*, p.2428.

Fang, L., Frossard, P., Boyet, M., Bouvier, A., Barrat, J. A., Chaussidon, M., Moynier, F. (2022) Half-life and initial Solar System abundance of  $^{146}\text{Sm}$  determined from the oldest andesitic meteorite. *Proceedings of the National Academy of Sciences* 119(12).

Faure, F. (2020) Early silica crust formation in planetesimals by metastable silica-rich liquid immiscibility or cristobalite crystallisation: the possible origin of silica-rich chondrules. *Scientific reports*, 10(1), 1-7.

Franchi, I. A., Greenwood, R. C. and Scott, E. R. D. (2013) The IIIAB-pallasite relationship revisited: the oxygen isotope perspective. *Meteoritics and Planetary Science Supplement*, 76, p.5326.

Gattacceca J., McCubbin F. M., Bouvier A., Grossman J. N. (2021). The Meteoritical Bulletin No. 109. *Meteoritics and Planetary Science*. 55(2) 460-462.

Glavin, D. P., Kubny, A., Jagoutz, E., Lugmair, G. W. (2004) Mn-Cr isotope systematics of the D'Orbigny angrite. *Meteoritics and Planetary Science*, 39(5), 693–700.

Graf, T., Marti, K. (1995) Collisional history of H chondrites. *Journal of Geophysical Research: Planets* 100(E10), 21247-21263.

Greenwood, R. C., Franchi, I. A., Jambon, A., Buchanan, P. C. (2005) Widespread magma oceans on asteroidal bodies in the early Solar System. *Nature* 435(7044), 916–918.

Greenwood, R. C., Franchi, I. A., Gibson, J. M., Benedix, G. K. (2012) Oxygen isotope variation in primitive achondrites: The influence of primordial, asteroidal and terrestrial processes. *Geochimica et Cosmochimica Acta*, 94, 146-163.

Honda, M., Imamura, M. (1971) Half-life of Mn53 *Physical Review C*. 4, 1182–1188.

Jacobsen, B., Yin, Q. Z., Moynier, F., Amelin, Y., Krot, A. N., Nagashima, K., Hutcheon, I. D., Palme, H. (2008)  $^{26}\text{Al}$ – $^{26}\text{Mg}$  and  $^{207}\text{Pb}$ – $^{206}\text{Pb}$  systematics of Allende CAIs: Canonical solar initial  $^{26}\text{Al}/^{27}\text{Al}$  ratio reinstated. *Earth and Planetary Science Letters* 272, 353–364.

Kita, N. T., Yin, Q. Z., MacPherson, G. J., Ushikubo, T., Jacobsen, B., Nagashima, K., Kurahashi, E., Krot, A. N. and Jacobsen, S. B. (2013)  $^{26}\text{Al}$ – $^{26}\text{Mg}$  isotope systematics of the first solids in the early solar system. *Meteoritics and Planetary Science*, 48(8), 1383-1400.

Kleine, T., Hans, U., Irving, A. J., Bourdon, B. (2012) Chronology of the angrite parent body and implications for core formation in protoplanets. *Geochimica et Cosmochimica Acta*, 84, 186-203.

Kruijer, T. S., Burkhardt, C., Budde, G., Kleine, T. (2017) Age of Jupiter inferred from the distinct genetics and formation times of meteorites *Proceedings of the National Academy of Sciences* 114(26), 6712–6716.

Larsen, K. K., Trinquier, A., Paton, C., Schiller, M., Wielandt, D., Ivanova, M. A., Connelly, J. N., Nordlund, Å., Krot, A. N. and Bizzarro, M., 2011. Evidence for magnesium isotope heterogeneity in the solar protoplanetary disk. *The Astrophysical Journal Letters*, 735(2), L37.

Lichtenberg, T., Golabek, G. J., Dullemond, C. P., Schönbächler, M., Gerya, T. V., Meyer, M.R. (2018) Impact splash chondrule formation during planetesimal recycling. *Icarus* 302, 27–43.



Lugmair, G. W., Shukolyukov, A. (1998) Early solar system timescales according to  $^{53}\text{Mn}$ - $^{53}\text{Cr}$  systematics. *Geochimica et Cosmochimica Acta*, 62(16), 2863-2886.

Mann, C. R., Boley, A. C., Morris, M. A. (2016) Planetary embryo bow shocks as a mechanism for chondrule formation. *The Astrophysical Journal* 818(2), 103.

Mitchell, J. T., Tomkins, A. G., Newton, C., Johnson, T. E. (2021) A model for evolving crust on 4 Vesta through combined compositional and thermal modelling. *Earth and Planetary Science Letters*, 571, 117105.

Nicklas, R. W., Day, J. M. D., Gardner-Vandy, K. G., Udry, A. (2021) Multi-stage differentiation history of andesitic achondrite Erg Chech 002. *Lunar and Planetary Science Conference* 2548, p.1074.

Pape, J., Mezger, K., Bouvier, A. S., Baumgartner, L. P. (2019) Time and duration of chondrule formation: Constraints from  $^{26}\text{Al}$ - $^{26}\text{Mg}$  ages of individual chondrules. *Geochimica et Cosmochimica Acta* 244, 416–436.

Peters, D. and Pettke, T. (2017) Evaluation of major to ultra trace element bulk rock chemical analysis of nanoparticulate pressed powder pellets by LA-ICP-MS. *Geostandards and Geoanalytical Research*, 41(1), 5-28.

Roszjar, J., Whitehouse, M. J., Srinivasan, G., Mezger, K., Scherer, E. E., Van Orman, J. A., Bischoff, A. (2016) Prolonged magmatism on 4 Vesta inferred from Hf–W analyses of eucrite zircon. *Earth and Planetary Science Letters*, 452, 216-226.

Rotaru, M., Birck, J. L., Allègre, C. J. (1992). Clues to early solar system history from chromium isotopes in carbonaceous chondrites. *Nature* 358(6386) 465-470.

Sanborn, M. E., Carlson, R. W., Wadhwa, M., 2015.  $^{147,146}\text{Sm}$ – $^{143,142}\text{Nd}$ ,  $^{176}\text{Lu}$ – $^{176}\text{Hf}$ , and  $^{87}\text{Rb}$ – $^{87}\text{Sr}$  systematics in the angrites: Implications for chronology and processes on the angrite parent body. *Geochimica et Cosmochimica Acta*, 171, 80-99.

Sanborn, M. E., Wimpenny, J., Williams, C. D., Yamakawa, A., Amelin, Y., Irving, A. J., Yin, Q. Z. (2019) Carbonaceous achondrites Northwest Africa 6704/6693: Milestones for early Solar System chronology and genealogy. *Geochimica et Cosmochimica Acta* 245, 577–596.

Schiller, M., Connelly, J. N., Glad, A. C., Mikouchi, T., Bizzarro, M. (2015) Early accretion of protoplanets inferred from a reduced inner solar system  $^{26}\text{Al}$  inventory. *Earth and Planetary Science Letters* 420, 45–54.

Scott, E. R., Greenwood, R. C., Franchi, I. A. and Sanders, I. S. (2009) Oxygen isotopic constraints on the origin and parent bodies of eucrites, diogenites, and howardites. *Geochimica et Cosmochimica Acta*, 73(19), 5835-5853.

Schoenberg, R., Merdian, A., Holmden, C., Kleinhanns, I. C., Haßler, K., Wille, M., Reitter, E. (2016) The stable Cr isotopic compositions of chondrites and silicate planetary reservoirs. *Geochimica et Cosmochimica Acta* 183, 14–30.

Shearer, C. K., Burger, P. V., Neal, C., Sharp, Z., Spivak-Birndorf, L., Borg, L., Fernandes, V. A., Papike, J. J., Karner, J., Wadhwa, M., Gaffney, A. (2010) Non-basaltic asteroidal magmatism during the earliest stages of solar system evolution: A view from Antarctic achondrites Graves Nunatak 06128 and 06129. *Geochimica et Cosmochimica Acta*, 74(3), 1172-1199.

Shields, W. R., Murphy, T. J., Catanzaro, E. J., Garner, E. L. (1966) Absolute isotopic abundance ratios and the atomic weight of a reference sample of chromium. *Journal of Research of the National Bureau of Standards Section A: Physics and Chemistry* 70A, 193.

Shukolyukov, A., Lugmair, G. W. (2006) Manganese-chromium isotope systematics of carbonaceous chondrites. *Earth and Planetary Science Letters* 250, 200–213.

Siron, G., Fukuda, K., Kimura, M., Kita, N. T. (2022) High precision  $^{26}\text{Al}$ - $^{26}\text{Mg}$  chronology of chondrules in unequilibrated ordinary chondrites: evidence for restricted formation ages. *Geochimica et Cosmochimica Acta*.

Sokol, A. K., Bischoff, A., Marhas, K. K., Mezger, K., Zinner, E. (2007) Late accretion and lithification of chondritic parent bodies: Mg isotope studies on fragments from primitive chondrites and chondritic breccias. *Meteoritics and Planetary Science*, 42(7-8), 1291-1308.

Srinivasan, P., Dunlap, D. R., Agee, C. B., Wadhwa, M., Coleff, D., Ziegler, K., Zeigler, R., McCubbin, F. M. (2018) Silica-rich volcanism in the early solar system dated at 4.565 Ga. *Nature Communications*, 9(1), 1-8.

Sturtz, C., Limare, A., Chaussidon, M. and Kaminski, É. (2022) Structure of differentiated planetesimals: A chondritic fridge on top of a magma ocean. *Icarus*, 115100.

Trinquier, A., Birck, J., Allegre, C. J. (2007) Widespread  $^{54}\text{Cr}$  Heterogeneity in the Inner Solar System. *The Astrophysical Journal* 655(2), 1179–1185.

Trinquier, A., Birck, J. L., Allègre, C. J. (2008a) High-precision analysis of chromium isotopes in terrestrial and meteorite samples by thermal ionization mass spectrometry. *Journal of Analytical Atomic Spectrometry* 23, 1565–1574.

Trinquier, A., Birck, J. L., Allègre, C. J., Göpel, C., Ulfbeck, D. (2008b)  $^{53}\text{Mn}$ - $^{53}\text{Cr}$  systematics of the early Solar System revisited. *Geochimica et Cosmochimica Acta* 72, 5146–5163.

Trinquier, A., Elliott, T., Ulfbeck, D., Coath, C., Krot, A. N. and Bizzarro, M. (2009) Origin of nucleosynthetic isotope heterogeneity in the solar protoplanetary disk. *Science*, 324(5925), 374-376.

Vaci, Z., Day, J., Paquet, M., Ziegler, K., Yin, Q. Z., Dey, S., Miller, A., Agee, C., Bartoschewitz, R., Pack, A., (2021) Olivine-rich achondrites from Vesta and the missing mantle problem. *Nature Communications*, 12(1), 1-8.

Van Orman, J. A., Cherniak, D. J., Kita, N. T. (2014) Magnesium diffusion in plagioclase: Dependence on composition, and implications for thermal resetting of the  $^{26}\text{Al}$ - $^{26}\text{Mg}$  early solar system chronometer. *Earth and Planetary Science Letters*, 385, 79-88.

Vermeesch, P. (2018) IsoplotR: A free and open toolbox for geochronology. *Geoscience Frontiers* 9(5), 1479–1493.

Villeneuve, J., Chaussidon, M., Libourel, G. (2009) Homogeneous distribution of  $^{26}\text{Al}$  in the Solar System from the Mg isotopic composition of chondrules. *Science* 325, 985–988.

Warren, P. H. (2011) Stable-isotopic anomalies and the accretionary assemblage of the Earth and Mars: A subordinate role for carbonaceous chondrites. *Earth and Planetary Science Letters*, 311(1-2), 93-100.

Wasserburg, G. J., Wimpenny, J. and Yin, Q. Z. (2012) Mg isotopic heterogeneity, Al-Mg isochrons, and canonical  $^{26}\text{Al}/^{27}\text{Al}$  in the early solar system. *Meteoritics and Planetary Science*, 47(12), 1980-1997.

Wasson, J. T. (2013) Vesta and extensively melted asteroids: Why HED meteorites are probably not from Vesta. *Earth and Planetary Science Letters* 381, 138–146.

Windmill, R. J., Franchi, I. A., Hellmann, J. L., Schneider, J. M., Spitzer, F., Kleine, T., Greenwood, R. C., Anand, M. (2022) Isotopic evidence for pallasite formation by impact mixing of olivine and metal during the first 10 million years of the Solar System. *PNAS Nexus*

Yamaguchi, A., Shirai, N., Okamoto, C., Ebihara, M. (2017) Petrogenesis of the EET 92023 achondrite and implications for early impact events. *Meteoritics and Planetary Science*, 52(4), 709-721.

Yamakawa, A., Yamashita, K., Makishima, A., Nakamura, E. (2010) Chromium isotope systematics of achondrites: Chronology and isotopic heterogeneity of the inner solar system bodies. *Astrophysical Journal* 720(1), 150–154.

Zhang, C., Miao, B., He, H. (2019) Oxygen isotopes in HED meteorites and their constraints on parent asteroids. *Planetary and Space Science*, 168, 83-94.

Zhang, X., Ganguly, J., Ito, M. (2010) Ca–Mg diffusion in diopside: tracer and chemical inter-diffusion coefficients. *Contributions to Mineralogy and Petrology*, 159(2), 175-186.

Zhou, Q., Yin, Q. Z., Young, E. D., Li, X. H., Wu, F. Y., Li, Q. L., Liu, Y., Tang, G. Q., (2013). SIMS Pb–Pb and U–Pb age determination of eucrite zircons at < 5  $\mu\text{m}$  scale and the first 50 Ma of the thermal history of Vesta. *Geochimica et Cosmochimica Acta* 110, 152-175.

Zhu, K., Moynier, F., Schiller, M., Alexander, C. M. O., Davidson, J., Schrader, D. L., van Kooten, E., Bizzarro, M. (2021) Chromium isotopic insights into the origin of chondrite parent

bodies and the early terrestrial volatile depletion *Geochimica et Cosmochimica Acta* 301, 158-186.

Zhu, K., Moynier, F., Wielandt, D., Larsen, K. K., Barrat, J. A., Bizzarro, M. (2019) Timing and origin of the angrite parent body inferred from Cr isotopes. *The Astrophysical Journal* 877, L13.

## 4

# Chromium isotopes identify the extraterrestrial component in impactites from Dhala Impact Structure, India

**Manuscript under review in Meteoritics and Planetary Science**

Anand, A., Singh, A. K., Mezger, K., and Pati, J. K.

## Abstract

The Dhala structure in north-central India is a confirmed complex impact structure of the Paleoproterozoic age. The presence of an extraterrestrial component in the impactites from the Dhala structure was recognised by geochemical analyses of highly siderophile elements and Os isotopic compositions, however, the impactor type was unidentified. The present study uses Cr isotopes to identify the type of impactor involved in the formation of the Dhala structure. Unlike siderophile element compositions and their inter-element ratios that may get compromised due to the extreme energy generated during an impact, Cr isotopes retain the distinct composition of the impactor. The distinct  $\epsilon^{54}\text{Cr}$  value of  $-0.31 \pm 0.09$  of a Dhala impact melt breccia (sample D6-57), indicates the inheritance from the impactor originating from the non-carbonaceous reservoir, i.e., the inner Solar System. Together with the Os isotope composition of the sample, the impactor is constrained to be of ureilites or acapulcoite achondrite type. Binary mixing calculations using Cr isotopes indicate a contamination of the target rock by ~1.2 wt% of material from a ureilite or 2-3 wt% from an acapulcoite-like impactor. Together with the previously identified impactors that formed El'gygytgyn, Zhamanshin and Lonar impact structures, the Cr isotopic compositions of the Dhala impactites argue for a much more diverse source of the objects that collided with the Earth over its geological history than has been supposed previously.

## 4.1 Introduction

Like all rocky bodies of the Solar System, the surface of the Earth has also been modified by extraterrestrial (asteroidal or cometary) impacts, the frequency of which has changed over time (e.g., Zellner, 2017; Mazrouei *et al.*, 2019). These impactors have also influenced the present-day chemical makeup of the Earth. Some small- and large-scale impacts throughout Earth's geological history are evident in the form of variably sized craters, layers of impact ejecta (tektites or spherules) and shock deformation features on its surface (French and Koeberl, 2010). Due to the presence of an atmosphere on Earth and its ongoing geological activities, most evidence of meteorite impacts is erased over time, but their chemical contributions to the Earth may still be significant (e.g., Fegley *et al.* 1986; Parkos *et al.* 2018). Of special significance is the origin of volatile components, particularly water, to the Earth, as the early Earth accreted most likely as a dry rocky body (e.g., Wänke 1988). The origin of water and other volatiles on Earth has been attributed to the material that was added to proto-Earth as part of the giant impact and as the late veneer. Compositionally, this later added material must have had some similarity to carbonaceous chondrites (e.g., Mezger *et al.*, 2021). This late addition of volatiles by impacts may have been essential in creating a habitable planet that ultimately enabled the emergence of life on Earth. It is ironic that a similar collision of an extraterrestrial projectile with the Earth has been attributed as the cause of the Cretaceous-Paleogene (K-Pg, formerly K-T) mass extinction about ~65.5 million years ago (Alroy, 2008). It is a chemical signature, i.e., the anomalously high abundance of Ir and other platinum group elements (PGEs) in the K-Pg boundary clay and impact ejecta (spherules, shocked minerals etc.) deposits that led to the discovery of the ~180 to 200-km-diameter Chicxulub impact structure on the Yucatan Peninsula, Mexico (Alvarez *et al.*, 1982; Smit and Klaver, 1981; Hildebrand *et al.*, 1991).

There are ca. 208 impact structures on the Earth, each confirmed by the presence of mesoscopic (shatter cones) and/or microscopic (e.g., planar deformation features (PDFs), planar fractures, feather features, diaplectic glasses, etc.) unambiguous evidence of shock metamorphism, ultrahigh-pressure mineral polymorphs (e.g., coesite, stishovite), and/or the chemical traces of extraterrestrial projectile within the impactites (Magna *et al.*, 2017; Schmieder and Kring, 2020). However, the identification of the projectile is limited to only a very few of them (see the review by Kenkmann 2021). The characterization of the projectile



component in impactites could help in constraining the source and composition of the impactors and better comprehend the chemical evolution of the Earth. Apart from tracing the origin and aftermath of collisions, the identification of projectile types for impacts is also crucial since many of the impact structures have been identified as the host of resources of economic significance (Grieve and Masaitis, 1994). However, tracing and identifying an extraterrestrial impactor is a challenging task since the extreme energy released during an impact event almost completely melts and/or evaporates the impactor. Nevertheless, commonly impactites such as impact melt breccia, diaplectic glasses, and impact spherules incorporate trace amounts ( $\leq 1$  wt%) of projectile components that can be characterized due to their distinct geochemical signature relative to the local or average crustal abundances (e.g., Koeberl, 1998; Koeberl et al., 2007). Most of the conventional methods of detecting and identifying the projectiles are based on recognizing the concentrations of siderophile elements including the PGEs, since meteorites (chondritic or achondritic) have several orders of magnitude higher concentrations of these elements than the target rocks in the upper continental crust (e.g., French and Koeberl, 2010; Koeberl *et al.*, 2012). However, these methods assume that the elemental abundances of siderophile/PGE elements are not significantly fractionated during the impact cratering process which is often not the case. The high thermal energy that is released during an impact event can change the behaviour of the elements and their chemical compounds and in addition, impact-induced heating can also produce hydrothermal systems that may significantly alter the elemental abundances of the impactites (Naumov 2002; Koeberl 2012), thus obscuring their presence. One way of bypassing the impact-related fractionation or hydrothermal alteration of the geochemical signatures is the application of Cr and Os isotopes. Almost all meteorite groups have high Cr concentrations and distinct Cr isotopic compositions due to nucleosynthetic variations and radiogenic ingrowth (Shukolyukov and Lugmair, 1998; Trinquier *et al.*, 2007). The high Cr concentration in most meteorites helps in detecting the extraterrestrial component while the distinct isotopic compositions of meteorite groups can help with the identification of the nature of the projectile. The element Cr shows variations in  $^{53}\text{Cr}$  and  $^{54}\text{Cr}$  among meteorites. The variation in  $^{53}\text{Cr}$  composition is the result of the decay of the now-extinct parent radionuclide  $^{53}\text{Mn}$  (half-life  $T_{1/2} = 3.7\text{Myr}$ ) into stable  $^{53}\text{Cr}$  in early-accreted Solar System matter. Whereas variations in  $^{54}\text{Cr}$  abundances are due to nucleosynthetic heterogeneity (Shukolyukov and Lugmair, 1998; Trinquier *et al.*, 2007) inherited from the solar nebula. The latter is characteristic of different meteorite classes. The precise measurement of Cr isotopic abundances has successfully provided evidence for the

presence of cosmic materials in impactites and has allowed the identification of the impactor (Koeberl *et al.*, 2007; Foriel *et al.*, 2013; Magna *et al.*, 2017; Mougél *et al.*, 2019). Thus, the Cr isotopes are used in this study to evaluate the presence of extraterrestrial materials and their origin in impact products of the 1.7-2.5 Ga old Dhala impact structure, Madhya Pradesh, India.

## 4.2 Geological Setting of the Dhala Impact Structure

The ~11 km diameter Dhala impact structure (N25°17'59.7"; E78°8'3.1") is located on the western part of the Archean Bundelkhand craton, India (Pati *et al.*, 2008a). The crystalline basement of this impact structure is predominantly composed of granitoids (~2.5 Ga) except few minor enclaves of older metasedimentary rocks and tonalite-trondhjemite-granodiorite gneisses. The target lithology and impactites of the Dhala structure are overlain by post-impact sediments of the Dhala Formation and the Kaimur Group of Vindhyan Supergroup, which jointly constitutes a mesa-like central elevated area (CEA) of about 5 km<sup>2</sup> in its central part. Nevertheless, the precise age of the Dhala impact event is not determined so far and is stratigraphically constrained between 2.5 and 1.7 Ga corresponding to the ages of the target granitoids and the post-impact sediments of the Vindhyan Supergroup, respectively (Pati *et al.*, 2010). In the Dhala area, the CEA is surrounded by a ring of >200 monomict breccia outcrops occurring in the outermost annular region of the structure (Singh *et al.*, 2021). These breccia bodies mostly comprise sheared, fractured and extensively brecciated fragments of the target rocks. Towards the inner edge of the breccia ring, at least eight irregular outcrops of impact melt breccia are observed in a semi-circular pattern between the villages of Maniar and Pagra (Pati *et al.*, 2019). These impact melt rocks are largely of granitic composition. The annular region between the CEA and the monomict breccia ring is mainly occupied by sub-horizontal intercalated purplish-brown siltstone and greenish-white sandy siltstone, together with pockets of conglomerate lenses within a clastic matrix (Pati *et al.*, 2008a). Despite the prolonged erosion and multiple post-impact tectono-thermal activities in the region, the impactites of the Dhala structure are relatively well-preserved. The presence of shatter cones, impact-diagnostic microscopic shock metamorphic features, and the chemical signature of extraterrestrial components within impact melt breccia also confirmed/reflected the well-shielded nature of the Dhala structure (Pati *et al.*, 2019 and references therein).

The maiden attempt to identify the impactor component in Dhala impactites was based on concentrations of siderophile elements (Cr and Ir) as well as Os isotopic measurements (Pati *et al.*, 2017). The obtained results were in agreement with the 0.3 wt% contribution of an extraterrestrial meteorite component (chondritic impactor?) as revealed by one impact melt sample from the Dhala structure even though the Ir content was below the detection limit for most of the analyzed samples (Pati *et al.*, 2017). More importantly, the study could not confirm the precise nature and type of the impactor. The present study provides constraints on the origin of the impactor that led to the formation of the Dhala impact structure using Cr isotopes of the impactites.

### 4.3 Samples and Analytical Methods

Rock samples from the Dhala impact structure were collected from the vicinity of the CEA (Pati *et al.*, 2008a, b) as well as from the impact melt breccia outcrops. It comprises impact melt/lithic breccia samples (D6-57, D6-33, MCB-7 and MCB-7/2) and a biotite-granitoid (MCB-10/5) and a gabbro (JAD-8/4) from the target lithologies. The meso- and microscopic characterization, trace element content and Os isotopic composition of the samples were previously published in Pati *et al.* (2017). For the present study, Cr isotope analyses were performed on samples D6-57, MCB-7/2, MCB-7 and JAD-8/4.

A fragment from each sample was crushed into a fine powder with an agate mortar and pestle, homogenized, and dried in an oven at 80°C for about 1 hour. Afterwards, 250-300 mg whole-rock material from each sample as well as geostandard OKUM was weighed in 14 ml Teflon<sup>®</sup> vials and subjected to a concentrated HF-HNO<sub>3</sub> mixture on a hot plate at 90 °C for 24 hours. Subsequently, the samples were dried and completely digested in concentrated inverse aqua regia on a hot plate at 120°C for 72 hours.

The procedure for Cr purification is adopted from Schoenberg *et al.* (2016) and described in Anand *et al.* (2021a, b). Each sample was split into two aliquots corresponding to ~10 µg Cr and loaded onto two separate ion exchange columns. The two aliquots were recombined after the elution of Cr from the column. This ensured a low matrix load on a single chromatographic column (Mougel *et al.*, 2019). Typical recovery of Cr was in excess of 90% for the whole

column chemistry and total chemistry blanks were below 20 ng, which are negligible compared to the amount of Cr processed through the columns.

Purified Cr samples were analysed on a Thermo Scientific TRITON Plus Thermal Ionization Mass Spectrometer at the Institute of Geological Sciences, University of Bern. Two  $\mu\text{g}$  Cr from each sample was loaded onto an outgassed Re filament and measured at a signal intensity between 7 and 10 V ( $10^{-11}$   $\Omega$  resistor) for  $^{52}\text{Cr}$ . Intensities of  $^{50}\text{Cr}$ ,  $^{51}\text{V}$ ,  $^{52}\text{Cr}$ ,  $^{53}\text{Cr}$ ,  $^{54}\text{Cr}$ ,  $^{55}\text{Mn}$  and  $^{56}\text{Fe}$  were measured on the Faraday cups L3, L2, L1, C, H1, H2 and H3, respectively (Trinquier *et al.*, 2008a). The alignment of all Cr peaks (peak scan) was ensured before each measurement and the peak centre was monitored on  $^{52}\text{Cr}$  in the L1 cup. Isobaric interference of  $^{54}\text{Fe}$  on  $^{54}\text{Cr}$  was corrected by monitoring  $^{56}\text{Fe}$ . The isotope  $^{51}\text{V}$  was measured and  $^{49}\text{Ti}$  was monitored to correct for isobaric interferences on  $^{50}\text{Cr}$ . However, both  $^{49}\text{Ti}$  and  $^{51}\text{V}$  intensities remained indistinguishable from background intensities for all samples, verifying the successful separation of V and Ti from Cr during column chromatography. A typical run for a single filament load consisted of 24 blocks with 20 cycles each (integration time = 8.389 s, idle time 3 s), obtained in static acquisition mode. Gain calibration was done once, at the beginning of every analytical session. Amplifiers were rotated and the baseline was measured after every block (baseline = 30 cycles, each of 1.05 s). The Cr standard reference material NIST SRM 979, was used as terrestrial reference material. The  $^{53}\text{Cr}/^{52}\text{Cr}$  and  $^{54}\text{Cr}/^{52}\text{Cr}$  ratios were normalized to  $^{52}\text{Cr}/^{50}\text{Cr} = 19.28323$  (Shields *et al.*, 1966) by applying the exponential mass fractionation law and are reported as  $\epsilon^i\text{Cr}$ , where  $\epsilon^i\text{Cr} = ([^i\text{Cr}/^{52}\text{Cr}]_{\text{sample}} / [^i\text{Cr}/^{52}\text{Cr}]_{\text{NIST SRM 979}} - 1) \times 10^4$  ( $i = 53$  or  $54$ ).

The  $\epsilon^i\text{Cr}$  reported for any one sample represents the mean of 2-4 replicate measurements. The replicate measurements for each sample are used to determine the external precision reported as 2 standard errors (Table 4.1). The isotope compositions ( $\epsilon^{53}\text{Cr}$  and  $\epsilon^{54}\text{Cr}$ ) of each sample are reported relative to the respective mean values of the standard reference material (NIST SRM 979) measured along with the samples in the measurement session (single turret). The external precision (2 standard errors,  $n = 5$ ) for the standard reference material (NIST SRM 979) in each measurement session was  $\sim 0.05$  for  $\epsilon^{53}\text{Cr}$  and  $\sim 0.10$  for  $\epsilon^{54}\text{Cr}$ .

## 4.4 Results

The Cr isotopic compositions of the samples are provided in Table 4.1. The Cr isotopic compositions of a geostandard OKUM and a meteorite sample Allende are consistent with the literature data confirming the analytical accuracy of the Cr isotope measurements (Zhu *et al.*, 2021a and references therein). Figure 4.1 shows a comparison between the Cr isotopic composition of the rock samples from the Dhala impact structure, and a compilation of the Cr isotopic composition of the terrestrial rock samples published in the previous studies (Zhu *et al.*, 2021a and references therein). The Cr isotopic composition of sample JAD-8/4 is indistinguishable from typical terrestrial values. Among the three impact melt/lithic breccia samples, D6-57 plots significantly outside the terrestrial array. This sample shows a resolved negative  $\epsilon^{54}\text{Cr}$  anomaly. The Cr isotopic compositions of the other two impact melt/lithic breccia samples, MCB-7/2 and MCB-7 are within the uncertainties of JAD-8/4 and other terrestrial rock samples.

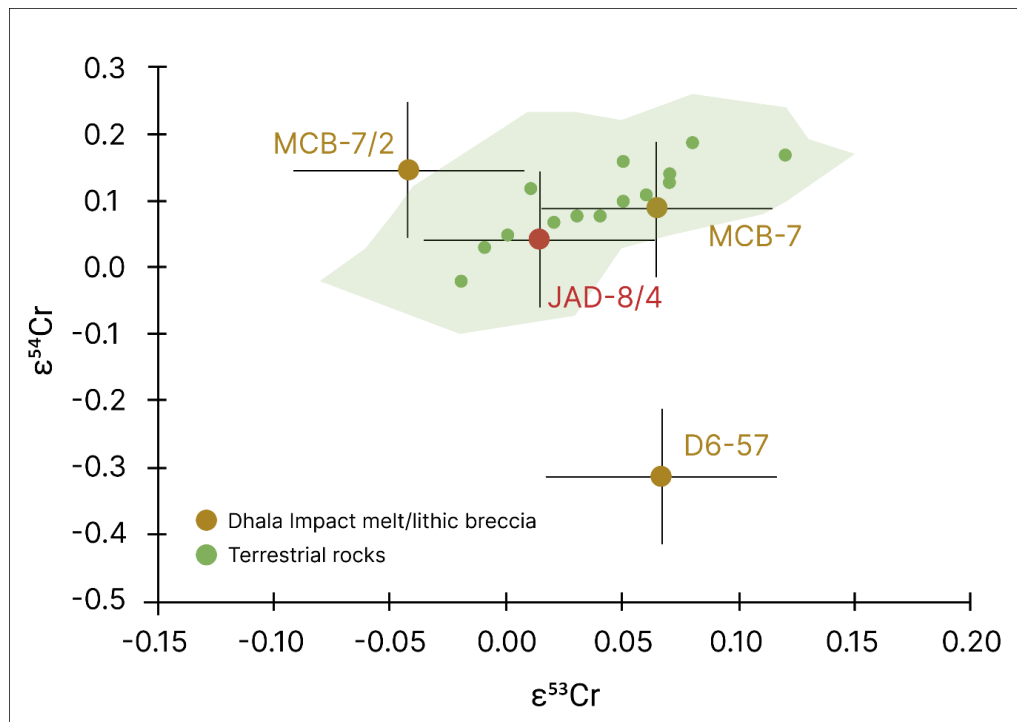


**Figure 4.1.** Comparison between Cr isotopic composition of the rock samples from Dhala impact structure and terrestrial rock samples (Zhu *et al.*, 2021a and references therein). Uncertainties associated with the Cr isotopic compositions of the Dhala rock samples are reported as 2 s.e. of the repeat analyses of the terrestrial Cr standard NIST SRM 979. The shaded region represents an error envelope covering the terrestrial rock Cr isotopic compositions.

**Table 4.1.** Chromium isotope compositions and Cr, Ni, Co abundances (ppm) of the bulk rock samples from Dhala impact structure and meteorites.

Sample	$\epsilon^{53}\text{Cr} \pm 2\text{se}$	$\epsilon^{54}\text{Cr} \pm 2\text{se}$	n	Ref.	[Cr] (ppm)	Ni/Cr	Ni/Co	Cr/Co
<u>Dhala</u>								
JAD-8/4	$0.01 \pm 0.01$	$0.04 \pm 0.05$	2		96.6	0.98	1.63	1.65
MCB-7/2	$-0.04 \pm 0.01$	$0.14 \pm 0.03$	2		84.4	0.69	3.43	4.99
MCB-7	$0.06 \pm 0.03$	$0.09 \pm 0.08$	3		68.6	0.63	2.29	3.65
D6-57	$0.07 \pm 0.04$	$-0.31 \pm 0.09$	4		66.8	1.23	20.55	16.74
D6-33	-	-	-		33.0	0.94	15.12	16.10
MCB-10/5	-	-	-		11.1	1.62	0.74	0.46
<u>Standards</u>								
SRM 979	$0.00 \pm 0.05$	$0.00 \pm 0.10$	7		-	-	-	-
OKUM	$0.03 \pm 0.07$	$0.01 \pm 0.11$	5		287.4	-	-	-
Allende	$0.07 \pm 0.07$	$0.88 \pm 0.12$	4		-	-	-	-
<u>Meteorites</u>								
H	$0.17 \pm 0.01$	$-0.38 \pm 0.02$	13	[1]	~3500	$4.38 \pm 0.42$	22.07	4.54
L	$0.19 \pm 0.04$	$-0.40 \pm 0.04$	4	[1]	~3690	$3.22 \pm 0.19$	22.67	6.40
LL	$0.25 \pm 0.02$	$-0.40 \pm 0.08$	6	[1]	~3680	$2.64 \pm 0.21$	21.19	7.78
EH	$0.17 \pm 0.03$	$0.02 \pm 0.04$	6	[1]	~3300	$5.79 \pm 0.36$	21.04	3.59
EL	$0.16 \pm 0.02$	$0.02 \pm 0.06$	6	[1]	~3030	$4.77 \pm 1.03$	20.18	4.33
CI	$0.28 \pm 0.01$	$1.56 \pm 0.04$	2	[1]	~2650	$3.87 \pm 0.25$	20.87	5.37
CM	$0.17 \pm 0.03$	$0.92 \pm 0.07$	13	[1]	~3050	$4.01 \pm 0.30$	21.27	5.25
CO	$0.11 \pm 0.03$	$0.90 \pm 0.19$	5	[1]	~3520	$3.96 \pm 0.09$	19.73	5.09
CV	$0.11 \pm 0.02$	$0.89 \pm 0.12$	6	[1]	~3480	$3.76 \pm 0.12$	21.26	5.55
Eucrite	$0.69 \pm 0.05$	$-0.72 \pm 0.02$	6	[2]	~2070	~-0.024	~-3.9	~-363
Diogenite	$0.12 \pm 0.13$	$-0.75 \pm 0.05$	3	[2]	~5683.15	$0.004 \pm 0.007$	$1.65 \pm 2.97$	$424.1 \pm 406.6$
Angrite (plutonic)	$0.21 \pm 0.06$	$-0.41 \pm 0.14$	2	[3]	2308.5	~-0.080	~-2.9	~-43
Aubrite	$0.00 \pm 0.02$	$-0.12 \pm 0.04$	1	[4]	~909	~-1.3	~-22	~-57

Winonaite	$0.06 \pm 0.01$	$-0.53 \pm 0.01$	2	[5]	~1963.9	~8.3	~47	~5.7
Acapulcoite	$0.12 \pm 0.04$	$-0.70 \pm 0.08$	1	[6]	3889.3	$3.61 \pm 2.67$	$18.20 \pm 1.84$	$5.36 \pm 3.23$
Lodranite	-	$-0.55 \pm 0.09$	2	[7]	~3345	~4.5	~18	~10
Ureilite	$0.18 \pm 0.04$	$-0.90 \pm 0.04$	20	[8]	4383.3	0.21-0.24	11-12	49
Mesosiderite	$0.11 \pm 0.01$	$-0.72 \pm 0.03$	3	[2]	-	-	-	-

Uncertainties associated with Cr isotopic compositions of the rock samples from the Dhala impact structure are reported as 2 s.e. of repeat analyses (n) for each sample. Uncertainties associated with Cr isotopic compositions of the meteorite groups are reported as 2 s.e. of multiple samples (n) analyzed within each group. Reference for Ni/Cr, Ni/Co, Co/Cr and Cr isotopic composition of Dhala rock samples: Pati *et al.* (2017). References for Cr isotopic composition of meteorites: [1] Zhu *et al.* (2021a) and references therein [2] Trinquier *et al.* (2007, 2008b) [3] Zhu *et al.* (2019) [4] Shallowater, Zhu *et al.* (2021b) [5] average of samples NWA 725 and Villabeto de la Pena clast, Schmitz *et al.*, (2016) [6] Ramlat Fasad 529, Anand *et al.*, (2021a) [7] Li *et al.*, (2018) [8] Zhu *et al.*, (2020) and references therein. References for Ni/Cr, Ni/Co, Co/Cr compositions of meteorites: Chondrites - Tagle and Berlin (2008), Achondrites - Tagle (2004), Patzer *et al.* (2004), Barrat *et al.* (2008). References for [Cr]: Wasson and Kallemeyn (1988), Mittlefehldt (2003), Lodders (2003), Tagle *et al.* (2004), Zhu *et al.* (2019), Patzer *et al.* (2004), Yamakawa *et al.*, (2010).

## 4.5 Discussion

Figure 4.1 shows a comparison between the Cr isotopic composition of the rock samples from the Dhala impact structure and different terrestrial rock samples published in the previous studies (Zhu *et al.*, 2021a and references therein). Although the Cr isotopic composition of the terrestrial rocks is considered constant due to the homogenization effects of melting and planetary differentiation, a slightly positive correlation between  $\epsilon^{53}\text{Cr}$  and  $\epsilon^{54}\text{Cr}$  of the terrestrial samples can be observed (Fig. 4.1). This correlation (slope of  $\sim 2$ ) has been linked to the ‘residual’ variability in terrestrial rock analyses highlighting the natural Cr isotope fractionation due to geological differentiation processes and/or during Cr purification and TIMS analysis that is not fully corrected during analysis using the kinetic law for Cr (Zhu *et al.*, 2021a). The Cr isotopic compositions of the country rocks at the Dhala impact structure represented by sample JAD-8/4 are within uncertainties of the terrestrial Cr isotopic compositions and can be used to identify the impactor contribution in impactites avoiding potential bias on the choice of the terrestrial reference value. The low to moderately-low Cr concentration of the granitoid and gabbroic target rocks ( $\sim 30$  ppm to 100 ppm, Pati *et al.*, 2017) indicates that the country rocks at the Dhala impact structure are sensitive to detecting and identifying contamination from a chondritic meteorite impactor using Cr isotopes due to the high contrast in Cr abundances (Table 4.1) between the impactor and target rock. Relative to the Cr isotopic composition of the sample JAD-8/4, the Cr isotopic composition of the impact melt breccia D6-57 is significantly distinct and shows a resolvable Cr-isotope composition that is not terrestrial but rather represents an isotope value that is at least partially inherited from the impactor. The Cr isotopic composition of the impactite sample D6-57 does not follow the positive correlation between  $\epsilon^{53}\text{Cr}$  and  $\epsilon^{54}\text{Cr}$  observed in the terrestrial samples and hence, its anomalous  $\epsilon^{54}\text{Cr}$  value cannot be the result of the ‘residual’ Cr isotope fractionation during Cr purification and TIMS analysis. Besides D6-57, the Cr isotopic composition of the other two analyzed impact melt/lithic breccia samples, MCB-7/2 and MCB-7, are within the uncertainties of the sample JAD-8/4. This indicates undetectable presence of meteoritic Cr in these two samples. These results are in agreement with the Re and Os abundances and the Os isotopic composition of the samples presented in Pati *et al.* (2017). The authors showed that this system identifies terrestrial values for samples MCB-7/2 and MCB-7, and a distinct Os isotope composition and abundance for sample D6-57.



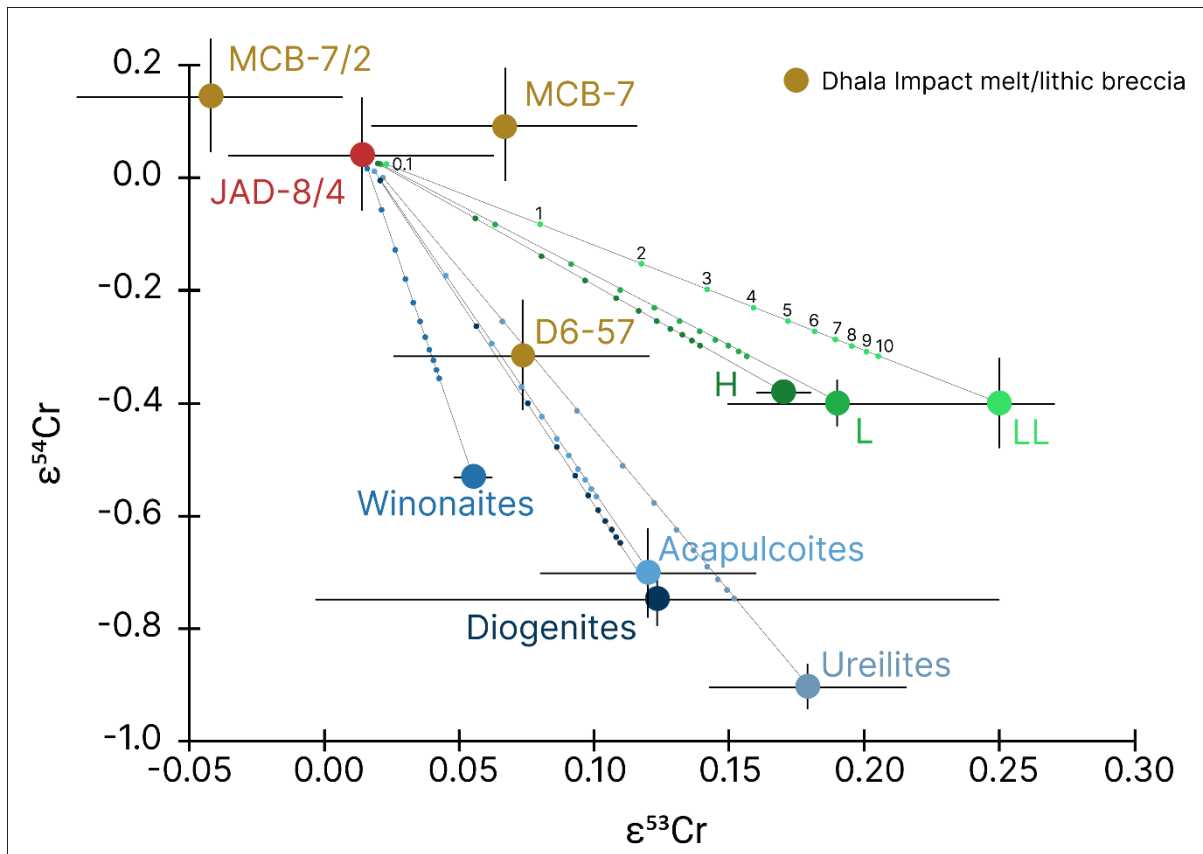


**Figure 4.2.** Comparison between Cr isotopic composition of the rock samples from Dhala impact structure and meteorite groups within ‘non-carbonaceous (NC)’ reservoir (References for the data are in Table 4.1). Solid lines with dots represent binary mixing models between the sample JAD-8/4 as a representative of the Cr isotopic composition of the target rocks and different meteorite groups. Each dot on the mixing line represents the amount of impactor component considered in the admixture (0.1%, 1%, 2%...10%). Confidence envelopes on the mixing lines are removed for the sake of clarity.

The mass-independent isotope variations in  $^{54}\text{Cr}$  have been established as a fundamental genealogical tool exhibiting a dichotomy between the non-carbonaceous (NC) and carbonaceous (CC) reservoirs, which most likely represent material from the inner and outer Solar System, respectively (e.g., Kruijer *et al.*, 2020). The bulk carbonaceous reservoir is characterized by excesses in the neutron-rich isotopes of  $^{54}\text{Cr}$  whereas materials originating in the non-carbonaceous reservoir have depleted  $^{54}\text{Cr}$  signatures with respect to a terrestrial standard (Kleine *et al.*, 2020 and references therein). The depleted  $\epsilon^{54}\text{Cr}$  isotope composition of the Dhala impactite D6-57 is clearly inherited from an impactor originating in the non-carbonaceous reservoir and disqualifies all the carbonaceous reservoir material (carbonaceous chondrites, iron meteorites, ungrouped achondrites etc.) as an impactor for the Dhala impact structure. In the non-carbonaceous reservoir, enstatite chondrites (or enstatite achondrites or

aubrites) have identical  $^{54}\text{Cr}$  isotopic composition to that of the Earth and hence, any contamination from an enstatite chondrite-like impactor would not be manifested as an anomaly in the impactites. Ordinary chondrites have been identified to dominate the percentage of the projectiles forming craters on Earth (McDonald *et al.*, 2001; McDonald 2002; Tagle and Claeys, 2005). They are assumed to have originated from the S-type asteroids which are abundant in the main asteroid belt and among the Near-Earth Objects (NEOs) (Ivezic *et al.*, 2001; Morbidelli *et al.*, 2002; Stuart and Binzel, 2004). However, the Cr isotopic compositions ( $\epsilon^{53}\text{Cr}$  and  $\epsilon^{54}\text{Cr}$ ) of the impactite D6-57 do not match contamination by an ordinary chondrite impactor. Figure 4.2 presents binary mixing models between target rock JAD-8/4 and meteorite groups within the non-carbonaceous reservoir using their Cr abundances and Cr isotopic compositions given in Table 4.1. The first-order mixing calculations indicate that the  $\epsilon^{54}\text{Cr}$  isotopic composition of the impactite D6-57 would require up to 9% mixing with an ordinary chondrite impactor. At most terrestrial impact structures, the impact melt rocks contain meteoritic contamination of  $\sim 1$  wt% or less (e.g., Koeberl, 1998), however, enrichments of several wt% is not completely unlikely (Morokweng and Clearwater East impact structures, McDonald *et al.*, 2001; McDonald, 2002). Nevertheless, up to 9 wt% chondritic contamination in impactite D6-57 should be conspicuous in its trace element geochemistry, particularly the PGEs. Such a high abnormality is not reflected in its Os abundance nor the Os isotope composition (Pati *et al.*, 2017). Moreover, ordinary chondrites have a higher Mn/Cr ratio ( $\text{Mn/Cr} = 0.74$ , Zhu *et al.*, 2021a) than the bulk silicate Earth ( $\text{Mn/Cr} = 0.38$ , Trinquier *et al.*, 2008b) which should be reflected in radiogenic  $\epsilon^{53}\text{Cr}$  of the impactite. However, the impactite sample DS-57 shows contamination from an impactor with a sub-chondritic evolved  $\epsilon^{53}\text{Cr}$  composition. Within the analytical uncertainties of the Cr isotopic compositions of the Dhala impactites and variations observed in the meteorites, an ordinary chondrite-like impactor although unlikely, cannot be completely ruled out as a source of the meteoritic component solely based on Cr isotope results. However, the  $\epsilon^{53}\text{Cr}$  and  $\epsilon^{54}\text{Cr}$  compositions of D6-57 are in much better agreement with an achondritic impactor from the ureilites, diogenites and acapulcoite meteorite groups (Fig. 4.2). The binary mixing calculations indicate that impactite D6-57 is compatible with a contamination of  $\sim 1.2$  wt% from a ureilite, 1.5 wt% from a diogenite or 2-3 wt% from an acapulcoite-like impactor (Fig. 4.2). Although, these estimates of 1-3 wt% addition of an achondritic impactor are higher than the estimated 0.3 wt% extraterrestrial (average chondritic) component from the Cr versus Ir concentrations of the

sample DS-57 reported in Pati *et al.*, (2017), but still more realistic than up to 9 wt% contribution from an ordinary chondritic impactor.

Abundances of siderophile elements (Ni, Cr, Co) and their inter-element ratios (Ni/Cr, Ni/Co, Co/Cr) are proven effective tools for the identification of chondritic impactors (e.g., Koeberl, 2014 or recent review by Day *et al.*, 2016). Strong enrichments of siderophile elements in impact melt rocks can be used to distinguish between a chondritic or iron impactor. But elemental fractionation during impact melting, vaporization, condensation, and crystallization of the melt rocks are known to modify or mask chemical signatures (Mittlefehldt *et al.*, 1992; Evans *et al.*, 1993). The Dhala impactites D6-33 and D6-57 have much higher Ni/Cr, Ni/Co, and Co/Cr compositions than the target rocks JAD-8/4 and MCB-10/5, and impact/lithic breccias MCB-7 and MCB-7/2, collected from the Dhala impact structure (Table 4.1) which indicates interaction with an impactor. However, none of the chondritic or achondritic meteoritic groups can concurrently satisfy the Ni/Cr, Ni/Co as well as Co/Cr element ratios of D6-57 and D6-33 when mixed with the target rock in any proportion. Moreover, Cr isotopic anomalies in impactites reported in the present study do not show any correlation with the Cr concentrations. Such decoupling between Cr isotope compositions and Cr abundances has also been reported in previous studies (Foriel *et al.*, 2013; Mougél *et al.*, 2017, 2019) and is attributed to (1) variability of siderophile element abundances in the target rock as well as their nonuniform redistribution in the impactites and (2) complex chemical processes during the formation of impact-derived products (Mougél *et al.*, 2019). In contrast, Cr isotope genealogical studies to detect and identify the meteoritic components are unaffected by these processes and hence, are a more reliable approach.

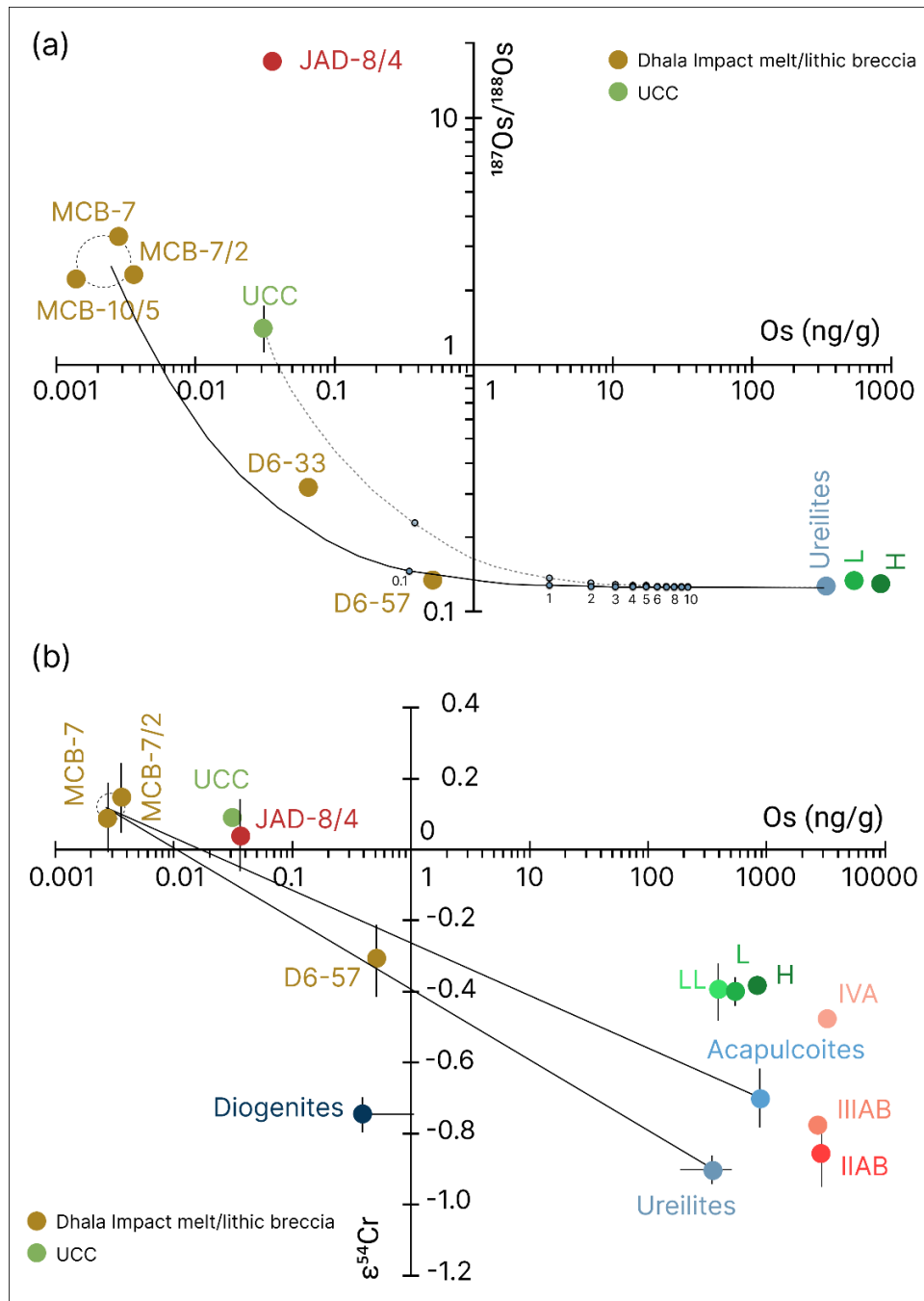


**Figure 4.3.** (a)  $^{187}\text{Os}/^{188}\text{Os}$  versus Os composition of the rock samples from Dhala impact structure and meteorite groups (References for the data are in Table 4.2). The solid line represents binary mixing between ureilites and average of the uncontaminated Dhala rocks, MCB-7/2, MCB-7 and MCB-10/5. The dotted line represents binary mixing between ureilites and average upper continental crust compositions (UCC). Each dot on the mixing lines represents the amount of impactor component considered in the admixture (0.1%, 1%, 2%...10%). (b)  $\epsilon^{54}\text{Cr}$  versus Os composition (plotted on a logarithmic scale for clarity) of the rock samples from the Dhala impact structure and meteorite groups (References for the data are in Tables 4.1 and 4.2). The solid lines represent binary mixing between ureilites and acapulcoites and the average of the uncontaminated Dhala rocks, MCB-7/2 and MCB-7. Confidence envelopes on the mixing lines are omitted for clarity.

The Cr isotopic compositions of the Dhala impactites reported in Table 4.1 correlate with the Os isotopic compositions of the samples presented in Pati *et al.* (2017). These authors noted that the impact melt breccias, D6-57 and D6-33, which are dominated by a granitic target component, have distinctly different  $^{187}\text{Re}/^{188}\text{Os}$  and  $^{187}\text{Os}/^{188}\text{Os}$  ratios that nearly overlap with the chondritic and iron meteorites-like compositions (Chen *et al.* 1998; Horan *et al.* 1998). Figure 4.3(a) presents the Os data of the rock samples from the Dhala impact structure and meteorites groups on a  $^{187}\text{Os}/^{188}\text{Os}$  versus Os abundances plot (references for the data are provided in Table 4.1). The Os abundances and Os isotope compositions of impactites D6-33 and D6-57 plot in between the region constrained by the binary mixing lines drawn between the average of the uncontaminated Dhala rock samples, MCB-7/2, MCB-7, MCB-10/5 or average upper continental crust and the average ureilite compositions (Fig 4.3a). The values for D6-33 and D6-57 are close to  $\leq 0.1$  wt% and  $\sim 0.1$  wt% ureilite contamination, respectively. On the  $\epsilon^{54}\text{Cr}$  versus  $^{187}\text{Os}/^{188}\text{Os}$  plot, Figure 4.3b, impactite D6-57 lies on the mixing line between the average upper continental crust (UCC) compositions and the average ureilite and acapulcoite compositions within uncertainties providing strong support for a ureilite or acapulcoite-like impactor. A differentiated achondrite diogenite that was identified as a probable impactor-type at the Dhala impact structure based solely on the Cr isotope compositions (Fig. 4.2) can be ruled out based on the combined Cr isotopic and Os abundances and its low PGE abundances (Fig. 4.3b).

**Table 4.2.** Os concentration and  $^{187}\text{Os}/^{188}\text{Os}$  isotopic composition of the bulk rock samples from Dhala impact structure, meteorites and upper continental crust.

Sample	[Os] $\pm$ 2se (ng)	$^{187}\text{Os}/^{188}\text{Os} \pm$ 2se
<u>Dhala</u>		
JAD-8/4	$0.0359 \pm 0.0004$	$17.05 \pm 0.19$
MCB-7/2	$0.0036 \pm 0.0001$	$2.33 \pm 0.06$
MCB-7	$0.0028 \pm 0.0001$	$3.31 \pm 0.09$
D6-57	$0.5090 \pm 0.0064$	$0.103 \pm 0.002$
D6-33	$0.0654 \pm 0.0009$	$0.317 \pm 0.006$
MCB-10/5	$0.0014 \pm 0.0001$	$2.228 \pm 0.181$
<u>UCC</u>	0.0310	$1.4 \pm 0.3$
<u>Meteorites</u>		
CC	$612.40 \pm 71.63$	$0.125 \pm 0.002$
H	$837.25 \pm 101.36$	$0.129 \pm 0.001$
L	544	0.133
LL	$391.0 \pm 41.6$	$0.127 \pm 0.004$
Diogenite	$0.39 \pm 0.65$	-

Acapulcoite	$833.3 \pm 190.7$	-
Ureilite	$347.0 \pm 161.7$	0.126

Reference for Os concentration and  $^{187}\text{Os}/^{188}\text{Os}$  isotopic composition of Dhala rock samples: Pati *et al.* (2017), Upper continental crust (UCC): Rudnick and Gao (2004), Peucker-Ehrenbrink and Jahn (2001), Meteorites: Fischer-Godde *et al.* (2010), Dale *et al.* (2012), Patzer *et al.* (2004), Janssens (1987), Spitz (1991), Rankenburg (2007). Uncertainties are reported as 2 s.e.

Chromium isotopes have successfully been used for the detection and identification of the impactor involved in the formation of the Morokweng, Bosumtwi, Clearwater East, Lappajarvi, Rochechouart, El'gygytgyn, Zhamanshin and Lonar impact structures (Koeberl *et al.*, 2007; Foriel *et al.*, 2013; Magna *et al.*, 2017; Mougél *et al.*, 2019). The identification of the impactors at Morokweng, Bosumtwi, Clearwater East, Lappajarvi and Rochechouart impact craters is only based on  $^{53}\text{Cr}$  (Koeberl *et al.* 2007). The method relies on the argument that most of the meteorite groups, such as ordinary and enstatite chondrites, primitive achondrites, and other differentiated meteorites, show a variable excess of  $^{53}\text{Cr}$  relative to the terrestrial standards, except carbonaceous chondrites, which show an apparent deficit in  $^{53}\text{Cr}$  of about  $-0.4 \text{ ‰}$  after second-order correction. The authors analyzed the impact melt rock and glass samples from Morokweng, Bosumtwi, Clearwater East, Lappajarvi and Rochechouart impact craters and based on the excesses of  $^{53}\text{Cr}$  relative to the terrestrial standard (and occasional correlations with siderophile abundances), concluded that the impactors are related to ordinary chondrites. However, taking the advantage of improved precision on the less abundant and mass-independently varying  $^{54}\text{Cr}$  and a richer Cr isotope dataset for meteorite groups, later studies (Foriel *et al.* (2013), Magna *et al.* (2017) and Mougél *et al.* (2019), could improve the efficacy of the Cr isotope approach to reveal the source of the impactors at the level of individual meteorite groups within the carbonaceous and non-carbonaceous reservoirs. Based on the combined  $^{53}\text{Cr}$ - $^{54}\text{Cr}$  analyses of the impactites, Foriel *et al.* (2013), Magna *et al.* (2017) and Mougél *et al.* (2019), identified a ureilites-like impactor at El'gygytgyn, a CI chondrite-like impactor at Zhamanshin and a CM-chondrite-like impactor at Lonar impact crater. The Cr isotope data of the Dhala impactites investigated in the present study together with the Os data of the same samples (Pati *et al.*, 2017) constrain the origin of the impactor that formed the Dhala impact structure to ureilites and acapulcoite achondrites, both of which originate from the non-carbonaceous reservoir. Foriel *et al.* (2013) argued that the discovery of asteroid 2008 TC<sub>3</sub> that exploded after entering the Earth's atmosphere, producing numerous ureilite

fragments in a strewn field in Sudan, indicates that such similar bodies may also cause impact structures (see also Goodrich *et al.*, 2019). Together with the identified impactors involved in the formation of the El'gygytgyn, Zhamanshin and Lonar impact structures (Foriel *et al.*, 2013; Magna *et al.*, 2017; Mougel *et al.*, 2019), the  $^{53}\text{Cr}$ - $^{54}\text{Cr}$  results of the Dhala impactites argue for a much diverse source of the objects that collided with the Earth over its geological history than has been supposed previously. Although ordinary chondrites dominate the current collection of meteorites on Earth, there could be a shift in the origin and composition of the influx of material accreting on Earth. Records of many smaller impacts could have been lost within the background rain of chemical, pyroclastic, and detrital sediments or episodes of volcanic activities (Lowe *et al.*, 2018). There could be an extensive record of the impact history of the early Earth in terrestrial rocks yet to be discovered and with the improvement in analytics, previously determined records should be updated.

## Acknowledgements

This study was partially funded by the 'Swiss Government Excellence Scholarship (2018.0371)'. We acknowledge funding within the framework of the NCCR PlanetS supported by the Swiss National Science Foundation grant no. 51NF40-141881. A.K.S. acknowledges the Council of Scientific and Industrial Research, New Delhi, Government of India, for awarding Shyama Prasad Mukherjee Fellowship (SPM-09/001(0328)/2020-EMR-I).

## References

- Alroy, J. (2008) Dynamics of origination and extinction in the marine fossil record. *Proceedings of the National Academy of Sciences*, 105 (Supplement 1), 11536-11542.
- Alvarez, W., Asaro, F., Michel, H.V. and Alvarez, L.W. (1982) Iridium anomaly approximately synchronous with terminal Eocene extinctions. *Science*, 216(4548), 886-888.
- Anand, A., Pape, J., Wille, M., Mezger, K., Hofmann, B. (2021a) Early differentiation of magmatic iron meteorite parent bodies from Mn-Cr chronometry. *Geochemical Perspectives Letters*, 20, 6-10.
- Anand, A., Pape, J., Wille, M., Mezger, K. (2021b) Chronological constraints on the thermal evolution of ordinary chondrite parent bodies from the  $^{53}\text{Mn}$ - $^{53}\text{Cr}$  system. *Geochimica et Cosmochimica Acta*, 307, 281-301.
- Barrat, J.A., Yamaguchi, A., Greenwood, R. C., Benoit, M., Cotten, J., Bohn, M., Franchi, I. A., (2008). Geochemistry of diogenites: Still more diversity in their parental melts. *Meteoritics & Planetary Science*, 43(11), 1759-1775.
- Chen J. H., Papanastassiou D. A., Wasserburg G. H. (1998) Re-Os systematics in chondrites and the fractionation of the platinum group elements in the early solar system. *Geochimica et Cosmochimica Acta*, 62, 3379-3392.
- Evans, N. J., Gregoire, D. C., Goodfellow, W. D. (1993) Use of platinum-group elements for impactor identification: Terrestrial impact craters and Cretaceous-Tertiary boundary. *Geochimica et Cosmochimica Acta*, 57(15), 3737-3748.
- Dale, C. W., Burton, K. W., Greenwood, R. C., Gannoun, A., Wade, J., Wood, B. J., Pearson, D. G. (2012) Late accretion on the earliest planetesimals revealed by the highly siderophile elements. *Science*, 336(6077), 72-75.
- Day, J. M., Brandon, A. D., Walker, R. J., (2016) Highly siderophile elements in Earth, Mars, the Moon, and asteroids. *Reviews in Mineralogy and Geochemistry*, 81(1), 161-238.



Fegley, B., Prinn, R.G., Hartman, H., Watkins, G.H. (1986) Chemical effects of large impacts on the Earth's primitive atmosphere. *Nature*, 319(6051), 305-308.

Fischer-Gödde, M., Becker, H. and Wombacher, F. (2010) Rhodium, gold and other highly siderophile element abundances in chondritic meteorites. *Geochimica et Cosmochimica Acta*, 74(1), 356-379.

Foriel, J., Moynier, F., Schulz, T., Koeberl, C. (2013) Chromium isotope anomaly in an impactite sample from the El'gygytgyn structure, Russia: Evidence for a ureilite projectile? *Meteoritics & Planetary Science*, 48(7), 1339-1350.

French, B.M. and Koeberl, C. (2010) The convincing identification of terrestrial meteorite impact structures: What works, what doesn't, and why. *Earth-Science Reviews*, 98(1-2), 123-170.

Goodrich, C.A., Zolensky, M.E., Fioretti, A.M., Shaddad, M.H., Downes, H., Hiroi, T., Kohl, I., Young, E.D., Kita, N.T., Hamilton, V.E., Riebe, M.E. (2019) The first samples from Almahata Sitta showing contacts between ureilitic and chondritic lithologies: Implications for the structure and composition of asteroid 2008 TC 3. *Meteoritics & Planetary Science*, 54(11), 2769-2813.

Grieve, R.A.F. and Masaitis, V.L. (1994) The economic potential of terrestrial impact craters. *International Geology Review*, 36(2), 105-151.

Hildebrand, A.R., Penfield, G.T., Kring, D.A., Pilkington, M., Camargo Z, A., Jacobsen, S.B., Boynton, W.V. (1991) Chicxulub crater: a possible Cretaceous/Tertiary boundary impact crater on the Yucatan Peninsula, Mexico. *Geology*, 19(9), 867-871.

Horan M. F., Smoliar M. I., Walker R. J. (1998)  $^{182}\text{W}$  and  $^{187}\text{Re}$ - $^{187}\text{Os}$  systematics of iron meteorites: Chronology for melting, differentiation, and crystallization in asteroids. *Geochimica et Cosmochimica Acta*, 62, 545-554.

Ivezic, Z., and 31 coauthors. (2001) Solar System objects observed in the Sloan digital sky survey commissioning data. *The Astronomical Journal*, 122, 2749-2784.

Janssens M. J., Hertogen J., Wolf R., Ebihara M., Anders E. (1987) Ureilites: trace element clues to their origin. *Geochimica et Cosmochimica Acta*, 51(9), 2275-2283.

Kenkmann, T. (2021) The terrestrial impact crater record: A statistical analysis of morphologies, structures, ages, lithologies, and more. *Meteoritics & Planetary Science*, 56(5), 1024-1070.

Kleine, T., Budde, G., Burkhardt, C., Kruijer, T. S., Worsham, E. A., Morbidelli, A., Nimmo, F., 2020. The non-carbonaceous–carbonaceous meteorite dichotomy. *Space Science Reviews*, 216(4), 1-27.

Koeberl, C. (1998) Identification of meteoritic components in impactites. *Geological Society, London, Special Publications*, 140(1), 133-153.

Koeberl C., Shukolyukov A., Lugmair G. W. (2007) Chromium isotopic studies of terrestrial impact craters: Identification of meteoritic components at Bosumtwi, Clearwater East, Lappajärvi, and Rochechouart. *Earth and Planetary Science Letters*, 256:534-546.

Koeberl, C., Claeys, P., Hecht, L., McDonald, I. (2012) Geochemistry of impactites. *Elements*, 8(1), 37-42.

Koeberl, C., (2014) The geochemistry and cosmochemistry of impacts. *Planets, asteroids, comets and the Solar System*, 2, 73-118.

Kruijer, T. S., Kleine, T., Borg, L. E. (2020) The great isotopic dichotomy of the early Solar System. *Nature Astronomy*, 4(1), 32-40.

Li, S., Yin, Q. Z., Bao, H., Sanborn, M. E., Irving, A., Ziegler, K., Agee, C., Marti, K., Miao, B., Li, X., Li, Y. (2018) Evidence for a multilayered internal structure of the chondritic acapulcoite-lodranite parent asteroid. *Geochimica et Cosmochimica Acta*, 242, 82-101.

Lodders, K. (2003) Solar system abundances and condensation temperatures of the elements. *The Astrophysical Journal*, 591(2), 1220.

Lowe, D.R. and Byerly, G.R. (2018) The terrestrial record of late heavy bombardment. *New Astronomy Reviews*, 81, 39-61.

Magna T., Zak K., Pack A., Moynier F., Mougél B., Peters S., Skala R., Jonasova S., Mizera J., Randa Z. (2017) Zhamanshin astrobleme provides evidence for carbonaceous chondrite and post-impact exchange between ejecta and Earth's atmosphere. *Nature Communications*, 8, 1-8.

Mazrouei, S., Ghent, R.R., Bottke, W.F., Parker, A.H., Gernon, T.M. (2019) Earth and Moon impact flux increased at the end of the Paleozoic. *Science*, 363(6424), 253-257.

Mezger, K., Maltese, A., Vollstaedt, H. (2021) Accretion and differentiation of early planetary bodies as recorded in the composition of the silicate Earth. *Icarus*, 365, 114497.

McDonald I., Andreoli M. A. G., Hart R. J., Tredoux M. (2001) Platinum-group elements in the Morokweng impact structure, South Africa: Evidence for the impact of a large ordinary chondrite projectile at the Jurassic-Cretaceous boundary. *Geochimica et Cosmochimica Acta*, 65, 299-309.

McDonald I. (2002) Clearwater East impact structure: A re-interpretation of the projectile type using new platinum-group element data. *Meteoritics & Planetary Science*, 37, 459-464.

Mittlefehldt, D. W., See, T. H., Hoerz, F. (1992) Dissemination and fractionation of projectile materials in the impact melts from Wabar Crater, Saudi Arabia. *Meteoritics*, 27(4), 361-370.

Mittlefehldt D. V. (2003) Achondrites. In Meteorites, comets, and planets, edited by Davis A. W. *Treatise on Geochemistry*, vol. 1. Oxford, Elsevier. 291-324.

Morbidelli, A., Jedicke, R., Bottke, W. F., Michel, P., Tedesco, E. F. (2002) From magnitudes to diameters: the albedo distribution of near-Earth objects and the Earth collision hazard. *Icarus*, 158 (2), 329-342.

Mougél, B., Moynier, F., Göpel, C., Koeberl, C. (2017) Chromium isotope evidence in ejecta deposits for the nature of Paleoproterozoic impactors. *Earth and Planetary Science Letters*, 460, 105-111.

Mougel, B., Moynier, F., Koeberl, C., Wielandt, D., Bizzarro, M. (2019) Identification of a meteoritic component using chromium isotopic composition of impact rocks from the Lonar impact structure, India. *Meteoritics & Planetary Science*, 54(10), 2592-2599.

Naumov, M.V. (2002) Impact-generated hydrothermal systems: Data from Popigai, Kara, and Puchezh-Katunki impact structures. In *Impacts in Precambrian shields*, (117-171). Springer, Berlin, Heidelberg.

Parkos, D., Pikus, A., Alexeenko, A., Melosh, H.J. (2018) HCN production via impact ejecta reentry during the late heavy bombardment. *Journal of Geophysical Research: Planets*, 123(4), 892-909.

Pati J. K., Reimold W. U., Koeberl C., Pati P. (2008a) The Dhala structure, Bundelkhand Craton, Central India-eroded remnant of a large Paleoproterozoic impact structure. *Meteoritics & Planetary Science*, 43, 1383-1398.

Pati J. K., Raju S., Malviya V. P., Bhushan R., Prakash K., Patel S. C. (2008b) Mafic dykes of Bundelkhand craton, Central India: Field, petrological and geochemical characteristics. In *Indian dykes: Geochemistry, geophysics and geochronology*, edited by Srivastava R. K., Sivaji C. H., and Chalapathi Rao, N. V. New Delhi, Narosa Publishing House Pvt. Ltd. pp. 547-569.

Pati, J.K., Jourdan, F., Armstrong, R.A., Reimold, W.U., Prakash, K. (2010) First SHRIMP U-Pb and  $^{40}\text{Ar}/^{39}\text{Ar}$  chronological results from impact melt breccia from the Paleoproterozoic Dhala impact structure, India. *Large Meteorite Impacts and Planetary Evolution IV, Special Paper*, 465, 571-591.

Pati, J. K., Qu, W. J., Koeberl, C., Reimold, W. U., Chakravorty, M., Schmitt, R. T., (2017) Geochemical evidence of an extraterrestrial component in impact melt breccia from the Paleoproterozoic Dhala impact structure, India. *Meteoritics & Planetary Science*, 52(4), 722-736.

Pati, J.K., Poelchau, M.H., Reimold, W.U., Nakamura, N., Kuriyama, Y., Singh, A.K. (2019) Documentation of shock features in impactites from the Dhala impact structure, India. *Meteoritics & Planetary Science*, 54(10), 2312-2333.

Patzer, A., Hill, D. H., Boynton, W. V. (2004) Evolution and classification of acapulcoites and lodranites from a chemical point of view. *Meteoritics & Planetary Science*, 39(1), 61-85.

Peucker-Ehrenbrink, B. and Jahn, B. M. (2001) Rhenium-osmium isotope systematics and platinum group element concentrations: Loess and the upper continental crust. *Geochemistry, Geophysics, Geosystems*, 2(10).

Rankenburg, K., Brandon, A. D., Humayun, M. (2007) Osmium isotope systematics of ureilites. *Geochimica et Cosmochimica Acta*, 71(9), 2402-2413.

Rudnick R. L. and Gao S. (2004) Composition of continental crust. In *Treatise on Geochemistry*, vol. 4, second ed. (ed. R. L. Rudnick). Elsevier, pp. 1-51.

Schmieder, M. and Kring, D.A. (2020) Earth's impact events through geologic time: a list of recommended ages for terrestrial impact structures and deposits. *Astrobiology*, 20(1), 91-141.

Schmitz, B., Huss, G. R., Meier, M. M., Peucker-Ehrenbrink, B., Church, R. P., Cronholm, A., Davies, M. B., Heck, P. R., Johansen, A., Keil, K., Kristiansson, P. (2016) A fossil winonaite-like meteorite in Ordovician limestone: A piece of the impactor that broke up the L-chondrite parent body? *Earth and Planetary Science Letters*, 400, 145-152.

Schoenberg, R., Merdian, A., Holmden, C., Kleinhanns, I. C., Haßler, K., Wille, M., Reitter, E. (2016) The stable Cr isotopic compositions of chondrites and silicate planetary reservoirs. *Geochimica et Cosmochimica Acta*, 183, 14-30.

Shields, W. R., Murphy, T. J., Catanzaro, E. J., Garner, E. L. (1966) Absolute isotopic abundance ratios and the atomic weight of a reference sample of chromium. *Journal of Research of the National Bureau of Standards Section A: Physics and Chemistry*, 70A, 193.

Singh, A.K., Pati, J.K., Sinha, R., Reimold, W.U., Prakash, K., Nadeem, M., Dwivedi, S., Mishra, D., Dwivedi, A.K. (2021) Characteristic landforms and geomorphic features associated with impact structures: Observations at the Dhala structure, north-central India. *Earth Surface Processes and Landforms*, 46(8), 1482-1503.

Shukolyukov A. and Lugmair G. W. (1998) Isotopic evidence for the Cretaceous-Tertiary impactor and its type. *Science*, 282, 927-929.

Smit, J. and Klaver, G. (1981) Sanidine spherules at the Cretaceous-Tertiary boundary indicate a large impact event. *Nature*, 292(5818), 47-49.

Spitz A. H., and Boynton W. V. (1991) Trace element analysis of ureilites: new constraints on their petrogenesis. *Geochimica et Cosmochimica Acta*, 55(11), 3417-3430.

Stuart, J. S. and Binzel, R. P. (2004) Bias-corrected population, size distribution, and impact hazard for the near-Earth objects. *Icarus*, 170(2), 295-311.

Tagle R. (2004) Platingruppenelemente in Meteoriten und Gesteinen irdischer Impaktkrater: Identifizierung der Einschlagskörper. *Ph.D. thesis*, Humboldt-Universität Berlin, Germany.

Tagle, R. and Claeys, P. (2005) An ordinary chondrite impactor for the Popigai crater, Siberia. *Geochimica et Cosmochimica Acta*, 69(11), 2877-2889.

Tagle, R., Berlin, J. (2008) A database of chondrite analyses including platinum group elements, Ni, Co, Au, and Cr: Implications for the identification of chondritic projectiles. *Meteoritics & Planetary Science*, 43(3), 541-559.

Trinquier, A., Birck, J. L., Allègre, C. J. (2007) Widespread  $^{54}\text{Cr}$  heterogeneity in the inner solar system. *The Astrophysical Journal*, 655, 1179–1185.

Trinquier, A., Birck, J. L., Allègre, C. J. (2008a) High-precision analysis of chromium isotopes in terrestrial and meteorite samples by thermal ionization mass spectrometry. *Journal of Analytical Atomic Spectrometry*, 23, 1565-1574.

Trinquier, A., Birck, J. L., Allègre, C. J., Göpel, C., Ulfbeck, D. (2008b)  $^{53}\text{Mn}$ - $^{53}\text{Cr}$  systematics of the early Solar System revisited. *Geochimica et Cosmochimica Acta*, 72, 5146-5163.

Wänke, H. and Dreibus, G. (1988) Chemical composition and accretion history of terrestrial planets. *Philosophical Transactions of the Royal Society of London. Series A, Mathematical and Physical Sciences*, 325(1587), 545-557.

Wasson, J. T. and Kallemeyn, G. W. (1988) Compositions of chondrites. *Philosophical Transactions of the Royal Society of London. Series A, Mathematical and Physical Sciences*, 325(1587), 535-544.

Yamakawa, A., Yamashita, K., Makishima, A., Nakamura, E. (2010) Chromium isotope systematics of achondrites: Chronology and isotopic heterogeneity of the inner solar system bodies. *The Astrophysical Journal*, 720(1), 150.

Zellner, N.E. (2017) Cataclysm no more: new views on the timing and delivery of lunar impactors. *Origins of Life and Evolution of Biospheres*, 47(3), 261-280.

Zhu, K., Moynier, F., Wielandt, D., Larsen, K. K., Barrat, J. A., Bizzarro, M., (2019) Timing and origin of the angrite parent body inferred from Cr isotopes. *The Astrophysical journal letters*, 877(1), L13.

Zhu, K., Moynier, F., Schiller, M., Wielandt, D., Larsen, K. K., van Kooten, E. M., Barrat, J. A. Bizzarro, M. (2020) Chromium isotopic constraints on the origin of the ureilite parent body. *The Astrophysical Journal*, 888(2), 126.

Zhu, K., Moynier, F., Schiller, M., Alexander, C.M.D., Davidson, J., Schrader, D.L., van Kooten, E. and Bizzarro, M. (2021a) Chromium isotopic insights into the origin of chondrite parent bodies and the early terrestrial volatile depletion. *Geochimica et Cosmochimica Acta*, 301, 158-186.

Zhu, K., Moynier, F., Schiller, M., Becker, H., Barrat, J. A. and Bizzarro, M. (2021b). Tracing the origin and core formation of the enstatite achondrite parent bodies using Cr isotopes. *Geochimica et Cosmochimica Acta*, 308, 256-272.

## Appendix



## A1. Cr and O Isotopes Link IVA Irons and LL Chondrites

Aryavart Anand<sup>1</sup>, Jonas Pape<sup>2</sup>, Klaus Mezger<sup>1</sup>, and Beda Hofmann<sup>1,3</sup>, <sup>1</sup>Institut für Geologie, Universität Bern, Baltzerstrasse 1+3, 3012 Bern, Switzerland (aryavart.anand@geo.unibe.ch), <sup>2</sup>Institut für Planetologie, Universität Münster, Wilhelm-Klemm-Str. 10, 48149 Münster, Germany, <sup>3</sup>Naturhistorisches Museum Bern, Bernastrasse 15, CH-3005, Bern, Switzerland.

### Introduction

Different magmatic iron meteorite groups are thought to sample the core of distinct parent bodies that experienced large-scale chemical fractionation, most notably metal-silicate melt separation. Combined Cr and O isotope data provide a means for identifying a possible genetic relationship among an iron meteorite group representing the core and a stony meteorite group representing the undifferentiated counterpart of a parent body or a body that formed from the same reservoir as the core material represented by iron meteorites. Previous studies have attempted to make such connections and indicated similarity within a  $\epsilon^{54}\text{Cr}$  vs.  $\Delta^{17}\text{O}$  space between IIIAB irons, main group pallasites and HEDs [1, 2], IIE irons and H chondrites [3], and Eagle Station pallasite and CV chondrites [4]. A similarity in  $\epsilon^{54}\text{Cr}$  and  $\Delta^{17}\text{O}$  isotopic composition between IVA irons and L/LL ordinary chondrites was also observed based on silicate inclusions from Steinbach and São João Nepomuceno meteorites [5]. The present study provides additional data on this association based on  $\epsilon^{54}\text{Cr}$  values obtained from chromite ( $\text{FeCr}_2\text{O}_4$ ) or daubréelite ( $\text{FeCr}_2\text{S}_4$ ) inclusions in magmatic iron meteorites. Chromite and daubréelite are the two main carrier phases of Cr in these meteorites. A particular advantage of measuring  $\epsilon^{54}\text{Cr}$  on these minerals is their very low Fe/Cr ratios of typically around  $\sim 0.5$ . As a consequence, cosmogenic contributions of  $^{54}\text{Cr}$  produced by galactic cosmic ray exposure from Fe are negligible; hence no correction for spallogenic Cr is required [6].

### Samples and Methods

Two meteorite samples, Duchesne and Yanhuitlan were analyzed from the IVA iron meteorite group for Cr isotope compositions. A chromite or daubréelite fraction was obtained from each whole-rock sample. After mineral digestion and chemical purification, Cr isotopes were

measured on a Triton™ Plus TIMS at the University of Bern.  $\Delta^{17}\text{O}$  data for IVA and L/LL and  $^{54}\text{Cr}$  data for L/LL chondrites are compiled from the literature [7,8,9,10,11].

## Results and Discussion

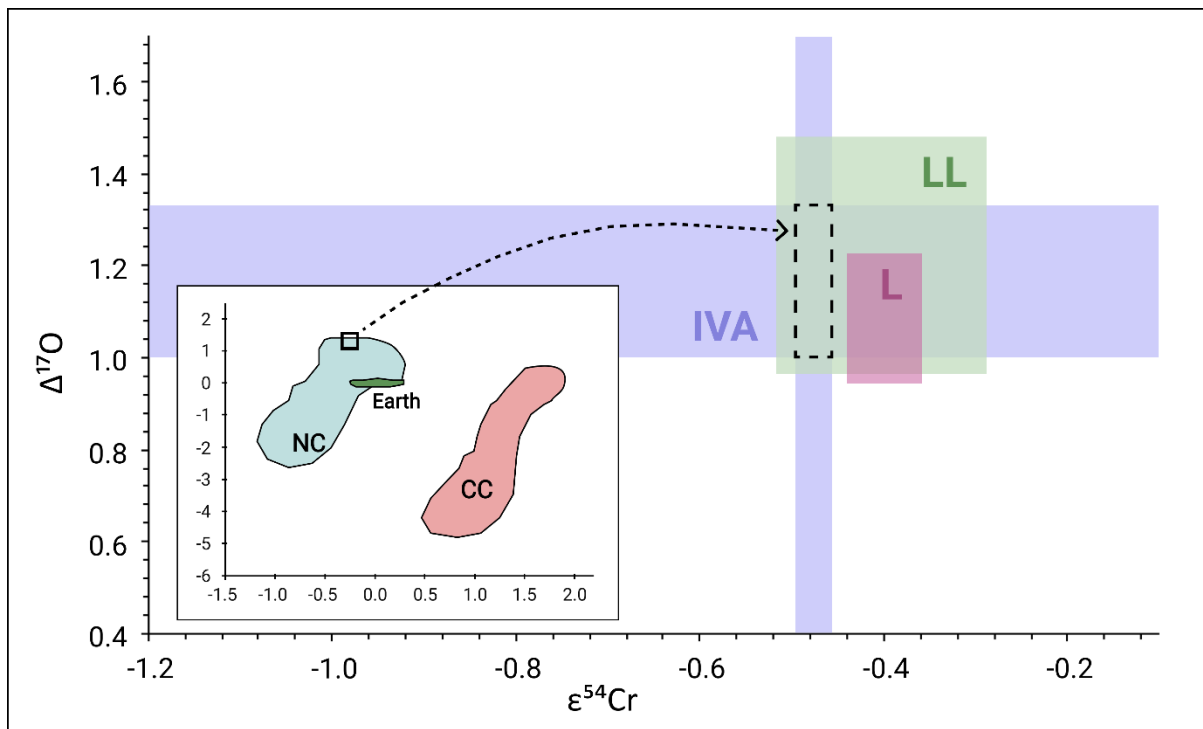


**Fig. A1.1.**  $\Delta^{17}\text{O}$ - $\epsilon^{54}\text{Cr}$  diagram of IVA irons and LL/L ordinary chondrites.

Duchesne and Yanhuítlan daubréelite/chromite inclusions display a well-defined  $\epsilon^{54}\text{Cr}$  with a mean value of  $-0.48 \pm 0.02$ . Combined with the mean  $\Delta^{17}\text{O}$  isotope data for IVA irons, these irons show a clear overlap with the LL ordinary chondrites when plotted on a  $\epsilon^{54}\text{Cr}$  vs.  $\Delta^{17}\text{O}$  diagram (Fig. A1.1). Such an overlap suggests that both are derived from a common isotope reservoir with the same O-Cr isotope composition and are therefore genetically related. This reservoir existed within 1 Ma after the birth of the solar system (CAI formation) as indicated by chromite/daubréelite model ages in IVA iron meteorites, inferred as the time of core formation in their parent body [12]. The reservoir was also the source of planetesimal formation at least up to 3 Ma as indicated by the accretion of the ordinary chondrites parent bodies constrained by the chondrule formation interval [13] and the onset of metamorphism on the chondrite parent bodies [14]. This implies that planetesimal accretion within this reservoir spans an interval of at least 3 Ma and planetary accretion and differentiation was

contemporaneous with chondrule formation. In some regions of the evolving solar system disk, planetesimals existed while others were still at the dust-gas stage.

## References:

- [1] Wasson J. (2013) *EPSL* 381, 138. [2] Wasson J. and Gopel C. (2014) *MetSoc77*, Abstract #5446. [3] Dey *et al.* (2019) *LPS V*, Abstract #2977. [4] Shukolyukov A. and Lugmair G. W. (2006) *EPSL*, 250, 200-213. [5] Sanborn *et al.* (2018) *LPSC XLIX*, Abstract #1780. [6] Liu J. *et al.* (2019) *GCA* 251, 73–86. [7] Clayton R. N. and Mayeda T. K. (1996) *GCA* 60(11), 1999–2017. [8] Wang *et al.* (2004), *GCA* 68(5), 1159-1171. [9] Trinquier A. *et al.* (2017) *TAJ* 655, 1179- 1185. [10] Trinquier A. *et al.* (2008) *JAAS* 23, 1565-1574. [11] Qin L *et al.* (2010) *GCA* 74, 1122-1145. [12] Anand A. *et al.* (2021) *LPSC LII*, Abstract #2548. [13] Pape J. *et al.* (2019) *GCA* 244, 419–436. [14] Anand A. *et al.* (2021) *GCA* (in press, <https://doi.org/10.1016/j.gca.2021.04.029>).

## A2. IIAB and IIG Iron Meteorites Originated from a Single Parent Body

A. Anand<sup>1</sup>, P. M. Kruttasch<sup>1</sup>, K. Mezger<sup>1</sup>, R. Windmill<sup>2</sup>, B. A. Hofmann<sup>1,3</sup>, R. C. Greenwood<sup>2</sup>, and I. Leya<sup>4</sup>, <sup>1</sup>Institut für Geologie, Universität Bern, Baltzerstrasse 1+3, 3012 Bern, Switzerland (aryavart.anand@geo.unibe.ch), <sup>2</sup>Planetary and Space Sciences, The Open University, MK7 6AA Milton Keynes, UK, <sup>3</sup>Naturhistorisches Museum Bern, Bernastrasse 15, 3005, Bern, Switzerland, <sup>4</sup>Physikalisches Institut, University of Bern, Sidlerstrasse 5, 3012 Bern, Switzerland.

### Introduction

Different magmatic iron meteorite groups are thought to sample the cores of distinct parent bodies that experienced large-scale chemical fractionation, most notably metal-silicate melt separation. IIAB and IIG are two such magmatic iron meteorite groups with Ga and Ge contents in the general “II” range. While IIAB irons represent the second largest group that formed by fractional crystallization, with more than 140 entries in the Meteoritical Bulletin Database, IIG is a relatively small group with only 6 members. On element vs. Au diagrams, IIG data plot near the high-Au end of the IIAB field leading past researchers to suggest that both groups might have formed from the same magma and thus in the same asteroidal core [1]. Combined Cr and O-isotope data provides a means to identify possible genetic relationships among meteorite groups. However, to date, no O or Cr-isotopic data for either the IIAB or IIG groups have been available that could provide critical information regarding this genealogy. Previous studies have attempted to make connections between different iron groups in  $\epsilon^{54}\text{Cr}$  vs.  $\Delta^{17}\text{O}$  space, such as between IIIAB irons, main group pallasites and HEDs [2, 3], IIE irons and H chondrites [4], IVA irons and L/LL chondrites [5, 6], and the Eagle Station pallasite and CV chondrites [7].

The present study utilizes Cr and O isotope data from chromite/troilite inclusions in the Twannberg (IIG) and Sikhote Alin (IIAB) meteorites to investigate their potential association. Chromite and daubréelite are the major carrier phases of Cr in iron meteorites. Due to a high “native”  $\epsilon^{54}\text{Cr}$  and low Fe/Cr (~0.5) ratio in chromite/daubréelite, the cosmogenic contribution to  $^{54}\text{Cr}$  is negligible and hence no correction for spallogenic Cr is required [8, 9, 10]. Both chromite and daubréelite are rare phases in iron meteorites and in the absence of

these phases, however, troilite can be used for Cr isotope analysis. In the case of troilite, high Fe/Cr (~400) combined with the typically long irradiation times for iron meteorites (Table 1) leads to significant production of spallogenic  $^{54}\text{Cr}$  and appropriate corrections are necessary. The Cape York (IIIAB) iron meteorite was used as a control to check the calculations correcting for spallogenic Cr contributions.

## Methods

A chromite and/or troilite fraction was obtained each from Sikhote Alin (IIAB), Cape York (IIIAB), and Twannberg (IIG). Chromite grains in the samples were first identified using an optical microscope and isolated in small whole-rock fragments. The fragments were digested in conc. aqua regia on a hot plate set to 90 °C for 48 h to completely dissolve the metal-sulphide dominated matrix, leaving behind residual chromite grains. Troilite fractions were obtained using a Dremel<sup>®</sup> micro drill. One part of the chromite fraction from Sikhote Alin and all of the recovered chromite fraction from Twannberg were consumed to measure O isotopes on a MAT 253 dual inlet mass spectrometer at the Open University following the protocol given in [11]. Chromite fractions from Sikhote Alin and Cape York and troilite fractions from Twannberg and Cape York were used to measure Cr isotopes on a Triton<sup>™</sup> Plus TIMS at the University of Bern. Cr isotope data for chromite fractions were reported in [12]. For troilite fractions, Cr purification and TIMS analysis follows the protocol described in [10, 12].  $^{53}\text{Cr}$  and  $^{54}\text{Cr}$  isotope compositions of the troilite fractions were corrected for spallogenic Cr contributions using the  $^{53}\text{Cr}$  and  $^{54}\text{Cr}$  production rates obtained for the interior of the iron meteorite Grant ( $2.9 \times 10^{11}$  atoms/Ma, [13]), the relation described in [14], and assuming a similar depth dependency as used in [15].

## Results and Discussion

$\Delta^{17}\text{O}$  and spallogenic corrected and uncorrected Cr isotope data of the selected chromite/troilite fractions are listed in Table 1. The  $^{53}\text{Cr}$  and  $^{54}\text{Cr}$  data, corrected for spallogenic contributions, for the troilite fraction of Cape York is in perfect agreement with its chromite fraction, which does not need any correction, validating the correction procedure (Fig. A2.1). Since the pre-atmospheric size of both Cape York ( $r \geq 120$  cm [16]) and Twannberg ( $r \geq 200$

cm [17]) is similar, the correction procedure for spallogenic Cr applied to Cape York troilite should also be valid for troilites from Twannberg. However, the pre-atmospheric radius of both Twannberg and Cape York is significantly larger than the pre-atmospheric radius of Grant ( $r \geq 40$  cm [18]) which is used to determine  $^{53}\text{Cr}$  and  $^{54}\text{Cr}$  production rates [13]. Hence, the correction for spallogenic Cr could be slightly overestimated. As a consequence, the corrected  $^{53}\text{Cr}$  and  $^{54}\text{Cr}$  data constrain lower limits.

**Table A2.1.** Cr-and O-isotope composition of samples.

Sample	Fraction	CRE age	Fe/Cr	$\epsilon^{53}\text{Cr} \pm 2\text{se}$	$\epsilon^{54}\text{Cr} \pm 2\text{se}$	$\Delta^{17}\text{O} \pm 2\text{se}$
Twann Troil.		$182 \pm 45$	352.6	$0.01 \pm 0.02$	$-0.31 \pm 0.04$	
	corrected	$182 \pm 45$	352.6	$-0.25 \pm 0.13$	$-1.12 \pm 0.40$	
	Chr.	$182 \pm 45$	-	-	-	-1.11
CY	Troil.	$82 \pm 7$	$\sim 350$	$-0.07 \pm 0.04$	$-0.46 \pm 0.09$	
	corrected	$82 \pm 7$	$\sim 350$	$-0.19 \pm 0.04$	$-0.82 \pm 0.09$	
	Chr.	-	0.46	$-0.20 \pm 0.04$	$-0.78 \pm 0.06$	
SA	Chr.	-	0.41	$-0.23 \pm 0.03$	$-0.92 \pm 0.05$	$-1.16 \pm 0.01$

Twann: Twannberg (IIG), CY: Cape York (IIIAB), SA: Sikhote Alin (IIAB). Chr.: Chromite, Troil.: Troilite. References for CRE ages: Twannberg [17], Cape York [19].

A large uncertainty of the CRE age of the Twannberg meteorite ( $182 \pm 45$  Ma) results in a large uncertainty of corrected  $^{53}\text{Cr}$  and  $^{54}\text{Cr}$  data for the troilite fraction (Fig. A2.1). Nevertheless, the Cr troilite from Twannberg data are in agreement with the Cr chromite data from Sikhote Alin, as well as with the other two IIAB iron meteorites studied in [10]. Spallation corrected  $^{53}\text{Cr}$  of the troilite fraction from Twannberg, translates into  $^{53}\text{Cr}/^{52}\text{Cr}$  model ages using the relation-ship given in [10], constrains core formation in the Twannberg iron meteorite parent body to  $0.7 \pm 2.0$  Ma after CAI formation, which agrees with the mean core formation age of  $\sim 1.3$  Ma for IIAB iron meteorites [10].

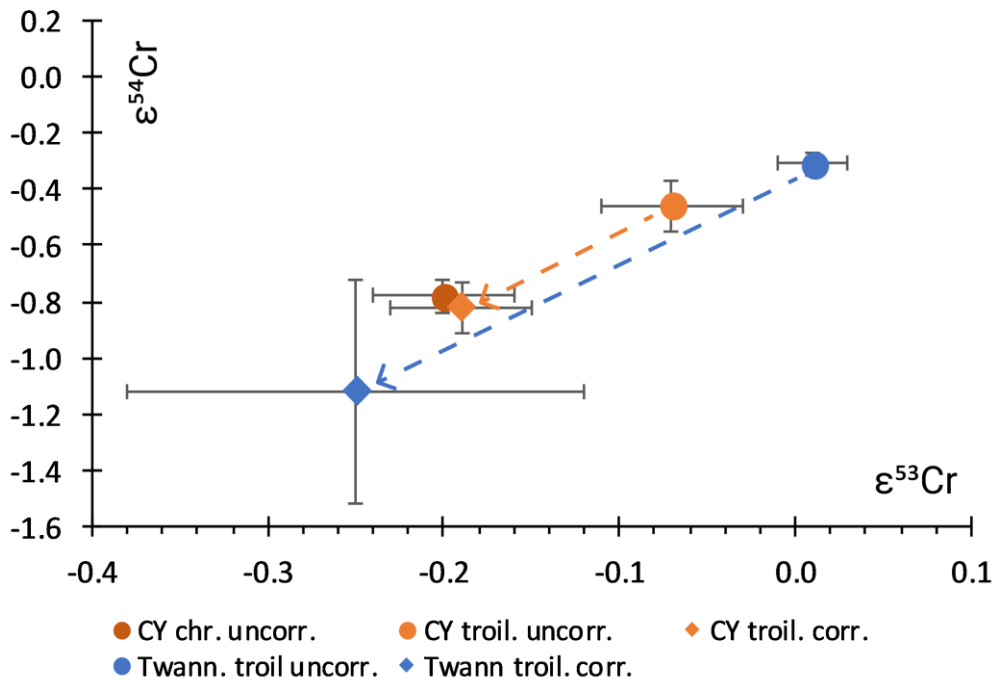


**Fig. A2.1.** Spallogenic Cr correction in troilite fractions from Twannberg (IIG) and Cape York (IIAB) iron meteorites.

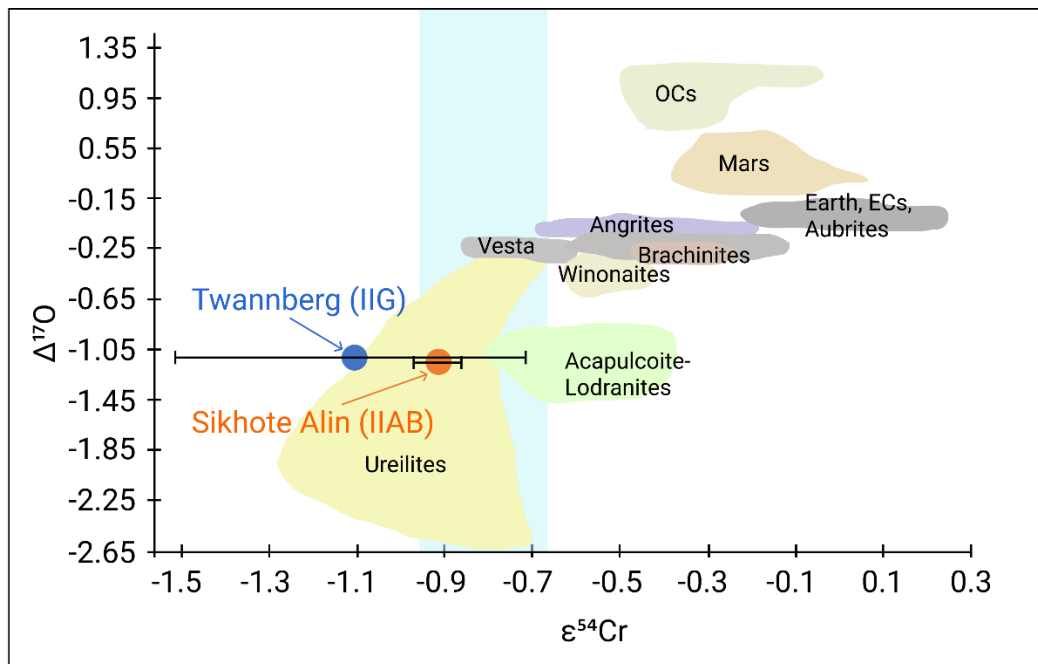


**Fig. A2.2.**  $\Delta^{17}\text{O}$ - $\epsilon^{54}\text{Cr}$  diagram for Twannberg (IIG) and Sikhote Alin (IIAB). The overlap in the isotope data supports an origin of both IIAB and IIG iron meteorites from a common isotope reservoir with the same O-Cr isotope composition and thus a genetic relationship between the two iron meteorite groups. The blue vertical bar represents the  $\epsilon^{54}\text{Cr}$  variation in IIAB iron meteorites [10].

The Twannberg troilite data, if combined with  $\Delta^{17}\text{O}$  isotope data of its chromite fraction, shows a clear overlap with the data from Sikhote Alin when plotted on an  $\varepsilon^{54}\text{Cr}$  vs.  $\Delta^{17}\text{O}$  diagram (Fig. A2.2). Moreover, both Twannberg and Sikhote Alin lie in the fields for ureilite/acapulcoite-lodranite meteorites. Such an overlap suggests that IIAB and IIG are derived from a common isotope reservoir with the same O-Cr isotope composition. Additionally, chemical element trends for IIAB and IIG irons suggest a genetic relationship between both groups, with IIG formation from the evolved IIAB metal melt.

Group IIG irons were most likely formed from a P-rich metal melt that separated due to liquid immiscibility in the later stages of the IIAB core crystallization [1,20]. The chemical element trends from Wasson and Choe (2009) [1] and O-Cr isotope data in the present study provide a strong argument in favour of the origin of IIAB and IIG iron meteorites within the same asteroidal core, which might be the core within the ureilite/acapulcoite-lodranite O-Cr field.

## References

- [1] Wasson J. T. and Choe W. H. (2009) *GCA* 73(16), 4879-4890. [2] Wasson J. (2013) *EPSL* 381, 138. [3] Wasson J. and Gopel C. (2014) *MetSoc*77, Abstract #5446. [4] Dey S. *et al.* (2019) *LPSC* L, Abstract #2977. [5] Shukolyukov A. and Lugmair G. W. (2006) *EPSL* 250, 200-213. [6] Anand A. *et al.* *MetSoc*84, Abstract #2609. [7] Sanborn M. E. *et al.* (2018) *LPSC* XLIX, Abstract #1780. [8] Trinquier A. *et al.* (2008) *GCA* 72, 5146-5163. [9] Liu J. *et al.* (2019) *GCA* 251, 73-86. [10] Anand A. *et al.* (2021a) *Geochem. Persp. Let.* 20, 6–10. [11] Greenwood R. C. *et al.* (2014) *EPSL* 390, 165-174. [12] Anand A. *et al.* (2021b) *GCA* 307, 281-301. [13] Birck J. L. and Allègre, C. J. (1985) In: Gautier, D. (Ed.) *Isotopic ratios in the solar system*, 21-25. [14] Trinquier A. *et al.* (2007) *ApJ* 655, 1179–1185. [15] Graf T. and Marti K. (1995) *J. Geophys. Res.* 100, 21247–21264. [16] Kruijer T. S. *et al.* (2012) *GCA* 99, 287-304. [17] Smith T. *et al.* (2017) *Meteorit. Planet. Sci.* 52(10), 2241-2257. [18] Feldmann H and Voshage H. (1979) *EPSL* 45, 293-308. [19] Mathew K. J. and Marti K. (2009) *Meteorit. Planet. Sci.* 44(1), 107-114. [20] Chabot *et al.* (2020) *Meteorit. Planet. Sci.* 55(4), 726-743.



# Supplementary Information

## Chapter 1

### S1.1 Analytical Methods

#### S1.1.1 Determination of Mn/Cr Ratios

Aliquots from all the chromite and silicate fractions were diluted in 10 mL 0.5 M HNO<sub>3</sub> to target for 50 ppb Cr solutions. These aliquots were used to determine Cr, Mn, and Fe concentrations using a 7700x Agilent ICP-MS at the Institute of Geography, University of Bern. An in-house standard solution was prepared using single element solutions of Cr, Fe, Mg, Ti, V and Mn to closely mimic the expected composition of the analyzed chromite grains. To measure the Mn/Cr ratio in chromite fractions precisely, this in-house standard solution of different dilution levels was employed to prepare calibration curves for Cr, Mn, and Fe by linear regression. The silicate fractions were measured using calibration with BHVO-2 rock standard solution, diluted to different concentrations. The rock standard OKUM was measured along with the silicate fractions. It was diluted to three dilution levels, covering the entire range of Mn/Cr ratios in the silicate fractions. The Mn/Cr ratio of OKUM was determined to be  $0.59 \pm 0.01$  (2SD) which is in good agreement with the Mn/Cr ( $= 0.58 \pm 0.01$ ) reported in Peters and Pettke (2017) confirming the accuracy of the method. Uncertainties on Mn/Cr ratios are reported in 2 standard error of the replicate measurements ( $n = 5$ ) and remained  $<5\%$  for all the samples (Table A1.1).

#### S1.1.2 Chemical separation of Cr

Purification of Cr was adopted from Schoenberg *et al.* (2016) and includes three steps of a combination of cation-anion exchange chromatography modified after Schoenberg and Von Blanckenburg (2005)(column 1), Trinquier *et al.* (2008a) and Yamakawa *et al.* (2009) (column 2 and 3). An aliquot containing 20  $\mu\text{g}$  of Cr from each silicate and chromite fraction was evaporated to dryness on a hot plate at 90 °C, taken up in 1 ml 6 M HCl and loaded on the first 7.5 mL Spectrum® polypropylene column containing 2 ml anion resin (BioRad AG 1X8 100-200 mesh size). The Cr fraction was eluted in 6 ml 6 M HCl together with Ni while Fe and Zn

remained on the column. The second column was applied only for the silicate fractions to remove major elements such as Ca, Mg and Al. The Cr eluate from the first column was dried down, redissolved in 400  $\mu\text{L}$  6 M HCl, equilibrated on a hotplate at 130 °C for ~30 min one day before the chemical separation and stored at room temperature overnight. Next day, the sample was reequilibrated on a hot plate at 130 °C for one hour, diluted with 2 ml of MilliQ water to obtain 2.4 ml 1 M HCl and loaded on the second column filled with 2 ml cation resin (BioRad AG 50W-X8 200-400 mesh size). The second column separation step produced a solution with mostly Cr, but incomplete separation from Ti and V. The third column with 0.5 ml BioRad AG 50W-X8 200-400 mesh was applied for both chromite (after first column) and silicate fractions (after second column) in order to obtain a clean Cr separate free of Ti and V. The aliquots were dried down on a hot plate (at 90 °C), taken up in 0.5 ml conc.  $\text{HNO}_3$  and dried down again immediately to transform samples into nitrate form. The residue was redissolved in 3 ml 0.4 M  $\text{HNO}_3$  for 30 min on a hotplate at 80 °C and let react cold for 5 days for the production of chloro-aquo complexes. Afterwards, each sample was loaded on the third column. Matrix was eluted in 8 ml 0.5 M HF and 9.5 ml 1 M HCl and Cr was collected in 8 ml 4 M HCl. Finally, the Cr separate was dissolved in sufficient amounts of 6 M HCl to yield concentrations of 0.7-1  $\mu\text{g}/\mu\text{L}$  for mass spectrometry. Typical recovery of Cr was in excess of 80% for the whole column chemistry, determined by spiked sample solutions on ICP-MS. Total chemistry blanks were below 10 ng, which is negligible compared to the  $\mu\text{g}$  range of Cr isolated and loaded on the filaments for each sample.

### S1.1.3 Mass spectrometry

Chromium was loaded on single Re filaments that had been outgassed stepwise under high vacuum conditions ( $10^{-5}$  bar) at 1.5 A (45 min), 2 A (30 min) and 4 A (70 min). About 0.7-1  $\mu\text{g}$  Cr in 1  $\mu\text{L}$  6 M HCl was mixed with 1.4  $\mu\text{L}$  alumina doped silica gel on a piece of Parafilm® and loaded on the filament, minimizing the spreading of the sample droplet. 0.7  $\mu\text{L}$   $\text{H}_3\text{BO}_3$  was then added to the top of this mixture. After drying the Cr salt at around 0.8 A, the filament was heated slowly to a dull red glow for less than one second. The samples were analyzed by Thermal Ionization Mass Spectrometer using a Thermo Scientific TRITON Plus instrument at the Institute of Geological Sciences, University of Bern. Aliquots of each sample were loaded on 4-6 filaments and measured at signal intensities between 8 and 12 V for  $^{52}\text{Cr}$  ( $10^{-11}$   $\Omega$  resistor). Following the procedure described in Trinquier *et al.* (2008a), the intensities of  $^{50}\text{Cr}$ ,

$^{51}\text{V}$ ,  $^{52}\text{Cr}$ ,  $^{53}\text{Cr}$ ,  $^{54}\text{Cr}$ ,  $^{55}\text{Mn}$  and  $^{56}\text{Fe}$  were measured on the Faraday cups L3, L2, L1, C, H1, H2 and H3, respectively. Peak center was monitored on  $^{53}\text{Cr}$  in the center cup. Isobaric interference of  $^{54}\text{Fe}$  on  $^{54}\text{Cr}$  was corrected by monitoring  $^{56}\text{Fe}$ . The isotopes  $^{49}\text{Ti}$  and  $^{51}\text{V}$  were measured to correct for isobaric interferences on  $^{50}\text{Cr}$ . However, the  $^{49}\text{Ti}$  and  $^{51}\text{V}$  intensities remained indistinguishable from background intensities for all samples, verifying successful separation of V and Ti from Cr during column chromatography. A typical run for a single filament consisted of 24 blocks with 20 cycles each, obtained in static acquisition mode. Amplifiers were rotated and baseline was measured after every block. The Cr standard reference material NIST SRM 979, was used as a terrestrial reference material. The  $^{53}\text{Cr}/^{52}\text{Cr}$  and  $^{54}\text{Cr}/^{52}\text{Cr}$  ratios were normalized to  $^{52}\text{Cr}/^{50}\text{Cr} = 19.28323$  (Shields *et al.*, 1966) by applying the exponential mass fractionation law and are reported as  $\epsilon^i\text{Cr}$ , where  $\epsilon^i\text{Cr} = ([^i\text{Cr}/^{52}\text{Cr}]_{\text{sample}} / [^i\text{Cr}/^{52}\text{Cr}]_{\text{NIST SRM 979}} - 1) \times 10^4$  ( $i = 53$  or  $54$ ). The isotope ratios reported for any one sample represent the average of multiple runs which are also used to determine the external precision reported as 2 standard error (Tables 1.4 and A1.2). Over a period of 9 months, a drift was observed in the Cr standard NIST SRM 979. To correct for the temporal drift, the analyzed data were grouped into 3 sessions, each two months long (Trinquier *et al.*, 2008a). The isotope compositions of each sample are reported relative to the mean value of the standard measured during each session. The external precision (2SD) on  $\epsilon^{53}\text{Cr}$  for the 3 sessions were 0.05, 0.06 and 0.07, respectively. The long term (9 months) reproducibility (2SD) for  $\epsilon^{53}\text{Cr}$  and  $\epsilon^{54}\text{Cr}$  along with the temporal drift was 0.07 and 0.28E respectively ( $n=53$ ) (Figure S1.1).

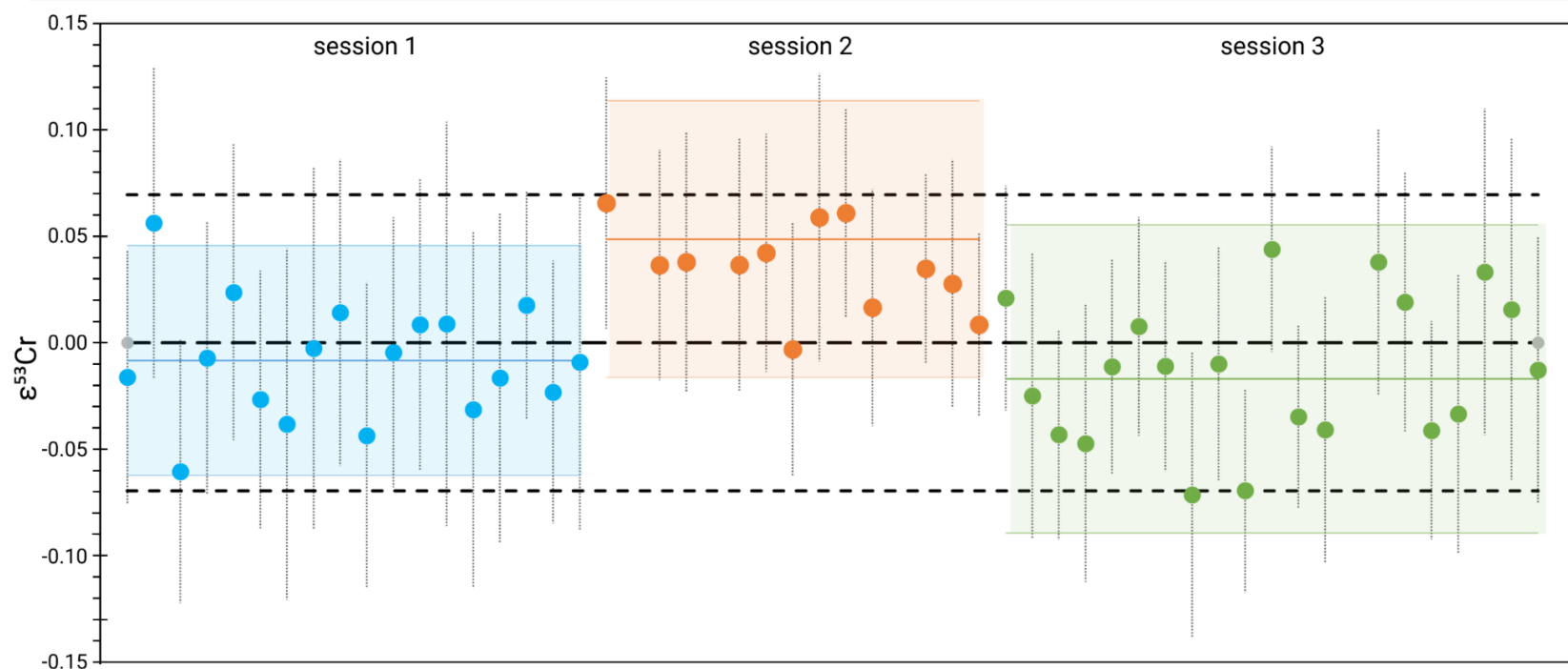


**Figure S1.1.** Drift in  $\epsilon^{53}\text{Cr}$  over a period of 9 months in Cr standard NIST SRM 979. The drift is corrected by grouping the measured  $\epsilon^{53}\text{Cr}$  values into 3 sessions: session 1 (blue circles), session 2 (orange circles) and session 3 (green circles). The  $\epsilon^{53}\text{Cr}$  value for each chondrite sample given in Table 1.4 is reported relative to the mean value of the standard measured during the session (coloured lines within the shaded region). The external precision (2SD) on  $\epsilon^{53}\text{Cr}$  for the 3 sessions was 0.05, 0.06 and 0.07, respectively (shaded boxes). The long term (9 months) NIST SRM 979  $\epsilon^{53}\text{Cr}$  average and reproducibility (2SD) along with the temporal drift was 0.07 (n=53) and shown here in dashed lines.

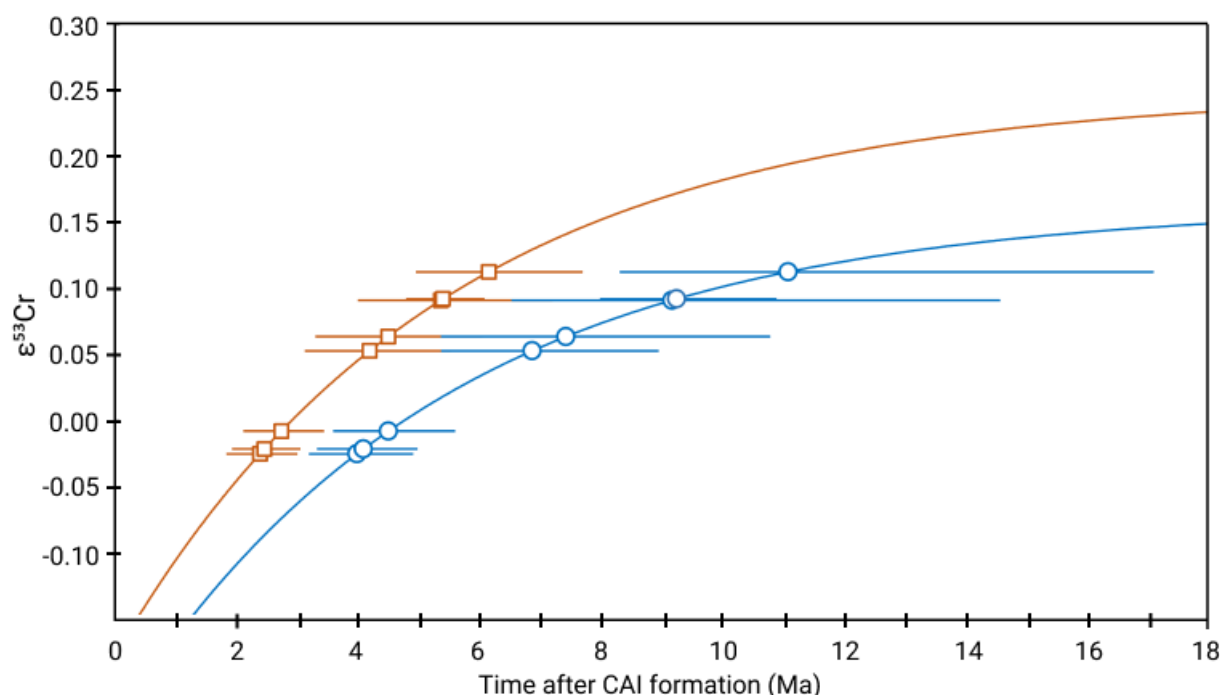


**Figure S1.2.** Comparison between the  $\epsilon^{53}\text{Cr}$  evolution curve of the chondritic reservoir using initial  $\epsilon^{53}\text{Cr} = -0.23$ , canonical  $^{53}\text{Mn}/^{55}\text{Mn} = 6.28 \times 10^{-6}$  as reported by Trinquier et al. (2008b) (blue line) and initial  $\epsilon^{53}\text{Cr} = -0.177$ , canonical  $^{53}\text{Mn}/^{55}\text{Mn} = 6.8 \times 10^{-6}$  as reported by Göpel et al. (2015) (orange line). The  $\epsilon^{53}\text{Cr}$  of the investigated chondrites samples are plotted on both the curves to obtain model ages. The chromite model ages obtained using  $\epsilon^{53}\text{Cr}_i$  and  $^{53}\text{Mn}/^{55}\text{Mn}_i$  reported by Göpel et al. (2015) (orange circles) are older than the model ages obtained using  $\epsilon^{53}\text{Cr}_i$  and  $^{53}\text{Mn}/^{55}\text{Mn}_i$  reported by Trinquier et al. (2008b) (blue circles). The older model ages determined using the initial  $^{53}\text{Cr}$  and  $^{53}\text{Mn}$  abundances by Göpel et al. (2015) do not agree with respective two-point isochron ages for type 3 and type 6 samples (see text).

**Table S1.1.**

Cr, Mn and Fe concentrations and Mn/Cr ratios in the chromite and silicate fractions of the studied samples using an in-house standard solution and BHVO2 rock standard.

Samples	Cr (ppb)	SD Cr	Mn (ppb)	SD Mn	Fe (ppb)	SD Fe	Mn/Cr	2SE Mn/Cr
<b>In-house standard solution (standard for chromite fraction)</b>								
Std. Cr 5	5.0	0.1	0.03	0.01	2.5	0.2	0.0068	0.0011
Std. Cr 25	24.9	0.2	0.18	0.01	13.1	0.1	0.0072	0.0004
Std. Cr 50	49.3	0.5	0.33	0.01	25.1	0.7	0.0066	0.0003
Std. Cr 100	101.0	1.3	0.68	0.03	51.2	0.5	0.0068	0.0003
Std. Cr 500	499.9	1.9	3.31	0.05	251.9	2.5	0.0066	0.0001
<b>Chromite fraction</b>								
SaU 246 (H3/4)	288.2	2.4	2.81	0.02	126.1	2.1	0.0098	0.0001
RaS 337 (H3.6)	80.7	1.0	0.77	0.03	33.3	1.0	0.0095	0.0004
JaH 578 (H6)	195.6	1.6	1.83	0.04	84.3	1.5	0.0093	0.0002
SaU 228 (H6)	50.8	0.5	0.55	0.01	22.2	0.8	0.0108	0.0002

JaH 596 (L3)	170.0	2.0	1.27	0.01	78.8	1.5	0.0075	0.0001
RaS 265 (L3)	82.2	0.5	0.52	0.02	35.4	1.0	0.0064	0.0002
Dho 1012 (L6)	299.5	4.2	2.23	0.03	137.6	1.8	0.0074	0.0001
AHu 017 (L6)	270.5	3.0	1.97	0.05	118.2	2.5	0.0073	0.0002
<b>BHVO2 rock standard (standard for silicate fraction)</b>								
BHVO2 d	0.10	0.01	0.47	0.01	8.4	0.2	4.5	0.4
BHVO2 c	1.94	0.04	8.84	0.14	64.6	1.0	4.6	0.1
BHVO2 b	3.82	0.06	17.21	0.26	129.6	0.7	4.5	0.1
BHVO2 a	11.49	0.18	52.43	0.90	481.3	5.1	4.6	0.1
<b>Silicate fraction</b>								
SaU 246 (H3/4)	1.64	0.03	2.27	0.06	282.2	2.7	1.39	0.04
RaS 337 (H3.6)	1.45	0.01	2.45	0.04	311.8	2.6	1.69	0.03
JaH 578 (H6)	0.75	0.04	2.44	0.05	300.8	3.6	3.24	0.15
SaU 228 (H6)	0.47	0.02	1.94	0.03	261.0	2.8	4.13	0.13
JaH 596 (L3)	2.51	0.02	2.80	0.06	229.9	2.4	1.12	0.02
RaS 265 (L3)	1.27	0.02	2.78	0.07	266.3	4.1	2.18	0.06
Dho 1012 (L6)	0.92	0.01	2.78	0.05	273.4	0.9	3.03	0.06
AHu 017 (L6)	1.29	0.04	2.75	0.06	262.8	2.8	2.13	0.08
<b>OKUM rock standard</b>								
OKUM b	3.34	0.02	1.98	0.03	130.6	1.6	0.59	0.01
OKUM c	1.66	0.03	0.96	0.02	64.2	1.6	0.58	0.01
OKUM d	0.44	0.01	0.26	0.02	16.9	0.8	0.59	0.03
<i>Mean OKUM</i>							0.59	0.01

Mn, Cr and Fe concentrations in the silicate and chromite fractions are determined using rock standard BHVO2 and an in-house standard solution, respectively. The in-house standard solution is prepared using single element solutions of Cr, Fe, Mg, Ti, V and Mn to closely mimic the expected composition of the analyzed chromite grains. Calibration curves are obtained using the standard solutions of different dilution levels by linear regression and then used to determine the Mn, Cr and Fe concentrations in the samples. The uncertainties on Mn, Cr and Fe concentrations determined by the linear regressions are given in 1 standard deviation. The uncertainties on Mn/Cr ratio is determined by replicate measurements; uncertainty is given in 2 standard error (n=5). The Mn/Cr ratio of OKUM rock standard measured along with the silicate fractions was determined to be  $0.59 \pm 0.01$  (2SD). It agrees with the Mn/Cr ( $= 0.58 \pm 0.01$ ) reported in Peters and Pettke (2017).

**Table S1.2.**

$\epsilon^{53}\text{Cr}$  and  $\epsilon^{54}\text{Cr}$  compositions of studied samples.

						<sup>53</sup> Cr		<sup>54</sup> Cr	
						mean	2SE <sup>b</sup>	mean	2SE <sup>e</sup>
Chromite fraction									
HaW017	HaW017_11_1	0.10	0.03	-0.77	0.06	0.05	0.04	-0.59	0.16
	HaW017_13_1	0.03	0.03	-0.42	0.06				
	HaW017_13_2	0.06	0.04	-0.50	0.07				
	HaW017_13_3	0.02	0.03	-0.68	0.06				
JaH596	JaH596_13_1	-0.02	0.04	-0.79	0.07				

SaU228	JaH596_13_2	-0.10	0.03	-0.65	0.07	-0.03	0.03	-0.57	0.17
	JaH596_13_3	-0.02	0.04	-0.73	0.08				
	JaH596_16_1	-0.01	0.03	-0.56	0.08				
	JaH596_16_2	0.00	0.03	-0.52	0.06				
	JaH596_16_3	0.00	0.04	-0.20	0.08				
	SaU288_14_1	0.07	0.03	-0.67	0.08				
	SaU288_14_2	0.05	0.03	-0.90	0.07				
	SaU288_14_3	0.15	0.04	-0.37	0.09				
RaS337	SaU288_14_4	0.09	0.03	-0.54	0.06	0.09	0.05	-0.62	0.22
	RaS337_15_1	-0.01	0.04	-0.39	0.08	-0.02	0.03	-0.40	0.01
	RaS337_15_2	-0.04	0.04	-0.39	0.07				
Dho1012	Dho1012_17_1	0.11	0.04	-0.25	0.08				
	Dho1012_17_2	0.10	0.03	-0.66	0.08				
	Dho1012_17_3	0.08	0.03	-0.33	0.07				
	Dho1012_17_4	0.11	0.03	-0.43	0.07				
	Dho1012_17_5	0.07	0.04	-0.60	0.09				
RaS265	RaS265_18_1	-0.04	0.03	-0.51	0.07	-0.01	0.03	-0.49	0.07
	RaS265_18_2	0.04	0.03	-0.43	0.07				
	RaS265_18_3	-0.01	0.04	-0.61	0.09				
	RaS265_18_4	-0.04	0.04	-0.42	0.08				
	RaS265_18_5	0.02	0.04	-0.46	0.08				
JaH578	JaH578_19_1	0.15	0.04	-0.55	0.07	0.11	0.03	-0.41	0.07
	JaH578_19_2	0.02	0.03	-0.38	0.07				
	JaH578_19_3	0.14	0.03	-0.39	0.07				
	JaH578_19_4	0.09	0.03	-0.53	0.06				
	JaH578_19_5	0.15	0.04	-0.27	0.09				
SaU246	JaH578_23_1	0.15	0.02	-0.37	0.05	0.06	0.05	-0.43	0.20
	JaH578_23_2	0.14	0.03	-0.34	0.06				
	JaH578_23_3	0.07	0.03	-0.49	0.05				
	SaU246_20_1	0.01	0.04	-0.38	0.07				
	SaU246_20_2	0.11	0.04	-0.71	0.07				
	SaU246_20_3	0.05	0.03	-0.39	0.07				
	SaU246_20_4	0.10	0.03	-0.24	0.06				
Silicate fraction									
JaH596 WR	JaH596_26_1	0.37	0.02	-0.55	0.05	0.36	0.02	-0.41	0.09
	JaH596_26_2	0.38	0.02	-0.31	0.04				
	JaH596_26_3	0.35	0.03	-0.46	0.06				
	JaH596_26_4	0.39	0.02	-0.35	0.05				
	JaH596_26_5	0.33	0.02	-0.36	0.05				
RaS337 WR	RaS337_27_1	0.46	0.02	0.09	0.05	0.43	0.02	-0.10	0.14
	RaS337_27_2	0.42	0.03	-0.12	0.05				
	RaS337_27_3	0.41	0.03	-0.08	0.05				
	RaS337_27_4	0.43	0.02	-0.26	0.05				
Dho1012 WR	Dho1012_27_1	0.20	0.03	-0.23	0.05	0.19	0.03	-0.22	0.04
	Dho1012_27_2	0.22	0.02	-0.27	0.04				
	Dho1012_27_3	0.17	0.02	-0.17	0.05				
	Dho1012_27_4	0.15	0.02	-0.20	0.04				
	Dho1012_27_5	0.24	0.02	-0.25	0.04				
HaW017 WR	HaW017_28_1	0.24	0.02	-0.30	0.05	0.19	0.03	-0.22	0.04
	HaW017_28_2	0.30	0.03	-0.26	0.05				
	HaW017_28_3	0.25	0.02	-0.24	0.05				

	HaW017_28_4	0.23	0.03	-0.40	0.05				
	HaW017_28_5	0.22	0.02	-0.17	0.05	0.25	0.03	-0.28	0.08
RaS265 WR	RaS265_28_1	0.57	0.04	-0.02	0.09				
	RaS265_30_2	0.60	0.05	0.14	0.11				
	RaS265_31_3	0.57	0.04	0.28	0.09	0.58	0.02	0.14	0.18
SaU246 WR	SaU246_30_1	0.34	0.03	-0.31	0.06				
	SaU246_30_2	0.38	0.03	-0.05	0.06				
	SaU246_30_3	0.31	0.03	0.02	0.07				
	SaU246_30_4	0.37	0.03	-0.23	0.06				
	SaU246_30_5	0.36	0.04	-0.15	0.08	0.35	0.02	-0.14	0.12
JaH578 WR	JaH578_30_2	0.75	0.05	0.37	0.10				
	JaH578_30_3	0.80	0.03	0.47	0.07				
	JaH578_30_4	0.76	0.03	0.47	0.07	0.77	0.03	0.44	0.07
SaU228 WR	SaU228_39_1	0.44	0.03	-0.32	0.06				
	SaU228_39_2	0.46	0.03	-0.27	0.06				
	SaU228_39_3	0.46	0.03	-0.22	0.07				
	SaU228_39_4	0.41	0.04	-0.19	0.07				
	SaU228_39_5	0.39	0.04	-0.21	0.08	0.43	0.03	-0.24	0.04
<b>Terrestrial chromite</b>									
Kalimashi Mines, Albania									
	CH_6_22_1	-0.05	0.03	0.04	0.07				
	CH_6_22_2	-0.03	0.03	0.07	0.05				
	CH_3_22_1	0.04	0.03	0.11	0.07				
	CH_3_22_2	0.07	0.03	0.21	0.07				
	CH_3_22_3	-0.04	0.03	0.10	0.07	0.00	0.05	0.10	0.06
OKUM	OKUM_50_1	0.05	0.03	0.14	0.07				
	OKUM_50_2	0.03	0.04	0.20	0.08				
	OKUM_50_3	0.01	0.03	0.06	0.06	0.03	0.02	0.13	0.07

<sup>a</sup> SE<sub>i</sub> refers to the internal error (reported as 1 standard error) for a single filament run consisted of 24 blocks with 20 cycles each.

<sup>b</sup> SE<sub>e</sub> refers to the external error of the replicate measurements (reported as 2 standard error).



## Supplementary Information References

Göpel C., Birck J. L., Galy A., Barrat J. A., Zanda B. (2015) Mn-Cr systematics in primitive meteorites: Insights from mineral separation and partial dissolution. *Geochimica et Cosmochimica Acta*, 156, 1-24.

Peters D. and Pettke T. (2017) Evaluation of major to ultra trace element bulk rock chemical analysis of nanoparticulate pressed powder pellets by LA-ICP-MS. *Geostandards and Geoanalytical Research*, 41(1), 5-28.

Schoenberg R. and Von Blanckenburg F. (2005) An assessment of the accuracy of stable Fe isotope ratio measurements on samples with organic and inorganic matrices by high-resolution multicollector ICP-MS. *International Journal of Mass Spectrometry*, 242(2-3), 257-272.

Schoenberg R., Merdian A., Holmden C., Kleinhanns I. C., Haßler K., Wille M., Reitter E. (2016) The stable Cr isotopic compositions of chondrites and silicate planetary reservoirs. *Geochimica et cosmochimica acta*, 183, 14-30.

Shields W. R., Murphy T. J., Catanzaro E. J., Garner E. L. (1966) Absolute isotopic abundance ratios and the atomic weight of a reference sample of chromium. *Journal of Research of the National Bureau of Standards. Section A, Physics and Chemistry*, 70(2), 193.

Trinquier A., Birck J. L., Allègre C. J. (2008a) High-precision analysis of chromium isotopes in terrestrial and meteorite samples by thermal ionization mass spectrometry. *Journal of Analytical Atomic Spectrometry*, 23(12), 1565-1574.

Trinquier A., Birck J. L., Allègre C. J., Göpel C., Ulfbeck D. (2008b)  $^{53}\text{Mn}$ - $^{53}\text{Cr}$  systematics of the early Solar System revisited. *Geochimica et Cosmochimica Acta*, 72, 5146-5163.

Yamakawa A., Yamashita K., Makishima A. and Nakamura E. (2009) Chemical separation and mass spectrometry of Cr, Fe, Ni, Zn, and Cu in terrestrial and extraterrestrial materials using thermal ionization mass spectrometry. *Analytical Chemistry*, 81(23), 9787-9794.

# Supplementary Information

## Chapter 2

### S2.1 Samples and Analytical Methods

Seven samples from IIAB, IIIAB and IVA iron meteorite groups were analysed in this study. Chromite from whole rock iron meteorites, Sikhote Alin, Agoudal & Cape York and daubréelite from samples NWA 11420, Yanhuítlan & Duchesne (all from the Natural History Museum Bern) were separated. Pre-isolated chromite grains from sample Saint Aubin were received from the Natural History Museum Vienna. Collection sample numbers are provided in Table 2.1. At the University of Bern, chromite grains were identified using an optical microscope and isolated in small whole-rock fragments. The fragments were hand crushed using a pre-cleaned agate mortar and treated in conc. aqua regia on a hot plate set to 90 °C for 48 hrs to completely dissolve the metal-sulphide dominated matrix, leaving behind residual chromite grains. To separate daubréelite, whole meteorite fragment or troilite (sulphide) nodules were treated with conc. aqua regia at room temperature for 12 hrs and the residue was further separated into a magnetic and non-magnetic fraction using a magnet. Daubréelite grains were isolated from the non-magnetic portion and confirmed with energy dispersive X-ray spectroscopy (EDS) on a ZEISS EVO50 SEM. Consecutively, individual grains were handpicked. Chromite and daubréelite grains weighing 1-3 mg from all the samples were transferred to a 7 ml Savillex® vial with 150-250 mg of ammonium bifluoride (ABF,  $\text{NH}_4\text{F} \cdot \text{HF}$ , Sigma-Aldrich®, Trace Metal grade) and completely digested following the protocol described in O'Hara *et al.* (2017). The sample and reagent mixture was thermalized in a convection oven set to 230 °C for 48 hrs. Upon cooling, the mixture was dried down twice, first after treatment with 2 ml conc.  $\text{HNO}_3$  and then after treatment with 1 ml conc.  $\text{HNO}_3$  and 2 ml MilliQ® water.

Before chemical separation, an aliquot from digested chromite/daubréelite fraction from each sample was diluted in 10 ml 0.5 M  $\text{HNO}_3$  to target for a 10 ppb Cr solution. These aliquots were used to determine Cr, Mn, and Fe concentrations using a 7700x Agilent ICP-MS at the Institute of Geography, University of Bern. Uncertainties on Mn/Cr and Fe/Cr ratios are reported in 2 standard error of the replicate measurements ( $n = 5$ ) and remained <5 % for all the samples.

The procedure for Cr purification was adopted from Schoenberg *et al.* (2016). It includes three steps of a combination of cation-anion exchange chromatography modified after Schoenberg and von Blanckenburg, (2005) (column 1), Trinquier *et al.* (2008a) and Yamakawa *et al.* (2009) (column 2 and 3). In brief, an aliquot containing 15 µg of Cr from each sample was taken up in 1 ml 6 M HCl and loaded on the first 7.5 mL Spectrum® polypropylene column containing 2 ml anion resin (BioRad® AG 1X8 100-200 mesh size). The Cr eluate from the first column was dried down, redissolved in 400 µl 6 M HCl, equilibrated on a hotplate set to 130 °C for ~30 min one day before the chemical separation and stored at room temperature overnight. The next day, the sample was re-equilibrated on a hot plate at 130 °C for one hour, diluted with 2 ml of MilliQ® water to obtain 2.4 ml 1 M HCl and loaded on the second column filled with 2 ml cation resin (BioRad® AG 50W-X8 200-400 mesh size). The second column separation step produced a solution with mostly Cr, but incompletely separated from Ti and V. The third column with 0.5 ml BioRad® AG 50W-X8 200-400 mesh was used in order to obtain a clean Cr separate, free of Ti and V. The elute from the second column was dried down on a hot plate (at 90 °C), taken up in 0.5 ml conc. HNO<sub>3</sub> and dried down again immediately to transform the samples into nitrate form. The residue was redissolved in 3 ml 0.4 M HNO<sub>3</sub> for 30 min on a hotplate at 80 °C and let react cold for 5 days for the production of chloro-aquo complexes. Afterwards, each sample was loaded on the third column. The matrix was eluted in 8 ml 0.5 M HF and 9.5 ml 1 M HCl, and Cr was collected in 8 ml 4 M HCl. Finally, the Cr separate was redissolved in 100 µl conc. HNO<sub>3</sub> and dried immediately at 130 °C on a hotplate. This step was repeated 2 times until the residual organics from the column chemistry was completely destroyed. Typical recovery of Cr was in excess of 80% for the whole column chemistry, determined by measurement of spiked sample solutions on an ICP-MS. Total chemistry blanks were below 10 ng, which are negligible compared to the µg range of Cr isolated and loaded on the filaments for each sample. The purified Cr was dissolved in a sufficient amount of 6 M HCl to yield a solution with a Cr concentration of ca. 1 µg/µl for loading on Re filaments for mass spectrometry. 1 µg/µl Cr was mixed with 1.4 µL 4% silica gel on a piece of Parafilm® and loaded on the filament, minimizing the spread of the sample droplet. 0.7 µL Al (1000 ppm) and 0.7 µL H<sub>3</sub>BO<sub>3</sub> (5000 ppm B) was then added to the top of this mixture. After drying the mixture at around 0.8 A, the filament was heated slowly to a dull red glow for less than one second.

The samples were analysed by Thermal Ionization Mass Spectrometer using a Thermo Scientific TRITON Plus instrument at the Institute of Geological Sciences, University of Bern. Aliquots of each sample were loaded on multiple filaments and measured at <sup>52</sup>Cr signal intensity between 8 and 12 V (10<sup>-11</sup> Ω resistor). Intensities of <sup>50</sup>Cr, <sup>51</sup>V, <sup>52</sup>Cr, <sup>53</sup>Cr, <sup>54</sup>Cr, <sup>55</sup>Mn and <sup>56</sup>Fe were measured on the Faraday cups L3, L2, L1, C, H1, H2 and H3, respectively (Trinquier *et al.*, 2008a). Alignment of all Cr peaks (peak scan) was ensured before each measurement and peak center was monitored on <sup>53</sup>Cr in the center cup. Isobaric interference of <sup>54</sup>Fe on <sup>54</sup>Cr was corrected by monitoring <sup>56</sup>Fe. The isotopes <sup>49</sup>Ti and <sup>51</sup>V

were measured to correct for isobaric interferences on  $^{50}\text{Cr}$ . However, the  $^{49}\text{Ti}$  and  $^{51}\text{V}$  intensities remained indistinguishable from background intensities for all samples, verifying successful separation of V and Ti from Cr during column chromatography. A typical run for a single filament consisted of 24 blocks with 20 cycles each (integration time = 8.389 sec.), obtained in static acquisition mode. Gain calibration was done once, at the beginning of every measurement day. Amplifiers were rotated and the baseline was measured after every block (baseline = 30 cycles, each of 1.05 sec.). The Cr standard reference material NIST SRM 979, was used as a terrestrial reference material. The  $^{53}\text{Cr}/^{52}\text{Cr}$  and  $^{54}\text{Cr}/^{52}\text{Cr}$  ratios were normalized to  $^{52}\text{Cr}/^{50}\text{Cr} = 19.28323$  (Shields *et al.*, 1966) by applying the exponential mass fractionation law and are reported as  $\epsilon^i\text{Cr}$ , where  $\epsilon^i\text{Cr} = ([^i\text{Cr}/^{52}\text{Cr}]_{\text{sample}} / [^i\text{Cr}/^{52}\text{Cr}]_{\text{NIST SRM 979}} - 1) \times 10^4$  ( $i = 53$  or  $54$ ).

## S2.2 Precision and accuracy of Cr isotope data

The  $\epsilon^i\text{Cr}$  ( $i = 53$  or  $54$ ) reported for any one sample represent the mean of the replicate measurements ( $n = 7$ -13, Tables 2.1 and A2.1). The replicate measurements for each sample are used to determine the external precision reported as 2 standard errors (Tables 2.1 and A2.1). The isotope compositions of each sample are reported relative to the mean value of the standard reference material (NIST SRM 979) measured along with the samples in each measurement session (single turret). The external precision (2 standard deviations) for the standard reference material (NIST SRM 979) in each measurement session was  $\sim 0.1$  for  $\epsilon^{53}\text{Cr}$  and  $\sim 0.2$  for  $\epsilon^{54}\text{Cr}$ .

To estimate the analytical accuracy of Cr isotopic data, we evaluated the consistency of results obtained on both terrestrial standards and meteorite samples and compared to the published results. The Cr isotope data ( $\epsilon^{53}\text{Cr} = 0.072 \pm 0.066$ ,  $\epsilon^{54}\text{Cr} = 0.881 \pm 0.120$ ) for Allende (CV) agrees with  $\epsilon^{53}\text{Cr} = 0.11 \pm 0.02$  and  $\epsilon^{54}\text{Cr} = 0.95 \pm 0.06$ , reported in Zhu *et al.* (2021). Cr isotope data for terrestrial rock standard IAG OKUM is also in good agreement with the Cr isotope data for terrestrial samples compiled in Zhu *et al.* (2021). Whole rock samples for an ordinary chondrite (Dergaon, H5) and Acapulcoite (RF 529) measured along with the iron meteorite chromite/daubréelite fractions are in good agreement with the literature (Zhu *et al.*, 2021). Additionally,  $\epsilon^{54}\text{Cr} = -0.779 \pm 0.061$  and  $\epsilon^{53}\text{Cr} = -0.268 \pm 0.029$  for Saint Aubin chromite reported in the present study is in perfect agreement with  $\epsilon^{54}\text{Cr} = -0.81 \pm 0.08$  and  $\epsilon^{53}\text{Cr} = -0.28 \pm 0.06$  reported in Trinquier *et al.* (2007, 2008b).

## S2.3 Correction for spallogenic Cr

Spallation reactions induced by cosmic-ray exposure (CRE) can alter  $^{53}\text{Cr}/^{52}\text{Cr}$  and  $^{54}\text{Cr}/^{52}\text{Cr}$  ratios in solar system objects. This alteration depends on the following parameters: (1) duration and intensity of cosmic ray exposure (2) Fe/Cr ratio and (3) shielding condition for any given sample/component. A particular advantage of analysing chromite and daubréelite in iron meteorites is that due to low Fe/Cr ratios in these phases, spallogenic contributions of  $^{53}\text{Cr}$  and  $^{54}\text{Cr}$  produced by galactic cosmic radiation (GCR) from Fe are negligible and hence no correction for spallogenic Cr is required (Trinquier *et al.*, 2008b; Liu *et al.*, 2019). Less suitable for dating is the iron metal of iron meteorites, because of its very high Fe/Cr combined with the typically long irradiation time in space for iron meteorites, which leads to significant production of spallogenic  $^{53}\text{Cr}$  and  $^{54}\text{Cr}$  that is difficult to correct for and results in high uncertainties. For instance, a Fe/Cr ratio of 0.5 (Figure S2.1(b)), which is typical in chromite and daubréelite would result in  $\epsilon^{53}\text{Cr}$  and  $\epsilon^{54}\text{Cr}$  excesses of 0.002 and 0.005, respectively, even if the CRE age for the iron meteorite is as high as 800 Ma ( $\epsilon^{53}\text{Cr}$  and  $\epsilon^{54}\text{Cr}$  excesses determined using equation given in Table 2 in Trinquier *et al.* (2007) and a  $^{53}\text{Cr}$  and  $^{54}\text{Cr}$  production rate of  $2.9 \times 10^{11}$  atoms/Ma in Fe targets (Birck and Allégre, 1985)). This spallogenic  $\epsilon^{53}\text{Cr}$  and  $\epsilon^{54}\text{Cr}$  contribution is well within the analytical uncertainties of the Cr isotopic measurements reported here.

Liu *et al.* (2019) measured Cr isotopic composition of 16 iron meteorites belonging to different chemical groups and showed that the CRE can cause coupled excesses in  $\epsilon^{53}\text{Cr}$  and  $\epsilon^{54}\text{Cr}$  with a linear correlation line of  $\epsilon^{54}\text{Cr} = (3.90 \pm 0.03) \times \epsilon^{53}\text{Cr}$ . This correlation is independent of the duration and intensity of cosmic ray exposure, Fe/Cr ratio and shielding condition for any given sample/component and hence provide an alternate way to test the need for spallogenic Cr correction. Figure S2.1(a) shows an  $\epsilon^{54}\text{Cr}$  vs.  $\epsilon^{53}\text{Cr}$  plot for the chromite and daubréelite separates from the analysed iron meteorites. The  $\epsilon^{54}\text{Cr}$  and  $\epsilon^{53}\text{Cr}$  values show no correlation for the analysed chromite/daubréelite fractions and corroborates to the negligible spallogenic contribution in these components.

## S2.4 Summary of $(^{53}\text{Mn}/^{55}\text{Mn})_i$ and $\epsilon^{53}\text{Cr}_i$

Table A2.4 provides a compilation of solar system initial  $(^{53}\text{Mn}/^{55}\text{Mn})_i$  and  $\epsilon^{53}\text{Cr}_i$  reported by different methods/approaches in the literature. Shukolyukov and Lugmair (2006), Moynier *et al.* (2007) and Göpel *et al.* (2015) determined the solar system initial  $(^{53}\text{Mn}/^{55}\text{Mn})_i$  and  $\epsilon^{53}\text{Cr}_i$  by evaluating the Mn/Cr data for bulk rock carbonaceous chondrites (CC) on a  $^{55}\text{Mn}/^{52}\text{Cr}$  versus  $\epsilon^{53}\text{Cr}$  diagram. Shukolyukov and Lugmair (2006) reported that the correlation line yields a  $^{53}\text{Mn}/^{55}\text{Mn}$  of  $8.5 \pm 1.5 \times 10^{-6}$  and initial  $\epsilon^{53}\text{Cr} = -0.21 \pm 0.09$  at the time of Mn/Cr fractionation. Göpel *et al.* (2015) obtained a

$(^{53}\text{Mn}/^{55}\text{Mn})_i = 6.24 \times 10^{-6}$  and  $\epsilon^{53}\text{Cr}_i = -0.15 \pm 0.10$  from the bulk rock CC isochron. Based on this value and with respect to the age of the solar system, the authors determined solar system initial  $(^{53}\text{Mn}/^{55}\text{Mn})_i = 6.8 \pm 0.66 \times 10^{-6}$  and corresponding initial  $\epsilon^{53}\text{Cr}_i = -0.177$  (see Fig. 8 of Gopel *et al.*, 2015). It is important to note that  $^{55}\text{Mn}/^{52}\text{Cr}$  versus  $^{53}\text{Cr}/^{52}\text{Cr}$  diagram for bulk rock CC is sensitive to the choice of samples that are included into the regression calculation (Gopel *et al.*, 2015; Zhu *et al.*, 2021). Trinquier *et al.* (2008b) constrained  $(^{53}\text{Mn}/^{55}\text{Mn})_i = 6.28 \pm 0.66 \times 10^{-6}$  using an isochron based on  $^{54}\text{Cr}$ -poor fractions of CI Orgueil and reported it as the best estimate for the solar system initial  $^{53}\text{Mn}$  abundance. However, Zhu *et al.* (2021) reported that the  $^{53}\text{Mn}$ - $^{53}\text{Cr}$  correlation could be a mixing line since chondritic components, e.g., CAIs, chondrules, matrix, metal, and carbonates have different origins and time of formation. To obtain the solar system initial  $\epsilon^{53}\text{Cr}_i$ , Trinquier *et al.* (2008b) back-calculated  $\epsilon^{53}\text{Cr}_i$  for a wide range of chondritic reservoirs using present-day  $^{53}\text{Cr}/^{52}\text{Cr}$  and Mn/Cr ratios to the time of CAI formation and reported the average of all  $\epsilon^{53}\text{Cr}_i$  as solar system initial  $\epsilon^{53}\text{Cr}_i = -0.23 \pm 0.09$ . Nyquist *et al.* (2009) used a correlation regression between initial  $(^{53}\text{Mn}/^{55}\text{Mn})_i$  and initial  $(^{26}\text{Al}/^{27}\text{Al})_i$  for solar system materials that have been analysed by both Mn-Cr and Al-Mg chronometers to determine the value of initial  $(^{53}\text{Mn}/^{55}\text{Mn})_{\text{ss}} = (9.1 \pm 1.7) \times 10^{-6}$  corresponding to the assumed  $(^{26}\text{Al}/^{27}\text{Al})_{\text{ss}} = 5.1 \times 10^{-5}$ . In the present study, the solar system initial  $\epsilon^{53}\text{Cr}_i = -0.30 \pm 0.05$  is proposed after calibrating the Mn-Cr model ages for the core formation in magmatic iron meteorite to the corresponding Hf-W core formation ages. The proposed value agrees with the previously reported solar system initial  $\epsilon^{53}\text{Cr}_i$  values. Additionally, it also agrees with solar system initial  $\epsilon^{53}\text{Cr}_i = -0.34$  when  $(^{53}\text{Mn}/^{55}\text{Mn})_i = 3.16 \pm 0.11 \times 10^{-6}$  and  $\epsilon^{53}\text{Cr}_i = -0.10 \pm 0.06$  (Zhu *et al.*, 2019) determined for bulk rock angrites are calibrated against the age of the solar system.

**Table S2.1.**

$\epsilon^{53}\text{Cr}$  and  $\epsilon^{54}\text{Cr}$  compositions of studied samples.

		$\epsilon^{53}\text{Cr}$	SEi <sup>a</sup>	$\epsilon^{54}\text{Cr}$	SEi <sup>a</sup>	$\epsilon^{53}\text{Cr}$			$\epsilon^{54}\text{Cr}$		
						mean	2SDe <sup>b</sup>	2SEe <sup>b</sup> (n)	mean	2SDe <sup>b</sup>	2SEe <sup>b</sup> (n)
IIAB											
Agoudal (Chr)	AG_36_1	-0.289	0.027	-0.895	0.055	-0.210	0.081	0.023 (12)	-0.784	0.206	0.060 (12)
	AG_36_1b	-0.161	0.024	-0.875	0.051						
	AG_36_1c	-0.197	0.027	-0.761	0.054						
	AG_36_1d	-0.235	0.027	-0.947	0.056						
	AG_36_1e	-0.251	0.028	-0.849	0.057						
	AG_36_3	-0.181	0.027	-0.752	0.058						
	AG_36_3b	-0.182	0.029	-0.789	0.059						
	AG_36_4	-0.187	0.031	-0.707	0.063						
	AG_36_5	-0.257	0.036	-0.693	0.074						
	AG_53_1	-0.234	0.032	-0.805	0.069						
	AG_53_2	-0.151	0.032	-0.792	0.062						
	AG_53_3	-0.193	0.029	-0.539	0.065						
Sikhote-Alin (Chr)	SA_36_1	-0.159	0.028	-0.821	0.053	-0.228	0.087	0.025 (12)	-0.923	0.177	0.051 (12)
	SA_36_2	-0.255	0.030	-1.014	0.062						
	SA_36_3	-0.249	0.026	-0.931	0.057						
	SA_36_4	-0.189	0.025	-1.036	0.059						
	SA_36_4b	-0.178	0.026	-0.972	0.049						
	SA_36_5	-0.237	0.025	-0.842	0.052						
	SA_36_5b	-0.253	0.024	-0.966	0.050						
	SA_53_1	-0.188	0.029	-0.846	0.060						
	SA_53_1b	-0.212	0.025	-0.813	0.052						
	SA_53_2	-0.231	0.029	-1.050	0.057						

<b>NWA 11420 (Daub)</b>	SA_53_3	-0.325	0.046	-0.803	0.078						
	SA_53_3b	-0.256	0.030	-0.978	0.062						
	Daub_37_2	-0.161	0.029	-0.808	0.063	-0.203	0.118	0.045 (7)	-0.768	0.147	0.055 (7)
	Daub_37_3	-0.183	0.031	-0.731	0.064						
	Daub_37_4	-0.131	0.026	-0.654	0.048						
	Daub_53_1	-0.161	0.029	-0.680	0.067						
	Daub_53_2	-0.222	0.024	-0.836	0.048						
	Daub_53_3	-0.320	0.032	-0.854	0.069						
	Daub_53_3b	-0.240	0.040	-0.810	0.077						
<b>IIIAB</b>											
<b>Cape York (Chr)</b>	CY_41_1	-0.164	0.030	-0.672	0.062	-0.196	0.154	0.043 (13)	-0.780	0.223	0.062 (13)
	CY_41_2	-0.188	0.034	-0.888	0.067						
	CY_41_3	-0.109	0.034	-0.588	0.072						
	CY_41_3b	-0.042	0.029	-0.692	0.059						
	CY_41_2b	-0.099	0.032	-0.859	0.057						
	CY_41_1b	-0.182	0.030	-0.870	0.058						
	CY_40_1	-0.176	0.024	-0.635	0.046						
	CY_54_1	-0.240	0.045	-0.956	0.089						
	CY_54_2	-0.293	0.046	-0.766	0.082						
	CY_54_3	-0.236	0.030	-0.789	0.060						
	CY_54_1b	-0.227	0.039	-0.802	0.067						
	CY_54_2b	-0.272	0.033	-0.700	0.066						
	CY_54_3b	-0.318	0.048	-0.923	0.084						
	S'Aub_50_1	-0.273	0.033	-0.810	0.073	-0.268	0.091	0.029 (10)	-0.779	0.193	0.061 (10)
<b>Saint Aubin (Chr)</b>	S'Aub_50_3	-0.242	0.039	-0.710	0.083						
	S'Aub_50_2	-0.330	0.031	-0.634	0.063						
	S'Aub_54_1	-0.249	0.032	-0.903	0.068						
	S'Aub_54_1b	-0.256	0.031	-0.880	0.068						
	S'Aub_54_2	-0.326	0.033	-0.926	0.070						
	S'Aub_54_2b	-0.221	0.033	-0.763	0.069						



	S'Aub_54_3	-0.193	0.028	-0.669	0.061						
	S'Aub_54_3b	-0.333	0.028	-0.803	0.061						
	S'Aub_54_3c	-0.255	0.029	-0.696	0.061						
<b>IVA</b>											
<b>Yanhuitlan (Daub)</b>	Yan_55_1	-0.192	0.030	-0.351	0.057	-0.272	0.085	0.027 (10)	-0.468	0.193	0.061 (10)
	Yan_55_1b	-0.273	0.027	-0.587	0.056						
	Yan_55_2b	-0.254	0.032	-0.529	0.065						
	Yan_55_2b	-0.285	0.032	-0.397	0.067						
	Yan_55_2c	-0.335	0.027	-0.583	0.061						
	Yan_55_2d	-0.234	0.029	-0.502	0.063						
	Yan_55_3	-0.228	0.029	-0.269	0.058						
	Yan_55_3b	-0.290	0.029	-0.509	0.063						
	Yan_55_3c	-0.307	0.028	-0.449	0.063						
	Yan_55_3d	-0.319	0.030	-0.499	0.062						
<b>Duchesne (Daub)</b>	Duch_55_1c	-0.144	0.038	-0.680	0.087	-0.160	0.097	0.037 (7)	-0.487	0.413	0.156 (7)
	Duch_55_1d	-0.134	0.040	-0.753	0.086						
	Duch_55_1e	-0.203	0.044	-0.674	0.103						
	Duch_55_1f	-0.092	0.046	-0.286	0.099						
	Duch_55_1g	-0.171	0.041	-0.509	0.084						
	Duch_55_1x	-0.249	0.050	-0.311	0.104						
	Duch_55_1xx	-0.127	0.045	-0.198	0.104						
<b>Standards</b>											
<b>IAG OKUM</b>	OKUM_50_1	0.046	0.032	0.140	0.067	0.020	0.159	0.065 (7)	0.083	0.270	0.110 (7)
	OKUM_50_2	0.034	0.038	0.204	0.081						
	OKUM_50_3	0.013	0.029	0.057	0.063						
	OKUM_61_1	-0.054	0.029	0.114	0.064						
	OKUM_61_1b	-0.106	0.029	-0.231	0.064						
	OKUM_61_2	0.168	0.031	0.173	0.063						
	OKUM_61_2b	0.036	0.031	0.125	0.062						
<b>Allende (CV)<sup>c</sup></b>	All1	0.045	0.031	0.967	0.061	0.072	0.132	0.066 (4)	0.881	0.241	0.120 (4)

	All1b	0.092	0.030	0.865	0.063						
	All2	-0.014	0.027	0.691	0.054						
	All2b	0.167	0.031	1.001	0.070						
<b>Dergaon WR (H5)</b>	D_W_63_1	0.057	0.031	-0.547	0.069	0.117	0.078	0.039 (4)	-0.380	0.244	0.122 (4)
	D_W_63_2b	0.138	0.035	-0.399	0.081						
	D_W_63_2	0.162	0.029	-0.203	0.060						
	D_W_63_1b	0.112	0.036	-0.371	0.080						
<b>RF 529 WR (Acap)</b>	Acap1	0.187	0.026	-0.677	0.058	0.122	0.089	0.045 (4)	-0.698	0.170	0.085 (4)
	Acap1b	0.077	0.026	-0.741	0.058						
	Acap2	0.138	0.029	-0.572	0.067						
	Acap2b	0.083	0.030	-0.801	0.064						

<sup>a</sup>SEi refers to the internal error (reported as 1 standard error) for a single filament run consisted of 24 blocks with 20 cycles each (integration time = 8.389 sec.).

<sup>b</sup>SDe and SEe refer to the external errors of the replicate measurements reported as 2 standard deviations and 2 standard errors, respectively. n = number of replicate measurements.

Abbreviations used: Daub = daubréelite, Chr = Chromite, WR = whole rock, Acap = Acapulcoite.

<sup>c</sup>Allende rock standard (Smithsonian standard powder, USNM 3529, Split 18 position 1).

**Table S2.2.**

Weighted mean  $\epsilon^{53}\text{Cr}$  and  $\epsilon^{182}\text{W}$  of combined IIAB, IIIAB and IVA groups and corresponding Mn-Cr and Hf-W model ages.

Sample	$\epsilon^{53}\text{Cr}$	Mn-Cr Model age (Ma)	Iron meteorite group	$\epsilon^{182}\text{W}$	Hf-W Model age (Ma)
Agoudal	$-0.210 \pm 0.023$		IIAB	$-3.40 \pm 0.03$	
Sikhote Alin	$-0.228 \pm 0.025$		IIIAB	$-3.35 \pm 0.03$	
NWA 11420	$-0.203 \pm 0.045$		IVA	$-3.32 \pm 0.05$	
Saint Aubin	$-0.268 \pm 0.029$				
Cape York	$-0.196 \pm 0.043$				
Yanhuitlan	$-0.272 \pm 0.027$				
Duchesne	$-0.160 \pm 0.037$				
Weighted mean	$-0.227 \pm 0.006$	$0.03 \pm 0.06^a$ $1.04 \pm 0.08^b$	Weighted mean	$-3.37 \pm 0.01$	$1.04 \pm 0.09$

Error associated with weighted means are given in 1 standard error.

Mn-Cr model ages are determined using  $\epsilon^{53}\text{Cr}_i = -0.23^a$  and  $\epsilon^{53}\text{Cr}_i = -0.30^b$  in eq. 2.1 (see text). The procedure to determine Hf-W model ages is adopted from Kruijer *et al.* (2017) and determined using the following equation and parameters:

$$\Delta T = (-1/\lambda) \cdot \ln [(\epsilon^{182}\text{W}_{\text{sample}} - \epsilon^{182}\text{W}_{\text{chondrites}}) / (\epsilon^{182}\text{W}_{\text{SSI}} - \epsilon^{182}\text{W}_{\text{chondrites}})]$$

$\Delta T$  represents the time elapsed since the start of the solar system,  $\epsilon^{182}\text{W}_{\text{sample}}$  represents the pre-exposure  $\epsilon^{182}\text{W}$  of any iron meteorite group (Kruijer *et al.*, 2017),  $\epsilon^{182}\text{W}_{\text{chondrites}}$  is the composition of carbonaceous chondrites ( $-1.91 \pm 0.08$ ) (Kleine *et al.*, 2004),  $\epsilon^{182}\text{W}_{\text{SSI}}$  is the Solar System initial of  $-3.49 \pm 0.07$  as obtained from CAI (Kruijer *et al.*, 2014), and  $\lambda$  is the decay constant of  $^{182}\text{Hf}$  of  $0.078 \pm 0.002 \text{ My}^{-1}$  ( $2\sigma$ ) (Vockenhuber *et al.*, 2004).

A better fit between Mn-Cr and Hf-W model ages are obtained when Mn-Cr model ages are determined using  $\epsilon^{53}\text{Cr} = -0.30$ .

**Table S2.3.**Summary of  $(^{53}\text{Mn}/^{55}\text{Mn})_i$  and  $(\epsilon^{53}\text{Cr})_i$ .

$(^{53}\text{Mn}/^{55}\text{Mn})_i$	$(\epsilon^{53}\text{Cr})_i$	References	Method/Approach
$(8.5 \pm 1.5) \times 10^{-6}$	$-0.21 \pm 0.09$	Shukolyukov and Lugmair (2006)	Bulk CC isochron
$(6.53 \pm 1.93) \times 10^{-6}$	$-0.23 \pm 0.11$	Trinquier <i>et al.</i> (2008b)	Inner solar system
$(6.28 \pm 0.66) \times 10^{-6}$		Trinquier <i>et al.</i> (2008b)	Orgueil (CI1) leachates
$(9.1 \pm 1.7) \times 10^{-6}$		Nyquist <i>et al.</i> (2009)	Best Estimate from $(^{53}\text{Mn}/^{55}\text{Mn})_i$ vs. $(^{26}\text{Al}/^{27}\text{Al})_i$
$6.8 \times 10^{-6}$	-0.177	Göpel <i>et al.</i> (2015)	Bulk CC isochron calibrated against the solar system age
	$-0.30 \pm 0.05$	This study	Proposed from combined Mn-Cr and Hf-W chronometry of IIAB, IIIAB and IVA iron meteorite groups

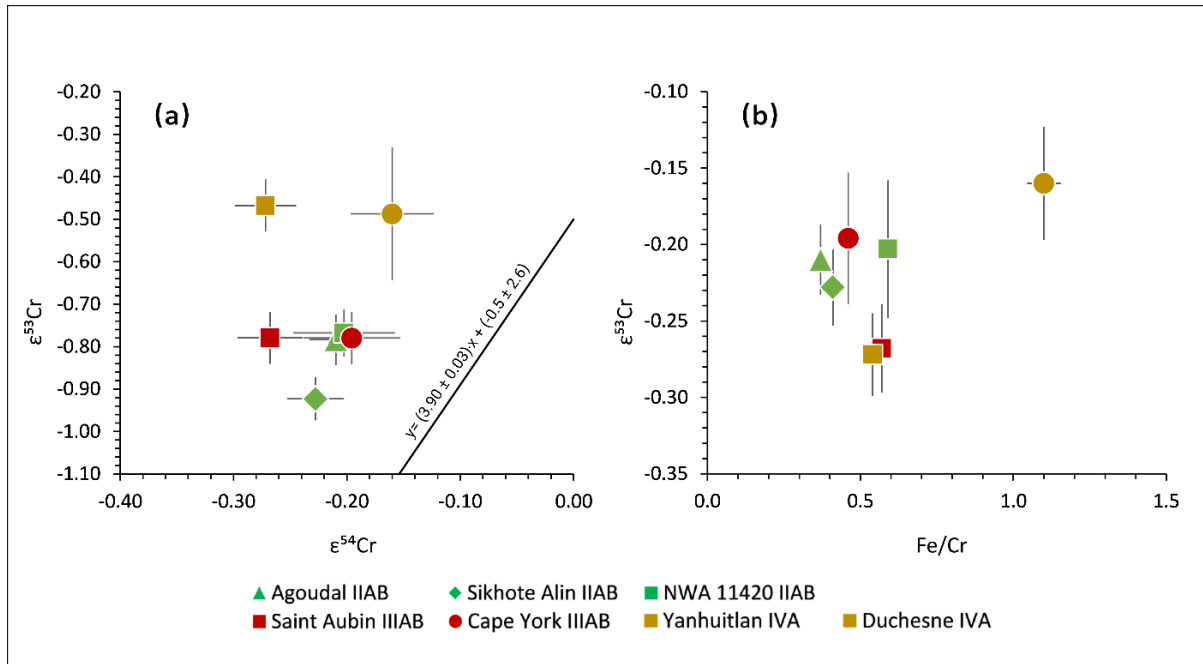


**Figure S2.1.** (a)  $\epsilon^{54}\text{Cr}$  vs.  $\epsilon^{53}\text{Cr}$  and (b)  $\text{Fe/Cr}$  vs.  $\epsilon^{53}\text{Cr}$  plots for the analysed iron meteorite samples. The black line in (a) shows a linear correlation between excesses in  $\epsilon^{54}\text{Cr}$  and  $\epsilon^{53}\text{Cr}$  [ $y = (3.90 \pm 0.03) \cdot x + (-0.5 \pm 2.6)$  (95% conf.)] determined by Liu *et al.* (2019) for iron meteorites analysed by Qin *et al.* (2010); Bonnand and Halliday (2018) and Liu *et al.* (2019). The error on the correlation line is not shown for the sake of clarity. The  $\epsilon^{54}\text{Cr}$  and  $\epsilon^{53}\text{Cr}$  values show no correlation for the analysed chromite/daubréelite fractions and corroborates to the negligible spallogenic contribution in these components.

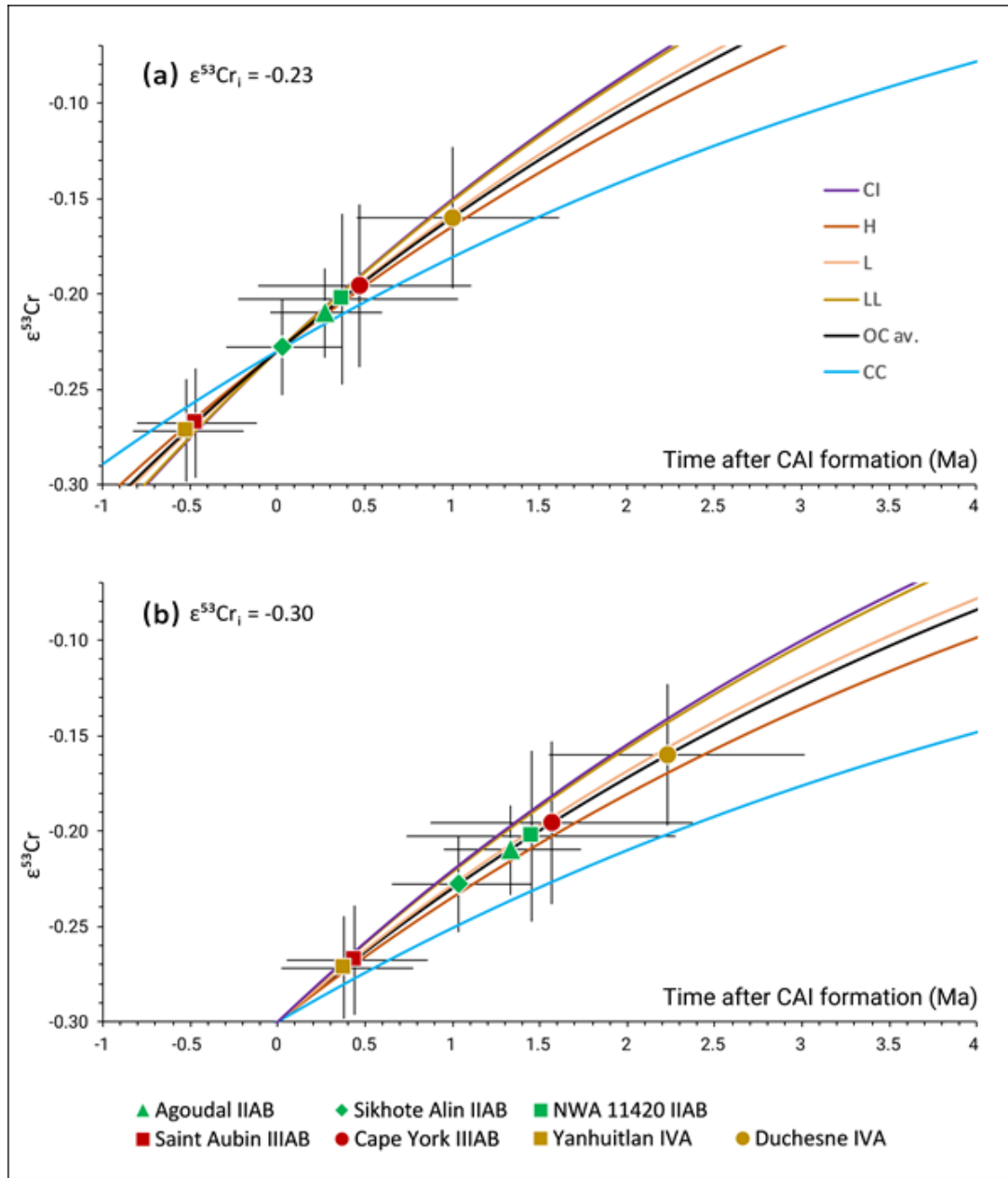


**Figure S2.2.** Mn-Cr model ages plotted on an  $\epsilon^{53}\text{Cr}$  evolution curve using Eq. 2.1 and solar system initial (a)  $\epsilon^{53}\text{Cr}_i = -0.23$  from Trinquier *et al.* (2008) and (b)  $\epsilon^{53}\text{Cr}_i = -0.30$  proposed in the present study (see text for the model age calculation). Different evolutionary paths represent different Mn/Cr ratios of the parent bodies. The trajectories are derived using Eq. 2.1 with the following Mn/Cr ratios: CI chondrites (0.84), H chondrites (0.69), L chondrites (0.76), LL chondrites (0.83), combined OCs (0.74) and combined CC chondrites (0.52) (Zhu *et al.*, 2021). Error bars represent 2SE uncertainties. Model ages for IIAB, IIIAB and IVA groups are unaffected by the growth trajectory chosen, given current analytical resolution. Assuming a Mn/Cr similar to carbonaceous chondrites would change the model ages by a maximum of 1 Ma for the youngest sample. However, since all samples belong to the non-carbonaceous group, the average composition of OCs is most appropriate.

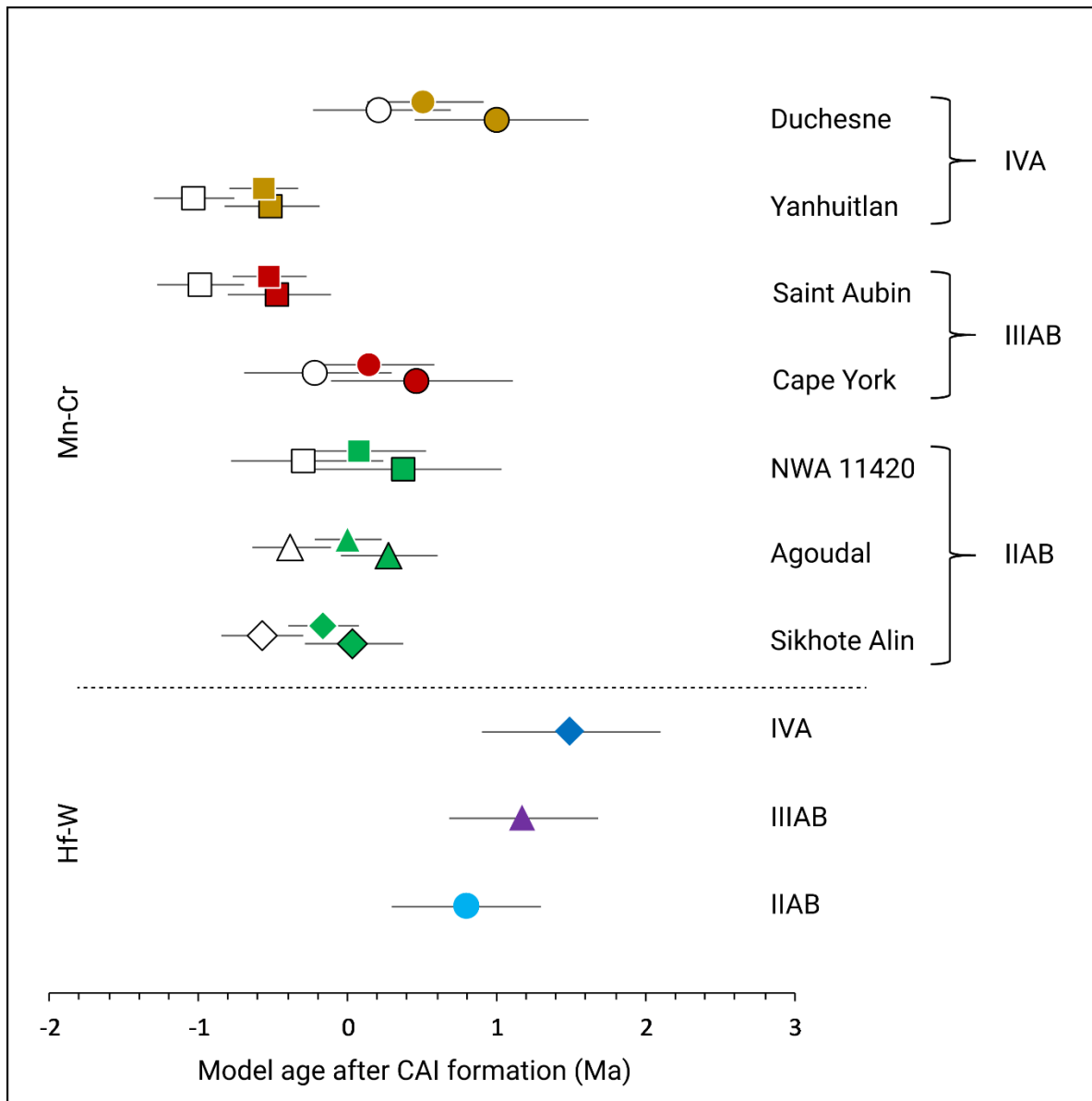


**Figure S2.3.** Mn-Cr (present study) and Hf-W (Kruijer *et al.*, 2017) core formation ages. Mn-Cr model ages for each sample are determined using solar system initial  $\epsilon^{53}\text{Cr}$  and canonical ( $^{53}\text{Mn}/^{55}\text{Mn}$ )<sub>ss</sub> values taken from Trinquier *et al.* (2008) (closed), Göpel *et al.* (2015) (open) and Shukolyukov and Lugmair, (2006) (uncoloured).

## Supplementary Information References

Birck, J.L. and Allègre, C.J. (1985) Isotopes produced by galactic cosmic rays in iron meteorites. *Isotopic ratios in the solar system 1*, 21–25.

Bonnand, P., Halliday, A.N. (2018) Oxidized conditions in iron meteorite parent bodies. *Nature Geoscience* 11, 401–404.

Göpel, C., Birck, J.L., Galy, A., Barrat, J.A., Zanda, B. (2015) Mn-Cr systematics in primitive meteorites: Insights from mineral separation and partial dissolution. *Geochimica et Cosmochimica Acta* 156, 1–24.

Kleine, T., Mezger, K., Palme, H., Münker, C. (2004) The W isotope evolution of the bulk silicate Earth: Constraints on the timing and mechanisms of core formation and accretion. *Earth and Planetary Science Letters* 228, 109–123.

Kruijer, T.S., Burkhardt, C., Budde, G., Kleine, T. (2017) Age of Jupiter inferred from the distinct genetics and formation times of meteorites. *Proceedings of the National Academy of Sciences* 114, 6712–6716.

Kruijer, T.S., Kleine, T., Fischer-Gödde, M., Burkhardt, C., Wieler, R. (2014) Nucleosynthetic W isotope anomalies and the Hf-W chronometry of Ca-Al-rich inclusions. *Earth and Planetary Science Letters* 403, 317–327.

Liu, J., Qin, L., Xia, J., Carlson, R.W., Leya, I., Dauphas, N., He, Y. (2019) Cosmogenic effects on chromium isotopes in meteorites. *Geochimica et Cosmochimica Acta* 251, 73–86.

Moynier, F., Yin, Q.Z., Jacobsen, B. (2007) Dating the first stage of planet formation. *The Astrophysical Journal Letters* 671, 181.

Nyquist, L.E., Kleine, T., Shih, C.Y., Reese, Y.D. (2009) The distribution of short-lived radioisotopes in the early solar system and the chronology of asteroid accretion, differentiation, and secondary mineralization. *Geochimica et Cosmochimica Acta* 73, 5115–5136.



O'Hara, M.J., Kellogg, C.M., Parker, C.M., Morrison, S.S., Corbey, J.F., Grate, J.W. (2017) Decomposition of diverse solid inorganic matrices with molten ammonium bifluoride salt for constituent elemental analysis. *Chemical Geology* 466, 341-351.

Qin, L., Alexander, C.M.O.D., Carlson, R. W., Horan, M.F., Yokoyama, T. (2010) Contributors to chromium isotope variation of meteorites. *Geochim. Cosmochim. Acta* 74, 1122–1145.

Schoenberg, R., Merdian, A., Holmden, C., Kleinhanns, I.C., Haßler, K., Wille, M., Reitter, E. (2016) The stable Cr isotopic compositions of chondrites and silicate planetary reservoirs. *Geochimica et Cosmochimica Acta* 183, 14–30.

Schoenberg, R., von Blanckenburg, F. (2005) An assessment of the accuracy of stable Fe isotope ratio measurements on samples with organic and inorganic matrices by high-resolution multicollector ICP-MS. *International Journal of Mass Spectrometry* 242, 257–272.

Shields, W.R., Murphy, T.J., Catanzaro, E.J., Garner, E.L. (1966) Absolute isotopic abundance ratios and the atomic weight of a reference sample of chromium. *Journal of Research of the National Bureau of Standards Section A: Physics and Chemistry* 70A, 193.

Shukolyukov, A., Lugmair, G.W. (2006) Manganese-chromium isotope systematics of carbonaceous chondrites. *Earth and Planetary Science Letters* 250, 200–213.

Trinquier, A., Birck, J.L., Allègre, C.J. (2007) Widespread  $^{54}\text{Cr}$  heterogeneity in the inner solar system. *The Astrophysical Journal* 655, 1179–1185.

Trinquier, A., Birck, J.L., Allègre, C.J. (2008a) High-precision analysis of chromium isotopes in terrestrial and meteorite samples by thermal ionization mass spectrometry. *Journal of Analytical Atomic Spectrometry* 23, 1565–1574.

Trinquier, A., Birck, J.L., Allègre, C.J., Göpel, C., Ulfbeck, D. (2008b)  $^{53}\text{Mn}$ - $^{53}\text{Cr}$  systematics of the early Solar System revisited. *Geochimica et Cosmochimica Acta* 72, 5146–5163.

Vockenhuber, C., Oberli, F., Bichler, M., Ahmad, I., Quitté, G., Meier, M., Halliday, A.N., Lee, D.C., Kutschera, W., Steier, P., Gehrke, R.J. (2004) New half-life measurement of  $^{182}\text{Hf}$ : Improved chronometer for the early solar system. *Physical Review Letters* 93, 172501.

Yamakawa, A., Yamashita, K., Makishima, A., Nakamura, E. (2009) Chemical separation and mass spectrometry of Cr, Fe, Ni, Zn, and Cu in terrestrial and extra-terrestrial materials using thermal ionization mass spectrometry. *Analytical Chemistry* 81, 9787–9794.

Zhu, K., Moynier, F., Wielandt, D., Larsen, K.K., Barrat, J.A., Bizzarro, M., (2019) Timing and origin of the angrite parent body inferred from Cr isotopes. *The Astrophysical journal letters*, 877(1), p.L13.

Zhu, K., Moynier, F., Schiller, M., Alexander, C.M.O., Davidson, J., Schrader, D.L., van Kooten, E., Bizzarro, M. (2021) Chromium isotopic insights into the origin of chondrite parent bodies and the early terrestrial volatile depletion. *Geochimica et Cosmochimica Acta* 301, 158-186.

## **Declaration of consent**

on the basis of Article 18 of the PromR Phil.-nat. 19

Name/First Name:

Registration Number:

Study program:

Bachelor ☐      Master ☐      Dissertation ☐

Title of the thesis:

Supervisor:

I declare herewith that this thesis is my own work and that I have not used any sources other than those stated. I have indicated the adoption of quotations as well as thoughts taken from other authors as such in the thesis. I am aware that the Senate pursuant to Article 36 paragraph 1 litera r of the University Act of September 5th, 1996 and Article 69 of the University Statute of June 7th, 2011 is authorized to revoke the doctoral degree awarded on the basis of this thesis.

For the purposes of evaluation and verification of compliance with the declaration of originality and the regulations governing plagiarism, I hereby grant the University of Bern the right to process my personal data and to perform the acts of use this requires, in particular, to reproduce the written thesis and to store it permanently in a database, and to use said database, or to make said database available, to enable comparison with theses submitted by others.

Place/Date

Signature

# Aryavart Anand

Institute of Geological Sciences, Baltzerstrasse 1+3, Bern, Switzerland, CH-3012

aryavart.anand@geo.unibe.ch • Skype – aryavart7 • +41-762947836

DOB - 01/11/1995

## Education

- 2018 – Present     **University of Bern** – Bern, Switzerland  
PhD candidature in Isotope Cosmochemistry  
Mass-independent Cr isotopic constraints on the accretion, differentiation, thermal history and genealogy of the earliest formed planetesimals of the Solar System.  
Supervisors: Dr. Klaus Mezger and Dr. Beda Hofmann
- 2013 – 2018     **Indian Institute of Technology Roorkee** – Roorkee, India  
Integrated Master of Technology in Geological Technology  
CGPA: 8.23/10.  
MTech Research Project: Reactivation of Northern and Southern margins of the Archaean Bundelkhand Craton: Studies from the marginal sedimentary basins.

## Publications

- submitted*     **Anand, A.**, Singh, A. K., Mezger, K. and Pati, J. K., Chromium Isotopes Identify the Extraterrestrial Component in Impactites from Dhala Impact Structure, India
- submitted*     **Anand, A.**, Kruttasch, P. M. and Mezger, K.,  $^{53}\text{Mn}$ - $^{53}\text{Cr}$  chronology and  $\epsilon^{54}\text{Cr}$ - $\Delta^{17}\text{O}$  genealogy of Erg Chech 002: the oldest andesite in the Solar System.
- 2021     **Anand, A.**, Pape, J., Wille, M., Mezger, K. and Hofmann, B., 2021. Early differentiation of magmatic iron meteorite parent bodies from Mn-Cr chronometry. *Geochemical Perspective Letters* 20, 6–10.
- 2021     **Anand, A.**, Pape, J., Wille, M. and Mezger, K., 2021. Chronological constraints on the thermal evolution of ordinary chondrite parent bodies from the  $^{53}\text{Mn}$ - $^{53}\text{Cr}$  system. *Geochimica et Cosmochimica Acta* 307, 281–301.
- 2021     Hifzurrahman, Nasipuri, P., Yi, K., **Anand, A.**, Misra S. and Champati A. K., 2021. An age-integrated geochemical and computational phase-equilibria study from the Wangtu Gneissic Complex, NW Himalaya, and its paleogeographic implications in Columbia assembly. *Mineralogy and Petrology* 115, 365–390.